THE ROLE OF LIPID IN MALARIA PIGMENT (HAEMOZOIN) FORMATION UNDER BIOMIMETIC CONDITIONS

MELVIN ANYASI AMBELE

Thesis Presented for the Degree of

DOCTOR OF PHILOSOPHY

In the Department of Chemistry

UNIVERSITY OF CAPE TOWN

October 2013

Supervisor: Professor Timothy. J. Egan

UNIVERSITY OF CAPE TOWN
IYUNIVESITHI YASEKAPA • UNIVERSITEIT VAN KAAPSTAD

ABSTRACT

Previous studies have proposed lipids and/or proteins to be involved in the biomineralization process of haemozoin formation in the malaria parasite which is a target for many antimalarial drugs. This study therefore investigated the biomolecules involved and established the role of lipids in mediating Hz formation under biomimetic conditions.

Hz crystals were isolated from mature trophozoites obtained from saponin-lysed iRBCs. Trophozoites were triturated to release digestive vacuoles and subjected to freeze/thaw cycles to release Hz. Supernatant from SDS-washed Hz crystals and solution of dissolved crystals in NaOH were used for SDS PAGE and LC-MS/MS protein identification. None of the proteins HRPII, HDP, or those belonging to the proposed protein complex previously suggested to be involved in Hz formation *in vivo*, were identified in the proteome associated with Hz crystals. In addition, no 'stand out' proteins with expected Hz-mediating activity in the malaria parasite were identified. Contrastingly, putative lipoproteins and uncharacterized proteins with roles in lipid binding and transport were identified for the first time in the proteome associated with Hz crystals. Lipids consisting of MSG, MPG, DPG, DLG and DOG (NLB) previously reported to be associated with Hz crystals were easily identified to be associated with Hz crystals. Lipid was also found to be in vastly greater abundance than proteins in the Hz crystal. The absence, therefore, of all proteins previously suggested to be involved in Hz formation from the proteome associated with the Hz crystal, coupled with the identification of lipoproteins and the easily detected abundance of lipids with Hz-mediating activity, strongly suggest that lipids are the biomolecules responsible for the biomineralization of Hz formation *in vivo*.

A solution mixture of NLB and haematin both prepared in acetone/methanol deposited on citrate buffer (50 mM, pH 4.8, 37^{o}C), was allowed to incubate at 37^{o}C for different lengths of time to investigate β-haematin formation. The product formed was confirmed by FT-IR to be β-haematin. The reaction was very fast giving yields of about 90% at 2.15 and 1.07 lipid-to-haem mol ratios and was completed in less than 10 min. The reaction only slowed when there were two haem molecules to one fatty acid chain, but still gave yields of about 90% in under 30 min. On the other hand, this slower kinetics allowed for the effects of relevant biological ions on the process to be investigated. Relevant biological ions at concentrations which they exist in RBC and/or blood are unlikely to greatly affect the lipid mediated process of Hz formation *in vivo* as only a 2.3 fold decrease in kinetics was observed in the presence of these

ions. β-Haematin formed over time during the reaction showed an increase in fluorescence measured using confocal laser microscopy. This qualitatively corresponds to that of bulk kinetic measurements and also demonstrates the formation of well-ordered crystals *in situ* in association with the lipid component of the emulsion. However, the β-haematin crystals formed seemed to have a distinct external morphology different from Hz itself and thus this was investigated further.

Solutions of NLB and haematin in acetone/methanol were mixed by means of vortexing, ultrasonication or micromixing before being used for β-haematin formation reactions. The β-haematin crystals formed at the emulsion layer as well as lipid droplets were characterized by TEM, TEM-ED and ESI/EELS and were compared to Hz. β-Haematin crystals formed from the vortexed mixture appeared to be smaller in size with external morphology and *hkl* indices different from Hz while ultrasonication or micromixing produced very long β-haematin crystals that are identical to Hz both in overall crystal habit and form. An observed difference in texture between the β-haematin crystals and Hz was likely due to the presence of proteins and lipids on the Hz crystal as shown in the proteomic and lipid studies of this work. The external morphology of the β-haematin formed was not affected by the NLB-to-haematin ratio at any given time nor by the kinetics of the crystal growth process. β-Haematin crystals formed at the emulsion layer were always seen to make contact with non-hollow lipid droplets with continuous hydrophobic interiors via their {100} faces. The lipid droplets in contact with crystals were found to control the length of the crystal. Growth stopped when the angle of contact between the lipid and crystal reached approximately 38^{o}. The invariable observation of β-haematin crystals with their {100} face in contact with lipid droplets that control their sizes strongly suggests that lipids act as the nucleator, providing a favourable microenvironment suitable for the interaction with the propionic acid groups at the {100} surface of the crystal via the glycerol –OH group of the lipid.

The proposal that lipids are the sole biomolecules responsible for Hz formation *in vivo* is strongly supported by the following findings: Firstly, all the proteins previously suggested to be involved in Hz formation were absent from the proteome associated with Hz. Interestingly, it was lipids that were found to be in relative abundance over these proteins in the Hz crystal. Secondly, these lipids were highly efficient in mediating β-haematin formation under biomimetic conditions producing crystals that were identical in overall habit and form to that of Hz itself. Finally, the lipid droplets invariably observed in contact with the crystals, controls their size and probably nucleate crystal growth via their {100} faces.

DECLARATION

I declare that “The role of lipid in malaria pigment (Haemozoin) formation under biomimetic conditions” is my own work and that all sources that I have used or quoted have been indicated and acknowledged by means of complete references.

Melvin A. Ambele

ACKNOWLEDGEMENTS

I would like to take this opportunity to express gratitude and thanks to my supervisor Prof. Timothy J. Egan for admitting me into his lab and providing the funds for this work. I am also grateful for his continuous guidance and oversight of this work.

I would also like to thank the following people for their contributions towards this thesis:

- Aneesa Omar for taking me into the lab on my birthday to do my first PhD experiment. Working with you in the lab was wonderful for you are a true partner indeed.
- David Kuter for preparing Figure 5.12 of this work and also for his technical assistance which I could always count on.
- Roxanne for bringing some life into the working environment and making it less stressful and more enjoyable. You are good team player and sharing office space with you was wonderful.
- Mrs Jill Combrinck for your kind donations of malaria parasites and many more materials relating to the parasite work.
- John Woodland for sacrificing your weekends to proof-read my work and other related materials. I can't be more grateful to you.
- Khwezi for your moral support.
- Kathryn Wicht for being a good team player to the Egan group.
- Dr Ncokazi for mentoring me during the first few months of my PhD work.
- Staff at the Pharmacology Department; Prof. Peter Smith, Sumaya and Dr Taylor.
- Staff at the Electron Microscopic Unit; Prof. Trevor Sewell, Dr Webber and Mr Jaffer.
- Friends; Mbandi, Apana, Chemuta, Azenwi, Shumbe.
- My siblings; Carl, Afor, Eric, Alain, Okawah, families; Florence, Dr Akwinga, Sahara, Dan, Martin, Essel's, Darkwa's and Nchinda's.
- My wife Akosua Ambele and our daughter Endah Ambele for being patient and supportive throughout this work.
- My Dad, Mr Lucas Ambele, of blessed memory and my Mom, Endah Ambele, for their unlimited support and investment in my life and education.
- This work was supported by the NIH and the University of Cape Town.

CONFERENCE PROCEEDINGS AND PUBLICATIONS ARISING FROM THIS WORK

CONFERENCE PROCEEDINGS

2011: 16–21st January, 40th Convention of the South African Chemical Institute, University of Witwatersrand, Johannesburg, South Africa.

Poster: "Effects of haematin and *rac*-Glycerol 1-myristate concentration on β-haematin formation"

2011: 7–12th August, 15th International Conference on Biological Inorganic Chemistry, British Columbia University, Vancouver, Canada.

Poster: "Kinetics of lipid mediated β-haematin formation"

2012: 15–18th October, H 3-D Symposium held, Cape Town, South Africa.

Poster: "Kinetics of lipid mediated β-haematin formation" (**Won best poster prize**).

2012: 2–7th December, 50th Annual Conference of the Microscopic Society of Southern Africa, University of Cape Town, South Africa.

Talk: "Structure of neutral lipid emulsions and the localization of β-haematin crystals".

2013: 22–26th July, 16th International Conference on Biological Inorganic Chemistry Grenoble, France.

Poster: "Nucleation of β-Haematin Crystals by Lipids and Effects of Chloroquine" (**Won best poster prize**).

PUBLICATIONS

Combrinck, J. M., Mabotha, T. E., Ncokazi, K. K., Ambele, M. A., Taylor, D., Smith, P. J., Hoppe, H. C. and Egan, T. J. Insights into the Role of Heme in the Mechanism of Action of Antimalarials. *ACS Chemical Biology*. **2012**.

Ambele, M., A. and Egan, T., J. Neutral lipids associated with haemozoin mediate efficient and rapid beta-haematin formation at physiological pH, temperature and ionic composition. *Malar. J*. **2012**, 11:337.

Ambele, M., A, Sewell, B., Cummings, F., Smith, P., J. and Egan, T., J. Synthetic Hemozoin (β-Hematin) Crystals Nucleate at the Surface of Neutral Lipid Droplets that Control Their Sizes. *Cryst. Growth Des.* **2013**, 13, 4442–4452.

ABBREVIATIONS

Å	Angstrom
CQ	Chloroquine
DiO	Lipophilic 3,3’-dioctadecyloxacarbocyanine perchlorate fluorescent dye
DLG	1,3-dilineoylglycerol
DOG	1,3-dipalmitoylglycerol
DPG	Dipalmitic glycerol
DV	Digestive vacuole
EELS	Electron energy-loss spectroscopy
ESI	Electron spectroscopic imaging
Fe(III)PPIX	Ferriprotoporphyrin IX
FT-IR	Fourier transform infrared spectroscopy
HAP	Histoaspartic protease
Hb	Haemoglobin
HDP	Haem detoxification protein
HEPES	4-(2-Hydroxyethyl)-1-piperazineethanesulfonic acid
HRPII	Histidine rich protein II
Hz	Hameozoin
iRBC	Infectde red blood cell
L/H	Lipid-to-haem mol ratio
LC-MS	Liquid chromatography coupled mass spectroscopy
LUV	Large unilamellar vesicle

MES	2-(N-morpholino)ethanesulfonic acid
MLV	Multilamellar vesicle
MPG	Monopalmitoylglycerol
MSG	Monostearoylglycerol
NLB	Neutral lipid blend
RBC	Red blood cell
SDS PAGE	Sodium dodecylsulphate polyacrylamide gel
SUV	Small unilamellar vesicle
TEM	Transmission electron microscopy
TEM-ED	Transmission electron microscopy- electron diffraction
WHO	World Health Organisation

TABLE OF CONTENTS

1. INTRODUCTION

2. MATERIALS, INSTRUMENTATION AND GENERAL METHODS

3. THE PROTEOME AND LIPIDS ASSOCIATED WITH HAEMOZOIN CRYSTALS

4. KINETIC STUDIES OF LIPID MEDIATED β-HAEMATIN FORMATION

1. INTRODUCTION

1.1 BACKGROUND REVIEW ON MALARIA

Giovanni Maria Lancisi was the first to describe a dark pigment found in the brains of malaria victims observed during a fever outbreak in Rome (Lancisi, 1717). It was only in 1847 that this pigment was again described by a German physician, H. Meckel, and later in 1849 it was linked to malaria by the pathologist Rudolf Virchow (Virchow, 1849). In 1880, Charles Laveran showed clear microscopic evidence of this pigment granule in the blood samples of people suffering from malaria (Laveran, 1880). It was the crystalline nature of the pigment that led Sir Ronald Ross to later on describe the transmission of the disease by mosquitoes (Ross, 1897).

Today, it is well established that malaria is caused by a parasitic protozoan belonging to the genus *Plasmodium*. There exist over 100 species of *Plasmodium* that cause malaria in various vertebrates, but of these, only *P. falciparum*, *P. malariae*, *P. vivax* and *P. ovale* are known to cause malaria exclusively in humans although the monkey malaria parasite *P. knowlesi* has also been reported to cause malaria in humans (Collins, 2012). Of all these species known to cause malaria in humans, *P. falciparum* is the most deadly. Infection in humans occurs from a bite of an infected female *Anopheles* mosquito in which sporozoites (the infective stage of the malaria parasite) are introduced into the bloodstream during the mosquito blood-feeding process.

The WHO World Malaria Report in 2011 showed approximately 3.3 billion people were at risk of malaria with a majority of the risk population living in sub-Saharan Africa. Children under 5 years of age and pregnant women living in sub-Saharan Africa constitute the most vulnerable group at risk and account for the majority of the cases estimated at 80% and 90% of malaria deaths worldwide (WHO, 2012). As of 2012, there were 104 countries and territories in which malaria was still considered endemic due to on-going malaria transmission. A world map of countries affected by malaria is shown in Figure 1.1. The disease burden cost an estimated 1.84 billion USD in 2012 in financing and implementation of malaria control programmes. Malaria is strongly linked to poverty as mortality rates remain high in very poor countries where a majority of the population survives on less than 1.25 USD a day. According to the WHO, the African countries of Nigeria, the Democratic Republic of the Congo, the United Republic of Tanzania, Uganda, Mozambique and Cote

d'Ivoire account for about 47% of all malaria cases in this region. India alone accounts for about 24 million cases per year in the South and South-East Asia region. Beside children under the age of five and pregnant women being the most vulnerable group to malaria morbidity and mortality, the recent WHO report has also classified people living with HIV/AIDS, non-immune migrants as well as mobile populations and travellers as belonging to the group of vulnerable individuals who need protection from malaria infection (WHO, 27 June, 2013). Despite efforts by WHO and the target set by Roll Back Malaria in combating malaria by 2015, only about 50 countries accounting for about 3% of total malaria cases are on track to reduce their malaria cases by 75%. Therefore, malaria still remains one of the major diseases of international public health interest.

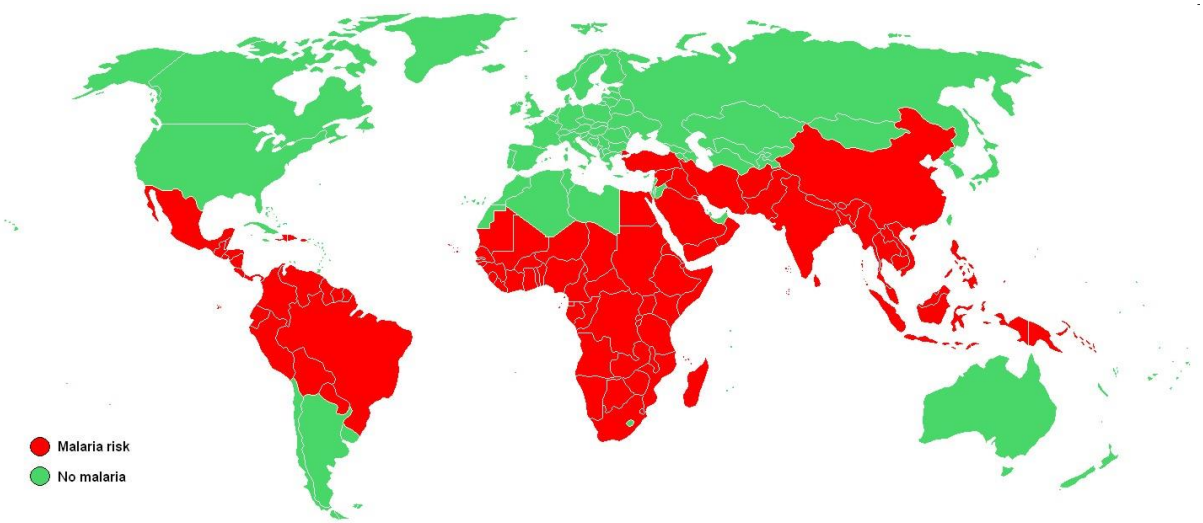

Figure 1.1: Countries shown on the map have malaria in at least part of their territory. (Reprinted from http://microbiologyspring2010.wikispaces.com/Malaria)

1.2 LIFE CYCLE OF MALARIA PARASITE

The parasite life cycle comprises two phases, a sexual phase which occurs in the mosquito and an asexual phase which occurs in humans as shown in Figure 1.2. During the mosquito blood feeding process, sporozoites released into the blood stream by the mosquito are transported to the liver where they undergo schizogony. Schizogony involves cell division (Mikolajczak et al. 2006) producing thousands of merozoites which are released into the bloodstream. In *P. vivax* but not in *P. falciparum* some of the parasites lie dormant in the liver (hypnozoites) and only become active some years later. Merozoites released into the bloodstream infect red blood cells (RBCs) and develop into the trophozoite stage (most

metabolically active stage of the parasite) in an intraerythrocytic life cycle. Trophozoites mature and undergo schizogony producing more merozoites which are eventually released into the bloodstream upon lysis of the RBC for another round of re-infection. Some of the merozoites develop into the male and female gametocytes (Mikolajczak et al. 2006). The gametocytes are ingested by a mosquito during its blood meal. Sexual reproduction forms zygotes which lead to the production of sporozoites in the mosquito intestine and are then transported to the salivary gland of mosquito. The sporozoites in the salivary gland can again be injected into a human during a subsequent blood meal and this continues the cycle (Figure 1.2).

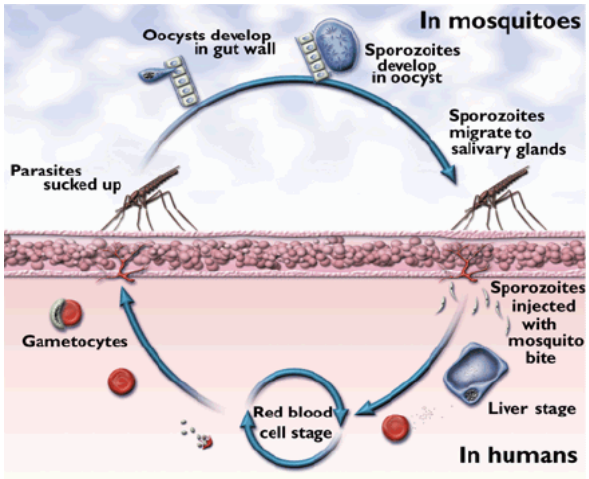

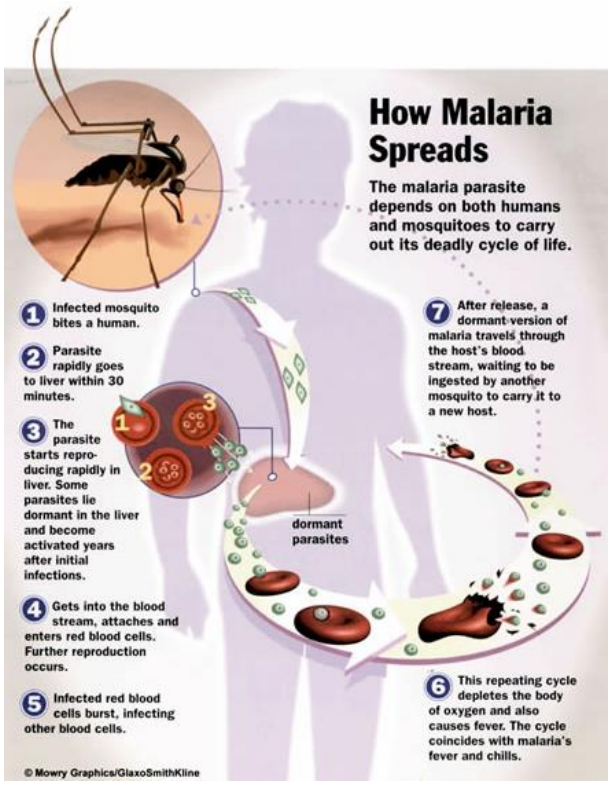

Figure 1.2. The life cycle of the malaria parasite. The sexual phase of the life cycle occurs inside the mosquito while the asexual phase occurs in the human. The asexual reproductive phase occurs predominantly in RBCs causing them to rupture thereby leading to the noticeable signs and symptoms of the disease in humans. (Reprinted from http://microbiologyspring2010.wikispaces.com/Malaria)

Parasites inside RBCs feed predominantly on RBC haemoglobin and lysis of the RBC to release new merozoites concurrently releases toxic parasitic waste into the bloodstream which sets off a wave of immunological reactions in the human body, resulting in some of the signs and symptoms of the disease. This therefore makes the intraerythrocytic stage of the

parasite life cycle a very important target in the study to develop drugs or vaccines in the fight against malaria.

1.3 HAEMOGLOBIN DIGESTION AND HAEM METABOLISM

Plasmodium falciparum is the most deadly species of *Plasmodium*. During its intraerythrocytic life cycle, it feeds on RBC haemoglobin to provide amino acids for its own protein synthesis (Rosenthal, 2004) and also to maintain osmotic stability (Lew et al. 2003). In this process, haemoglobin is first transported into the acidic digestive vacuole of the parasite through transport vesicles. The parasite in the RBC digests approximately 80% of the host cell haemoglobin during it intraerythrocytic life cycle (Mauritz et al. 2011 & Gligorijevic et al. 2006). The digestion of haemoglobin in the parasite digestive vacuole releases free haem which accumulates in the digestive vacuole and could result in parasite death through the generation of oxidative free radicals (Ziegler et al. 2001), peroxidization of membranes (Francis et al. 1997) and also damage to cellular metabolism through the inhibition of enzymes (Gluzman et al. 1994). Free haem released during the parasite feeding process is therefore potentially toxic to the parasite itself as it is not recycled or metabolised (Eckman et al. 1997). However, the parasite has developed a novel mechanism of detoxifying free haem by converting it into a non-toxic microcrystalline structure known as haemozoin or malaria pigment. Haemoglobin catabolism in the digestive vacuole is an orderly process which is carried out by a series of proteinases and includes aspartic proteases plasmepsin I & II, cysteine protease falcipains, metalloprotease falcilysin, dipeptidylaminopeptidase (PfDPAP1) and neutral aminopeptidases (Gorka et al. 2013) as shown in Figure 1.3. Plasmepsins I & II begin the enzymatic digestion of haemoglobin inside the digestive vacuole by cleaving the undenatured haemoglobin at the hinge region between amino acid residue α33Phe and α34Leu (Goldberg et al. 1991). Cleavage disrupts the tetrameric haemoglobin structure responsible for oxygen transport (Perutz et al. 1998) and exposes other protease cleavage sites. This initial cleavage of the undenatured haemoglobin also results to the release of its haem content (Goldberg et al. 1992). The resultant fragments from the initial plasmepsin digestion are further broken down into even smaller fragments by cysteine proteases falcipain II & III (Rosenthal, 2011) along with plasmepsin I, II & IV (Schlagenhauf et al. 2010 & Wyatt et al. 2002) and histo-aspartic protease, HAP (Gorka et al. 2013). These fragments are finally digested to 5-10 amino acid residues by a metalloprotease falcilysin by cleavage at polar and charged residues. A recently identified *P. falciparum*

dipeptidylaminopeptidase (PfDPAP1) in the DV (Klemba et al. 2004) which is an orthologue of cathepsin C lysosomal exopeptidase and is homologous to the mammalian type I dipeptidylaminopeptidase (DPAP1) is responsible for digesting the 5-10 residues into dipeptides (Klemba et al. 2004). The dipeptides are transported from the DV to the parasite cytoplasm by an unknown mechanism (Gorka et al. 2013) where they are then digested into amino acids by neutral aminopeptidase (Gavigan et al. 2001). The M1-family alanyl aminopeptidase (PfM1AAP) and M17-family leucyl aminopeptidase (PfM1LAP) are two neutral aminopeptidases described in the *Plasmodium falciparum* genome (Dalal et al. 2007). The latter is located in the cytoplasm while the former is a transmembrane protein which is proteolytically activated to its active form (Allary et al. 2002). The inhibition of these two aminopeptidases correlate with the inhibition of parasite growth (Skinner-Adams et al. 2007, Grembecka et al. 2003 & Gavigan et al. 2001) suggesting that the complete digestion of haemoglobin is required for parasite development. Incubation of purified digestive vacuole lysate with denatured globin at acidic pH has shown that aspartic proteases and cysteine proteases account for 60-80% and 20-40% of globin degrading activity in the digestive vacuole respectively (Francis et al. 1996, Gluzman et al. 1994 & Goldberg et al. 1990). The activities of these two groups of enzymes are completely blocked by a combination of pepstatin and E-64, which are specific inhibitors for aspartic and cysteine proteases respectively, thereby suggesting these two enzymes are responsible for globin degradation in the digestive vacuole (Gluzman et al. 1994).

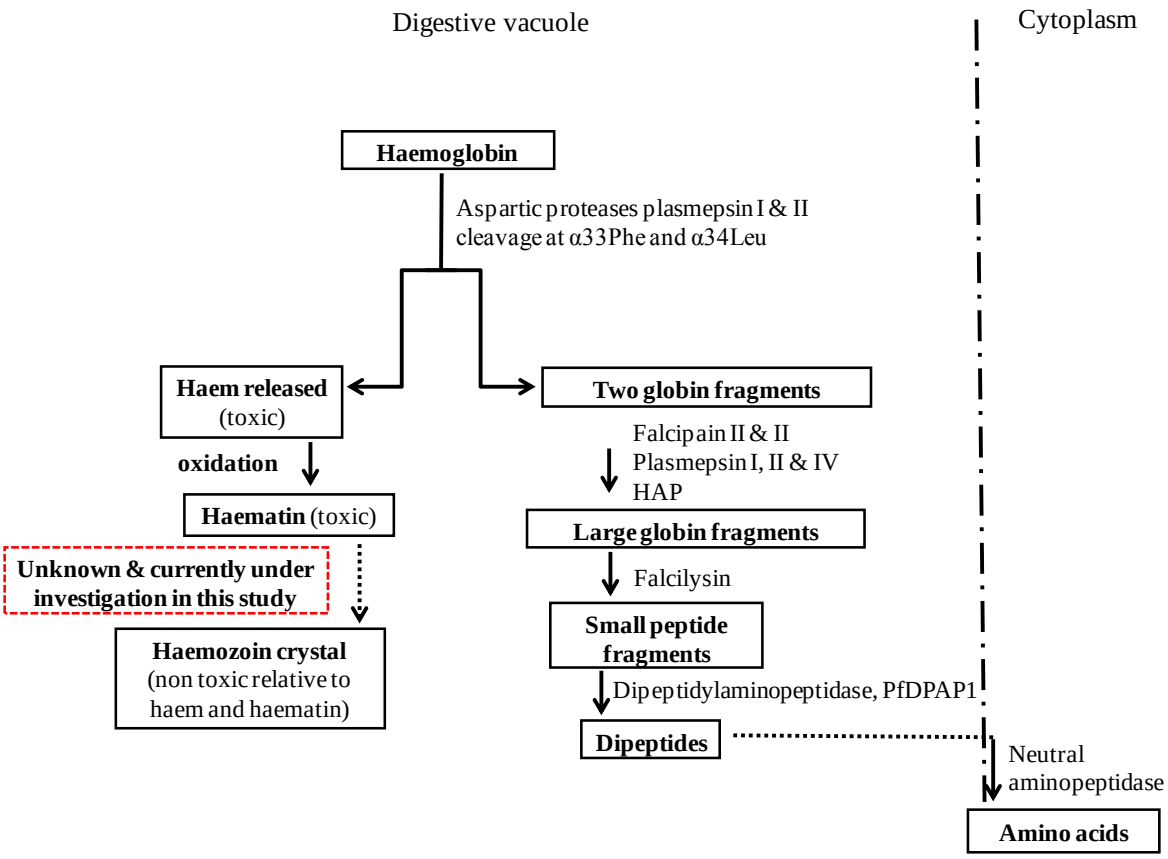

Figure 1.3. Schematic representation of haemoglobin digestion and haemozoin formation in *P. falciparum*.

Despite the well-known functions of protein-bound haem in biologically-important processes such as oxygen transport, signal transduction and respiratory photosynthesis (Ponka et al. 1999), the presence of free haem in a biological system can contribute to alkyl and peroxyl radicals formation, by means of hydroperoxide decomposition mediated by haem (Davies, 1988 and Van der Zee et al. 1996) which can cause potential damage to other biological structures such as interferance with membrane integrity (Schmitt et al. 1993). However, in most biological systems where free haem is known to be produced, the organism has evolved to develop unique ways of protecting itself against the adverse effect of free haem (Schacter et al. 1988) with haemozoin formation being the mechanism of detoxification of free haem in *P. falciparum* (Egan et al. 2002).

1.4 A BRIEF OVERVIEW OF HAEMOZOIN: A HAEM DETOXIFICATION PRODUCT IN THE MALARIA PARASITE

As stated above, haemozoin (malaria pigment) was described as far back as 1849 by Rudolf Virchow and was later shown to comprise haem which gives it its dark colour (Carbone, 1891

& Brown, 1911). Interest in the study of haemozoin only developed much later in the late 1980s when Fitch et al. (1987) showed that haemozoin consists entirely of iron(III)protoporphyrin IX (Fe(III)PPIX) (Fitch et al. 1987). This was followed by the determination of its chemical composition in the early 1990s by Slater et al. (1991). Haemozoin crystal formation is thought to occur via a biomineralization process (Egan et al. 2001) in the malaria parasite. The formation of this crystal has also been observed in several blood-feeding organisms such as *R. prolixus* (Oliveira et al. 1999), *S. mansoni* (Oliveira et al. 2000) and *H. columbae* (Chen et al. 2001). Blood-feeding organisms that produce haemozoin obtain their nutrients by feeding on haemoglobin and in the process produce large quantities of free haem (Francis et al. 1997). Haemozoin formation in the digestive vacuole of the malaria parasite is the main haem detoxification process of the parasite as shown by electron spectroscopic imaging (ESI) and electron energy loss spectroscopy (EELS) of *P. falciparum* infected erythrocytes and by Mössbauer spectra of parasites accounting for at least 95% of ingested haem (Egan et al. 2002). Many antimalarial drugs are now known to act by inhibiting the haemozoin formation process (Egan et al. 1994, Tekwani et al. 2005, Hänscheid et al. 2007, Sandlin et al. 2011 & Combrinck et al. 2012). Great advances have been made so far in studying the formation of synthetic haemozoin (β-haematin) crystals both under physiological and non-physiological (Egan et al. 2006) conditions of temperature and pH in the presence of organic solvents such as pentanol and octanol (Egan et al. 2006), MeOH-DMSO and $CHCl_3$ (Buller et al. 2002), polyethylene glycols (Stiebler et al. 2010b), lipids (Egan et al. 2006, Hoang et al. 2010 a, b, Pisciotta et al. 2007 and Jackson et al. 2004) and proteins (Jani et al. 2008, Sullivan et al. 1996 and Chugh et al. 2012) to better understand how this process occurs *in vivo*. However, current knowledge still does not fully explain the detailed biomineralization process by which haemozoin formation occurs *in vivo* in the malaria parasite. Therefore, this subject is an interesting area of current research as that could open up new avenues for drug discovery in malaria.

1.5 CHARACTERIZATION OF HAEMOZOIN CRYSTALS

The characteristics of the haemozoin crystal can be described in terms of its physicochemical properties and also its morphological and crystallographic properties.

1.5.1 Physicochemical properties

Haemozoin, described by Fitch et al. in 1987 as consisting entirely of Fe(III)PPIX, was shown to be chemically identical to a synthetic precipitate known as β-haematin (Table 1.1).

Spectroscopically, the infrared (IR) spectrum and x-ray powder diffraction pattern of β-haematin crystals prepared by Slater et al. (1991) under acidic conditions (pH 4.5) by heating Cl-Fe(III)PPIX in 4.5 M acetic acid at 70^{o}C showed it is identical to natural haemozoin. Similarly, the solubility properties of both β-haematin and haemozoin were also shown to be identical as they both dissolve in DMSO and aqueous alkaline solution (Slater et al. 1991).

Table 1.1. Elemental compositions of haemozoin and β-haematin as determined in 1991 by Slater et al. Reproduced from Slater, A. F. G., Swiggard, W. J., Orton, B. R., Flitter, W. D., Goldberg, D. E., Cerami, A. & Henderson, G. B. An iron-carboxylate bond links the heme units of malaria pigment. *Proc. Natl Acad. Sci. USA*. **1991**, 88, 325-329.

	Percent by weight		
Element	**Hemozoin**	**β-Hematin**	**Hematin (theory)**
Carbon	63.7	64.7	64.5
Hydrogen	5.6	5.0	5.3
Nitrogen	7.5	8.7	8.8
Iron	7.5	8.3	8.8
Chlorine	<0.1	<0.3	–
Oxygen*	15.6	13.3	12.6

*As an accurate elemental analysis for oxygen cannot be performed in the presence of significant amounts of iron, the oxygen values represent the percent weight remaining.

Furthermore, the chemical structures of both β-haematin and haemozoin were investigated by Fourier transform infrared (FT-IR) spectroscopy. Both exhibit intense peaks at 1664 and 1211 cm^{-1}, vibrational stretching frequencies corresponding to C=O and C–O bonds typical of a carboxylate group coordinated to Fe(III) (Figure 1.4A). Meanwhile, the FT-IR spectrum of haematin was completely different from that of both haemozoin and β-haematin (Figure 1.4B). In addition, the x-ray powder diffraction patterns of both β-haematin and haemozoin were identical (Figure 1.5), confirming that this synthetic counterpart of haemozoin is structurally identical to natural haemozoin isolated from the parasite itself.

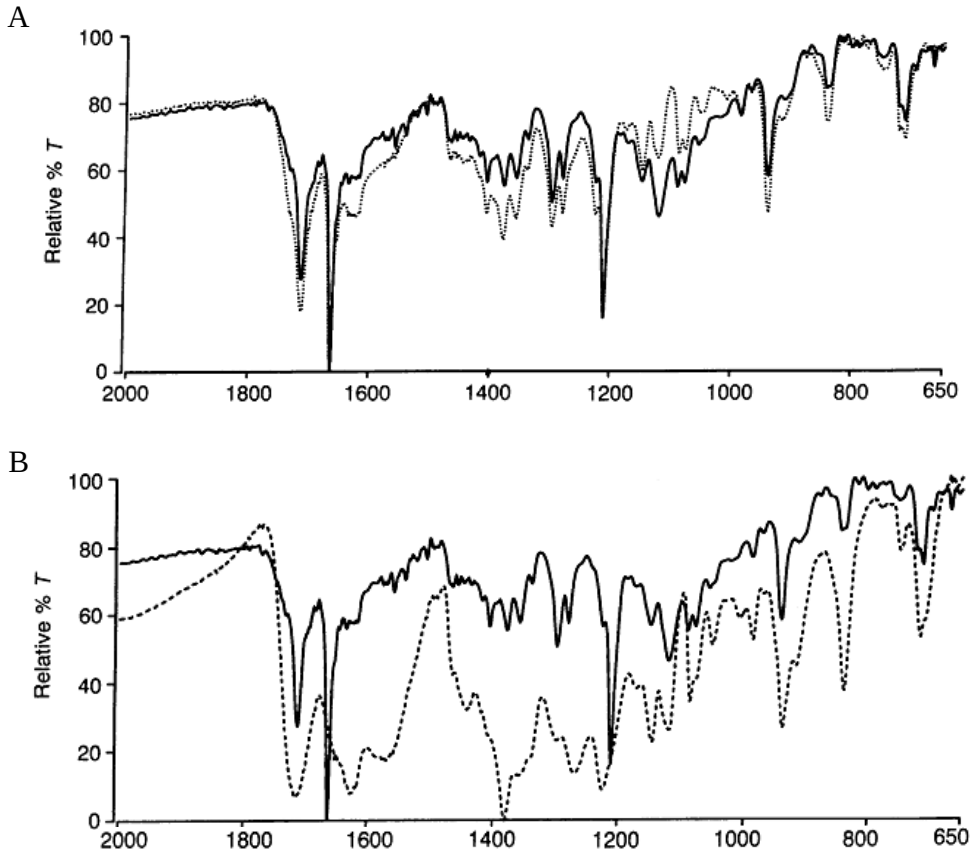

Figure 1.4. FT-IR spectra of haemozoin (–) and β-haematin (**...**), (A). Those of hemozoin (–) and haematin (---) appeared to be completely different, (B). T is transmittance. Reprinted from A. F. G Slater, W. J. Swiggard, B. R Orton, W. D. Flitter, D. E. Goldberg, A. Cerami and G. B. Henderson, *Proc. Natl Acad. Sci.*, 1991, **88**, 325.

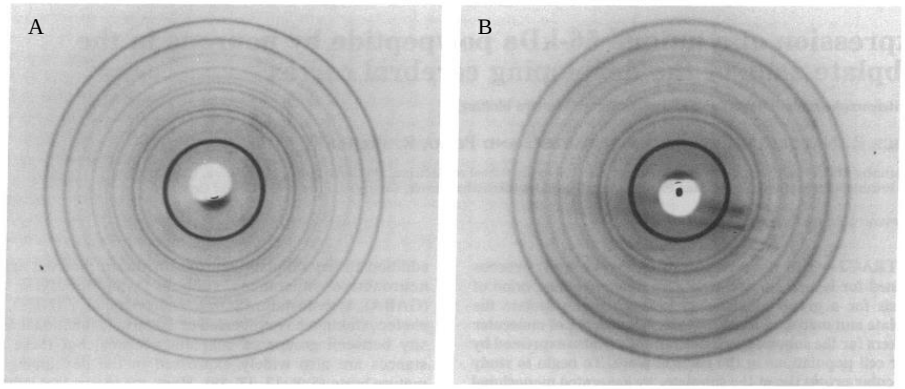

Figure 1.5. X-ray powder diffraction pattern of haemozoin (A) is identical to that of β-haematin (B). Reprinted from Slater, A. F. G., Swiggard, W. J., Orton, B. R., Flitter, W. D., Goldberg, D. E., Cerami, A. & Henderson, G. B. An iron-carboxylate bond links the heme units of malaria pigment. *Proc. Natl Acad. Sci. USA*. **1991**, 88, 325-329.

Bohle et al. (1997) further confirmed that the high resolution powder diffraction pattern of β-haematin prepared by dehydrohalogenation of haemin in dry methanol was identical to that of freeze-dried whole parasitized RBCs as shown in Figure 1.6 (Bohle et al. 1997) and also showed the β-haematin crystal structure to belong to the $P\bar{1}$ centrosymmetric space group.

This led to the proposal that the structure consisted of Fe(III)PPIX chains growing in anti-parallel directions with the iron(III) centre on one Fe(III)PPIX coordinated to the propionate side chain of the next with hydrogen bonds linking the chains to one another (Bohle et al. 1997). Later, the same group showed that it consists of cyclic dimers linked by reciprocal propionate to Fe(III) coordination, with neighbouring dimers linked by hydrogen bonds as shown in Figure 1.7 (Pagola et al. 2000).

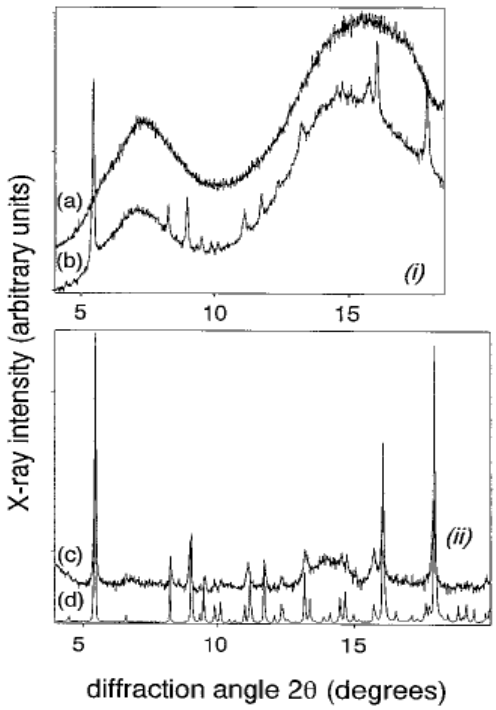

Figure 1.6. In panel (i), (a) and (b) represent the powder diffraction pattern of lyophilized uninfected and infected RBC respectively. In panel (ii), (c) is the difference between (a) and (b) in panel (i) while (d) represents the powder diffraction pattern of β-haematin. Reprinted from Bohle, D. S., Dinnebier, R. E., Madsen, S. K. and Stephens, P. W. Characterization of the products of the heme detoxification pathway in malarial late trophozoites by x-ray diffraction. *J. Biol. Chem*. **1997**, 272, 713-716.

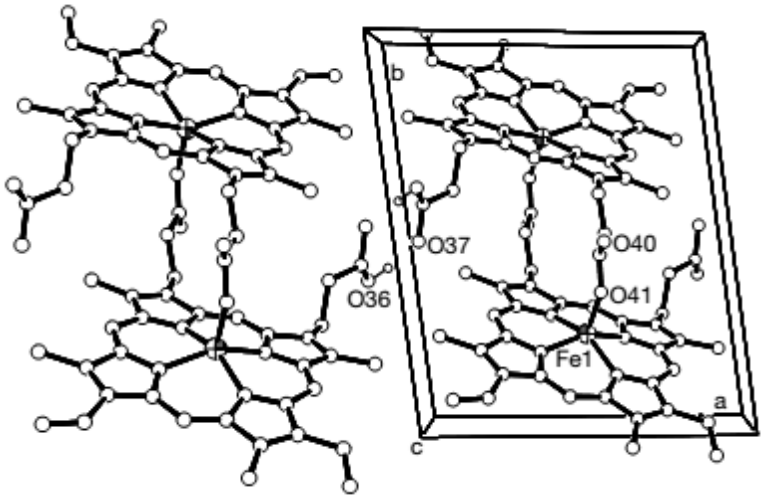

Figure 1.7. The β-haematin crystal structure viewed along the {001} direction showed the coordination of Fe1–O41 bond to form dimers linked through O36 and O37 hydrogen bond to another dimer. Reprinted from Pagola, S., Stephens, P. W., Bohle, D. S., Kosar,A. D. & Madsen, S. K. The structure of malaria pigment (β-haematin). *Nature*. **2000**, 404, 307-310.

Structural determination of natural haemozoin isolated from *S. mansoni* and *R. prolixus* by Oliveira et al. (2005) using synchrotron x-ray powder diffraction showed it to be identical to that formed in the malaria parasite (Oliveira et al. 2005) as the parameters of the crystallographic unit cell were almost identical to that of β-haematin. Finally, solution of the structure of haemozoin itself from malaria parasites from the X-ray powder diffraction pattern using an iterative combination of the Rietveld refinement method and the maximum entropy method different from a simulated annealing algorithm used by Pagola et al. (2000) yielded an overall identical unit cell structure and virtually identical molecular structure to that of β-haematin (Klonis et al. 2010). The only noticeable difference was the Fe(III)–O bond having a greater degree of disorder compared to that of β-haematin. However, this difference may arise from the lower occupancy of the oxygen site as was reported by Walczac et al. (2005) based on extended X-ray absorption fine structure (EXAFS) spectroscopy studies. A recent study reported the formation of crystalline DMSO solvate of β-haematin from a solution containing approximately 2 mole equivalents of CQ relative to Fe(III)PPIX (Gildenhuys et al. 2012). The external morphology of the β-haematin DMSO solvate crystal was identical to that of the haemozoin crystal itself. These authors showed using single crystal X-ray diffraction that the unit cell of this crystal structure belongs to the centrosymmetryic space group and consist of μ-propionato coordination dimers of

Fe(III)PPIX as shown in Figure 1.8 (Gildenhuys et al. 2012) which again is identical to previously reported structures of β-haematin (Pagola et al. 2000 & Klonis et al. 2010).

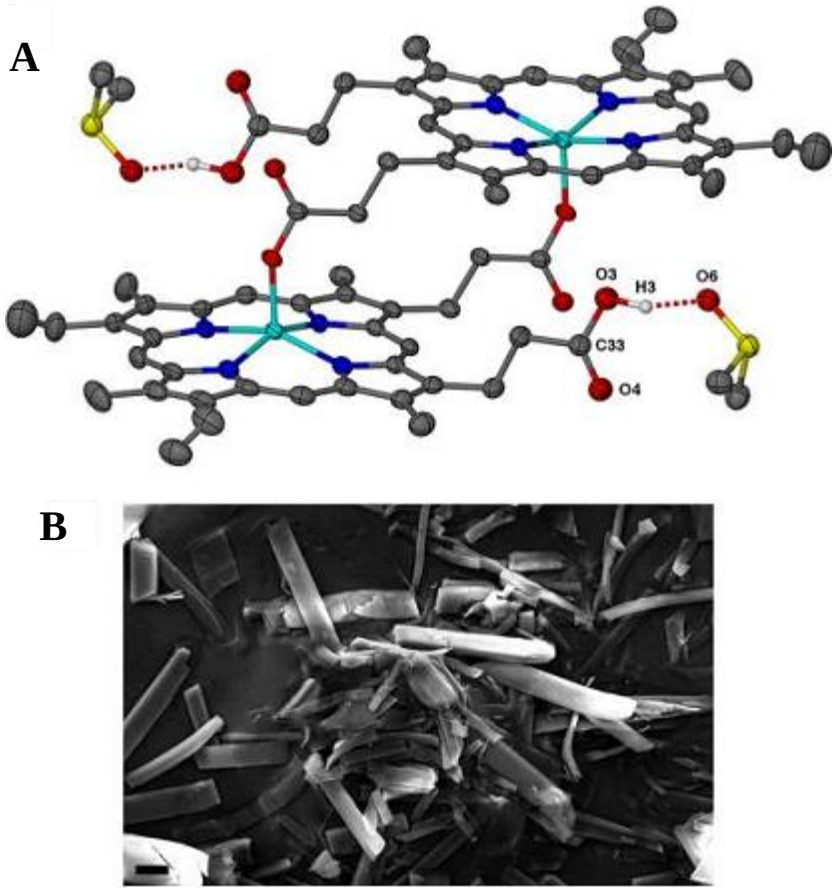

Figure 1.8. (A) Single crystal x-ray diffraction showing the μ-propionato coordination dimers of Fe(III)PPIX in the β-haematin DMSO solvate. (B) The H3····O6 in (A) represents the hydrogen bond formed between the propionic acid group of Fe(III)PPIX and a DMSO molecule in the crystal structure. Reprinted from Gildenhuys, J., le Roex, T., Egan, T.J. & de Villiers, K.A. The single crystal X-ray structure of β-hematin DMSO solvate grown in the presence of chloroquine, a β-hematin growth-rate inhibitor. *J. Am. Chem. Soc*. **2013**, 135, 1037-47.

Bellemare et al. (2009) reported that haemozoin and β-haematin crystals exhibit autoflourescence. The excitation of β-haematin is the result of a Frankel excitation from the lowest singlet π—π* transition in the porphyrin crystal structure which corresponds to the Q(0,0) band (Gouterman et al. 1978 and Bellemare et al. 2009). The fluorescence was only observed in the fully hydrated or the fully dehydrated crystal. The excitation and emission maximum was observed at 555 and 575 nm respectively. The autofluorescence of β-haematin and haemozoin crystals can therefore be exploited to monitor crystal formation *in vivo* and *in vitro* since non-crystalline Fe(III)PPIX does not fluoresce.

1.5.2 Morphological and crystallographic properties

β-Haematin formed by different methods is known to exhibit external morphologies (shape) different from haemozoin itself although they are chemically, spectroscopically and crystallographically identical to one another (Pagola et al. 2000). The external morphology of a crystal is defined by the relative growth rate of its crystal faces (Buller et al. 2002) with the slowest growing face being expressed most prominently in the overall crystal morphology. Growth of the different faces in β-haematin crystals is determined by the attachment energy (E_{att}) of the different crystal faces. In the case of β-haematin crystal growth, E_{att} can be defined as the energy released per molecule when one new layer of β-haematin dimer is attached to the growing crystal face. E_{att} of the different β-haematin crystal faces are shown in Table 1.2.

Table 1.2. Calculated E_{att} of the different crystal faces used to determine the theoretical growth form of β-haematin. Reproduced from Buller, R., Peterson, M. L., Almarsson, O. & Leiserowitz, L. Quinoline Binding Site on Malaria Pigment Crystal: A Rational Pathway for Antimalaria Drug Design. *Cryst. Growth Des.* **2002**, 2, 553-562.

Face	**E_{att} (kcal/mol)**	**Face**	**E_{att} (kcal/mol)**	**Face**	**E_{att} (kcal/mol)**	**Face**	**E_{att} (kcal/mol)**
{100}	–30.6	{110}	–52.6	{111}	–80.4	$\{\bar{1}21\}$	–106.8
{010}	–27.6	{011}	–82.4	$\{\bar{1}11\}$	–92.8	{112}	–112.6
{001}	–101.5	$\{1\bar{1}0\}$	–52.9	$\{11\bar{1}\}$	–112.1		
		$\{10\bar{1}\}$	–108.1				

The {100}, {010}, {011} and {001} faces are the most commonly observed β-haematin crystal faces as determined by Buller et al. (2002). The more negative the E_{att} of any crystal face, the less important that face is in the overall crystal morphology, so therefore in order of importance {001}< {011}<{100}<{010} in the overall visible crystal morphology. Buller et al. (2002) described the morphology of β-haematin crystals as lath-like, growing fastest along its minor {001} face exhibiting well-formed {100} and {010} faces and a less developed {011} face (Figure 1.9A & B) which is similar in both habit (overall shape) and form ({hkl}) to that of the haemozoin crystal itself (Figure 1.9C).

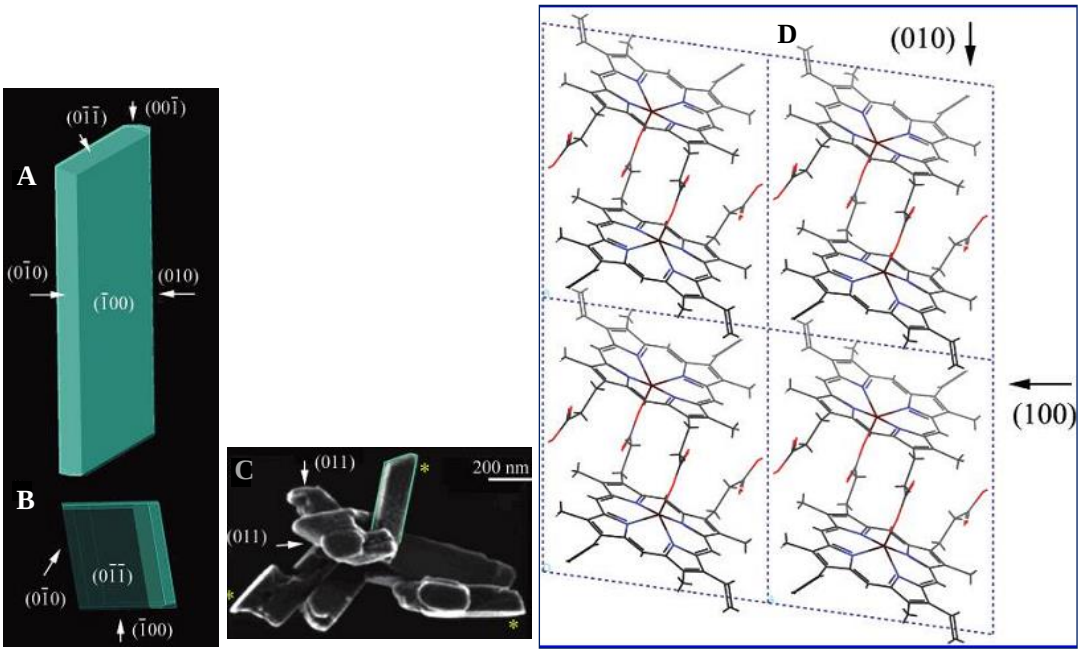

Figure 1.9. Based on E_{att} calculations, the theoretical growth form of β-haematin in A & B is similar to that of haemozoin crystals, C. D represents a view of the molecular dimeric structure of the β-haematin unit cell from the {001} face. Reprinted from Buller, R., Peterson, M. L., Almarsson, O. & Leiserowitz, L. Quinoline Binding Site on Malaria Pigment Crystal: A Rational Pathway for Antimalaria Drug Design. *Cryst. Growth Des.* **2002**, 2, 553-562.

Solomonov et al. (2007) went further to show using transmission electron microscopy (TEM) and TEM-electron diffraction (TEM-ED) patterns that β-haematin crystals grown in MeOH-DMSO and $CHCl_3$ solution predominantly lie exposing their {100} face with a few showing their {010} face and that their structure was consistent with that described by Buller et al. (2002). Most of the crystals also appeared to have a regular lath-like shape belonging to the $P\bar{1}$ centrosymmetric space group.

1.6 MECHANISM OF HAEMOZOIN FORMATION: ADVANCES MADE SO FAR

The different approaches taken to understand the biomineralization process of haemozoin formation *in vivo* using proteins and lipids implicated in its formation as well as solvents, buffers and detergents used in mediating the formation of its synthetic counterpart, β-haematin, *in vitro* are all discussed below.

1.6.1 Proteins

Slater and Cerami demonstrated in 1992 that under acidic conditions mimicking those in the parasite digestive vacuole, Fe(III)PPIX can be converted to haemozoin by *P. falciparum* trophozoite lysate. An enzyme called haem polymerase was proposed to be responsible for this conversion with its activity shown to be inhibited by quinoline drugs. Studies with *P.*

berghei lysates also showed similar activity demonstrating the conversion of Fe(III)PPIX to haemozoin (Chou et al. 1996). The proposed theory of a 'haem polymerase' involvement in haemozoin formation was dismissed by studies carried out by Dorn et al. (1995) which showed that heating the parasite extract or haemozoin crystals as well as the presence of proteases does not affect their β-haematin formation activity. This led to the proposal that haemozoin crystal formation is not an enzymatic process but a chemical process (Dorn et al. 1995).

Histidine rich protein II (HRPII) found in large quantities in the parasite digestive vacuole was also implicated in haemozoin formation as it has been reported to bind to Fe(III)PPIX and convert it to haemozoin (Sullivan et al. 1996). HPRII was later shown to be very inefficient in converting Fe(III)PPIX into synthetic haemozoin (β-haematin) *in vitro* (Pandey et al. 2003 and Papalexis et al. 2001). HPRIII (Histidine rich protein III) which is a homologue of HPRII acts in a similar manner. However, although both HPRII and HPRIII genes are present in clinical isolates of *P. falciparum,* some laboratory strains of *P. falciparum* lack one or the other of the genes. Genetic crosses of these *P. falciparum* strains lacking both genes for HPRII and HPRIII as well as *P. vivax* and *P. berghei* which do not possess these genes still produce haemozoin crystals as shown in Figure 1.10 (Noland et al. 2003 and Sullivan et al. 2002), thereby suggesting that this protein is unlikely to be primarily responsible for haemozoin formation *in vivo*.

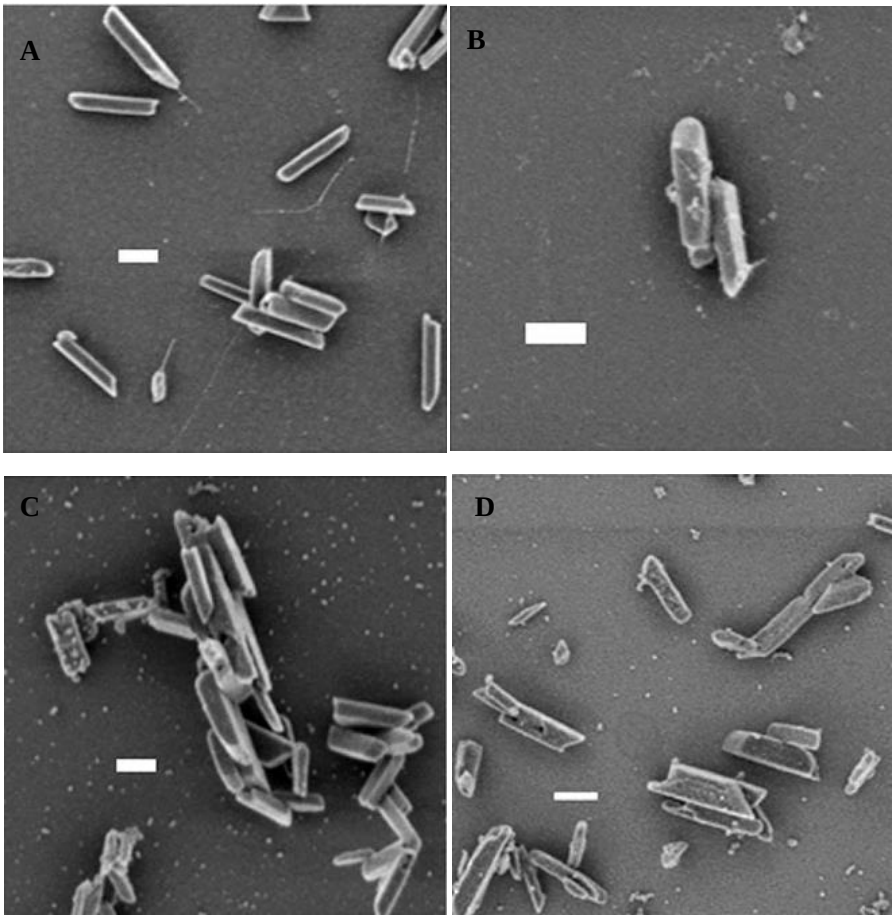

Figure 1.10. *P. falciparum* clones lacking HRPII (A) and HRPIII (B) and both HRP II & III (C) or having both HRP II & III (D) gene still produce haemozoin crystals *in vivo*. The scale bar is 300 nm for all images. Reprinted from Sullivan, D. J. Theories on malarial pigment formation and quinoline action. *Int. J. Parasitol*. **2002**, 32, 1645-53.

Later, Jani et al. (2008) proposed the haem detoxification protein (HDP) as a novel malaria parasite protein responsible for converting free haem to haemozoin crystals *in vivo*. This study also showed using powder X-ray diffraction, scanning electron microscopy (SEM) and TEM that the haemozoin crystals produced with HDP were spectroscopically and morphologically similar to that of β-haematin and that they crystallized in the same space group as haemozoin. Orthologues of HDP have been identified in several other *Plasmodium* species (Carlton et al. 2002 & Protozoan genomes, 2008) while its homologues have been identified in the genomes of *Theileria* (Pain et al. 2005), *Babesia* (Protozoan genomes, 2008) and *Toxoplasma gondii* (Kissinger et al. 2003). The overall sequence identity of HDP was 15% with respect to all other related HDP proteins and 60% with those of the *Plasmodium* genus. HDP was found to bind very strongly to haem (K_d = 80 nM) with 2.7 haem binding sites. Testing of the ability of recombinant HDP to mediate β-haematin formation showed that it converted about 50% of haematin to β-haematin in a concentration dependent manner,

with most of the product formed within 20 min (Jani et al. 2008). On the other hand, HDP has been shown not to have any N-terminal signal sequence which normally predicts possible transport of proteins to their target site (Marti et al. 2004 & Hiller et al. 2004). Jani et al. (2008) also reported that HDP produced by *P. falciparum* is exported and concentrated in the RBC cytoplasm during the early stage of parasite infection of the RBC and is trafficked together with haemoglobin via cytostome derived structures to the parasite digestive vacuole where it becomes functional in the haemozoin formation process. Recently, a protein complex of about 200 kDa was proposed to be responsible for the conversion of haemoglobin to haemozoin *in vivo* (Chugh et al. 2012). This protein complex consists of falcipain 2/2′, plasmepsin II, plasmepsin IV, HAP, falcilysin and HDP which were all reported to be associated with the haemozoin crystal *in vivo* as represented in the schematic diagram in Figure 1.11A. HDP and falcipain 2 were reported to interact strongly with one another in this protein complex and to directly associate with the haemozoin crystal. This interaction was shown to be necessary for haemoglobin conversion to β-haematin as neither of them could mediate the conversion of haemoglobin to β-haematin alone *in vitro* (Chugh et al. 2012). HDP was reported to be thermostable (Jani et al. 2008) as heating of this protein in the falcipain 2/HDP complex did not affect the *in vitro* β-haematin formation activity of the complex. Chugh et al. (2012) reported HDP to be about 1000 times more efficient in mediating β-haematin formation than previously reported lipids (Pisciotta et al. 2007 & Fitch et al. 1999). However, a previous study using about 10 million sucrose purified trophozoites, corresponding to about 10 nmol of haemozoin for protein separation and identification on a 12% SDS-PAGE (Sodium Dodecyl Sulfate Polyacrylamide Gel Electrophoresis) stained with Coomassie brilliant blue (Figure 1.11B) (Pisciotta et al. 2007), did not identify any proteins associated with haemozoin crystals isolated from parasites (Pisciotta et al. 2007) calling into question the proposed role of the protein complex, or suggesting that it is present in only very small quantities.

A

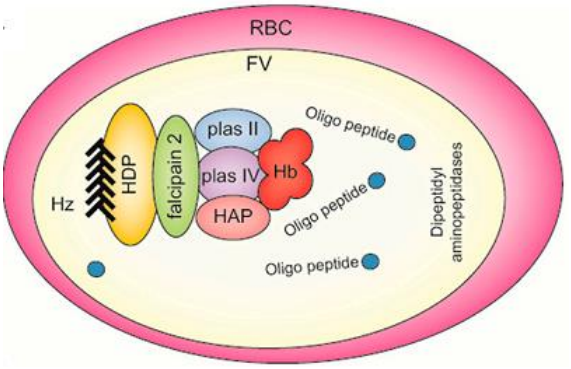

B

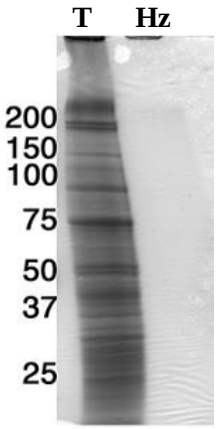

Figure 1.11. A. Schematic representation of the protein complex associated with haemozoin (Hz) *in vivo* claimed to be responsible for the conversion of haemoglobin to haemozoin in the parasite digestive vacuole as proposed by Chugh et al. (2012). Reprinted from Chugh, M., Sundararaman, V., Kumar, S., Reddy, V.S., Siddiqui, W.A., Stuart, K.D. & Malhotra, P. Protein complex directs hemoglobin-to-hemozoin formation in *Plasmodium falciparum*. *Proc. Natl Acad. Sci. U S A.* **2013**, 110, 5392-7. B. 10 nmol of Hz crystals used for protein separation on a 12% SDS-PAGE gel stained with Coomassie blue failed to identify any protein associated with Hz, while there was an abundance of proteins in the trophozoite extract (T). Reprinted from Pisciotta, J. M., Coppens, I., Tripathi, A. K., Scholl, P. F., Shuman, J., Bajad, S., Shulaev, V. and Sullivan, D. J. The role of neutral lipid nanospheres in Plasmodium falciparum haem crystallization. *Biochem. J.* **2007**, 402, 197-204.

1.6.2 Lipids

Dorn et al. (1995) reported β-haematin formation to be mediated by parasite extract as well as haemozoin crystals from parasites where they showed that heating the parasite extract or haemozoin crystals as well as the presence of proteases do not affect *in vitro* β-haematin formation activity. In response to this, Bendrat et al. (1995) were the first to suggest that lipids were responsible for the activity of the parasite extract and of haemozoin formation. This allowed the process of β-haematin formation by haemozoin and pre-formed β-haematin to be developed further, eventually even leading to high-throughput screening of compounds for haemozoin/β-haematin inhibition activity (Kurosawa et al. 2000 & Chong et al. 2003). Later on, Dorn et al. (1998) showed that the acetonitrile extracts from both trophozoite infected and uninfected RBCs promote β-haematin formation *in vitro* (Dorn et al. 1998). The chloroform extract from parasites recovered about 70% of β-haematin mediating activity thereby supporting the role of lipids in mediating this process of β-haematin formation. Fitch et al. (1999) then showed that mono- and dioleoylglycerols were efficient in mediating β-haematin formation as well as some detergents too. It was reported that cholesterol and trioleoylglycerol as well as saturated fatty acids such as palmitic and stearic acid did not mediate β-haematin formation *in vitro* (Fitch et al. 1999). TEM studies of *P. falciparum*-

infected erythrocytes (iRBC) by Pisciotta et al. (2007) showed that lipid particles were closely associated with haemozoin crystals in the parasite digestive vacuole (Figure 1.12A). These were mainly mono- and diacylglycerols and a series of mono-, di- and triacylglycerols which were shown to promote the formation of β-haematin *in vitro* under physiological conditions of 37°C and pH 4.8 (Pisciotta et al. 2007). Analysis by global mass spectrometry lipidomics of these lipids identified monopalmitic glycerol and monostearic glycerol to be closely associated with haemozoin, but not monooleic glycerol. The lipid structures associated with haemozoin crystals in the digestive vacuole were found to consist of monostearic glycerol (MSG), monopalmitic glycerol (MPG), dipalmitic glycerol (DPG), dilinoleic glycerol (DLG) and dioleic glycerol (DOG) (MSG/MPG/DPG/DLG/DOG) in the ratio 4:2:1:1:1 by volume which was referred to as neutral lipid blend (NLB) (Pisciotta et al. 2007).

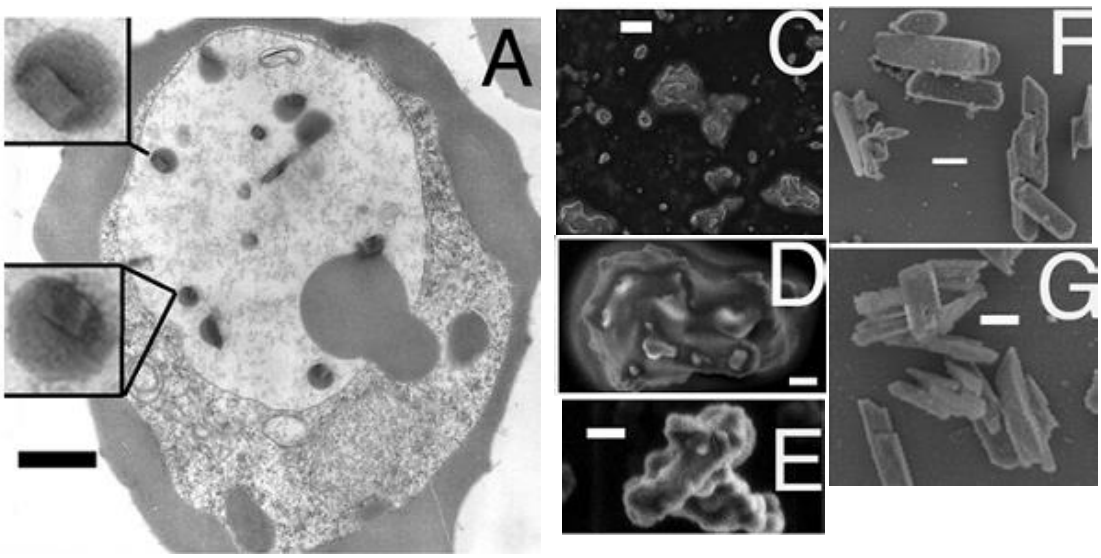

Figure 1.12. TEM of iRBC stained with malachite green showed haemozoin inside the parasite DV to be associated with lipid structures (A) and scanning electron microscopy of sucrose purified haemozoin from parasites fixed with malachite green also showed lipid surrounding it (C, D & E) while delipidated Hz showed little or no lipid around the Hz crystal (F & G). Scale bar represents 1µm. Reprinted from Pisciotta, J. M., Coppens, I., Tripathi, A. K., Scholl, P. F., Shuman, J., Bajad, S., Shulaev, V. and Sullivan, D. J. The role of neutral lipid nanospheres in *Plasmodium falciparum* haem crystallization. *Biochem. J.* **2007**, 402, 197-204.

.

Egan et al. (2006) and others have extensively demonstrated that neutral lipids and NLB efficiently mediate β-haematin formation under biomimetic conditions (Hoang et al. 2010 a, b & Egan et al. 2006). De Villiers et al. (2009) showed using grazing incidence synchrotron X-ray diffraction and X-ray reflectivity that the neutral lipid 1-myristoyl-glycerol (MMG) nucleates formation of β-haematin crystal which float on their {100} faces. It was proposed to be aided by stereospecific interactions between the OH group of MMG and the β-haematin

crystal nucleation face. Furthermore, Egan et al. (2006) showed MMG, monooleoylglycerol, 1,3-dimyristoylglycerol, 1,3-dioleoylglycerol, trioleoylglycerol, 1,2-dioleoyl-glycero-3-phosphoethanolamine, 1,2-dimyristoyl-glycero-3-phosphocholine, 1,2-dioleoyl-glycero-3-phosphocholine, cholesterol, 1,2-dipalmitoyl-glycero-3-phosphocholine and n-octyl-b-D-glucopyranoside to all promote β-haematin formation *in vitro*. The nucleation of β-haematin by epitaxial crystal growth on a lipid such as a phospholipid was proposed to occur as a result of the interaction between the carboxylic acid groups of haematin emerging from the {100} face and the lipid polar head groups (Egan, 2008) as shown in a schematic representation in Figure 1.13.

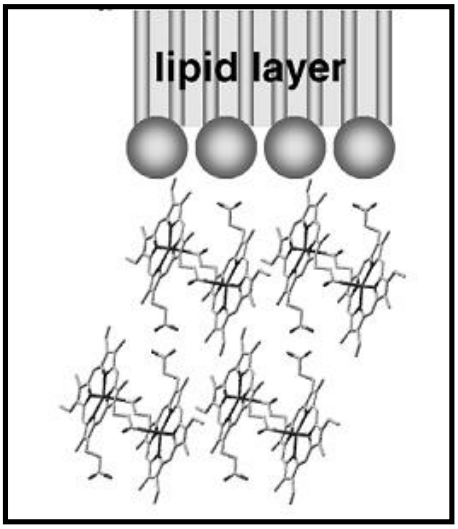

Figure 1.13. Interaction of carboxylic acid groups of haematin with polar head groups of phospholipid proposed to induce nucleation of β-haematin via its {100} face. Reprinted from Egan, T. J. Recent advances in understanding the mechanism of hemozoin (malaria pigment) formation. *J. Inorg. Biochem*. **2008**, 102, 1288-1299.

S. mansoni and *R. prolixus* are also known to produce regularly-shaped haemozoin crystals which crystallize in the same unit cell as that of haemozoin from *P. falciparum*. However, even though in these organisms the haemozoin crystals are produced extracellularly in the gut and not intracellularly as with *P. falciparum*, TEM imaging has also shown that haemozoin crystals are closely associated with hydrophobic lipid droplet-like structures or vesicles (Oliveira et al. 2005) as shown in Figure 1.14. Lipid droplet-like particles associated with haemozoin in the gut of *S. mansoni* appeared not to have a phospholipid bilayer membrane structure whereas the lipid vesicles derived from perimicrovillar membranes associated with haemozoin in *R. prolixus* are hollow and have a phospholipid bilayer membrane.

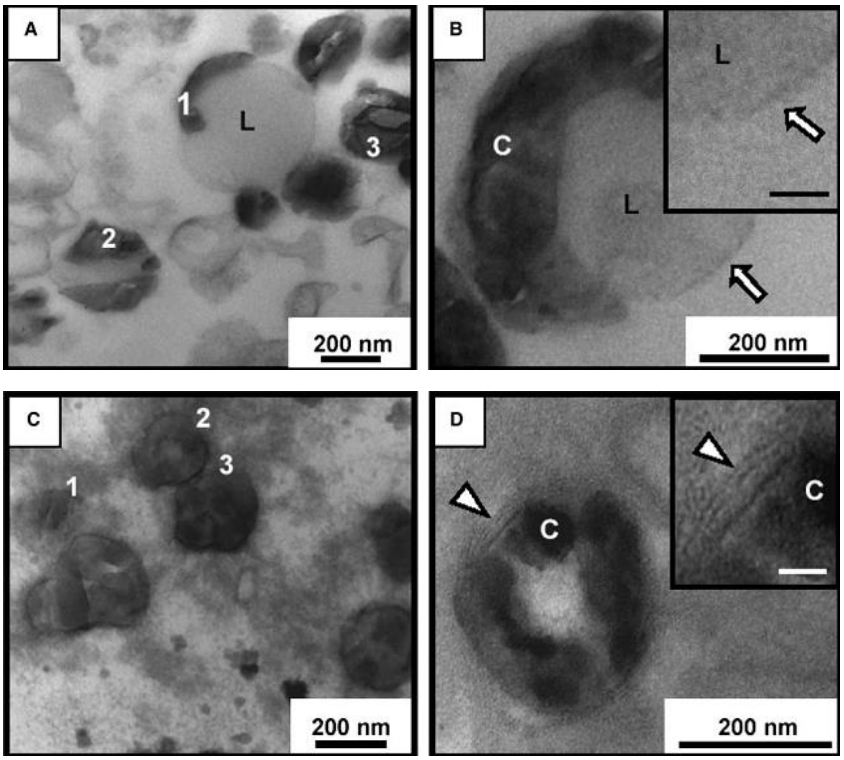

Figure 1.14. TEM of haemozoin crystals associated with lipid structures in the gut of *S. mansoni* (A, B) and *R. prolixus* (C, D). "L" marks lipid droplet structures and the arrow in (B) shows the absence of a bilayer membrane in the lipid structure associated with haemozoin in *S. mansoni*. Phospholipid bilayer membrane can be seen in the lipid vesicle structures associated with haemozoin in *R. prolixus* as shown in the insert in (D). 1, 2 & 3 represent respectively the initial, intermediate and final developmental stages of the crystals in these organisms. Reprinted from Oliveira, M. F., Kycia, S., Gonzales, A., Kosar, A. D., Bohle, D. S., Hempelmann, E., Menezes, D., Vannier-Santos, M., Oliveira, P. L. & Ferreira, S. T. Structural and morphological characterization of hemozoin produced by *Schistosoma mansoni* and *Rhodnius prolixus*. *FEBS Lett*. **2005**, 579, 6010-6016.

A recent report by Huy et al. (2013) showed phospholipids to be efficient in mediating β-haematin formation under physiological conditions of temperature (37°C) and pH 4.8 in 50 mM acetate buffer. Dilauroyl-phosphatidylcholine and dioleoyl-phosphatidylcholine were shown to be the most efficient mediators of β-haematin under these conditions with about 70-80% conversion rate of haematin to β-haematin at low molar concentrations (Huy et al. 2013). Dimyristoyl-phosphatidylcholine was found to have a lower β-haematin conversion rate with a maximum of about 30-40% at slightly higher concentrations while dipalmitoyl-phosphatidylcholine, distearoyl-phosphatidylcholine, dimyristoyl- phosphatidylethanolamine, dipalmitoyl- phosphatidylethanolamine, and dipalmitoyl- phosphatidylserine were shown not to have any β-haematin formation activity under these conditions (Huy et al. 2013). However, all the above phospholipids were shown to induce β-haematin formation to different extents at temperatures higher than their respective T_m (gel-to-fluid transition temperature) but not below their T_m. The ability of the phospholipids to induce β-haematin formation was found to be statistically correlated negatively with their T_m only but not with any other physical

properties of the phospholipids such as molecular weight, total net charge, freely rotating bonds, polar surface area, hydrogen bond donors, octanol-water partition coefficient, distribution coefficient at pH 5.5, hydrogen bond acceptors, number of anion charges and polarizability (Huy et al. 2013). The maximum yield of β-haematin obtained with each phospholipid positively correlates with the temperature of the reaction system which further suggests that the ability of an individual phospholipid to mediate the reaction of β-haematin correlates with its membrane fluidity (Huy et al. 2013).

Recent TEM studies of iRBC in the Egan laboratory (unpublished) showed regular-shaped haemozoin crystals formed in the *P. falciparum* digestive vacuole which are aligned parallel to each other (Figure 1.15) even though no clear visible lipid droplet was seen associated with the haemozoin crystal despite fixing the iRBCs with malachite green. A report by Kapishnikov et al. (2012a) has argued that if the haemozoin crystals in the parasite digestive vacuole were located within NLB, it would have been difficult for them to be aligned in one direction in such a cluster. They went on to suggest that this alignment maybe due to face-oriented nucleation which causes the crystals to become aligned to one another due to contact. With the use of 3D serial surface view microscopy, the DV of the malaria parasite was observed to change from a disk-like to an oval shape as the parasite matures from early trophozoite to schizont stages with the larger haemozoin crystals located at the centre while the smaller haemozoin crystals were aligned close to the inner membrane surface of the DV. This was clearly illustrated using cryo-x-ray tomographic (cryo-XT) reconstruction from the 3D EM image (Figure 1.15B). The alignment of smaller haemozoin crystals on the inner membrane surface of the digestive vacuole was consistent with those viewed using cryo-SEM (Figure 1.15C) with STEM tomographic reconstructed of the DV clearly showing haemozoin crystals are aligned along the DV inner membrane (Figure 1.15D). This alignment was reported to be suggestive of some kind of nucleation at that surface (Kapishnikov et al. 2012 b).

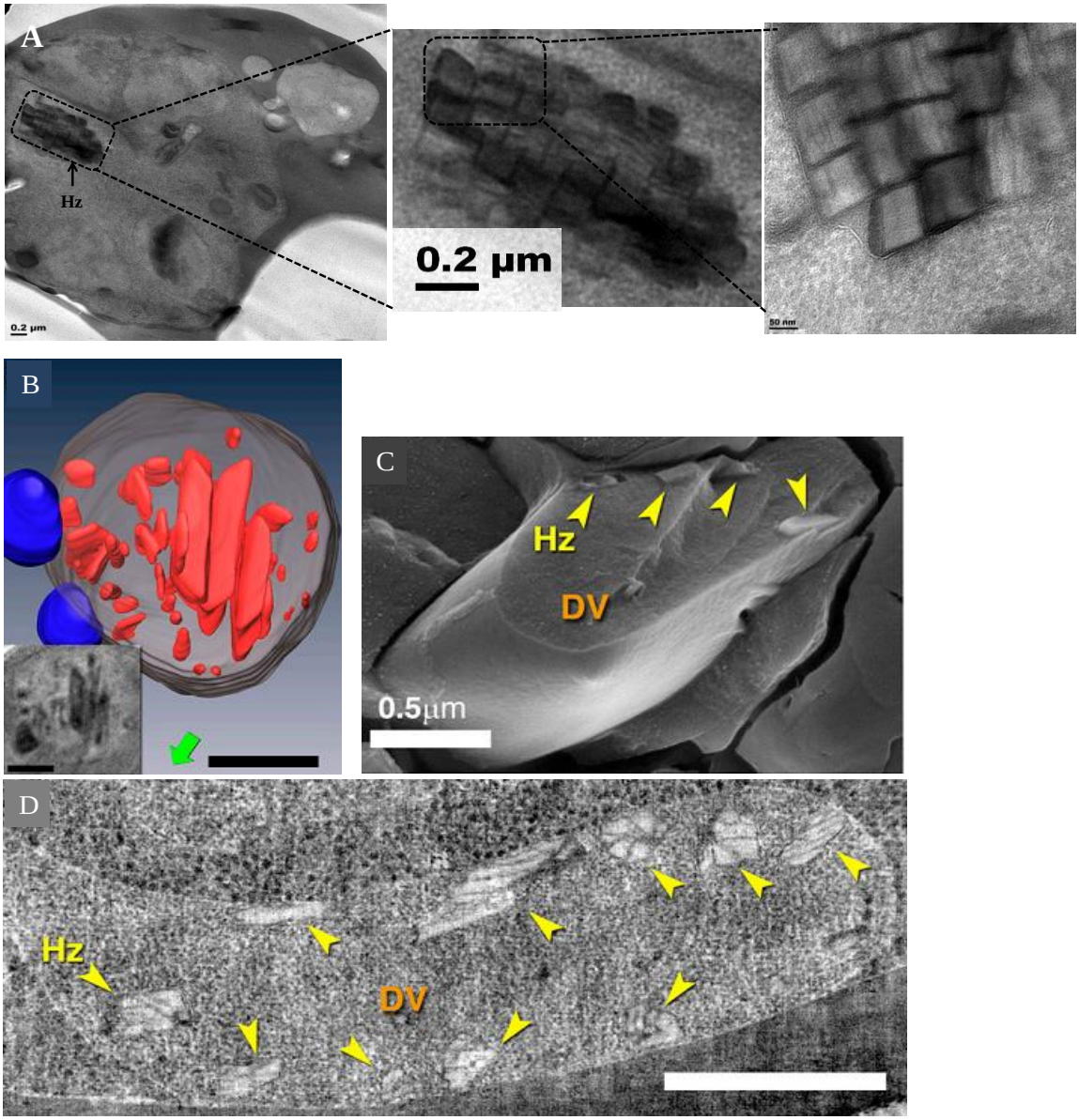

Figure 1.15. A: TEM image of iRBC stained with malachite green showed Hz crystals inside the DV aligned parallel to one another. B: Cryo-XT of late stage trophozoite with larger haemozoin crystals in the middle and smaller ones aligned along the inner DV membrane. C: Cryo-SEM of an early trophozoite with haemozoin crystals aligned along the DV inner membrane. D: Haemozoin crystals (yellow arrows) aligned to the DV inner membrane as seen using STEM tomographic reconstruction. B, C & D are reprinted from Kapishnikov, S., Weiner, A., Shimoni, E., Guttmann, P., Schneiderc, G., Dahan-Pasternakd, N., Dzikowski, R., Leiserowitz, L. and Elbaum, M. Oriented nucleation of hemozoin at the digestive vacuole membrane in Plasmodium falciparum. *Proc. Natl Acad. Sci. USA*. **2012b**, 109, 11188–11193.

1.6.3 Solvent, detergent and buffer systems

Solvents have been shown to influence the relative growth rates of crystals along different crystallographic axes, although much is not known concerning the exact role a particular solvent plays in inhibiting or enhancing crystal growth (Weissbuch et al. 1995). Benema and others (Bennema et al. 1973 & 1992, Bourne et al. 1976 & Elwenspoek et al. 1987) proposed

that the interaction of solvent and solute on a specific crystal surface is favourable when it leads to a transition from smooth to rough interface, thereby causing the crystal to grow faster on that surface while on the other hand, adsorption of solvent on a crystal surface may also inhibit growth of that surface since additional energy is required to remove the bound solvent. Thus an energy barrier is created by the adsorbed solvent on the crystal surface. When Fitch et al. (1999) demonstrated fatty acid and lipid mediation (arachidonic, linoleic, oleic, and palmitoleic acids, 1-mono and di-oleoylglycerol) in β-haematin formation, they also showed that detergents such as Tween 80, SDS (sodium dodecyl sulfate) and *n*-octyl-glucopyranoside promote β-haematin formation at physiologically relevant temperature (37°C) after 2 h incubation. With regard to β-haematin formation in homogenous solvent systems, Egan et al. (2001) showed using IR absorbance that the crystal growth kinetics of β-haematin formation in this kind of system was sigmoidal and can be modelled by the Avrami equation (Equation 1).

$[m/m_0 = \exp(-zt^n)]$..... (1)

m: mass of the unreacted haematin,
m_o: initial mass of haematin,
t: reaction time,
z: rate constant,
n: Avrami constant which can either be 1,2,3 or 4.

In this study, the Avrami constant for β-haematin formation in acetate buffer at 60^{o}C was found to be four, indicating a sporadic nucleation process and three dimensional crystal growth (Egan et al. 2001). Results in this study were later reproduced spectrophotometrically using 0.05 M benzoic acid/benzoate (pH 4.5, 60 ^{o}C) to promote the reaction and using 5% pyridine to measure unreacted haematin (Egan and Tshivhase, 2006). It was suggested from these studies that π-π interaction between the carboxylic acid and Fe(III)PPIX at low pH solubilises the Fe(III)PPIX, keeping it in the dissolved state and thereby aiding its conversion to β-haematin. Egan et al. (2006) further showed clearly the formation of β-haematin crystals at pentanol-water and octanol-water interfaces (Figure 1.16E). Water miscible alcohols such as *n*-butanol, *n*-propanol, ethanol and methanol have also been reported to mediate the formation of β-haematin (Figure 1.16A-D) and it was shown that the efficiency with which they promote β-haematin formation was proportional to their hydrophobicity (Huy et al.

2007), which in this case correlated with their chain length. The hydrophobicity of the alcohols again helps to maintain the Fe(III)PPIX in the dissolved state so as to facilitate it conversion to β-haematin.

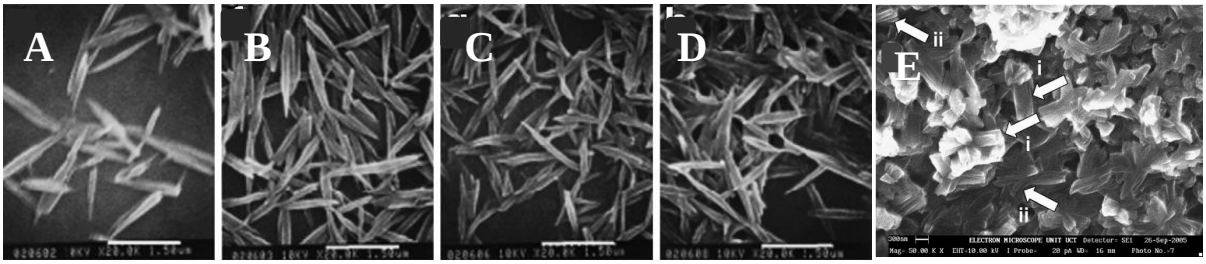

Figure 1.16. Field emission scanning electron microscopy showed β-haematin crystals produced with methanol (A), ethanol (B), *n*-propanol (C) and *n*-butanol (D). Image scale bar represents 1.5µm. Reprinted from Huy, N.T., Maeda, A., Uyen, D.T., Trang, D.T., Sasai, M., Shiono, T., Oida. T., Harada, S. & Kamei, K. Alcohols induce beta-hematin formation via the dissociation of aggregated heme and reduction in interfacial tension of the solution. *Acta Trop*. **2007**, 101, 130-138. SEM showed β-haematin crystals produced at the octanol-water interface (E) to be similar to haemozoin crystals isolated from parasites. (i) and (ii) are respectively larger and smaller crystals indicated with arrows. Scale bar represents 1µm. Reprinted from Egan, T.J., Chen, J.Y-J., de Villiers, K.A., Mabotha, T.E., Naidoo, K.J., Ncokazi, K.K., Langford, S.J., McNaughton, D., Pandiancherri, S., Wood, B.R. Haemozoin (β-haematin) biomineralization occurs by self-assembly near the lipid/water interface. *FEBS Lett*. **2006**, 580, 5105–5110.

The importance of solubilization of Fe(III)PPIX to facilitate β-haematin formation has gained strong support from other related studies where aqueous DMSO (dimethyl sulfoxide) and several polyethylene glycols (PEG 3350, PEG 6000, PEG 8000 and PEG 22 000) have been used to prepare β-haematin crystals (Stiebler et al. 2010b). The rate of β-formation was found to be proportionate to Fe(III)PPIX solubility in these systems. The formation of β-haematin in these systems again followed the Avrami kinetics equation with most of them having an Avrami constant of four.

β-Haematin has also been shown to grow on self-assembled monolayers (SAM) of the form $HS(CH_2)_{11}X$ with nucleation of crystal growth induced via the {100} face when X=OH and via {100} or {010} face when $X=CH_3$ although more preferably on the {010} face in the latter. Nucleation was induced via both {100} and {010} when X=COOH (de Villiers et al. 2009). Unlike β-haematin formation on SAMs as reported by de Villiers et al. (2009) in a non-aqueous environment, a similar study of SAMs with $HS(CH_2)_{15}COOH$ but this time in the presence of aqueous propionic acid over 48 h gave 100% surface coverage and was found to nucleate β-haematin via its {100} face (Wang et al. 2010). The nucleation by $HS(CH_2)_{15}COOH$ SAM in this case was proposed to be brought about as a result of interaction between the COOH group of the SAM and π–π dimers of haematin. These then

converted to μ-propionate dimers, therefore nucleating β-haematin crystal formation as illustrated in Figure 1.17.

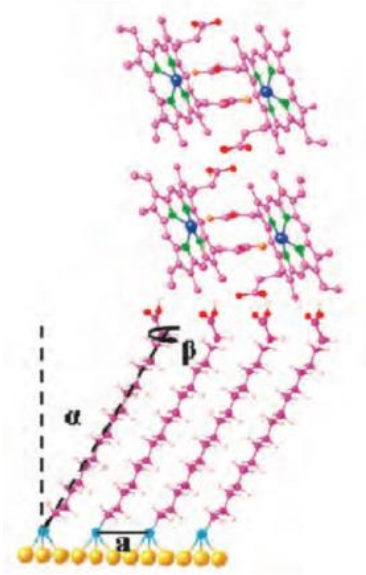

Figure 1.17. The interaction between the COOH group of a $HS(CH_2)_{15}COOH$ SAM and β-haematin as proposed by Wang et al. (2010). Reprinted from Wang, X., Ingall, E., Lai, B. & Stack, A. G. Self-assembled monolayers as templates for heme crystallization. *Cryst. Growth Des.* **2010**, 10, 798-805.

Carter et al. (2010) showed that detergents such as Tween 80, Tween 20 and NP40 are efficient in promoting β-haematin formation giving yields of about 74%. On the other hand, detergents such as Triton X-100, SDS and Chaps were reported not to be efficient in mediating β-haematin formation as only yields of about 10% could be obtained using these detergents. However, Huy et al. (2007b) has shown using Tween 80 that when detergents are below their critical micellar concentration, they can efficiently promote β-haematin formation.

1.7 THE HAEMOZOIN FORMATION PROCESS AS A TARGET FOR ANTIMALARIAL DRUGS

Although the effects of antimalarials on haemozoin formation are not a focus of this current study, no discussion of haemozoin is complete without some mention of haemozoin inhibition by antimalarials. Therefore a brief review is provided here.

As early as the 1960s, Cohen et al. (1964) showed that chloroquine forms a complex with haematin and its effect was demonstrated *in vivo* in a malaria mouse model (Macomber et al. 1967). Later, haematin was proposed to be the target of this antimalarial drug (Chou et al.

1980). Since then, evidence of chloroquine inhibition of Fe(III)PPIX conversion to haemozoin has accumulated over the years (Egan, 2006 review, Chong et al. 2003 and Scholl et al. 2005) but its exact mode of action is still not fully understood. Different modes of interaction between the haemozoin crystal and antimalarial quinoline drugs have been proposed. Slater and Cerami (1992) proposed that chloroquine exhibits its antimalarial activity by inhibiting the supposed 'haem polymerase' activity of the enzyme responsible for haemozoin formation *in vivo*. Sullivan et al. however proposed that the drug acts by being adsorbed onto what was then believed to be a growing polymer chain thereby interfering with the process of haemozoin crystal growth (Sullivan et al. 1996 and 1998). Dorn et al. (1998) further showed that antimalarial drugs belonging to the quinoline family bind directly to the monomer or dimers of Fe(III)PPIX in solution. The 4-aminoquinoline nucleus of these compounds was confirmed to be responsible for complex formation with haematin in solution (Egan et al. 1997 & Dorn et al. 1998). Following the revelation of the dimeric, not polymeric structure of haemozoin (Pagola et al. 2000) some of the proposed mechanisms of action of quinoline drugs based on the formerly proposed structure, such as its ability to inhibit haemozoin polymerization activity *in vivo* (Slater et al. 1992) were therefore no longer considered valid and such mechanisms would need further assessment and explanation in terms of the new structure. Furthermore, Pagola et al. (2000) noted that haematin was by far in molar excess over chloroquine and it would be difficult therefore to imagine inhibition of the haemozoin formation process by a stoichiometric mechanism. However, Sullivan et al. proposed that the haematin-chloroquine complex binds to haemozoin, thereby preventing the crystal from growing further. This brought into question whether haematin or haemozoin is the target for chloroquine. Egan et al. (2000) showed the 4-amino group in chloroquine to be essential for both haematin binding and haemozoin inhibition but that the 7-chloro group was required only for haemozoin inhibition, suggesting that solution binding and inhibition are not directly coupled. Recently, Combrinck et al. (2012) unequivocally showed direct evidence of the inhibition of cellular haemozoin formation *in vivo* by chloroquine in a dose-dependent fashion. Artesunate, amodiaquine, lumefantrine, mefloquine, and quinine were also shown to have similar but smaller effects, the importance of which remains to be fully investigated (Combrinck et al. 2012). Buller et al. (2002) previously reported that chloroquine, amodiaquine, quinine and mefloquine each protonated at the exocyclic amine can bind to the {001} face of the growing β-haematin crystal. The stereochemical binding of these quinoline derivatives to the fastest growing crystal face is through the formation of salt bridges between the porphyrin propionates of β-haematin and amine of quinoline while the

quinoline rings are sandwiched between the aromatic groups of β-haematin as clearly illustrated with chloroquine in Figure 1.18 (Buller et al. 2002).

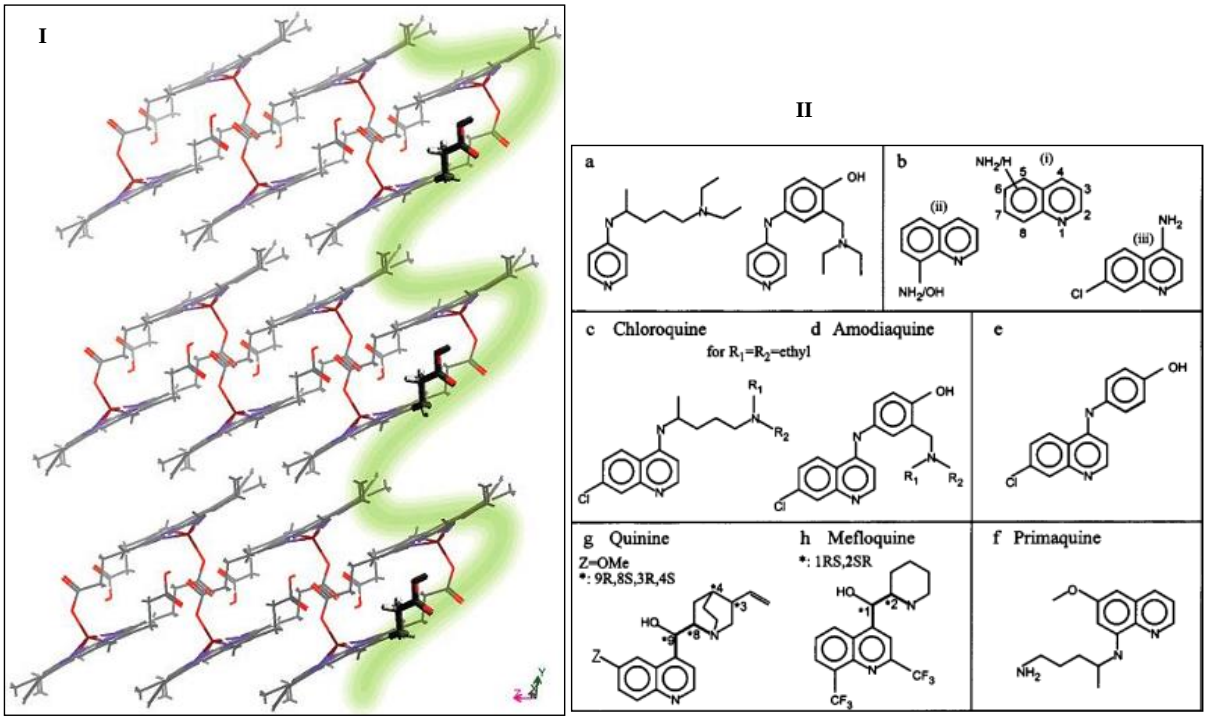

Figure 1.18. In panel I, β-haematin viewed perpendicular to the {100} face along the a-axis showed how chloroquine capped the fastest growing {001} face (outlined in green). Panel II showed structures of some antimalarial quinoline drugs. Reprinted from Buller, R., Peterson, M. L., Almarsson, O. & Leiserowitz, L. Quinoline Binding Site on Malaria Pigment Crystal: A Rational Pathway for Antimalarial Drug Design. *Cryst. Growth Des.* **2002**, 2, 553-562.

1.8 STUDIES OF BIOMINERALIZATION PROCESS IN OTHER ORGANISMS

Given the fact that haemozoin formation is now recognized to be a form of biomineralization, it is worth considering how other organisms bring about biomineralization. By so doing, it will help in understanding general strategies used to study other biominerals to identify biomolecules that are directly involved in their formation. Such strategies may also be used to study haemozoin in order to identify protein(s) or other biomolecules that are directly involved in its formation *in vivo*.

Well-organized inorganic minerals formed in a biological environment in a three dimensional (3D) framework with an organic matrix are known as biominerals. Biomineralization involves the organization of this 3D structural framework by the organic material which provides crystal nucleation sites and compartments which contain molecules that determine the crystal shape and mineral polymorphism as well as crystallization inhibitors for the termination of crystal growth (Addadi et al. 1992, Weiner et al. 1997 and Wilt et al. 2005).

Living organisms are known to produce such well-organized 3D composite structures consisting of bioorganic molecules and inorganic ions ranging from nano- to macroscopic scale (Mann et al. 1996, Addadi et al. 1997 and Pouget et al. 2007). The haemozoin crystal, with its well established structure (as discussed above) is no exception and is formed via a complex biomineralization process in the digestive vacuole of the malaria parasite and in other blood-feeding organisms.

Lipids are known to be involved in some biomineralization processes in different unrelated organisms. For example, in *E. huxleyi* algae the formation of the biocrystal coccoliths is known to be lipid mediated (Young et al. 1999). The cellular cytoskeletal elements found in the crystallization compartment are known to control the crystal shape by controlling the shape of the phospholipid vesicle. In vertebrates, lipid vesicles and protein aggregates are known to be the site of crystal growth initiation. For example, growing dentine in humans is known to contain a non-cellular phospholipid vesicle (matrix vesicle) which serves as the calcification initiation site (Anderson et al. 1995). Phospholipase enzymes, calcium-binding phospholipids and proteins and calcium ion channels also play a role in this biomineralization process. Nucleation here occurs at the inner membrane surface of the vesicle aided by structural and chemical complementarity between an assembly of phospholipids and protein of the matrix vesicle and the mineral phase. In magnetotactic bacteria, magnetite is encapsulated in a lipid bilayer bounded vesicle (Komeili et al. 2007). The templating effect of the lipid vesicle is known to have a high level of control over the crystallization process. It is therefore evident in all the above organisms that lipid can provide an organic phase for nucleation to occur aided by stereochemical and electrostatic complementarity between the lipid surface and growing inorganic crystal phase.

On the other hand, proteins have also been implicated in biomineralization processes in many unrelated organisms. Use of SDS-PAGE and nano LC-MS/MS to study the human bone matrix proteome identified over 70% of the proteins expressed by osteoblasts to be present in the tissue that they produce. Interestingly, the ANXA2, ANXA6, and ANXA5 proteins, ranked amongst the twenty most abundant proteins identified in this study, have been reported to be highly concentrated in matrix vesicles, initiators of mineralization, where they function as calcium channels. Thus, the study of bone matrix proteome led to the identification of proteins that are functionally linked to mineralization and mineral metabolism in high abundance (Alves et al. 2011). Proteomic studies of sea urchin shells and spines using SDS-PAGE and MS/MS techniques also led to the identification of many

proteins including matrix metalloproteins and proteins belonging to the mesaenchyma-specific MSP130 family implicated in biomineralization. These had been previously described in inhibition studies using antibodies or specific enzyme inhibitors. The proteomic study also showed that the matrices did not only contain previously known or supposed specific matrix components, but also proteins possibly involved in the regulation of mineral or matrix formation (Karlheinz et al. 2008). Study of the bacterial magnetic protein (BacMP) membrane proteome from the magnetic bacteria *Magnetospirillum spp.* that produces magnetic particles (magnetite) through a biomineralization process led to the discovery and identification of a novel protein named Mms6, which was characterized and found to bind to iron ions to initiate magnetite crystal formation and/or to regulate the morphology by producing a self-assembly framework structure (Arakaki et al. 2008). In another study of shell matrix proteome from Manila clams *Venerupis philippinarum* using SDS-PAGE and LC-MS/MS, six novel proteins that are conserved within different mollusc and cnidarian species were identified. Bioinformatic characterization of these proteins found them to have a new function in calcium carbonate formation and hence a direct involvement in the biomineralization process (Marie et al. 2011). Similar proteomic studies of the proteomes of other biomineral matrices like the radular teeth in the giant pacific chiton (Nemoto et al. 2012) and the chicken egg shell proteome using SDS-PAGE and LC-MS techniques (Mann et al. 2006) have led to the identification of the proteins involved in the biomineralization processes. Therefore, it is evident that proteomic studies of the matrix of biominerals in many diverse species have invariably led to the identification of the proteins involved in the biomineralization process.

The identification of the proteins involved in the biomineralization process of haemozoin in the DV using an ‘omics’-related approach has not been attempted. Since proteomic studies of biomineral matrix proteomes in other organisms where biomineralization occurs has invariably led to the identification of the proteins involved in the biomineralization process, such an approach could be of great value. The availability of the complete genomic sequences of both *P. falciparum* and *H. sapiens* permits the use of proteomic techniques combined with lipidomic techniques to study the haemozoin crystal in order to identify and characterize biomolecules that could be implicated in its formation. Such biomolecules could themselves serve as potential targets for antimalarial drug design.

1.9 THE *Plasmodium falciparum* DIGESTIVE VACUOLE PROTEOME

The biomineralization process of Hz formation is compartmentalized to the parasite DV. So any proteins that are involved in mediating this process must be present in the DV. Hence, it is relevant to review what is known about the DV proteome.

The main protein in RBC, haemoglobin, is digested in the DV by a series of enzymes present in the DV to provide the parasite with amino acid needed as nutrients. The ingestion of haemoglobin via a specialized structure called a cytostome occurs together with parasite plasma membrane and the parasitophorous vacuole (Slomianny et al. 1990 & Elliott et al. 2008). The cytostome eventually fuses with the lysosome-like single membrane bound DV. Enzymes involved in haemoglobin digestion have been localized in the DV and these include the plasmepsins (PM) PMI, PMII, PMIV and HAP (Goldberg et al. 1991, Gluzman et al. 1994, Francis et al. 1994, Banerjee et al. 2002, Dame et al. 2003). Falcipain 2 and 3 (cysteine proteases), falcilysin (metallo-protease) and aminopeptidases which all act downstream in the haemoglobin digestion process are all known DV proteins (Sijwali et al. 2004, Dahl et al. 2005, Klemba et al. 2004, Murata et al. 2003).

Lamarque et al. (2008) has extensively studied the DV using SDS-PAGE and LC-MS techniques to identify the full proteome of this structure. Besides the known DV proteins that are involved in haemoglobin digestion that were identified, other proteins involved in key processes in the parasite were also identified. The chloroquine resistance transporter, multidrug resistance transporter, V-type H^+-ATPase, H^+-pyrophosphatase and three other ATP synthases listed as putative proteins in PlasmoDB were identified together with other known DV proteins (Lamarque et al. 2008). ADP-Ribosylation Factor, GTPase Sar1, p24 and GTPases Rab1, Rab2, Rab7 and Rab11 and many others which are involved in vesicle trafficking, assembly, docking and fusion were identified, suggesting the existence of protein trafficking pathways in the parasite (Lamarque et al. 2008). Hexose transporter 1, nucleoside transporter 1 and aquaglyceroporin located in parasite plasma membrane and Exp1and Exp2 localized in the parasitophorous vacuole were also identified. This suggested that proteins derived from these structures are trafficked with them together with haemoglobin to the DV (Lamarque et al. 2008). Enzymes involved in basic metabolic processes such as glyceraldehyde-3-phosphate dehydrogenase, fructose biphosphate aldolase, phosphoglycerate kinase were identified. So too were methionine and polyamine metabolism enzymes (adenosyl-methionine synthetase, adenosylhomocysteinase) as well as those involved in

purine salvage and pyrimidine base metabolism (Lamarque et al. 2008). This suggests a mechanism exists by which these proteins are trafficked from parasite cytoplasm into the DV. Chaperones such as mitochondrial HSP60, ER-resident calcium-binding protein and protein disulfide isomerase, three other putative proteins belonging to the HSP70 family described in PlamsoDB with putative roles in clathrin-dependent traffic that may play a part in cytostome formation and many others were identified (Lamarque et al. 2008). See Lamargue et al. (2008) for a complete list of proteins that consist of the DV proteome.

Seemingly, amongst all the known proteins identified including putative proteins for which functions were assigned, it would have been expected that proteins which are likely to be involved in the biomineralization process of haemozoin formation inside the DV would also be identified. Of those proteins previously implicated in haemozoin formation *in vivo* only proteases, falcipain 2/2′, plasmepsin II, plasmepsin IV and HAP which have been implicated in the proposed protein complex with HDP were detected in the DV (Lamarque et al. 2008). However, HDP itself was not detected in the DV and nor were HRPII or HRPIII. The question remains as to whether small amounts of HDP may be able to be detected in association with haemozoin owing to an affinity to the crystal arising from involvement in its formation.

1.10 AIMS AND OBJECTIVES

Keeping in mind the challenges faced by many developing countries in combating malaria and the widespread resistance to many of the current antimalarial drugs available, elucidating the mechanism of haemozoin formation is of considerable interest and could eventually open up new avenues for drug discovery as new potential antimalarial drug targets could be identified. This study was therefore designed to achieve the aims and objectives stated below.

1.10.1 Aims

The three aims of this study were as follows:

1. To study the proteome and lipids associated with haemozoin crystals in order to identify potential biomolecules that are involved in mediating the biomineralization process of haemozoin formation *in vivo*.

2. To systematically investigate the kinetics of synthetic haemozoin (β-haematin) formation mediated by the previously identified neutral lipid blend (NLB) under biomimetic conditions mimicking the parasite digestive vacuole (DV).
3. To study the nucleation of β-haematin crystals at the surface of NLB for comparison with haemozoin and to evaluate the direct effect of chloroquine on haemozoin crystal growth in the malaria parasite.

1.10.2 Specific objectives

To achieve these aims, the specific objectives of this study were follows:

1. To use SDS-PAGE and LC-MS to separate and identify all proteins (proteome) associated with haemozoin, both at the crystal surface and in the matrix to determine whether any potential haemozoin-mediating proteins could be identified.
2. To use thin layer chromatography to separate and identify all lipid classes associated with the haemozoin crystal.
3. To investigate the NLB and its individual constituent lipids in mediating β-haematin formation.
4. To investigate the effect of lipid and haematin concentrations on the kinetics of β-haematin formation.
5. To investigate the effect of buffers and low molecular weight substances such as the ions sodium, potassium, magnesium, calcium, phosphate, carbonate, adenosine 5′-triphosphate (ATP), reduced glutathione and 2,3-diphospho-D-glycerate (2,3-DPG) at concentrations at which they are present in RBC and/or serum on the kinetics of β-haematin formation under biomimetic condition mimicking those in the parasite digestive vacuole
6. To characterize β-haematin produced with MPG and NLB emulsions prepared in different ways as well as at the pentanol-water interface and compare them to haemozoin crystals isolated from malaria parasite itself using TEM and TEM-electron diffraction.
7. To investigate the nucleation and location of β-haematin crystals formed with respect to NLB particles, the nature and structure of neutral lipid blend emulsions and also if there is any relationship between the size of lipid particles formed and β-haematin crystal growth lengths.
8. To investigate the effect of chloroquine on haemozoin crystals in parasite cells.

2. MATERIALS, INSTRUMENTATION AND GENERAL METHODS

2.1 MATERIALS

All the materials used in this study were of the highest commercial grade available and no further purification was done before they were used.

2.1.1 Solid materials (salts and powders)

Solid materials excluding stains used in this study are listed in Table 2.1.

Table 2.1. List of solid materials used in this study.

Material	**Commercial supplier**
1,2-Dimyristoyl-*sn*-glycero-3-phosphocholine (DMPC)	Avanti Polar Lipids, Alabaster, USA
rac-1-Monopalmitoylglycerol (MPG)	Sigma-Aldrich
rac-1-Monostearoylglycerol (MSG)	Sigma-Aldrich
1,3-Dipalmitoylglycerol (DPG)	Sigma-Aldrich
Citric acid monohydrate	Sigma-Aldrich
4-Morpholineethanesulfonic acid (MES)	Sigma-Aldrich
Adenosine 5′-triphosphate disodium salt (ATP)	Sigma-Aldrich
Phosporus pentoxide	Sigma-Aldrich
Porcine haemin	Fluka
Sodium hydroxide	KIMIX
4-(2-Hydroxyethyl)-1-piperazineethanesulfonic acid (HEPES)	Sigma-Aldrich
Acetic acid, glacial	Sigma-Aldrich
L-Glutathione reduced	Sigma-Aldrich
2,3-Diphospho-D-glyceric acid pentasodium salt	Sigma-Aldrich
Ammonium persulphate	Sigma-Aldrich
Sodium dodecylsulphate (SDS)	Sigma-Aldrich
Caesium chloride	ANALAR
Chloroquine diphosphate salt	Sigma-Aldrich
Paraformaldehyde	Sigma-Aldrich
Tanic acid	Sigma-Aldrich
Osmium tetroxide	Electron Microscopy Sciences-USA
Phosphate buffered saline (PBS) tablet	Sigma-Aldrich
Saponin	Sigma-Aldrich

2.1.2 Liquid materials (solvents and suspensions)

Liquid materials excluding stains used in this study are listed in Table 2.2.

Table 2.2. List of liquid materials used in this study.

Material	**Commercial supplier**
1,3-Dilinoleoylglycerol (DLG)	Sigma-Aldrich
1,3-Dioleoylglycerol (DOG)	Sigma-Aldrich
Pyridine	Sigma-Aldrich
Acetone	KIMIX
Methanol	KIMIX
Diethylether	KIMIX
Chloroform	KIMIX
Ethanol	KIMIX
Pentanol	Sigma-Aldrich
n-Hexane	KIMIX
Nujol (mineral oil)	Sigma-Aldrich
TEMED (tetramethylethylenediamine)	Merck
2-Mercaptoethanol	Merck
Pre-stained Protein ladder	Fermentas
Acetonitrile	Fluka
DNAse I	Sigma-Aldrich
Gluteraldehyde	Agar Scientific
RBC (group O+) obtained from expired blood bank whole blood	University of Cape Town, teaching hospital
Spurr's resin	Agar Scientific-UK

2.1.3 Stains

Stains used in this study are listed in Table 2.3.

Table 2.3. List of stains used in this study.

Material	**Commercial supplier**
Malachite green	Sigma-Aldrich
Premuline	Sigma-Aldrich
Silver stain kit	Sigma-Aldrich
Coomassie blue R250	Saarchem
Lipophilic 3,3'-dioctadecyloxacarbocyanine perchlorate fluorescent dye (DiO)	Molecular Probes
Uranyl acetate	Electron Microscopy sciences
Giemsa azur-eosin methylene blue	Merck

2.1.4 Accessories and devices

Accessories and devices used in this study are listed in Table 2.4.

Table 2.4. List of accessories and devices used in this study.

Material	**Commercial supplier**
Schott-Duran crystallization dishes	Sigma-Aldrich
Surgical blades	Lasec
Disposable 1 mL syringes and needles	Lasec
Carbon grids	Agar Scientific
Whatmann filter paper number 1	Lasec
Filtration device	Sigma-Aldrich
Microscope glass slides	Lasec
Thin glass coverslips	Lasec
Cryo holders	Gatan-UK
Transparent polycarbonate Nalgene® centrifuge tubes	Sigma-Aldrich
Quantifoil holey grids	SPI Supplies-USA
250 mL culture flasks	Greiner
NaCl plates	PIKE Technologies
REICHERT ultra-microtome	Leica

2.1.5 Software

The *SingleCrystal* application of *CrystalMaker® Software Version 2.2* was used to index electron diffraction patterns obtained from β-haematin and haemozoin crystals **(**CrystalMaker® Version 2.2, 2009, Oxford, England). *Prism 3* was used to construct all graphs and *Image J* developed at the National Institutes of Health, USA, was downloaded for free (http://imagej.en.softonic.com/) and used to invert colours of some β-haematin crystal images and electron diffraction patterns taken using TEM for colour consistency.

2.2 INSTRUMENTATION

2.2.1 Light microscopy

A Laborlux 12 Leitz Light microscope was used to look at thin films of malaria parasites prepared on glass microscope slides to determine growth stages of parasites in culture, to check if the parasites in culture were growing normally, to check if parasite cultures were

infected, to quantify parasitaemia and to count isolated haemozoin crystals on a haemocytometer.

2.2.2 UV-Visible spectrophotometry

UV-Vis spectrophotometry was used to quantify β-haematin formed. The absorption spectrum of aqueous Fe(III)PPIX exhibits a weakened and broadened Soret band relative to the monomer, a weaker Q band and a weak, but nonetheless prominent, charge transfer band. Addition of pyridine to Fe(III)PPIX solution causes the weak Soret band to become sharper and more intense with a red shift from 389 to about 404 nm in its absorption spectrum. This intense Soret band results from the formation of a low-spin coloured coordination complex of pyridine with the Fe(III) centre of Fe(III)PPIX (Ncokazi et al., 2004). The intensity of the coloured complex formed obeys the Beer-Lambert law. Thus, the absorbance of the coloured complex formed is proportionate to the concentration of free Fe(III)PPIX in the solution. Quantification of β-haematin formed for yield determination and for kinetics measurements was done using a Varian Cary 100 UV-Visible spectrophotometer to measure absorbance at 405 nm of the coloured pyridine-Fe(III)PPIX complex.

2.2.3 Fourier Transform Infrared (FT-IR) spectroscopy

FT-IR spectroscopy was used to characterize β-haematin formed at lipid-water interfaces. The resultant absorption/transmission spectrum is unique for each bond type producing a molecular fingerprint for each bond type. The IR spectrum of β-haematin or haemozoin has peaks at 1662 cm^{-1} and 1210 cm^{-1} corresponding to its unique characteristic C=O and C–O bonds in the crystal respectively. Therefore, dried β-haematin product formed with NLB and MPG, was finely ground using a mortar and pestle and prepared as nujol mulls and observed on a NaCl plate between 2000 and 1000 cm^{-1} using a Perkin–Elmer Spectrum 100 FT-IR spectrometer located in the Department of Chemistry, University of Cape Town.

2.2.4 Water bath

All β-haematin formation experiments were done at physiological temperature (37°C). A YIH DER BL-710 water bath with thermometer to measure the temperature of the water was heated to the required temperature before any experiment for β-haematin formation was

carried out. An external thermometer was also used to measure the temperature of buffer solution in the reaction vessel incubated in the water bath to confirm that they were actually heated to the required temperature before any experiment was conducted.

2.2.5 Confocal laser microscopy

This was used to characterize both β-haematin and NLB droplets formed at the lipid-water interface. This instrument measures the fluorescence from a sample. When the laser, which acts as the light source, is passed through a sample containing fluorescent molecules at a particular wavelength, it causes excitation of the molecules (at the excitation wavelength) and, as the excited electron returns to the ground state, it emits energy at a longer wavelength (emission wavelength) which can be measured as fluorescence arising from the molecule. β-Haematin autoflouresces when excited at 516 nm with emission measured between 575–630 nm. The DiO dye, which was used to stain NLB droplets, fluoresces under conditions of 488 nm excitation with emission of 500-530 nm. A LSM510-META Zeiss confocal laser microscope was used to characterize the β-haematin as a function of time and NLB stained with DiO by measuring fluorescence emission with excitation at their respective wavelengths.

2.2.6 Transmission electron microscopy (TEM)

This was used to characterize β-haematin formed by different methods using different starting materials, haemozoin isolated from parasites and also within parasites, NLB droplets formed under different conditions and liposome preparations. TEM allows for the visualization of structures in the nanometre range with high resolution. The TECNAI TF20 TEM which operates at a high voltage of 200 kV further allows for the visualization of elements in materials. Thus, the TECNAI TF20 TEM was used to visualize and characterize haemozoin inside parasitized RBCs, isolated haemozoin, β-haematin prepared by different methods, lipid emulsions formed under different conditions and liposome structures. This instrument was also used to obtained electron diffraction patterns from β-haematin and haemozoin crystals.

2.2.7 Glow-discharger

EMS 100X Glow-discharge (Electron Microscopy Sciences-UK) equipment was used to glow-discharge carbon-coated grids to make the surface more hydrophilic for materials in solution to adsorb on it for imaging using TECNAI TF20 TEM.

2.2.8 pH meter

This was used to adjust the pH of all solutions to their respective working pH values. All buffers used in this study were adjusted to their respective working pH using a CRISON Micro pH 2000 pH meter. Standard solutions at pH 4.00 ± 0.01 (Buffer, reference standard, B5020) and 7.00 ± 0.01 (Buffer, reference standard, B4770) were used to calibrate the pH meter.

2.2.9 Centrifuge

Centrifugation of all solutions, mixtures or suspensions of volumes greater than 5 mL was done using an Eppendorf Centrifuge 5810R while volumes less than 5 mL were centrifuged using an Eppendorf Centrifuge 5410.

2.2.10 Weighing balance

All salts and solid substances used in this study were weighed using an Adventurer^{TM} OHAUS weighing balance which was regularly calibrated with mass standards.

2.3 GENERAL METHODOLOGY

2.3.1 Parasite culture

2.3.1.1 Preparation of solutions

Preparation of 5 % sorbitol solution

A 5% sorbitol solution was prepared in deionized water (50 g/L). The solution was filtered through a 0.22 μm filter and stored at 4^{o}C.

Preparation of incomplete culture medium

This contained 10.4 g/L RPMI 1640 with glutamine but without $NaHCO_3$, 4 g/L glucose, 6 g/L HEPES (buffer), 0.088 g/L hypoxanthine, 5 g/L Albumax, and 1.2 mL/L (0.05 g/L) gentamycin. The medium was pre-filtered with a 0.45 μm filter then filter sterilized using a 0.22 μm filter.

Preparation of wash medium

Wash medium was prepared in the same way as incomplete culture medium but without any Albumax.

Preparation of complete culture medium

To the incomplete culture medium, 5% bicarbonate was added to make a complete culture medium (8.4 mL to 200 mL incomplete medium).

Preparation of reaction buffer

This contained 0.5 g $MgSO_4.7H_2O$, 7.4 g KCl, 0.58 g NaCl and 6 g HEPES dissolved in 1 L of deionized water and adjusted to pH 7.5 using 1 M NaOH. The solution was stored at room temperature.

Preparation of 1 % saponin solution

A 1% saponin solution (0.01 g/mL) was prepared in deionized water.

Preparation of Giemsa stain solution

A 10% Giemsa stain solution was prepared in 1x PBS.

Giemsa staining precedure

A thin film of parasite preparation on a glass microscope slide was sprayed with methanol and allowed to dry in order to fix the cells. A 10% Giemsa stain was added onto the fixed glass slide to completely cover the thin film. This was allowed to stand for about 10 min, after which the Giemsa stain was washed under slow running tap water and the slide was allowed to dry before it was viewed under a light microscope using oil immersion.

Preparation of red blood cells (RBCs)

20 mL expired whole blood from the University of Cape Town teaching hospital blood bank was transferred into sterile centrifuge tubes. 30 mL wash medium was added and spun down at 750 rpm for 5 min. The supernatant was discarded and the process repeated. The resulting washed RBCs were stored at 4^{o}C.

Synchronization

To the pellet of parasitized RBCs (iRBCs), 5 volumes of 5% sorbitol were added and allowed to stand for 10 min at 37°C in a water bath. Sorbitol lysed all stages of the parasites except for the ring stage and the uninfected RBCs. The solution was spun down at 750 rpm, the superntant discarded and the pellet put back into a 250 mL culture flask for further culturing.

2.3.1.2 Experimental procedures

Parasitized RBCs (NF54 or D10 strains) were maintained in continuous culture with complete culture medium according to the method described by Trager and Jensen with some minor modifications. Starting with the synchronized ring stage, iRBCs were diluted to 5% hematocrit with complete culture medium in 250 mL culture flasks. The culture flask was gassed with 3% O_2 and 4% CO_2 for about 2 min before being incubated in a CO_2 incubator at 37°C for parasite growth. After 24 h of culturing, the flask was taken out of the incubator into a sterile laminar flow hood. The cultured mixture was spun down at 750 rpm for 5 min. The

supernatant decanted and a small volume of iRBC pellet was placed on a glass microscope slide and spread across the slide with the aid of another microscope slide to form a thin film. The thin film was stained with 10% Giemsa solution before being viewed with an oil immersion lense on a light microscope to check if parasites in the RBCs had actually grown to their trophozoite stage. The remaining iRBC pellet was subcultured in a different 250 mL culture flask with the addition of complete culture medium and washed RBCs (group O+) to 5% hematocrit. The flask was gassed again with with 3% O_2 and 4% CO_2 for about 2 min before being incubated at 37°C in a CO_2 incubator for growth to continue. After another 24 h of incubation, the flask was taken out and iRBCs spun down at 750 rpm for 5 min in a sterile 50 mL falcon tube. The supernatant was discarded and the pellet synchronized with 5% sorbitol solution. The synchronized iRBCs at ringe stage were then put back into culture. This cycle was continued until sufficient parasites were harvested at the trophozoites stage.

2.3.2 Isolation of haemozoin crystals

Parasites for haemozoin isolation were harvested at the trophozoite stage in their intraerythrocytic life cycle. The trophozoites were harvested from iRBCs by lysing the iRBCs using 1% saponin solution with 2 min incubation. The lysed iRBCs were then centrifuged at 1500 rpm for 10 min. The supernatant was decanted leaving behind the pelleted trophozoites. The trophozoites were then washed twice with PBS by centrifuging at 1500 rpm for 10 min for each wash. The pellets were again washed further with reaction buffer by centrifuging at 1300 rpm for 1 min. The supernatant was decanted and the pellet resuspended in deionized water (pH 4.6). The suspension was triturated 10 times using a 26.5 gauge needle to break open the trophozoites releasing the parasite digestive vacuoles (DVs) and other cytosolic materials into solution. The lysate was centrifuged at 1300 rpm for 1 min. The supernatant was decanted and the pelleted DVs resuspended in 1 mL of reaction buffer. 10 µL DNase I was added to the solution to digest any DNA present and the solution was incubated for 5 min at 37°C. The incubated solution was then centrifuge at 1300 rpm for 1 min. The supernatant was decanted and the pelleted DVs were washed twice with reaction buffer by centrifuging at 1300 rpm for 1 min for each wash. Isolated DVs were further resuspended in deionized water, frozen and thawed at -80 ^{o}C to break open the DVs to release the haemozoin crystals. The mixture was spun down at 1300 rpm for 1 min. The supernatant was decanted

leaving the pelleted haemozoin crystals. This process was repeated at least three times to ensure all DVs were completely lysed.

2.3.3 Quantification of isolated haemozoin crystals

A 4 µL haemozoin crystal pellet was made up to 100 µL with deionized water. A suspension of the haemozoin crystal was placed carefully between a thin glass cover slip and placed on the surface of a bright light hemocytometer mounted on a Laborlux 12 Leitz light microscope. The setup was allowed to stand for some time for any movement in the suspension to completely stop. Haemozoin crystals in 5 of the 25 larger squares on the hemocytometer were manually counted under the light microscope.

2.3.4 Preparation β-haematin from lipid and Fe(III)PPIX

2.3.4.1 Preparation of solutions

0.1 M NaOH

NaOH pellets (1.0 g) were weighed out and dissolved in 250 mL of distilled water.

1:9 v/v acetone/methanol mixture

Acetone (10 cm^3) and methanol (90 cm^3) were both measured using a measuring cylinder and mixed together to give a 1:9 v/v mixture of acetone/methanol.

2 mg/mL haematin solution

Porcine haemin (2 mg) was dissolved in 400 µL of 0.1 M NaOH. The solution was vortexed and sonicated for 3-5 min and then made up to 1 mL with 1:9 v/v acetone/methanol.

50 mM citric acid buffer, pH 4.8

Citric acid (10.507 mg) was dissolved in 1 L of distilled water to give a concentration of 50 mM. The pH was adjusted to 4.8 with NaOH slurry.

3.31 mM MSG solution

MSG powder (11.86 mg) was dissolved in 10 mL of 1:9 acetone/methanol mixture.

3.31 mM MPG solution

MPG powder (10.98 mg) was dissolved in 10 mL of 1:9 acetone/methanol mixture.

3.31 mM DPG solution

DPG powder (18.56 mg) was dissolved in 10 mL of 1:9 acetone/methanol mixture.

3.31 mM DLG solution

From the liquid DLG stock, 22.2 μL was pipetted out and made up to 10 mL with 1:9 acetone/methanol mixture.

3.31 mM DOG solution

From the liquid DOG stock, 21.84 μL was pipetted out and made up to 10 mL with 1:9 acetone/methanol mixture

3.31 mM neutral lipid blend (NLB) solution

The constituent lipids prepared in 1:9 v/v acetone/methanol were made up in the ratio MSG, MPG, DPG, DLG, DOG (4:2:1:1:1 v/v) to give a total concentration of 3.31 mM.

5% pyridine solution (100 mL)

To 5 mL pyridine solution, 50 mL acetone, 10 mL HEPES (0.2 M, pH 7.5) and 35 mL of distilled water were added and thoroughly mixed together.

Extrusion of liposomes and micromixing of lipid or lipid mixed with Fe(III)PPIX solution

Liposomes or solutions of neutral lipids (NLB or MPG) or neutral lipids mixed with Fe(III)PPIX at different concentrations were extruded or micromixed by passing them several times through a 10 μm pore filter using an Avanti® Mini-Extruder.

2.3.4.2 Experimental procedures

β-Haematin was prepared using a method previously described by Hoang et al. (2010a & b) with some slight modifications as follows: 50 mL citric acid buffer (50 mM, pH 4.8) in a Schott-Duran crystallization dish with internal diameter of 9 cm was pre-incubated for 30 min at 37°C in a water bath. 1 mL of 3.31 mM MPG or NLB solution was mixed with 500 µL of 2 mg/mL Fe(III)PPIX solution to give a total volume of 1.5 mL of the mixture. The solution was layered carefully on the surface of the pre-incubated citric acid buffer using a 1 mL syringe and this was incubated further at 37°C for either 30 min or at different lengths of time to monitor β-haematin formation. A control reaction mixture for β-haematin preparation was set up exactly as described above but without lipid.

2.3.5 Collection and processing of β-haematin crystals for TEM imaging and TEM-ED pattern acquisition

Samples where carefully taken from the milky emulsion layer and placed on a glow-discharged carbon-coated grid. Excess solution was blotted on Whatmann filter paper number 1 and the grid was immediately stained with a negative stain (uranyl acetate) by carefully placing the grid on a drop of the uranyl acetate solution and it was allowed to stand for about 3-5 min. Excess stain on the grid was blotted on Whatmann filter paper number 1 and the grid was allowed to dry at room temperature. A TECNAI TF20 TEM operating at 200 kV located at the Electron Microscope Unit, University of Cape Town, was used for normal imaging of crystalline materials on the grid and also for acquisition of diffractions pattern from the imaged crystalline structures.

2.3.6 Indexing of diffraction patterns

The SingleCrystal™ application of CrystalMaker® Software Version 2.2 was used to index the diffraction patterns obtained from β-haematin crystals (CrystalMaker, Oxford, 2009). The calculated structural data for β-haematin described by Pagola et al. (2000) was used to build a structural model of the β-haematin crystal using CrystalMaker®. The single crystal diffraction software was then used to predict a simulated diffraction pattern based on this structure. The Grid tool in SingleCrystal™ was used to index the diffraction pattern obtained from β-haematin crystals as follows; The observed electron diffraction pattern obtained from the β-haematin crystals was opened using the single crystal window of the software. In the same

window, the CrystalMaker® file for the reported β-haematin crystal structure was loaded. The Grid tool was superimposed on the observed diffraction pattern, making sure that all observed diffraction spots coincided. The grid was adjusted such that all grid points lay directly over the observed points. The software was then used to match the simulated pattern with the observed pattern, with the strongest reflections being indexed in this manner.

3. THE PROTEOME AND LIPIDS ASSOCIATED WITH HAEMOZOIN CRYSTALS

3.1 INTRODUCTION

As discussed in Chapter 1, the Hz crystal, with its well-known structure (Pagola et al. 2000), is formed via a complex biomineralization process in the malaria parasite and other blood-feeding organisms such as *S. mansoni* (Oliveira et al. 2000), *H. columbae* (Chen et al. 2001) and *R. prolixus* (Oliveira et al. 1999). Proteins belonging to the *P. falciparum* proteome such as HRP II (Sullivan et al., 1996), HDP (Jani et al. 2008) and lipids (Fitch et al. 1999 & Pisciotta et al. 2007) isolated from *P. falciparum* have been shown to efficiently promote β-haematin formation *in vitro*.

The involvement of lipids in biomineralization processes has been described in different, unrelated organisms such as the formation of coccoliths in *E. huxleyi* algae (Young et al. 1992) and the growth of dentine in humans (Anderson et al. 1995) which are known to be lipid-mediated processes. Lipid involvement in crystal growth is therefore evident as it provides an organic phase for nucleation to occur.

Alternatively, proteomic studies of biomineral matrix proteins in different unrelated organisms such as human bone matrix (Alves et al. 2011), shell matrix from Manila clams (Marie et al. 2011), sea urchin shell and spine (Mann et al. 2008), radular teeth in the giant pacific chiton (Nemoto et al. 2012), chicken egg shell (Mann et al. 2006) and the bacterial magnetic protein (BacMP) membrane from magnetite producing bacteria (Alves et al. 2011) using SDS-PAGE and LC-MS techniques have all led to the identification of the proteins involved in these biomineralization processes.

The question of which bioorganic molecules (lipids and/or proteins) are involved in the biomineralization of Hz *in vivo* has been a subject of intense debate. Given that proteomic studies of biomineral matrix proteomes in other organisms have invariably led to the identification of the protein(s) involved in biomineralization process, it was decided to use SDS-PAGE and LC-MS/MS to study the proteome related to the Hz crystal so as to identify proteins associated with Hz to determine whether any potential Hz-mediating proteins could be identified. At the same time, the lipids associated with the Hz crystal surface were also investigated and will be discussed in this chapter.

3.2 METHODS

3.2.1 Parasite culture, isolation, quantification and TEM of Hz crystals

Parasitized RBCs (*P. falciparum* NF54 strain) were maintained in continuous culture with complete culture medium according to the method described by Trager & Jensen with some minor modifications as described in Section 2.3.1.2 of Chapter 2. Trophozoite stage iRBCs were harvested and Hz crystals isolated and quantified as described in Section 2.3.2 in Chapter 2. Isolated Hz crystals in deionized water were placed on a carbon-coated grid. Excess aqueous solution was blotted with Whatmann filter paper number 1 and the grid was allowed to dry at room temperature before visualizing using a TECNAI TF20 TEM operating at 200 kV for normal imaging.

3.2.2 Casting and running of 15% SDS-PAGE gel

Sodium dodecyl sulfate polyacrylamide gel electrophoresis (SDS-PAGE) was used to separate proteins associated with haemozoin crystals. SDS-PAGE is a technique that uses a potential difference to separate proteins according to their molecular weight based on their differential mobility in the polyacrylamide gel. Higher gel percentages separate proteins of smaller molecular weight with better resolutions. A 15% SDS-PAGE was used to separate all the proteins found on the surface and in the matrix of haemozoin crystals isolated from *P. falciparum* based on their molecular weight before subsequent identification using LC-MS.

3.2.2.1 Sample preparation

Preparation of resolving buffer

A solution of 0.185 g/mL of Tris and 0.004 g/mL SDS was prepared in distilled water and the pH adjusted to 8.8.

Preparation of stacking buffer

A solution of 0.0605 g/mL Tris and 0.004 g/mL SDS was prepared in distilled water and the pH adjusted to 6.8.

Preparation of 5× running buffer

A solution containing 15.1 g Tris, 72 g glycine and 5 g SDS water was prepared in 1 L of distilled water (pH was between 8.3-8.5).

Preparation of 4× sample buffer

This contained 10 mL stacking buffer, 8 ml glycerol, 0.8 g SDS, 0.8 mL of 2-mercapto-ethanol, 0.2 mg bromophenol blue and 1.2 mL distilled water.

Preparation of 15% resolving gel (10 mL)

This contained 3.55 mL distilled water, 3.75 mL of 40% acrylamide, 2.60 mL resolving buffer, 0.100 mL of 10% ammonium persulphate (APS) and 0.006 mL TEMED (tetramethylethylenediamine).

Preparation of 5% stacking gel (10 mL)

This contained 1.480 mL distilled water, 0.250 mL of 40% acrylamide, 0.270 mL stacking buffer, 0.020 mL of 10% APS and 0.004 mL TEMED. In all cases TEMED was added last prior to pouring the gel solution into the casting device.

3.2.2.2 Experimental procedures

Resolving gel solution was poured carefully into the gel casting device (BIO-RAD Mini-PROTEAN® 3 Cell system) to avoid the formation of air bubbles. The gel solution was allowed to solidify. The stacking gel solution was carefully poured on top of the solidified resolving gel. Combs were fitted into the stacking gel solution and the latter was allowed to solidify. After solidification of the stacking gel, the comb was removed forming wells in the gel. Hz sample preparation for protein separation by SDS-PAGE was as illustrated in Figure 3.1.

Samples (4% SDS-washed extract from Hz crystal surface, PBS-rinsed solution from washed Hz crystals and dissolved Hz crystals) were mixed with 4× sample buffer in the ratio 3:1. The samples were heated in boiled water for about 5 min. 20 µL of each sample was then loaded into an appropriate well on the 15% SDS-PAGE gel mounted in a BIO-RAD Mini-PROTEAN® 3 Cell system. The gel was run at constant current of 30 mA for 75 min. The molecular weight marker used was PageRuler^{TM} Plus, Prestained protein ladder (Fermentas).

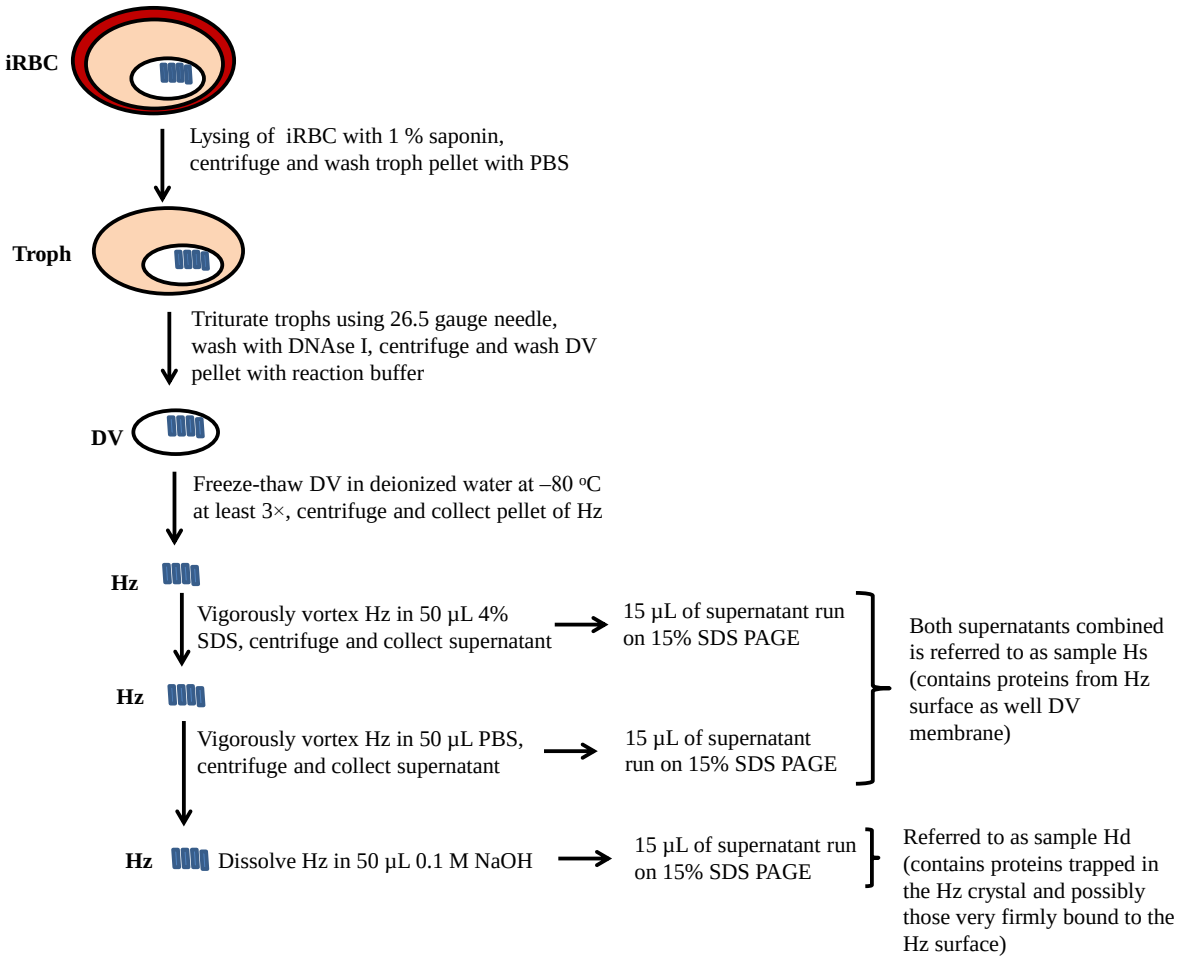

Figure 3.1. Schematic representation of the Hz isolation process to sample preparation for SDS-PAGE protein separation. “Troph” represent trophozoites.

3.2.3 Staining and destaining of gels

3.2.3.1 Sample preparation

Preparation of Coomasie Blue stain solution

A 0.25% Coomassie Blue R250 solution was prepared by first disolving the Coomassie Blue R250 in methanol (450 mL) before adding 450 mL water and 100 mL acetic acid to it.

Preparation of destaining solution

This contained 600 mL water, 300 mL methanol and 100 mL acetic acid.

3.2.3.2 Experimental procedures

Gels containing extracts from Hz surface and dissolved Hz crystals were placed in a solution of Coomassie Blue stain overnight with continuous shaking on a shaker device (FINEPCR orbital shaker SH30). The overnight stained gel was destained with a destaining solution while shaking until the gel was clear leaving behind only stained protein bands. ProteoSilver^{TM} Plus Silver Stain Kit (SIGMA) was used to stain and destain the gel containing PBS-rinsed solution from washed Hz crystals according to the procedure described in the kit manual. Pictures of stained gels were taken using a ChemiDOC^{TM} XRS+ with image lab^{TM} software located at the Molecular and Cellular Biology Department at the University of Cape Town. Gel pieces were carefully cut out from different protein bands and gel portions using surgical blades. Each gel piece was placed in a labelled Eppendorf tube containing 50 µL acetonitrile to dehydrate the gel pieces for 15 min. The dehydrated gel pieces were sent to the Center for Proteomic and Genomic Research at the University of Cape Town for protein identifcation by LC-MS/MS.

3.2.4 LC-MS/MS protein identifcation from gel pieces

3.2.4.1 In-gel digestion

Gel slices were destained in an Eppendorf 1.5 mL tube with 200 mM NH_4HCO_3:acetonitrile 50:50 (Burdick & Jackson; Sigma) until clear. The gel pieces were further dehydrated and desiccated. They were then washed with 25 mM NH_4HCO_3 followed by another dehydration step. Proteins were digested by rehydrating gel pieces in 20 ng/µL trypsin (Promega) solution and incubating overnight at 37°C. Peptides were extracted from the gel pieces with 50 µL of

0.1% trifluoroacetic acid (TFA) (Sigma), 2% acetonitrile (ACN) followed by a second extraction with 50% acetonitrile/H_2O containing 0.1% trifluoroacetic acid (TFA). The samples were dried down and 200 μL water added and dried down again to remove residual NH_4HCO_3.

3.2.4.2 Chromatography

Nano-RP-LC chromatography was performed on a Dionex Ultimate 3000 nano-HPLC system. The solvent system employed was solvent A, 2% ACN/water; 0.15% TFA and solvent B 80% ACN/water; 0.12% TFA. The gradient was generated at 300 nL/min as follows; 0-10 min 5-12.5% B, 10-120 min 15-40% B, 120-140 min 40-55% B, 140-150 min 90% B and 150-165 min 5% B. The gradient from 5-55% B used for sample analysis was generated using a combination of a linear and Chromeleon non-linear gradient 6 gradients. Fraction collection commenced after 20 min with 120 min duration. The eluted peptides were spotted onto a MALDI target plate using a Probot (LC packings) robotic spotter. MALDI matrix (7.5 mg/mL CHCA, 10 mM monobasic ammonium phosphate; calibration mixture in solvent B) was added at 1:2 ratios to the column outflow (600 μL/min) through a micro-T connector. Final matrix concentration was 5 mg/mL. Spots were collected at 15 s intervals.

3.2.4.3 Mass spectrometry

Mass spectrometry of collected fractions was performed as follows. The laser was set at 4400 arbitrary units, 500 laser shots/spectrum, and grid voltage at 16 kV. All spots were internally calibrated using a 5 point calibration mixture with minimum of 1 point to match with mass tolerance of m/z = 0.1, maximum outlier error of 10 ppm. The interpretation method used for ion selection was: minimum signal/noise ratio = 35, excluded adducts = 22.99, global exclusion lists were generated from the calibration spectra with m/z tolerance equal to 0.1. In addition, all precursors within 150 FWHM (full width half maximum) resolution were excluded. Tandem mass spectrometry acquisition parameters were: laser set at 4800 arbitrary units, a maximum of 5000 laser shots/spectrum, grid voltage at 16 kV. Stop conditions were set to cease acquisition once the following criteria were met: 8 peaks with signal to noise ratio equal or greater than S/N = 100.

3.2.4.4 Data analysis

Database interrogation was performed with the Mascot algorithm using the Swissprot database on a GPS workstation. Search parameters were set as in Table 3.1.

Table 3.1. Specification for search parameters used to perform MASCOT analysis for protein identification.

Parameters	**Specification**
Species	*Plasmodium falciparum* and *Homo sapiens*
Enzyme	Trypsin
Maximum number of missed cleavages	1
Fixed modifications	Carbamidomethyl
Variable modifications	Oxidation and deamination
Precursor tolerance	0.1 da
Fragment tolerance	0.2 da
Minimum peptide confidence interval	95%

3.2.5 Lipid TLC

3.2.5.1 Sample preparation

Preparation of premuline stain

A 0.05 mg/mL solution of premuline stain was prepared in acetone:water (80:20).

3.2.5.2 Experimental procedures

The 4% SDS washed extracts from Hz crystals were mixed with chloroform:methanol (2:1) solvent so as to facilitate the extraction of lipids from the solution. About 2-4 µL of the mixture was spotted on a silica gel TLC plate using a thin capillary glass tube. Control lipids of individual MSG, MPG, DPG, DLG, DOG (2.5 mg/300 µL each) were prepared in chloroform:methanol (2:1) solvent and about 2-4 µL of each spotted on the TLC plate. The bottom of the plate was immersed in solvent I (chloroform:methanol:water at 50:20:3 v/v) in a closed system allowing the different classes of lipid to be separated along the TLC plate as the solvent moved up the plate by capillary action. Using a soft pencil, a line was drawn across the TLC plate at the maximum height reached by solvent I. The TLC plate was

removed from solvent system I and placed in another closed system of solvent II (hexane:diethyether:acetic acid at 16:10:1 v/v) for further separation of lipid on the TLC plate as the solvent moved further up the plate by capillary action. Another line was drawn on the TLC plate where movement of solvent II was stopped. Premuline stain was sprayed on the TLC plate and it was then visualized under ultravoilet (UV) light.

3.3 RESULTS AND DISCUSSION

3.3.1 TEM of isolated Hz crystals

Hz crystals isolated from *P. falciparum* for proteomic study were viewed using TEM as shown on Figure 3.2. This showed Hz crystals were successfully isolated from the parasite and confirmed the starting material used for proteomic study indeed consisted of intact Hz crystals.

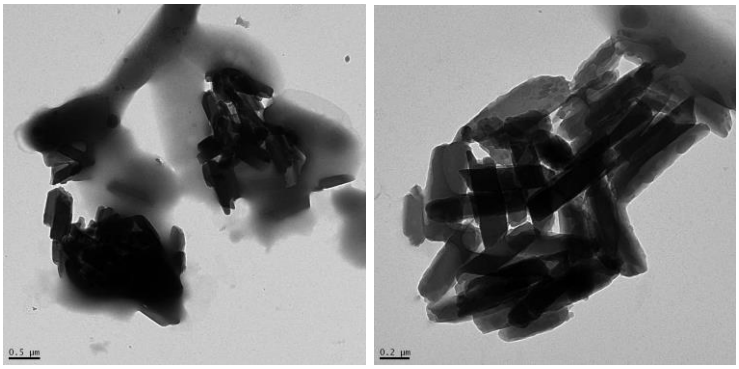

Figure 3.2. TEM imaging of isolated Hz crystals used for proteomic study.

3.3.2 Possible origins of some proteins likely to be identified with isolated Hz crystals

Haemoglobin is transported from the RBC cytoplasm to the parasite by invagination of a specialized cytostome structure together with parasite plasma membrane and the PV membrane which eventually fuse together to form one single membrane-bound DV (Elliot et al. 2008) as illustrated in a schematic diagram in Figure 3.3. Proteins coming from some of these parasite structures engulfed together with haemoglobin would likely be identified in this study too. Some RBC proteins are likely to be ingested together with haemoglobin and transported to the DV during the parasite feeding process. The lysing of iRBC to isolate trophozoites, followed by the DV and finally the Hz crystals, also causes some membranous

structures in the parasite cytoplasm to break open releasing their contents (membranes and soluble proteins) which are likely to be present with Hz crystal preparations. So therefore, it would be expected that some proteins coming from nuclear envelope, ER, Golgi bodies, plastid, lysosomes and parasite cytosol would be likely to be carried over as contaminants. The isolated Hz crystals are expected not to have large quantities of RBC and parasite membrane since they were isolated from DVs, but since lipid material was not removed from isolated crystals, the 4% SDS washed extracts would not only have proteins present on the surface of Hz crystals but also DV membranes. This fraction is hereafter referred to as sample Hs. The dissolved Hz crystals would be expected to contain proteins incorporated into the crystal matrix as well as any proteins that might be so strongly adsorbed on the crystal surface that were not dislodged by SDS. This fraction is hereafter referred to as sample Hd.

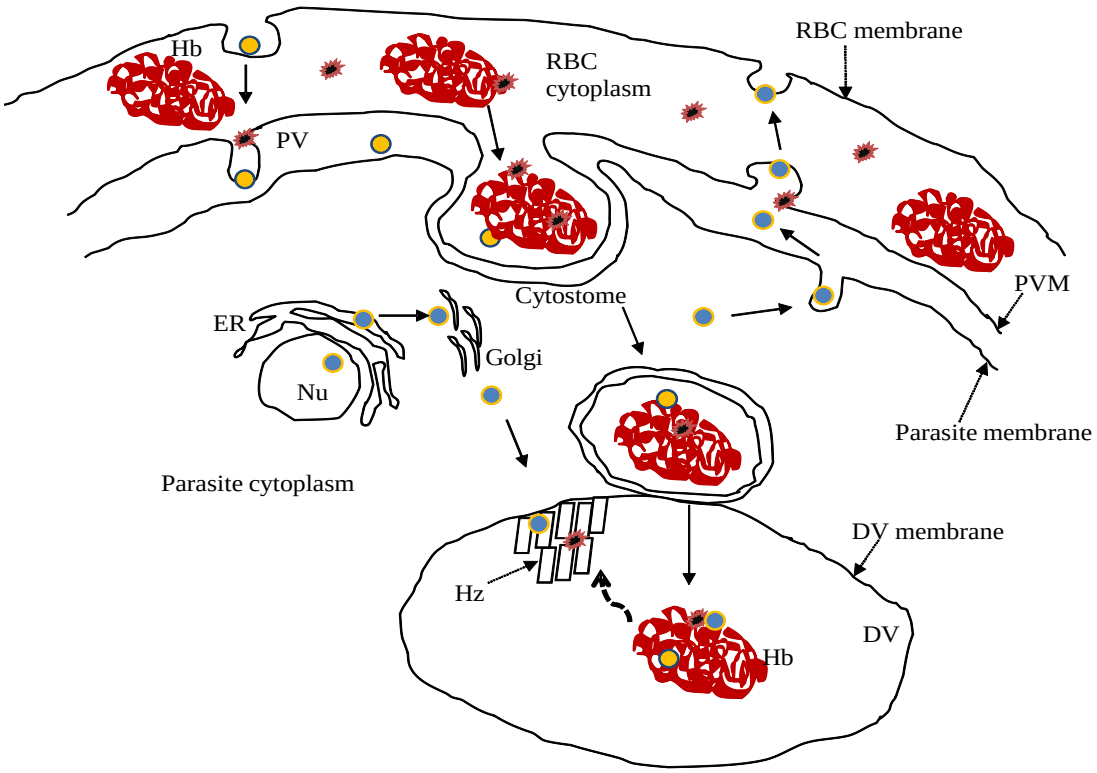

Figure 3.3. Schematic representation of invagination and transportation process of haemoglobin together with other RBC cytoplasmic proteins to the parasite DV via specialized cytostome structures. Hb; haemoglobin, Hz; haemozoin crystal, DV; digestive vacuole, PV; parasitophorous vacuole, PVM; PV membrane, Nu; nucleus, ER; endoplasmic reticulum, → possible protein trafficking route, ⇢ labels, ✸ RBC cytoplasmic proteins, ● possible plasma protein or RBC membrane protein, ● parasite proteins, ⇝ process of interest under investigation.

P. falciparum infection of human RBC is known to cause several changes and modifications of the proteome in both the parasite itself and it host cell, such as the incorporation of exported parasite proteins in the erythrocyte membrane cytoskeleton (Pei et al. 2005, Waller et al. 2007 and Pei et al. 2007) which results in an increase in iRBC plasma membrane permeability and rigidity (Glenister et al. 2002). Other related studies have also identified several RBC cytoplasmic proteins to be modified by the presence of *P. falciparum* in it (Fontaine et al. 2012). Moreover, the PVM is known to contain proteins derived from RBC plasma membrane (Murphy et al. 2007). Proteins trafficked via the PVM or cytostome derived structures from the PVM are therefore most likely to contain both cytoplasmic and membrane-derived RBC proteins.

3.3.3 A 15% SDS-PAGE of 4% SDS washed Hz extract and dissolved Hz crystal (Hz matrix)

SDS-PAGE is the most widely and extensively used proteomic technique in separating proteins according to their molecular weights. It was first used to separate the different proteins present in samples Hs and Hd before identification by LC-MS/MS. A 15 µl extract (supernatant) obtained from approximately 2.06×10^9 Hz crystals isolated and washed thoroughly with 50 µL of 4% SDS (sample Hs) was used to run a 15% SDS-PAGE and developed with coomassie blue R250 stain as shown in Figure 3.4A. The 15 µL extract used in lane 2 translates to material obtained from approximately 0.618×10^9 Hz crystals. The washed Hz crystals were then rinsed by a second wash with 50 µL PBS buffer, of which 15 µL of the supernatant was used to run another 15% SDS-PAGE and developed using silver stain kit (Sigma-Aldrich) as shown on lane 1 in Figure 3.4B. The washed Hz crystals were then dissolved in 50 µL of 0.1 M NaOH. Of the 2.06×10^9 completely dissolved Hz crystals, 15 µL was used for loading on lane 1 (sample Hd) in Figure 3.4A.

The average length of a Hz crystal is measured to be 500 nm as in Section 5.3.1 and the length to width ratio is 3.4, giving an average width of 147 nm for Hz crystals. Buller et al. (2002) measured the average width to thickness of haemozoin crystals to be 1.3 which gives an average thickness of 113 nm for Hz crystals. An average Hz crystal thus has a volume of 500 nm × 147 nm × 113 nm (8.3×10^6 nm^3). The Hz crystal unit cell dimension is 1.2 nm × 1.4 nm × 0.8 nm (1.344 nm^3). This implies there is an average of 6.175×10^6 unit cells per

Hz crystal. Considering there are 2 haem molecules per unit cell, there is an average of 12.35 $\times 10^6$ haem molecules per crystal. Since material from approximately 0.618 x 10^9 Hz crystals was used per lane, this corresponds to material associated with about 7.63 x 10^{15} haem molecules per lane. This translates to material from about 12 nmol of haem per lane on the gel. The instrument used for LC-MS/MS protein identification has a detection limit of around 5 to 10 fmol (measured for pure BSA). This corresponds to 1.3-2.5 $\times 10^6$ haem molecules per protein molecule at the detection limit, corresponding to 5-10 protein molecules per Hz crystal at the detection limit of the instrument.

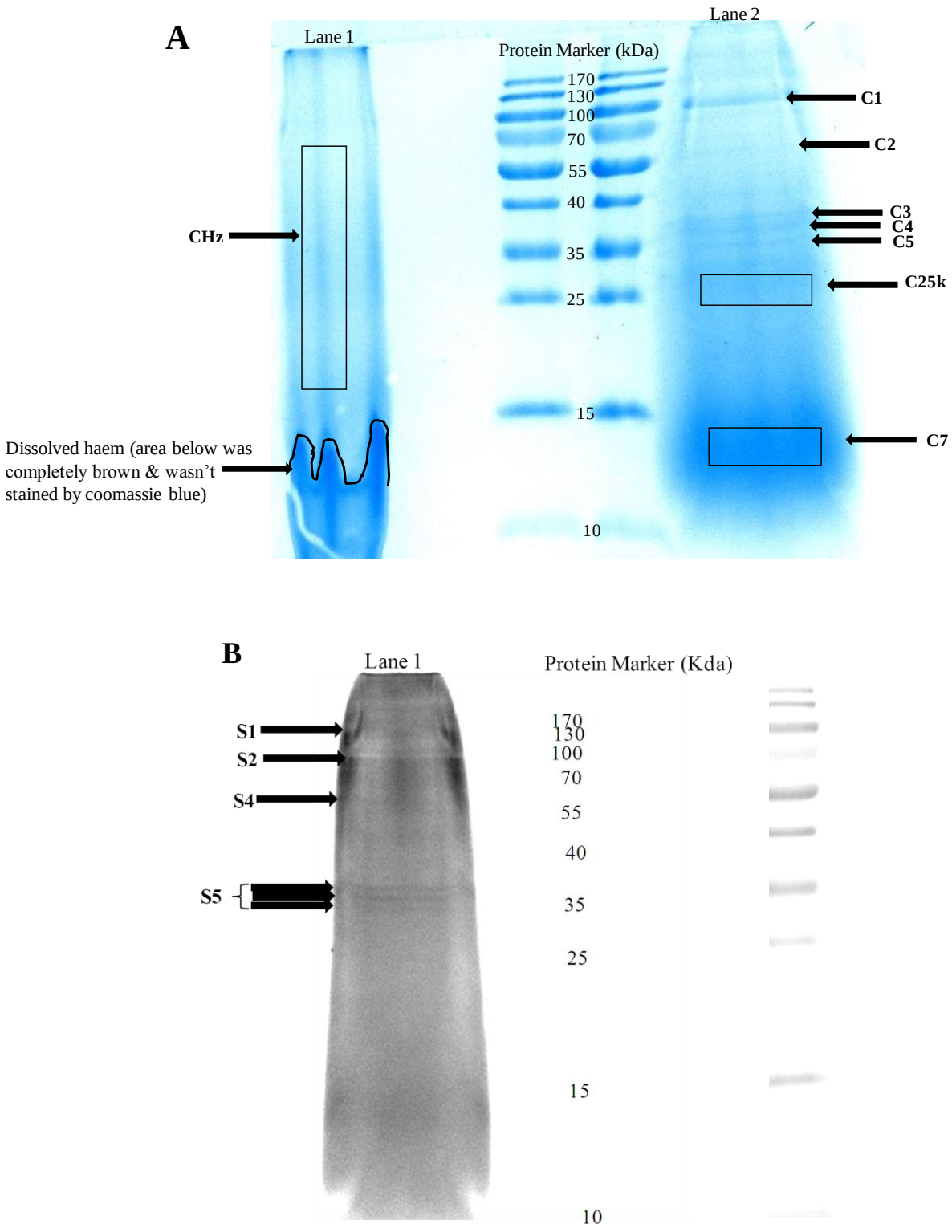

Figure 3.4. 15% SDS-PAGE of Hz crystal sample. A: Dissolved Hz crystals in lane 1 showed no distinct protein bands while the extract washed from the surface of Hz crystals with 4% SDS in lane 2 showed several distinct bands with coomassie blue stain. B: Silver-stained gel of material obtained from the surface of 4% SDS washed Hz crystals also showed distinct protein bands.

3.3.4 LC-MS/MS protein identification from gel sections

The different sections of both gels labelled from C1 through C7, C25k (gel section at 25 kDa), CHz (Figure 3.4A) and S1, S2, S4 & S5 (Figure 3.4B) were cut out for LC-MS/MS analysis for protein identification. Peptide fragments generated from LC-MS/MS were used for MASCOT analysis to interrogate both the *P. falciparum* and *H. sapiens* protein data bank. MASCOT is a probabilistic scoring algorithm that incorporates the MOWSE (Molecular Weight Search) scoring algorithm used for peptide mass fingerprinting (Pappin et al. 1993), fragment ion series, mass accuracy, and peptide length. The results from MASCOT are reported as a probability-based "Ions Score" (Kapp et al. 2005). This led to the identification of 71 unique *P. falciparum* proteins and 73 unique *H. sapiens* proteins (a complete list of all proteins identified from the respective gel sections is found in Appendix 1). Some of the identified proteins appeared not to be separated on the 15% SDS-PAGE according to their molecular weights calculated from their amino acid sequences. Proteins identified from bands at molecular weight lower than their predicted mass might be as a result of digestion by proteases in the DV, or released from lysed DVs during the Hz isolation process. Some proteins were also identified from bands at molecular weights higher than their predicted mass. This phenomenon of irregular migration of proteins on gels is not surprising as SDS-PAGE gel mobility studies of the proteomes of some organisms have shown that more than 40% of the proteins do not migrate within 10% of the predicted position calculated from their amino acid sequences (Shirai et al. 2008). This therefore indicates that it is difficult to predict the absolute molecular weight of proteins based on their mobility in SDS-PAGE solely from their amino acid sequences. Hydrophobicity, denoted by a GRAVYscore (Kyte et al. 1982), is one of the factors which is known to greatly affect the mobility of proteins on gels as hydrophilic proteins tends to exhibit slower migration. This is so because SDS preferentially binds to the hydrophobic regions of proteins in an approximate ratio of one SDS molecule to two amino acid residues (Shirai et al. 2008). Subcellular localization of proteins is also known to affect their mobility on gels as nuclear proteins tend to migrate slower such as P38545 (GTP-binding nuclear protein Ran) and P40282 (Histone H2A) identified in this study. Whereas proteins from mitochondria, ER and Golgi bodies tend to migrate faster compared to their predicted/calculated molecular weight e.g P34940 (Chaperonin CPN60, mitochondrial precursor), although it is difficult to distinguish amongst them those that are caused by degradation or digestion by proteases. Post-translational modification of proteins such as phosphorylation, glycosylation, ubiquitination etc. causes them to migrate slowly on

gels (Cook et al. 2003, Poly et al. 1997 & Zhu et al. 2002). On the other hand, cytosolic proteins are expected to migrate normally as predicted from their amino acid sequence. In this study, the majority of proteins were identified from gel bands at lower molecular weight than their respective predicted masses. This was expected since the proteins came from the DV which contains many proteases. Moreover, parasite proteins have also been shown to degrade host proteins (Dua et al. 2001 and Hanspal et al. 2002) and this may be the case with some of the human proteins identified in this study at gel bands below their expected molecular weight, such as P02730 (band 3 anion transport protein), P11678 (eosinophil peroxidase precursor), O14830 (serine/threonine protein phosphatase with EF-hands-2), etc.

Of the 71 unique *P. falciparum* proteins identified, 68 were from sample Hs and 24 from sample Hd respectively. *P. falciparum* is known to spend most of it life cycle in the human host inside the RBC. For this reason, all 73 unique *H. sapiens* proteins identified were interrogated against the human RBC proteome which is freely available on the Internet (http://proteome.biochem.mpg.de/rbc/_rbcsearch.jsp?flag=listall) (Pasini et al. 2006). Of the 73 unique *H. sapiens* proteins identified (Appendix 2), 37 belonged to the human RBC proteome. RBC proteins identified were found to be present associated with both the Hz crystal surface and matrix irrespective their supposed function there. Although the remaining 36 human proteins were not found in the human RBC proteome available on the Internet (Pasini et al. 2006), searches of the UNIPROTKB site with the protein accession number, identified them to have come from other human cells or cells from specific body tissues. These may be contaminants, although interestingly the RBC proteome available on the web also contains proteins that originate from cells in the brain, liver, bones, B cells, eosinophils, serum, etc. thus making it seemingly possible that some of the identified known non-RBC proteins might have entered the iRBC cytoplasm from the blood via the permeable iRBC cell membrane and were further engulfed together with haemoglobin and transported to the DV where haemoglobin digestion and Hz formation takes place. All 73 unique *H. sapiens* proteins identified were present on the surface of the Hz crystal while 19 were found in the Hz crystal matrix. Since it is possible that these proteins could merely be contaminants, for this study only the 37 proteins found in the RBC proteome available on the web together with the 71 unique *P. falciparum* proteins as indicated in Table 3.2 were considered for further discussion.

Table 3.2. Total number of identified *P. falciparum* and *H. sapiens* proteins considered in this study.

	Sample Hs		Sample Hd	
	P. falciparum protein	*H. sapiens* protein	*P. falciparum* protein	*H. sapiens* protein
Total proteins identified	68	73	24	19
No. of human proteins found in RBC proteome		37 (51%)		17 (89%)
Total protein considered for analysis	**68**	**37**	**24**	**17**
No. of proteins previously reported in DV	21 (31%)		10 (42%)	

A second algorithm known as X!Tandem was also used to interrogate the *P. falciparum* protein database using all peptide fragments generated from LC-MS/MS. X!Tandem is a heuristic algorithm for MS/MS protein identification that uses information of intensity patterns associated with particular amino acid residues to generate theoretical spectra for the peptide sequences which are then correlated with the experimental data using a dot product from which an expectation value is calculated (Kapp et al. 2005). So therefore, besides looking at how it compares to protein identification by MASCOT analysis, this was used to widen the spectrum of proteins identified by using both algorithms and, more importantly, to increase the chances of identifying proteins that have been suggested to be associated with Hz crystal formation inside the DV. A total of 91 unique proteins were identified using the X!Tandem algorithm (Appendix 3) of which only eight were also identified using MASCOT. Despite the differences in these two algorithms used for MS/MS protein identification, differences in software versions used has also been shown to account for the difference in the numbers and types of protein identified using these two algorithms from the same biological sample (Kapp et al. 2005). This may also be the reason why only eight proteins were identified by both algorithms. This gives a grand total of 154 unique proteins identified using the MASCOT and X!Tandem algorithms as shown in the Venn diagram in Figure 3.5. There were 10 putative uncharacterized *P. falciparum* proteins identified using the X!Tandem algorithm. Blastp (basic local alignment search tool for proteins only genome) search together with a Pfam (protein family) and/or Interpro (inter-protein domain) search found on

the UNIPROTKB site was used to assign some functions to these 10 putative proteins. None of these proteins seem to have known functions related to nucleation and/or initiation of the biomineralization process of Hz formation as summarized in Table 3.3.

On the contrary, two of the putative uncharacterized proteins, Q8IEJ0_PLAF7 and Q8ILM8_PLAF7 appear to be involved in lipid transport or binding. Furthermore, a putative phospholipid scramblase 1(Q8IJH8_PLAF7) presumably involved in the redistribution of phospholipid after cell activation or injury and also in the translocation of lipids from one monolayer to the other in a lipid bilayer cell membrane, and a putative long chain polyunsaturated fatty acid elongation enzyme (C6KSQ7_PLAF7) involved in the elongation of long chain polyunsaturated fatty acid, were also identified using the X!Tandem algorithm. Putative phospholipid scramblase 1 may be located in the DV membrane while putative long chain polyunsaturated fatty acid elongation enzyme presumed to be located on the surface of ER and in other organisms such as yeast is known to affect plasma membrane H^+-ATPase activity and might have been trafficked via the formation of Golgi-like transport vesicle to the DV membrane for lipid biosynthesis.

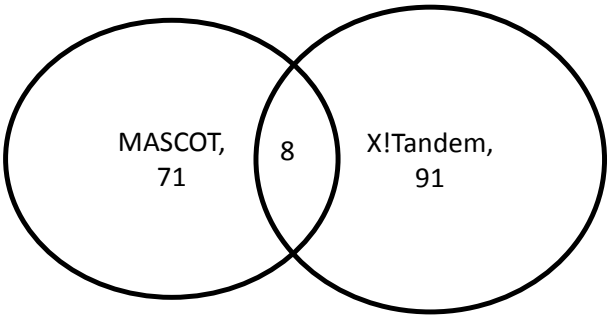

Figure 3.5. Using MASCOT and X!Tandem algorithm to interrogate *P. falciparum* genome respectively identified 71 and 91 unique proteins with 8 proteins common to both analysis.

Table 3.3. Assigned function of putative *P. falciparum* proteins identified using the X!Tandem algorithm based on either a Blastp search for proteins with known function having similar sequence or Pfam or interpro.

	Blastp identification	Pfam and/or interpro	Assigned function
Q8IEJ0_PLAF7	F0V7J3_NEOCL Lipocalin-like protein, related (*Neospora caninum*), e-value 7.0×10^{-4}	http://pfam.sanger.ac.uk/family/PF08212	Transport of small hydrophobic molecules such as steroids and lipids
Q8ILE3_PLAF7		http://pfam.sanger.ac.uk/family/PF01459	Family of porin ion channel located on mitochondria outer membrane
Q8ILM8_PLAF7		http://pfam.sanger.ac.uk/family/PF13639	Zinc finger protein motif that binds, RNA, DNA, proteins and/or lipids
Q8ILY8_PLAF7	Q8IFP4_PLAF7 putative Erythrocyte membrane-associated antigen, e-value 3.0×10^{-4}		
Q8IJR6_PLAF7			WD40-repeat proteins, helps in assembly of multi-protein complexes
Q8IM26_PLAF7	No closely related proteins		
Q8IE80_PLAF7	No closely related proteins		
Q8I490_PLAF7	B3L0F6_PLAKH. Liver stage antigen 3, putative, e-value 2.7×10^{-1}		
Q8IAU7_PLAF7	Q8WSK5_PLAFA CCAAT-box DNA binding protein subunit B, e-value 7.0×10^{-27}	http://pfam.sanger.ac.uk/family/PF00808	Involved in protein-protein interactions
Q8I2Q0_PLAF7	Q8IES7_PLAF7 Peptidase, putative, e-value 4.3	http://www.ebi.ac.uk/interpro/entry/IPR011009	

MASCOT and X!Tandem has been shown to have the highest specificity and therefore ability to calculate low-ranking scores for random matches in MS/MS identification of protein compared to other algorithms such as SEQUEST and Spectrum Mill and using trypsin digest in the search parameter, it was also shown that MASCOT perform better than X!Tandem (Kapp et al. 2005). For this reason proteins identified by MASCOT analysis from both *P. falciparum* and *H. sapiens* are discussed in detail and also because protein identification by MASCOT analysis of peptide fragments generated by LC-MS/MS is the most widely used in proteomic studies.

3.3.5 Proteins identified in sample Hs

A total of 105 proteins originating from both *Plasmodium falciparum* and the human RBC proteome were identified with material isolated from the surface of the Hz crystals, of which 68 (65%) were from *P. falciparum*, while 37 (35%) were from the human RBC proteome as indicated in the pie chart in Figure 3.6.

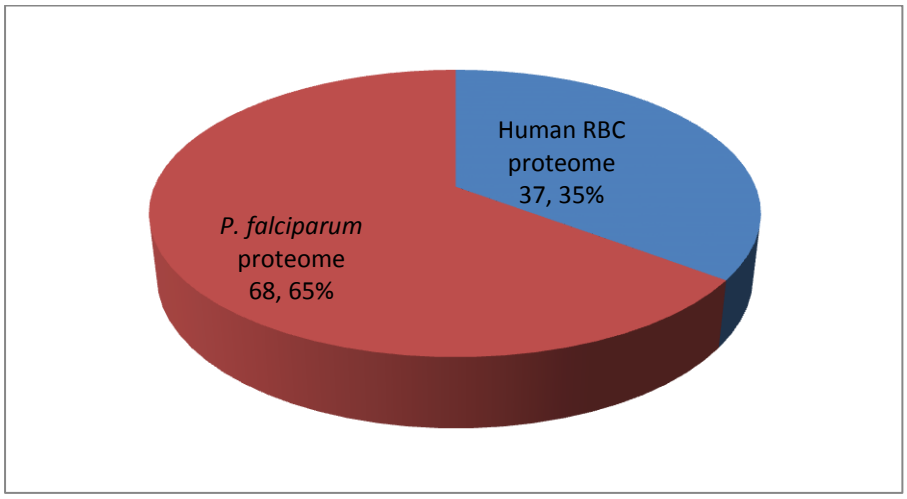

Figure 3.6. Pie chart distribution of protein found associated with the surface of Hz crystals showed 65% and 35% of the proteins originated from *P. falciparum* and human RBC proteome respectively.

Of the 68 *P. falciparum* proteins found associated with the Hz crystal surface which are listed in Table 3.4, 21 (25%) have previously been found in the DV (Lamarque et al. 2008). The remainder of the proteins are known to be located in different compartments inside the parasite and their distribution in different subcellular locations is shown in the pie chart in Figure 3.7A & B. Some of the proteins have been described in more than one subcellular compartment within the parasite. Of the 37 human RBC proteins identified (Table 3.5) from sample Hs, 14 (38%) are located on the RBC cell membrane and 24 (62%) in the cytoplasm as shown in a pie chart distribution in Figure 3.8.

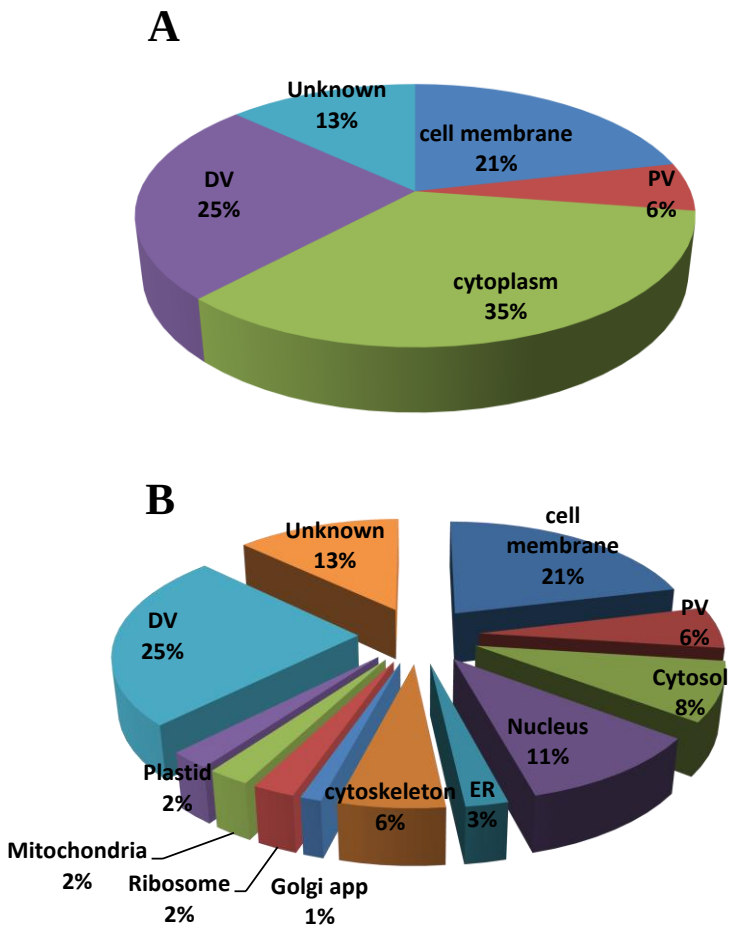

Figure 3.7. Pie chart showing the distribution of *P. falciparum* proteins identified associated with the surface of the Hz crystal, listed by cellular compartment (A) and subcellular location (B).

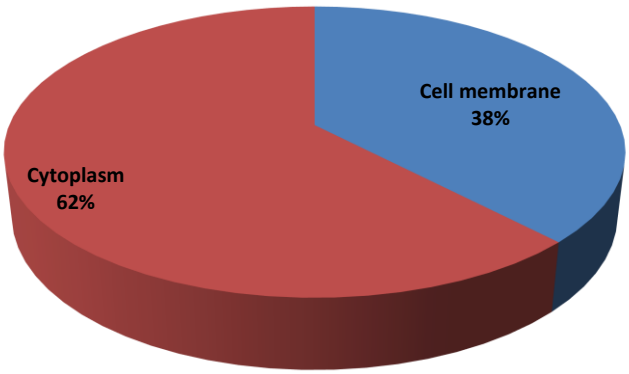

Figure 3.8. Distribution of RBC proteins found associated with the surface of Hz crystals based on location of origin.

Table 3.4. List of all *P. falciparum* proteins found associated with the surface of Hz crystals.

Protein name
(P13830) Ring-infected erythrocyte surface antigen precursor
(P13819) Merozoite surface protein 1 precursor
(P04932) Merozoite surface protein 1 precursor
(P22621) Apical membrane antigen 1 precursor
(P13568) Multidrug resistance protein
(Q8I3H7) T-cell immunomodulatory protein homolog precursor
(P50489) Apical membrane antigen 1 precursor
(P68875) Transmission-blocking target antigen S230 precursor
(Q04956) Probable cation-transporting ATPase 1
(Q08853) Calcium-transporting ATPase (EC 3.6.3.8)
Q9UAR6) Myosin A (PfM-A)
(P22620) 101 kDa malaria antigen (P101)
(P19214) Erythrocyte-binding antigen EBA-175
(P13814) Circumsporozoite protein precursor (CS)
(P02895) Glycophorin-binding protein (GBP-130)
(P05691) Circumsporozoite protein (CS) (Fragment)
(P62343) Calcium-dependent protein kinase 1 (EC 2.7.1.37)
(Q02595) Probable serine/threonine-protein kinase 2 (EC 2.7.1.37)
(P16405) Octapeptide-repeat antigen (ORA) (Fragment)
(P22620) 101 kDa malaria antigen (P101)
(P09593) S-antigen protein precursor
(P04928) S-antigen protein precursor
(Q03400) S-antigen protein precursor
(Q8I4V5) Probable U3 small nucleolar RNA-associated protein 11
(P40282) Histone H2A
(P30315) DNA polymerase delta catalytic subunit (EC 2.7.7.7)
(P27625) DNA-directed RNA polymerase III largest subunit
(P41001) DNA topoisomerase II (EC 5.99.1.3)
(P38545) GTP-binding nuclear protein Ran
(P14248) DNA-directed RNA polymerase II largest subunit
(P13825) Aspartic acid-rich protein precursor
(Q25998) DNA primase small subunit (EC 2.7.7.)
(O96935) M1-family aminopeptidase (EC 3.4.11.)
(P61076) Thioredoxinreductase (EC 1.8.1.9) (TrxR)
(Q00080) Elongation factor 1-alpha (EF-1-alpha)
(Q07805) Ornithine aminotransferase (EC 2.6.1.13)
(P20147) Heat shock 90 kDa protein homolog (Fragment)
(Q07785) Cell division control protein 2 homolog (EC 2.7.1.37)
(Q27727) Enolase (EC 4.2.1.11)
(Q05866) 78 kDa glucose-regulated protein homolog precursor
(P33948) ER lumen protein retaining receptor
(P14643) Tubulin beta chain (Beta tubulin)
(P34787) Tubulin gamma chain
(P10988) Actin I
(P14883) Actin II
(P46468) Putative cell division cycle ATPase

(Q94650) ADP-ribosylation factor
(O97231) 60S ribosomal protein L44
(Q94660) 60S acidic ribosomal protein P0
(P34940) Chaperonin CPN60, mitochondrial precursor
(Q08210) Dihydroorotate dehydrogenase homolog
(O15865) Calcium-dependent protein kinase 2 (EC 2.7.1.37)
(P21422) DNA-directed RNA polymerase beta' chain (EC 2.7.7.6)
(P12078) Heat shock 70 kDa protein PPF203 (Fragment)
(P24044) Calmodulin (CaM)
(P39898) Plasmepsin 1 precursor
(Q27743) L-lactate dehydrogenase
(P69193) Serine-repeat antigen protein precursor
(P11144) Heat shock 70 kDa protein (HSP70)
(P38545) GTP-binding nuclear protein Ran
(Q8IBS5) Calcium-dependent protein kinase 4
(Q9NJU9) Calcium-dependent protein kinase 3 (EC 2.7.1.37)
(P13922) Bifunctional dihydrofolate
(P13824) Clustered-asparagine-rich protein
(P25407) Hypothetical protein in calmodulin 5' region (Fragment)
(P50647) Ribonucleoside-diphosphatereductase large chain
(P25805) Trophozoite cysteine proteinase precursor (EC 3.4.22.)
(Q02155) Hexokinase (EC 2.7.1.1)

Table 3.5. List of Human RBC proteins identified associated with the surface of Hz crystals.

Protein name
(P11166) Solute carrier family 2, facilitated glucose transporter, member 1
(P02730) Band 3 anion transport protein (Anion exchange protein 1
(Q99569) Plakophilin 4
(P27105) Erythrocyte band 7 integral membrane protein (Stomatin)
(O75131) Copine III
(Q13683) Integrin alpha-7 precursor
(Q02094) Rhesus blood group-associated glycoprotein
(O94973) Adapter-related protein complex 2 alpha 2 subunit
(Q8WUD1) Ras-related protein Rab-2B
(P59190) Ras-related protein Rab-15
(Q15907) Ras-related protein Rab-11B (GTP-binding protein YPT3)
(P02768) Serum albumin precursor
(P08311) Cathepsin G precursor (EC 3.4.21.20
(P51956) Serine/threonine-protein kinase Nek3 (EC 2.7.1.37)
(P68871) Haemoglobin beta chain
(P69905) Haemoglobin alpha chain
(Q9H293) Interleukin-17E precursor (IL-17E)
(P14778) Interleukin-1 receptor, type I precursor
(P42330) Aldo-ketoreductase family 1 member C3
(P27105) Erythrocyte band 7 integral membrane protein (Stomatin)
(P04406) Glyceraldehyde-3-phosphate dehydrogenase, liver (EC 1.2.1.12)
(P08107) Heat shock 70 kDa protein 1 (HSP70.1)
(P62988) Ubiquitin **(**P0CG47,P0CG48,P62979,P62987)
(P02261) Histone H2A.c/d/i/n/p (H2A.1) (H2A/c) (H2A/d) (H2A/i) (H2A/n) (H2A/p) (H2A.1b) H2AC_HUMAN; Demerged into P0C0S8 (H2A1_HUMAN)
(P62805) Histone H4
(Q01543) Friend leukemia integration 1 transcription factor
(P62826) GTP-binding nuclear protein Ran (GTPase Ran) (Ras-like protein TC4)
(O14830) Serine/threonine protein phosphatase with EF-hands-2 (EC 3.1.3.16)
(Q9Y6X8) Zinc fingers and homeoboxes protein 2
(Q99569) Plakophilin 4
(Q8WUD1) Ras-related protein Rab-2B
(Q9H082) Ras-related protein Rab-33B
(Q9NRW1) Ras-related protein Rab-6B
(P61106) Ras-related protein Rab-14
(Q9NP58) ATP-binding cassette, sub-family B, member 6, mitochondrial precursor
(P11171) Protein 4.1 (Band 4.1) (P4.1) (EPB4.1)

3.3.6 Proteins identified from sample Hd

A total of 41 proteins originating from both *P. falciparum* and the RBC proteome were identified from dissolved Hz crystals, of which 24 (59%) were *P. falciparum* proteins and 17 (41%) were human RBC proteins as illustrated in a pie chart distribution diagram in Figure

3.9A. Of the 24 parasite proteins coming from the Hz crystal matrix listed in Table 3.6, only 3 of the proteins (shaded in violet in Table 3.6) were not identified on the Hz crystal surface. Different subcellular location and functions have previously been asigned to these 3 proteins. The protein P50250 (adenosylhomocysteinase), involved in methionine and polyamine metabolism, is also known to be located in the cytoplasm and DV; P16893 (thrombospondin related anonymous protein) is known to be located in the parasite membrane, while P25408 (hypothetical protein in calmodulin 3' region, fragment) has an unknown location. None of the 24 parasite proteins is known or suspected to be involved in the biomineralization process of Hz crystal formation in the DV. The distribution of parasite proteins by subcellular location showed 10 (31%) of the 24 proteins, were already known to be present in the DV (Figure 3.9B). Interestingly, the same number of proteins (10, 31%) were also known to come from the cytoplasm. The presence of these cytoplasmic proteins in sample Hd could only be considered as contaminants if they bound so strongly to the Hz surface that they could not be dislodged even after washing thoroughly with 4% SDS and rinsed with PBS. This seems very unlikely as only very few of these proteins would have been expected to still be present on Hz surface. Moreover, the proportion of cytoplasmic and DV proteins found on the Hz crystal surface (Figure 3.7A) to that in the matrix (Figure 3.9B) are almost similar. This, together with the equal number of DV and cytoplasmic proteins present in the Hz crystal matrix, strongly suggests that these cytoplasmic proteins trapped in the crystal matrix are actually present in the DV and as a result some were incorporated into the crystal matrix during Hz formation. In addition, the similarity in the proportions of cytoplasmic and DV proteins present in the Hz surface to that in the matrix also showed that the use of 4% SDS efficiently washed off proteins on the surface of the Hz crystal. Some of these proteins have also been identified in more than one subcellular location in the parasite as shown in Appendix 4 (which also includes the number of unique peptide fragements from each protein identified). All 17 human RBC proteins identified in sample Hd listed in Table 3.7 were also identified in sample Hs. None of these proteins has a known function related to Hz formation. It is worth mentioning that none of the expected proteins belonging to the protein complex proposed to convert haemoglobin to haemozoin (Chugh et al. 2012) (falcipain 2/2′, plasmepsin II, plasmepsin IV, histo aspartic protease (HAP), and haem detoxification Protein) were identified in the Hz crystal matrix with MASCOT analysis.

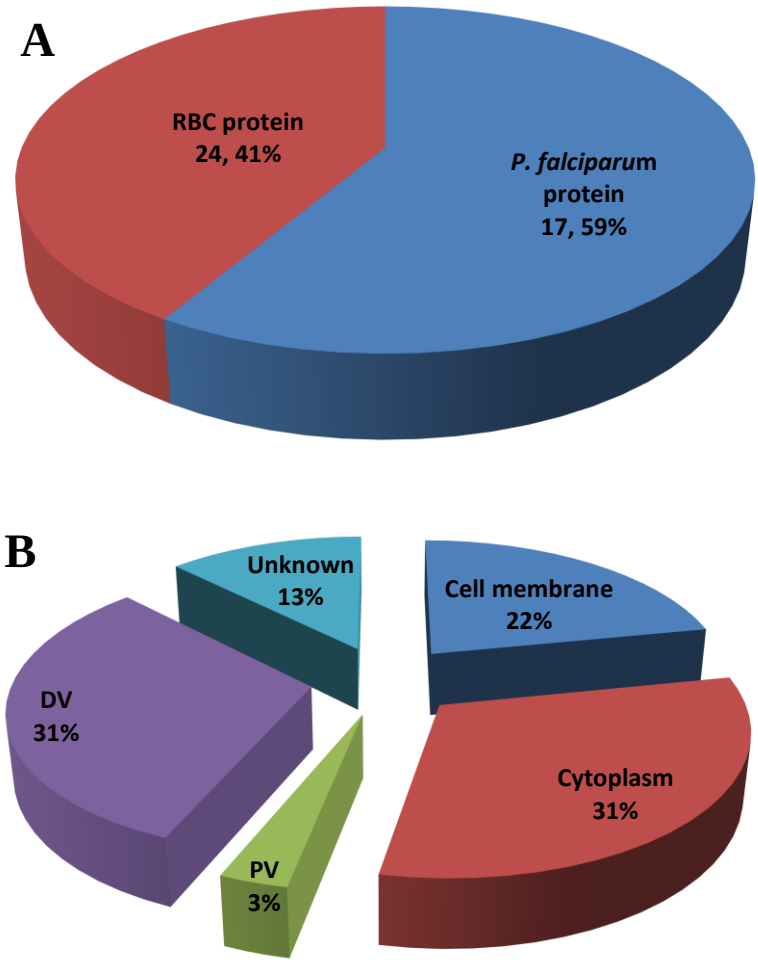

Figure 3.9. Distribution of the origin of proteins constituting the Hz matrix proteome showed the majority to be *P. falciparum* proteins (A) and further analysis of the *P. falciparum* proteins by subcellular location showed that the majority come from the DV and cytoplasm (B).

Table 3.6. List of all *P. falciparum* proteins found in sample Hd.

(P25408) Hypothetical protein in calmodulin 3'region (fragment)
(P16893) Thrombospondin related anonymous protein
(P50250) Adenosylhomocysteinase (EC 3.3.1.1)
(Q8I3H7) T-cell immunomodulatory protein homolog precursor
(Q00080) Elongation factor 1-alpha (EF-1-alpha)
(P11144) Heat shock 70 kDa protein (HSP70)
(P39898) Plasmepsin 1 precursor (EC 3.4.23.38)
(P04932) Merozoite surface protein 1 (P195)
(P38545) GTP-binding nuclear protein Ran (GTPase Ran)
(Q07805) Ornithine aminotransferase (EC 2.6.1.13)
(P10988) Actin I
(P14643) Tubulin beta chain (Beta tubulin)
(Q04956) Probable cation-transporting ATPase 1 (EC 3.6.3.-)
(P40282) Histone H2A
(P50647) Ribonucleoside-diphosphatereductase large chain (EC 1.17.4.1)
(P13830) Ring-infected erythrocyte surface antigen
(P14883) Actin II
(P13922) Bifunctionaldihydrofolatereductase-thymidylate synthase
(P34787) Tubulin gamma chain (Gamma tubulin)
(P25805) Trophozoite cysteine proteinase precursor (EC 3.4.22.-)
(Q8I3H7) T-cell immunomodulatory protein homolog precursor
(Q9UAR6) Myosin A (PfM-A)
(P16405) Octapeptide-repeat antigen (ORA) (Fragment)
(Q08210) Dihydroorotate dehydrogenase homolog, mitochondrial precursor

Table 3.7. List of all human RBC proteins found in sample Hd.

(P13727) Eosinophil granule major basic protein precursor
(P61106) Ras-related protein Rab-14
(P68871) Haemoglobin beta chain
(P27105) Erythrocyte band 7 integral membrane protein (Stomatin)
(P62805) Histone H4
(P02768) Serum albumin precursor
(P11166) Solute carrier family 2, facilitated glucose transporter,
(P69905) Haemoglobin alpha chain
(P02730) Band 3 anion transport protein
(Q9Y6X8) Zinc fingers and homeoboxes protein 2
(P62988) Ubiquitin (P0CG47 (UBB_HUMAN), P0CG48(UBC_HUMAN), P62979 (RS27A_HUMAN)**,** P62987 (RL40_HUMAN)
(P08107) Heat shock 70 kDa protein 1 (HSP70.1) (HSP70-1/HSP70-2)
(P59190) Ras-related protein Rab-15
(Q9H082) Ras-related protein Rab-33B
(Q9NRW1) Ras-related protein Rab-6B
(P08311) Cathepsin G precursor (EC 3.4.21.20) (CG) CATG_HUMAN
(P02261) Histone H2A.c/d/i/n/p (H2A.1)(H2A/c)(H2A/d)(H2A/i)(H2A/n)(H2A/p) (H2A.1b)

3.3.7 Proteins previously implicated in Hz crystal formation in the DV

In view of recent reports, surprisingly, using MASCOT analysis with peptide identification set at 95% confidence level, none of the proteins belonging to the proposed protein complex (falcipain 2/2′, plasmepsin II, plasmepsin IV, HAP, or haem detoxification protein) suggested as being required for haemoglobin degradation and Hz formation was identified (Chugh et al. 2012). On the other hand, plasmepsin I (PMI), which begins the digestion of haemoglobin and is thought to be the most abundant and important aspartic protease, was found both on the Hz crystal surface and in the matrix. This protein has also been found to be abundant in the DV (Lamarque et al. 2008) and has been shown with immunoelectron microscopy study of trophozoites using anti-PM I antibodies to colocalize with haemozoin in the DV (Banerjee et al. 2002). Another protein known to convert haem to β-haematin, HRPII, previously thought to be responsible for Hz formation (Sullivan et al. 1996), was not detected either on the Hz crystal surface or in the matrix proteome. HRPII is known to be located mainly in the erythrocyte periphery, although it has been suggested that about 3% of can be trafficked into the DV (Lamarque et al. 2008). This also implies that it is possible for other erythrocyte proteins to be trafficked into the parasite DV as illustrated in Figure 3.2. Indeed, many such proteins were readily identified.

For curiosity purposes, MASCOT analysis was also set at a peptide confidence interval of 80% to determine if any of the proteins belonging to the proposed haemozoin-forming complex could be identified, but again none were found (data not shown). A second analysis with the X!Tandem algorithm could only identify one protein, HAP (Q8IM15_PLAF7), belonging to the proposed protein complex. Haem detoxification protein (HDP) (PlasmoDB # PF14_0446) is the most important protein in this complex for haemozoin formation and has been reported to be approximately 1000-fold more efficient in converting haem to haemozoin *in vitro* (Jani et al . 2012). HDP is thought to have 2.7 haem binding sites and binds strongly to haem with a binding constant (K_d) of 80 nM (Jani et al. 2008), yet HDP was not present either on the Hz surface or in the matrix proteome in any of the analyses using either the X!Tandem algorithm or MASCOT set at the 95% or 80% peptide confidence level. Study by Lamarque et al. (2008) of DV proteome identified amongst other proteins HAP, plasmepsin II, plasmepsin IV, and falcipain 2 belonging to the proposed protein complex, therefore they are certainly detectable in the DV, but appear to show no affinity for Hz. HDP was not reported to be present in the DV proteome by these authors. Indeed, HDP is known to be

produced in the parasite cytoplasm and is supposed to be trafficked into the DV. The absence of it in the DV proteome and, most especially, on the Hz crystal surface or in the matrix cannot completely exclude its presence in the DV. The study of proteomes of various crystal matrices in a variety of biominerals in different organisms has invariably led to the identification of those protein(s) involved in the nucleation and/or initiation of crystal growth (Alves et al. 2011, Mann et al. 2008, Arakaki et al. 2008, Marie et al. 2011, Nemoto et al. 2012 and Mann et al. 2006). The absence of HDP in the proteome associated with either the Hz crystal surface or the matrix therefore tends to suggest that it is unlikely to be involved in the Hz formation in the DV. The high affinity binding of HDP to haem as determined by Jani et al. (2008) may mean HDP is more likely to function as either a haem transporter (haem transport protein) from the site of haemoglobin digestion where haem is released to the inner walls of the DV where crystal growth is said to take place (Kapishnikov et al. 2012) or HDP is temporarily recruited into the DV to bind free haem in stressful conditions in the parasite when more haem is released than can be efficiently sequestered into Hz due to interference, e.g. treatment with drug, or is involved in protection from haem outside the DV or has some other function.

3.3.8 Some known proteins identified associated with the Hz crystal surface and matrix

The identification of human proteins in parasite structures is in line with other studies which have found mature parasite-infected erythrocyte surface antigen to be associated with protein 4.1 (Waller et al. 2003), a human RBC protein also identified on the surface of Hz crystals in this study as well as parasite surface proteins such as P04932 (merozoite surface protein 1 (P190)), P50489 (apical membrane antigen 1 precursor) and P13819 (merozoite surface protein 1 precursor). The merozoite surface proteins and other surface proteins expressed in mature schizonts or in merozoites and found to be present in this study could arise from enrichment of mature trophozoite stage iRBCs of which some might have already advanced into schizonts expressing these proteins. Proteins such as Q00080 (elongation factor 1-alpha protein) and others involved in cell protein translational machinery are known to always be present in 1D gels as classical contaminants due to their high abundance in the parasite (Le Roch et al. 2003). ADP-ribosylation factor (Q94650) identified associated with the surface of the Hz crystal is a key protein required for protein trafficking in the parasite as it assembles proteins that coat transport vesicles. This protein has also been previously indentified in the DV (Lamarque et al. 2008). This study showed that an active trafficking route exists for proteins produced in some cytoplasmic organelles to be trafficked or diverted into the DV to

carry out certain functions. DV membrane proteins such as P13568 (multidrug resistance protein) identified on the Hz crystal surface could come from the lysed DV membrane. This was expected since nothing was done to remove such components from sample Hs since a conservative washing protocol was deliberately employed. Enzymes involved in basic metabolism such as (Q02155) hexokinase and (Q27727) enolase identified on the surface of the Hz crystal are highly abundant in cells and therefore may be cytosolic contaminants. Glycophorin-binding protein (P02895), elongation factor 1 alpha (Q00080) and the heat shock 70 kDa protein (P11144) identified on the Hz surface have also been found to be differentially up- and down-regulated by greater than five-fold between RBC and iRBC membranes (Fontaine et al. 2012), which again highlights the fact that protein produced in the parasite cytoplasm or cytoplasmic vesicles can either be trafficked or diverted into the host cell cytoplasm or membrane and/or into the DV. Thioredoxinreductase (P61076), also found to belong to the DV proteome, is known to play a role in various cellular functions such as in antioxidant defence, redox-sensitive signal transduction, transcriptional activation of stress-response genes etc (Nickel et al. 2006).

Actin I (P10988), actin II (P14883), tubulin beta-chain (P14643) and tubulin gamma chain (P34787) are some of the cytoskeletal proteins found in Hz crystal matrix proteome. Another organism known to form biocrystals (magnetite) through a biomineralization process is the magnetotactic bacteria. The magnetite surrounded by lipid bilayer membrane has a dedicated cytoskeleton which organizes it into chains (Komeili et al. 2007). Lipid-mediated formation of Coccolith biocrystals in *Emiliania huxleyi* algae also has cellular cytoskeletal elements which control the crystal shape. However, the cytoskeletal proteins identified in dissolved Hz crystal may just be involved in the DV cytoskeleton as they have not been shown to play a similar role in Hz crystal growth shape.

Heat shock 70 KDa protein (HSP 70) (P11144) and heat shock 70 KDa protein1 (P08107) from the parasite and RBC proteome respectively are some of the chaperones found present in the Hz crystal matrix. The heat shock 70 KDa protein and heat shock 90 KDa protein (HSP90) are among the most widely-studied molecular chaperones whose function is to facilitate the folding of other proteins both under normal and stressful conditions and in the case of malaria parasite they are known to play an important role in parasite development (Shonhai et al. 2005 and 2007). The malaria parasite experiences a heat shock during transmission from about 25^{o}C in the insect vector to about 37°C in humans (Bayoh et al.

2003) although it is not known if the parasite heat shock proteins play an important role in its adaption to such drastic change in temperature. HSP70 and HSP90 are known to be associated with Fe(III)PPIX (Famin and Ginsburg, 2003) and have therefore been earmarked as potential targets for antimalarial drug development (Pesce et al. 2010 and Shonhai, 2010). For example, some pyrimidinone compounds are known to exhibit their antimalarial activity by binding to the EEVD motif of Hsp70 while geldanamycin (benzoquinone ansamycin class of drugs) is said to exhibit its antimalarial activity by inhibiting HSP90 chaperone activity (Stebbins et al. 1997) which results in the inhibition of parasite growth although its exact mechanism of action is not known. This therefore highlights the importance of HSP70 and HSP90 in parasite development and survival. In effect, the presence of some of these proteins (both from parasite and RBC) in the matrix therefore makes it seem likely that these proteins were incorporated into the intracrystalline matrix because they are present in the crystallization compartment at the time when the Hz crystal growth started in the DV.

Since only about 60% of the *P. falciparum* genome has been annotated, it might have been expected that uncharacterized proteins belonging to the parasite genome which play a role in the nucleation of Hz crystal growth would also be identified in the Hz crystal matrix. But none of these putative uncharacterized proteins belonging to the parasite genome was identified using MASCOT analysis set at 95% peptide confidence level. Alternatively, one or more proteins constituting the proteome of the Hz crystal matrix could play an alternative or secondary role in Hz crystal growth besides their known function in the parasite. However, this seems somewhat unlikely as haem sequestration into Hz is a major process and would be expected to required proteins or other bioorganic molecules dedicated for that process. Based on the proteins identified, constituting the proteomes associated with both the Hz crystal surface and matrix, it would seem likely that bioorganic molecules other than proteins may be actively responsible for Hz crystal growth in the DV.

3.3.9 Protein versus lipid in mediated Hz formation

Since HDP was not detected either associated with the Hz crystal surface or in the matrix using an LC-MS instrument sensitive enough to detect 5-10 protein molecules per Hz crystal using the quantities of material utilized in this study, this suggests that if HDP is present in association with Hz, it is present in extraordinarily low abundance.

On the other hand, Pisciotta et al. (2007) showed neutral lipids to be present at a ratio of 15 per 100 haem molecules. This corresponds to a NLB amount of 1.8 nmol in a sample corresponding to a lane in the present study. Thus, at the reported protein detection limit of 5-10 fmol there would be 180 000-360 000 times more lipid than HDP. Thus, notwithstanding the reported 1000-fold greater efficiency of conversion of haem to Hz by HDP, at the amounts present in association with Hz lipids are still likely to bring about the conversion 200 times faster and play the dominant role in Hz formation.

This calculation, coupled with the absence of proteins belonging to the protein complex proposed to be involved in Hz formation from the proteome associated with the Hz surface or matrix, raises the question of any involvement of these proteins in the biomineralization process of Hz formation. If any proteins are involved, those found in the Hz matrix proteome are more likely candidates and could be investigated further to see whether, besides their known function, they do play an alternative role in the biomineralization process of Hz formation. The absence of any evidence of HDP or members of its putative protein complex in Hz matrix together with the identification of known lipoproteins responsible for lipid transport/biosynthesis and other uncharacterized proteins with assigned function mainly to transport hydrophobic molecules such as lipids across the membrane seems to further strengthen the proposed involvement of lipids in the biomineralization process of Hz formation in the DV.

3.3.10 Lipid TLC of Hz crystal

Separation of chloroform/methanol (2:1) washed extracts from Hz crystals isolated from malaria parasites on a TLC plate in two different solvent systems gave several spots upon UV visualization of the premuline stained TLC plate. The R_f of TLC separations of known individual lipids constituting the NLB identified by Pisciotta et al. (2007) in the same solvent system was used as a control to identify the different lipid spots coming from the Hz crystal surface as shown in Figure 3.10.

Based on the R_f of the reference lipids, all the NLB lipid constituents were found associated with the Hz sample, confirming that this lipid blend is indeed associated with the surface. The lipid spot at the top of the TLC plate (which could ether be triacylglycerol or non-esterified fatty acid) and another spot below that of MSG and MPG (which could also be either

phosphatidylcholine or phosphatidylethanolamine) was also previously shown to be present on the Hz crystal surface by Pisciotta et al. (2007).

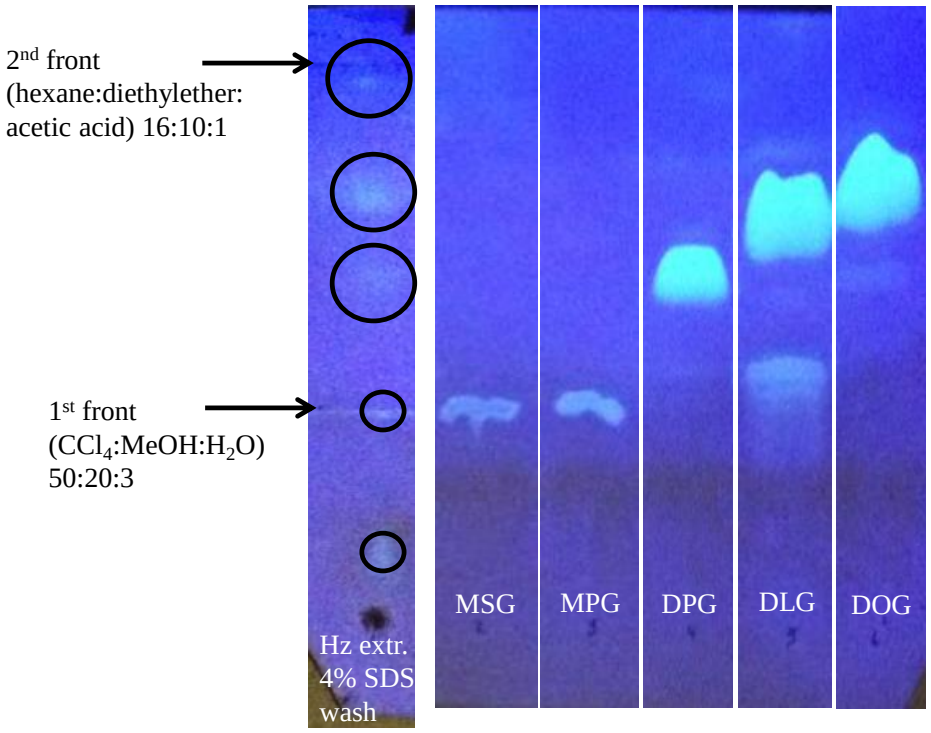

Figure 3.10. Lipid TLC of chloroform/methanol washed Hz crystals showed the presence of MSG, MPG, DPG, DLG and DOG on its surface.

3.4 CONCLUDING REMARKS

The availability of the complete genomic sequence of both *P. falciparum* and its host RBC presented a good starting point to use proteomic tools to study the proteome of the Hz surface and matrix in order to identify protein(s) that may be responsible for Hz formation and which could potentially serve as new antimalarial targets. This study led to the identification of more than a hundred proteins of both parasite and RBC origin. Some of the proteins identified were already described in locations other than the DV and some may be contaminants arising from the Hz isolation process. Proteins found in DV not identified in this study are most likely not bound to the surface or incorporated into the matrix of Hz crystal. Seemingly, this is the first ever comprehensive study of the proteome of the Hz surface and matrix and also showed the presence of RBC proteins on the surface and in the matrix of Hz. This study also produced the first comprehensive list of the proteome associated with the Hz crystal in the DV. Finally, the idea of Hz crystal growth in the DV being nucleated and/or initiated by any of the proteins previously implicated in the process

seem very unlikely as none were found to be bound to the crystal surface let alone incorporated into Hz crystal matrix. So far, proteomic studies of the Hz crystal did not identify any "stand-out" protein and/or previously described proteins that could be implicated solely in mediating this process of Hz formation in the malaria parasite. On the contrary, in this study, lipids stood out as the most likely bioorganic molecules actively involved in mediating the process based on their vastly greater abundance over proteins implicated in mediating this process. In addition, for the first time, putative lipoproteins and uncharacterised proteins with roles in lipid binding and transport were identified as part of the Hz crystal associated proteome.

4. KINETIC STUDIES OF LIPID MEDIATED BETA-HAEMATIN FORMATION

4.1 INTRODUCTION

From proteomic and lipodomic studies of the Hz crystal in the previous chapter, none of the proteins previously implicated in Hz formation such as HDP and HRP II or any unknown "stand-out" proteins that could be implicated in Hz formation *in vivo* were identified. In contrast, lipid constituting MPG/MSG/DPG/DOG/DLG was confirmed to be associated with the Hz crystal surface and lipids were proposed to be the most likely biomolecules responsible for Hz formation *in vivo* based on their vastly greater abundance over putative haemozoin-forming proteins associated with the Hz crystal. Previous TEM studies of *P. falciparum* iRBC by Pisciotta et al. (2007) had shown evidence of Hz in the DV associated with MPG/MSG/DPG/DOG/DLG in the ratio 2:4:1:1:1 by mass, which will be referred to as neutral lipid blend (NLB) (Pisciotta et al. 2007).

As described in Chapter 1, the involvement of lipids in Hz formation was suggested by Bendrat et al. (1995) where they showed that acetonitrile extracts from haemozoin contains lipids which promote β-haematin formation. Fluorescence microscopic studies of Nile Red-stained iRBC has also shown neutral lipid bodies to be associated with parasite DV which was confirmed by TEM studies of iRBCs (Jackson et al. 2004). Furthermore, previous studies have clearly shown some of the individual constituent lipids of NLB as well as NLB itself to be very efficient in mediating β-haematin formation *in vitro* (Picsiotta et al. 2007, Egan et al. 2006, Hoang et al. 2010a and Hoang et al. 2010b). However, detailed kinetic information on effects of lipid concentration, lipid-to-Fe(III)PPIX ratio and biologically relevant ions on β-haematin formation in the presence of NLB and its constituent lipids is still lacking.

In this chapter, therefore, the kinetics of β-haematin formation with respect to the effects of NLB and its individual constituent lipids were further investigated. The effect of lipid and Fe(III)PPIX concentration on the kinetic of β-haematin formation and finally the influence of buffers and low molecular weight ions such as sodium, potassium, magnesium, calcium, phosphate, carbonate, ATP, reduced glutathione and 2,3-diphospho-D-glycerate (2,3-DPG) at concentrations at which they are present in RBC and/or serum on the kinetics of β-haematin formation under biomimetic conditions mimicking that in the DV was also investigated.

4.2 METHODS

4.2.1 Determination of yield of β-haematin formation with lipid

4.2.1.1 Experimental procedures

β-Haematin was prepared using a method previously described (Hoang et al. 2010a) with some slight modifications as follows: 50 mL citric acid buffer (50 mM, pH 4.8) in a Schott-Duran crystallization dish with internal diameter of 9 cm was pre-incubated for 30 min at 37°C in a water bath. 1 mL of 3.31 mM lipid solution (NLB or an individual constituent lipid) was mixed with 500 μL of 2 mg/mL Fe(III)PPIX solution (2.15 lipid/ Fe(III)PPIX mol ratio) to give a total volume of 1.5 mL. Keeping the concentration of Fe(III)PPIX constant (3.07 mM), that of the lipid (NLB or an individual constituent lipid) was varied to give lower lipid/Fe(III)PPIX (L/H) mol ratios of 1.07, 0.54, 0.27, 0.13 and 0.067, each with a total volume of 1.5 mL. The control experiment which had no lipid consisted of 500 μL of 2 mg/mL Fe(III)PPIX and 1 mL of 1:9 v/v of acetone/methanol. The above mixtures of lipid and Fe(III)PPIX at different mol ratios and that of the control were layered carefully on the surface of the pre-incubated citric acid buffer using a 1 mL syringe and this was incubated further at 37°C for 30 min for β-haematin formation. Each experiment was repeated at least three times.

4.2.1.2 Quantification of β-haematin formed

After 30 min incubation, the bulk reaction mixture in the Schott-Duran crystallization dish was completely transferred into a 50 mL transparent polycarbonate Nalgene® centrifuge tube and centrifuged at 10 000 rpm for 15 min using an Eppendorf 5810 R centrifuge. The supernatant was discarded and the pellet used to quantify the amount of β-haematin (yield) formed using a reliable method previously described by Ncokazi et al. (2004). In this method the pellet was washed with 1 mL of 5% pyridine (pyridine does not dissolve β-haematin but will dissolve all the free Fe(III)PPIX in solution by forming a low-spin coloured complex with the Fe(III) centre of Fe(III)PPIX which has an absorption maximum at 405 nm). The 1 mL of washed pellet was centrifuged at 14 000 rpm for 10 min in a small plastic 1.5 mL Eppendorf tube using an Eppendorf 5410 centrifuge. 50 μL of the coloured supernatant was

diluted with 1 mL of deionised water (1:20 dilution) and the absorbance was measured at 405 nm using a Varian Cary 100 UV-Visible spectrophotometer. The yield was then calculated using equation 2.

$$\%\ \text{Yield of } \beta\text{-haematin formed} = \left[1 - \frac{\text{Absorbance at 405 nm of test experiment}}{\text{Absorbance at 405 nm of control experiment}}\right] \times 100 \quad \text{.....(2)}$$

4.2.2 Effect of lipid identity and concentration on the kinetics of β-haematin formation

4.2.2.1 Experimental procedures

Kinetic studies were done for NLB and its indidvidual constituent lipids (MSG, MPG, DPG, DLG and DOG) at lipid/Fe(III)PPIX ratios of 2.15, 1.07 and 0.54. β-Haematin was prepared as described above in Section 4.2.2.1. In this case, incubation of the lipid and Fe(III)PPIX mixture for β-haematin formation was allowed to go on for varying lengths of time for the different L/H mol ratios. Each experiment was repeated at least three times for each time point. At the end of each incubation time, β-haematin formed was quantified as described in Section 4.2.1.2. The yield values obtained at different incubation times for a particular L/H mol ratio were used to generate a kinetic plot for that particular L/H mol ratio.

4.2.3 Effect of Fe(III)PPIX concentration on yield of β-haematin formation

4.2.3.1 Experimental procedures

Keeping the concentration of MPG constant (16.1 μM), which is the concentration of lipid at a 0.54 L/H mol ratio, the Fe(III)PPIX concentration used for β-haematin preparation as described in Section 4.2.2.1 was varied starting with a lower Fe(III)PPIX concentration of 7.44 μM (0.5 mg/mL) to a higher concentration of 4.1 mg/mL. The yield of β-haematin formed at each Fe(III)PPIX concentration was determined as described in Section 4.2.1.2.

4.2.4 Kinetic study of β-haematin formation at Fe(III)PPIX concentrations greater than 2 mg/mL

4.2.4.1 Experimental procedures

Fe(III)PPIX concentrations of 2.3 and 3.0 mg/mL corresponding to 0.47 and 0.36 L/H mol ratios respectively were used to generate kinetic data for β-haematin formation as described in Section 4.2.3.1. Yield values of β-haematin formed at different incubation time were determined as described in Section 4.2.1.2 and used to generate a kinetic plot. All kinetic experiments were repeated at least three times.

4.2.5 FT-IR characterization of product formed with Fe(III)PPIX and lipid

4.2.5.1 Experimental procedures

Products formed from β-haematin formation kinetic experiments with NLB at 2 min and with MPG at 30 min incubation times, as described in Section 4.2.3.1, were harvested by centrifugation at 10 000 rpm for 15 min using an Eppendorf 5810 R centrifuge. The supernatant was discarded and the pellets dried in a dessicator over phosporous pentoxide for 3-5 days. The dried product was ground to fine powder using a morter and pestle and then suspended in Nujol to form a nujol mull. The IR spectrum of the nujol mull was recorded using a Perkin-Elmer Spectrum 100 FT-IR spectrophotometer.

4.2.6 Characterization of product formed with Fe(III)PPIX and lipid using TEM and TEM-ED

4.2.6.1 Experimental procedures

Samples containing product formed with Fe(III)PPIX and lipid were carefully taken from the reaction mixture using a micropipette and placed on a glow-discharged carbon-coated grid.

Excess solution was blotted on Whatman filter paper number 1 and the grid was immediately stained with a negative stain (uranyl acetate) for 3-5 min. Excess stain was blotted on Whatman filter paper number 1 and the grid was allowed to dry at room temperature. The TECNAI TF20 TEM operating at 200 kV located at the Electron Microscope Unit, University of Cape Town, was used for imaging the grid and also for acquisition of the electron diffraction pattern from imaged crystals.

4.2.7 Confocal laser microscopy study of product formed with Fe(III)PPIX and lipid

4.2.7.1 Experimental procedures

From the reaction mixture of the kinetic study of β-haematin formation with MPG at 0.54 L/H mol ratio, 2 μL of the suspension was taken from the reaction mixture at 10, 20, 30 and 60 min incubation time and placed on different glass microscope slides. A thin glass cover slip was placed on top of each solution carefully to avoid air bubble formation in the liquid between the glass slide and cover slip. The glass microscope slides were carefully inverted and mounted in the LSM510-META Zeiss confocal microscope sample chamber located at the Confocal and Light Microscope Imaging facility at the University of Cape Town. The samples were viewed with water immersion. Continuous z-stacked images of autoflourescence arising from the product formed at different incubation times were acquired under the following conditions; pin hole diameter of 444 μm, excitation laser at 488 nm, 20% transmission power out, detection band pass 500-530 nm (emission) and LD C-Apochromat 40x/1.1 W objective.

4.2.8 Effect of dish diameter on the kinetics of β-haematin formation

4.2.8.1 Experimental procedures

The kinetics experiment using MPG at 0.54 L/H mol ratio was repeated as described above in Section 4.2.3.1, except that a 100 mL beaker with an internal diameter of 5 cm was used instead of the usual 9 cm Schott-Duran crystallization dish.

4.2.9 Effect of Buffers on the kinetics of β-haematin formation

4.2.9.1 Sample preparation

50 mM MES (4-morpholineethanesulfonic acid) buffer, pH 4.8:

4-Morpholineethanesulfonic acid (9.76 g) was dissolved in 1 L deionised water. The pH was adjusted to 4.8 with NaOH slurry.

50 mM Sodium acetate buffer, pH 4.8:

Sodium acetate anhydrous (4.102 g) was dissolved in 1 L deionised water. The pH was adjusted to 4.8 with perchloric acid.

4.2.9.2 Experimental procedures

Kinetic experiments for β-haematin formation with MPG at 0.54 L/H were done as previously described in Section 4.2.3.1. In this case, MES and sodium acetate buffers were used instead of the usual citric acid buffer. Quantification of β-haematin yields for kinetic plots were determined as described in Section 4.2.2.2.

4.2.10 Effect of physiologically relevant ions and other low molecular weight bio-molecules on kinetics of β-haematin formation

4.2.10.1 Sample preparation

RBC concentration of low molecular weight bio-molecules:

8.0 mM sodium ions:

NaCl (0.4675 g) was dissolved in 1 L of 50 mM citric acid buffer (pH 4.8) and minor pH adjustments to 4.8 were made with NaOH slurry.

150 mM potassium ions:

KCl (11.184 g) was dissolved in 1 L of 50 mM citric acid buffer (pH 4.8) and minor pH adjustments to 4.8 were made with NaOH slurry.

1.75 mM Magnesium ions:

$MgCl_2.6H_2O$ (0.3558 g) was dissolved in 1 L of 50 mM acetate/acetic acid buffer (pH 4.8) and minor pH adjustments to 4.8 were made with NaOH slurry.

1 mM phosphate ions:

Na_2HPO_4 (0.14196 g) was dissolved in 1 L of 50 mM citric acid buffer (pH 4.8) and minor pH adjustments to 4.8 were made with NaOH slurry.

15 mM hydrogen carbonate ions:

$NaHCO_3$ (1.26015 g) was dissolved in 1 L of 50 mM citric acid buffer (pH 4.8) and minor pH adjustments to 4.8 were made with NaOH slurry. This leads to the formation of sodium citrate and CO_2 at this pH.

1.5 mM ATP:

Adenosine 5′-triphosphate disodium salt (0.82671 g) was dissolved in 1 L of 50 mM citric acid buffer (pH 4.8) and minor pH adjustments to 4.8 were made with NaOH slurry.

2.48 mM Glutathione:

L-glutathione reduced powder (0.76210 g) was dissolved in 1 L of 50 mM citric acid buffer (pH 4.8) and minor pH adjustments to 4.8 were made with NaOH slurry under argon.

4.5 mM of 2,3-diphospho-D-glyceric acid pentasodium salt:

2,3-DPG salt (0.3382g) was dissolved in 200 mL 50 mM citric acid buffer (pH 4.8) and minor pH adjustments to 4.8 were made with NaOH slurry.

Ions at RBC concentration combined:

A solution of 8.0 mM Na^+, 150 mM K^+, 1.75 mM Mg^{2+}, 1 mM $H_2PO_4^-$, 15 mM HCO_3^- and 1.5 mM ATP was prepared in 1 L of 50 mM citric acid buffer (pH 4.8) and minor pH adjustments to 4.8 were made with NaOH slurry.

Plasma concentration of low molecular weight bio-molecules:

150 mM sodium ions:

NaCl (8.766 g) was dissolved in 1 L of 50 mM citric acid buffer (pH 4.8) and minor pH adjustments to 4.8 were made with NaOH slurry.

1.5 mM Magnesium ions:

$MgCl_2.6H_2O$ (0.30495 g) was dissolved in 1 L of 50 mM citric acid buffer (pH 4.8) and minor pH adjustments to 4.8 were made with NaOH slurry.

3.0 mM calcium ions:

$CaCl_2.2H_2O$ (0.44106 g) was dissolved in 1 L of 50 mM acetate/acetic acid buffer (pH 4.8) and minor pH adjustments to 4.8 were made with NaOH slurry.

Ions at serum concentration combined:

A solution of 150 mM Na^+, 1.75 mM Mg^{2+} and 3 mM Ca^{2+} was prepared in 1 L of 50 mM citric acid buffer (pH 4.8) and minor pH adjustments to 4.8 were made with NaOH slurry.

4.2.10.2 Experimental procedures

Kinetic experiments for β-haematin formation with MPG at 0.54 L/H were done as previously described in Section 4.2.3.1, but in the presence of all the above bio-molecules dissolved in citric acid buffer individually and in combination at their respective concentrations at which they are present in RBC or plasma. Determination of β-haematin yields for preparing the kinetic plots was done as described in Section 4.2.1.2.

4.3 RESULTS AND DISCUSSION

4.3.1 Infrared characterisation of crystalline product mediated by NLB and MPG

FT-IR was used to characterise the crystalline products formed with NLB and MPG after 2 and 30 min incubation respectively. This was done because quantification of β-haematin formed was done indirectly by measuring the amount of unreacted Fe(III)PPIX and this alone does not prove that the remaining product formed is β-haematin. Therefore the products formed with these lipids were dried over P_2O_5 in a desiccator and FT-IR spectra of the dried products prepared as Nujol mulls were obtained using a Perkin-Elmer Spectrum 100 FT-IR spectrophotometer. The spectrum showed characteristic peaks at 1661 and 1210 cm^{-1} arising from C=O and C−O stretching vibrations of β-haematin. This β-haematin spectrum is identical to those of Slater et al. (1991) obtained from β-haematin and Hz crystals. Peaks at 1550 and 1320 cm^{-1} are from nujol (Figure 4.1).

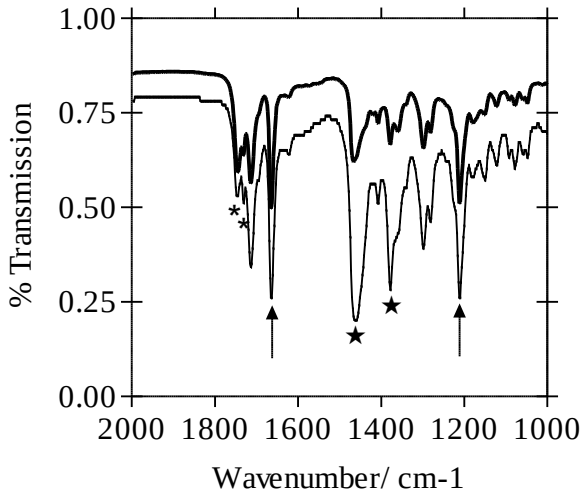

Figure 4.1: FT-IR spectra of dried product formed with NLB or MPG and Fe(III)PPIX. Products formed with NLB and Fe(III)PPIX (thick line) or MPG and and Fe(III)PPIX (thin line) showed characteristic β-haematin peaks at 1662 cm^{-1} and 1210 cm^{-1} (arrows). Thus confirming β-haematin is formed with both lipids. Peaks marked as (★) and (*) arising from nujol and lipid respectively. Reaction conditions: 2.15 L/H ratio (64.3 μM total lipid), citric buffer (50 mM, pH 4.8), 37°C, 2 min and 30 min incubation for NLB and MPG respectively.

4.3.2 TEM and electron diffraction characterisation of β-haematin

Besides FT-IR characterization of products formed with lipids, β-haematin is well known to be crystalline in nature and based on this criterion further characterization of the product was done using TEM. TEM imaging of the wet product formed with MPG within 30 min of incubation showed β-haematin formed during this reaction process to be crystalline in nature with a corresponding diffraction pattern exhibiting strong diffraction spots which unequivocally confirmed β-haematin crystals formed during this process (Figure 4.2). The indexed TEM-ED shows that the crystal lies at an arbitrary orientation of {972} exposing randomly selected diffraction planes to the electron beam as seen from diffraction spots arising from higher order Miller indices, with none of the principal crystallographic axes seen even with a double tilt goniometer stage. The β-haematin crystals are smaller than natural Hz in size and also exhibit a distinct external morphology. These differences in size and external morphology of β-haematin may account for the difference in the crystal {hkl} plane seen with TEM-ED to that of Hz (Solomonov et al. 2007) although this needs to be investigated further.

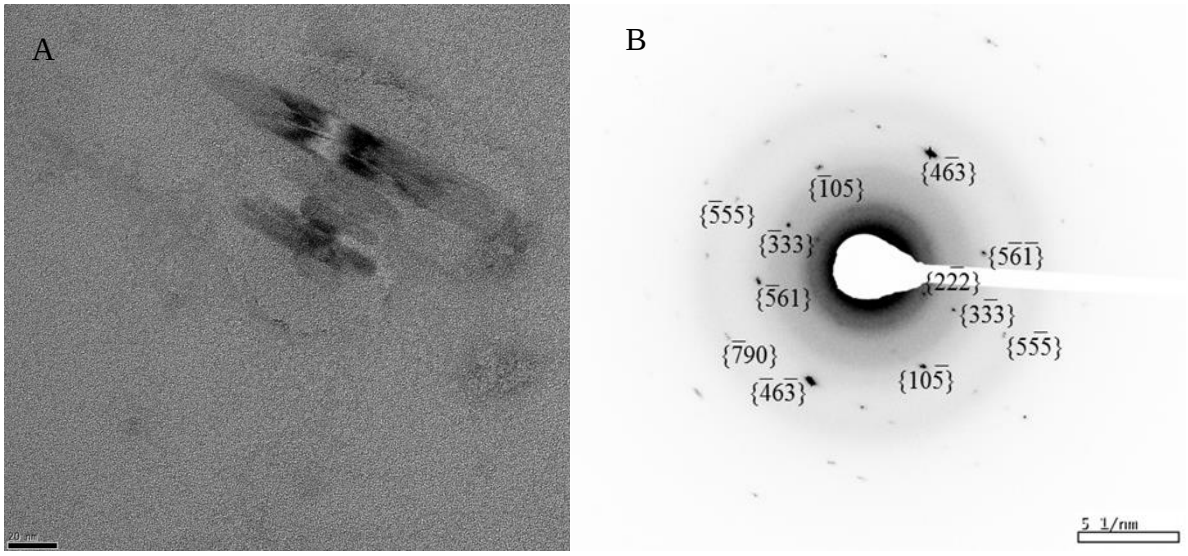

Figure 4.2: (A) TEM imaging of product formed with lipid and Fe(III)PPIX at the end of a typical kinetic reaction run showed they are crystalline in nature and (B) the electron diffraction pattern obtained from these structures gave bright spots of higher Miller indices from randomly selected diffraction planes which unequivocally demonstrated that β-haematin is formed during the reaction. Scale bar in A = 20 nm.

4.3.3 Yields of β-haematin formation as a function of lipid concentration

Starting with 64.27 μM NLB (2.15 L/H mole ratio) an initial high yield of about 90% β-haematin was obtained. When Fe(III)PPIX concentration was kept constant and the concentration of NLB was decreased, the yield remained relatively constant over a range of concentrations. This yield started to decrease below a mol ratio of 0.54 L/H and levelled out with a low yield at lower concentrations (Figure 4.3). Looking at the yield pattern of β-haematin formed with the different lipid constituents of the NLB, a similar pattern was obtained with monopalmitic glycerol (MPG) as shown in Figure 4.4A. Monostearic glycerol (MSG) and dipalmitic glycerol (DPG) with observed precipitation in the assay gave relatively lower yields of about 40% at the highest concentration of the lipid (64.27 μM) used in this study (Figure 4.4B & C) which was similar to yields obtained with NLB at lower lipid cencentrations. The lower yields at higher lipid concentration might be due lower solubilty of these two lipids since precipitated lipid was evident with DPG in solution. Dilinoleic glycerol (DLG) and dioleic glycerol (DOG) gave higher yields of about 80-90% β-haematin similar to that of NLB and MPG at higher lipid concentrations. DLG had a yield of about 40% at 0.27 L/H mol ratio (Figure 4.4D) and DOG appears to be even more effecient as it gave a much higher yield of β-haematin of about 80% even at a much lower lipid concentration of 0.27 L/H mol ratio (Figure 4.4E) and only started to decrease below this concentration. The L/H mol ratio at which the sharp decrease in yield was observed is hereafter refered to as the cut-

off point in this study. In the case of NLB and MPG this corresponds to an approximate mol ratio of 0.54 L/H. Pisciotta et al. reported that the extracted NLB from Hz crystals exists in the proportion of 15 lipid to 100 Fe(III)PPIX molecules. β-Haematin yield formed by NLB under relevant physiological conditions in this study showed this ratio to lie below the cut-off point where poor conversion of Fe(III)PPIX to β-haematin occurred. Other studies have also suggested that precipation of Fe(III)PPIX slows its conversion to β-haematin, if it is finally converted to β-haematin at all (Egan et al. 2001 & 2006). This is because the rate of conversion of Fe(III)PPIX to β-haematin is controlled by dissolution rather than crystallization, therefore, the drop in yields at higher Fe(III)PPIX concentrations (below 0.54 L/H) coupled with the difficulty in obtaining a 100% yield with any of these lipids despite the longer incubation time at the highest concentration tested may be as a result of precipitation of fraction of the Fe(III)PPIX before it could be partitioned into lipid droplets. The precipitation of Fe(III)PPIX is likely not to occur in the parasite DV as Fe(III)PPIX is released at the rate at which haemoglobin is digested, meaning all the Fe(III)PPIX is not introduced into the crystallization compartment where Hz formation takes place at once in contrast to what was done at the beginning of the reaction in this study.

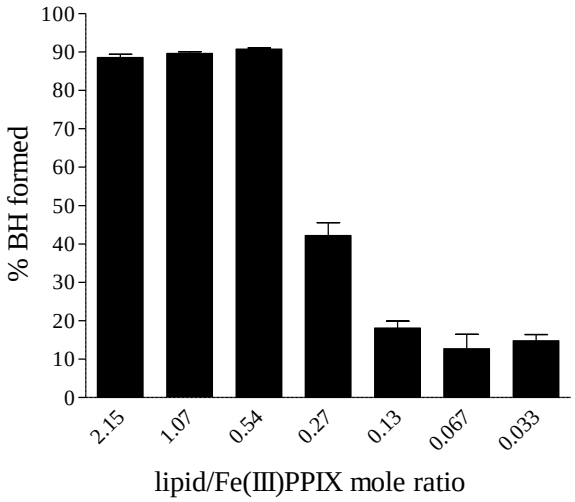

Figure 4.3: Yields of β-haematin formed with NLB. NLB gave a high yields of about 80-90% β-haematin at higher lipid/Fe(III)PPIX mol ratios staying relatively constant from 2.15 L/H (64.3 μM total lipid) to 0.54 L/H after which it suddenly drops to a value of about 10 % below 0.067 L/H. Reaction conditions: Citric buffer (50 mM, pH 4.8), 37°C, 30 min incubation. Error bars represent SEM (L/H = 2.15 and 1.07, n = 6; L/H = 0.54 and 0.27, n = 8; L/H = 0.13 and 0.067, n = 4; L/H = 0.033, n = 2).

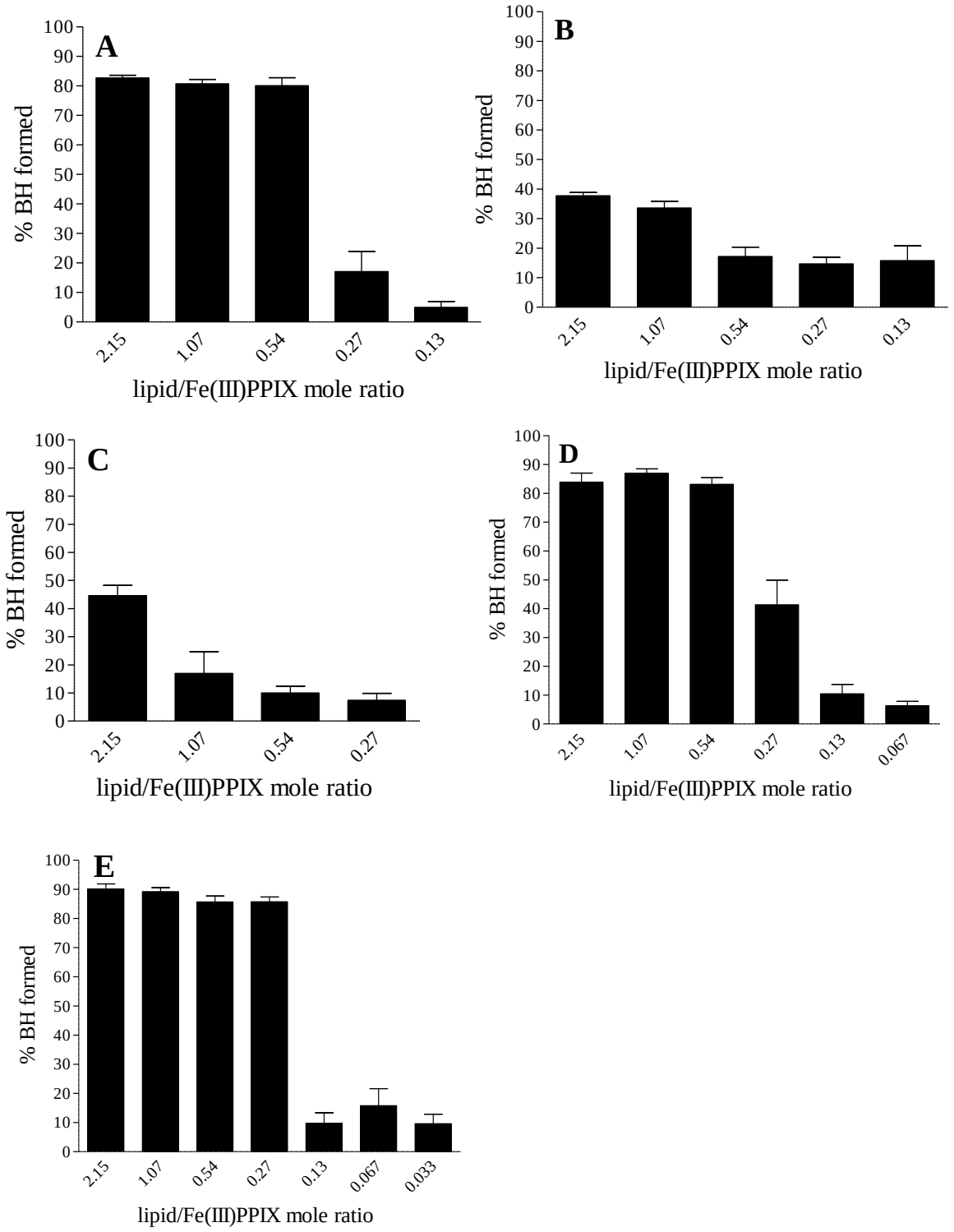

Figure 4.4: Yields of β-haematin formed with individual constituent lipids of NLB. MPG gave high yields of about 80-90% at L/H ratios from 2.15 to 0.54 which decreased to about 10-20% at 0.27 L/H (A). MSG and DPG gave lower yields of about 40% at 2.15 L/H which decreased sharply to about 10-20% at L/H ratios of 0.54 and 1.07 (B and C respectively). DLG gave high yields around 80-90% at higher mol ratios (2.15-0.54) which decreased sharply to about 30-40% at 0.27 L/H mol ratio and dropped further to about 10% and lower at 0.13 L/H (D). DOG appears to be the most efficient lipid with a high yield of almost 90% between 2.15 L/H and 0.27 L/H before decreasing sharply between 0.27 and 0.13 L/H (E). Reaction conditions: Citric buffer (50 mM, pH 4.8), 37°C, incubated for 30 min. Constant total Fe(III)PPIX concentration of 30 μM. Error bars represent SEM (A, n=3; B, n=4; C – E, n=3).

4.3.4 Yields of β-haematin formation with DPG at non-physiological temperature of 60^{o}C

As a result of the low yield of β-haematin observed in the reaction mediated by DPG at 37°C, the β-haematin yield was also determined at a much higher temperature of 60^{o}C. This was done to check if the low β-haematin yield obtained was as a result of lower temperature causing the lipid to precipitate in solution or whether this lipid is just not as efficient as the other lipids in mediating β-haematin formation. β-Haematin yield obtained at 60^{o}C with DPG increased tremendously (Figure 4.5) from about 40% at 37°C to about 90% at 60^{o}C (64.3 μM total lipid), with no observed precipitation of lipid in the reaction mixture. DPG has saturated hydrocarbon chains and had been shown to have a higher melting point (T_m) and activation energy compared to the other lipids with unsaturated hydrocarbon chains such as DLG and DOG (Hoang et al. 2010b), which may explain why it did not completely dissolved at 37°C. Meanwhile at a much higher temperature of 60^{o}C, it dissolved completely. The complete dissolution of DPG at 60^{o}C therefore increases the amount of lipid droplets in solution which helps to maintain much of the Fe(III)PPIX in the dissolved state and also to nucleate β-haematin crystal formation which translates into increased yield at this elevated temperature. The yield trend obtained at 60^{o}C with DPG was similar to that of DLG (Figure 4.4D).

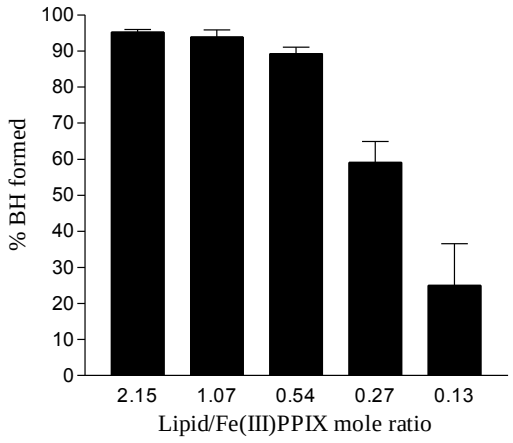

Figure 4.5: Yields of β-haematin formed with DPG at 60^{o}C. The yield of β-haematin formed increased greatly to about 90% at 2.15 L/H mol ratio (64.3 μM total lipid) and stayed relatively constant through 0.54 L/H before gradually dropping to about 60% at 0.27 L/H, down to 20% at 0.13 L/H. Reaction conditions: Citric buffer (50 mM, pH 4.8), 37°C, 30 min incubation. Error bars represent SEM (n=4).

4.3.5 Kinetics of β-haematin formation with NLB and the effects of lipid identity and concentration on the kinetics of β-hematin formation

The kinetics of β-haematin formation with NLB was very fast at mol ratios of 2.15 L/H and 1.07 L/H (64.3 and 32.2 μM total lipid respectively). These reactions were completed within 10 min with yields of above 80%. This is in accordance with previous studies (Hoang et al. 2010a & Pisciotta et al. 2007) which showed NLB to be very efficient in mediating β-haematin formation. The kinetics at 0.54 L/H mol ratio was slower but the reaction also gave a similar yield of about 80% when allowed to go to completion, which occurred within about 1 hour (Figure 4.6). The above kinetics of β-haematin formation were modelled with the Avrami equation given in Chapter 1 as described previously by Egan et al. (2001). The kinetic process fitted well to the Avrami model with an Avrami constant n = 1 describing a solid-state process of nucleation and growth which conformed to pseudo first-order kinetics. Of the constituent lipids of the NLB, MPG showed the most similar kinetics. The reaction was very fast at 2.15 L/H and 1.07 L/H mol ratios reaching completion within less than 10 min. The slow kinetics at 0.54 L/H mol ratio (Figure 4.7A) is comparable to the NLB at the same mol ratio. The kinetic plot started to level off after 30 min of incubation time which means the reaction effectively reached completion within 30 min. Thus, the drop in yield below the 0.54 L/H may be as result of the decrease in the rate of β-haematin formation. MSG at 2.15 L/H mol ratio mediated relatively slow kinetics (Figure 4.7B) with a lower yield of about 35% after 45 min compared to NLB and MPG at a much lower mol ratio of 0.54 L/H. The kinetics mediated by DLG at 1.07 and 0.54 L/H mol ratios were relatively faster (Figure 7C) than NLB and MPG at the same 0.54 L/H mol ratio, indicating this lipid on its own promotes β-haematin formation faster than the NLB at same concentration. DOG, which has been shown above to be very efficient in forming β-haematin also exhibits the fastest kinetics at all the different L/H mol ratios studied (Figure 4.7D). The relatively slow kinetics of β-haematin formation with DOG at 0.27 L/H mol ratio can be compared to NLB and MPG at 0.54 L/H mol ratio. This study showed the unsaturated lipids (DLG and DOG) or the diaglycerides DLG, DOG and DPG (as seen at a much higher temperature of 60^{o}C) are more efficient in mediating the formation of β-haematin than their monoglyceride counterparts (MPG and MSG). The efficiency with which these lipids mediate β-haematin formation remains high and only starts to drop significantly when there is one lipid molecule to two Fe(III)PPIX. Moreover, DOG and DLG which are liquid at room temperature are known to have lower activation energy (Hoang et al. 2010b) with respect to β-haematin formation at 37°C since their T_m is below this temperature. The monoglycerides MPG and MSG are

known to form two crystalline polymorphs termed α and sub-α. The conversion of the α to the sub-α occurs at temperatures below 37°C for MPG (Hoang et al. 2010b), thus, this may account for its greater efficiency in mediating β-haematin formation than MSG at 37°C. The similarity in kinetic data at 0.54 L/H mol ratio for both the NLB and MPG (Figure 4.6 and 4.7A) with almost the same rate constants, *k*, suggest that MPG is a good lipid model of the NLB to study the effect of other substances on the kinetics of β-haematin formation. It is also much cheaper than some of the other constituent lipids of the NLB. Furthermore, the very fast rate of β-haematin formation by NLB and MPG could be decreased to an appreciably slower rate without any significant change in the overall yield obtained by decreasing the lipid to Fe(III)PPIX ratio to about 0.54. This allowed the effect of other low molecular weight ions on the kinetics of β-haematin formation to be conveniently investigated.

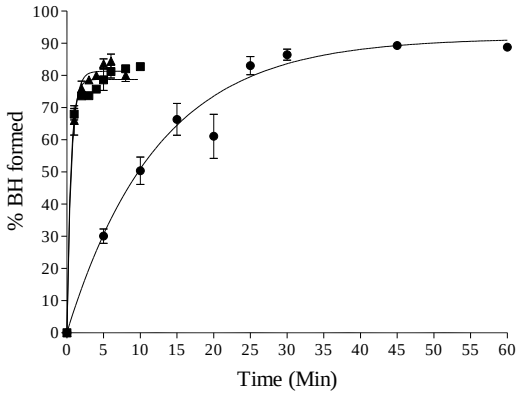

Figure 4.6: Kinetics of β-haematin formation with NLB. NLB showed fast kinetics at higher mol ratios of 2.15 (■) and 1.07 L/H (▲) with the reactions completed within 10 min giving yields of about 80 %. The kinetic curve conformed to the Avrami equation with Avrami n = 1 describing pseudo first-order kinetics. The rate constants obtained were 1.9 ± 0.2 and 1.6 ± 0.1 min^{-1} respectively. 0.54 L/H (●) gave relatively slower kinetics with k = 0.082 ± 0.006 min^{-1}. Reaction conditions: incubation at different times, citric buffer (50 mM, pH 4.8), 37 °C.

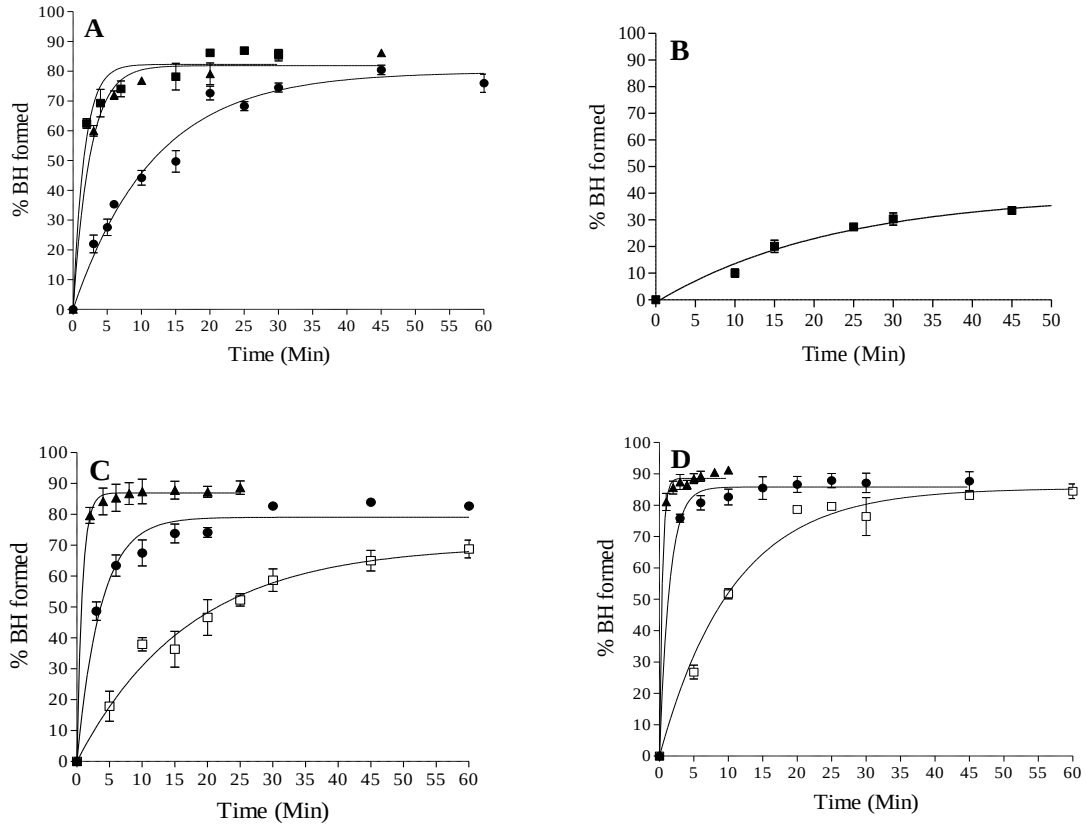

Figure 4.7: Kinetics of β-haematin formation with individual lipid constituent of NLB. MPG showed fast kinetics at 2.15 L/H (■) and 1.07 L/H mol ratio (▲) with k = 0.61 ± 0.07 and 0.40 ± 0.03 min^{-1} respectively, which slowed down at 0.54 L/H mol ratio (●) with k = 0.085 ± 0.006 min^{-1}, similar to that of NLB (**A**). MSG at the highest lipid concentration (2.15 L/H) showed slower kinetics than NLB and MPG at 0.54 L/H mol ratio, with k = 0.044 ± 0.007 min^{-1} (**B**). DLG at 1.07 L/H (▲) and 0.54 L/H (●) appeared to give relatively faster kinetics than that of NLB at same mol ratio with k = 1.2 ± 0.2 and 0.27 ± 0.02 min^{-1} respectively, while at 0.27 L/H mol ratio (□) the reaction was relatively slower with k = 0.058 ± 0.009 min^{-1} (**C**). The kinetics with DOG were exceptionally fast at 1.07 L/H (▲) and 0.54 L/H mol ratio (●) with k = 2.4 ± 0.2 and 0.69 ± 0.08 min^{-1} respectively while at 0.27 L/H (□) the kinetics were slower with k = 0.094 ± 0.008 min^{-1}, comparable to NLB and MPG at mol ratio of 0.54 L/H (**D**). Reaction conditions: Citric buffer (50 mM, pH 4.8), 37°C. Constant total Fe(III)PPIX concentration of 30 μM. Error bars represent SEM (n = 4, except D for which n = 3).

4.3.6 Effect of Fe(III)PPIX concentration on yields of β-haematin formed

The concentration of MPG corresponding to the cut-off L/H mol ratio (16.06 μM) in the experiments described above was used to study the effect of varying Fe(III)PPIX concentration on the yield of β-haematin formed. Starting at 7.44 μM (0.5 mg/ml) of Fe(III)PPIX the yield of β-haematin formed stayed relatively constant through 30 μM (2.0 mg/mL), after which it started to decline before levelling off at 45 μM (3.0 mg/ml) with a yield of about 10 % (Figure 4.8). The cut-off ratio here is identical to that obtained by decreasing lipid concentration while keeping Fe(III)PPIX constant.

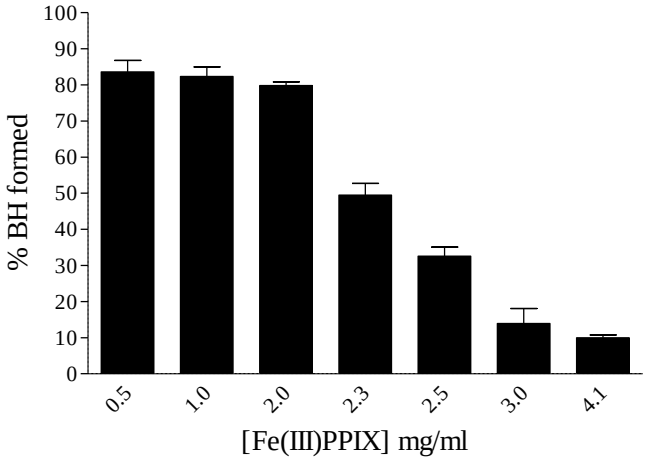

Figure 4.8: Effect of Fe(III)PPIX concentration on yields of β-haematin formed. About 80% yields of β-haematin were obtained with 0.5 mg/ml (2.15 L/H) to 2.0 mg/mL (0.54 L/H) Fe(III)PPIX and 16.1 μM MPG which started to decline from 2.3 mg/mL (0.46 L/H) to 2.5 mg/mL Fe(III)PPIX to about 30-50% and levelled out to a lower yield of about 10% at 3.0 mg/mL (0.36 L/H) and 4.1 mg/mL (0.27 L/H). Reaction conditions: Incubation time was 30 min at 37 °C, citric buffer (50 mM, pH 4.8). Error bars represent SEM, (n = 3).

4.3.7 Kinetic studies of β-haematin formation at Fe(III)PPIX concentrations higher than 2 mg/mL and MPG at 16 μM (below cut-off concentration of lipid/Fe(III)PPIX ratio)

Looking at the differences in the yield of β-haematin formed above and below the 0.54 L/H cut-off mol ratio, an experiment was performed to investigate if the difference in β-haematin yield arose from slower kinetics or a decrease in the extent to which the reaction occurred. Starting at 2.3 mg/mL (0.46 L/H) through 3.0 mg/mL (0.36 L/H) Fe(III)PPIX concentration, the rates of β-haematin formation were relatively constant (Figure 4.9) compared to that at 0.54 L/H. This therefore suggests that the decrease in β-haematin yield below the cut-off ratio is not due to the rate at which β-haematin is formed but the extent to which it is formed. The observed general decrease in yield below this cut-off point of 0.5 L/H might be as result of the precipitation of Fe(III)PPIX in solution, which slows down its dissolution and partitioning into lipid droplets in solution thereby decreasing its conversion to β-haematin as previously described by Egan et al. (2001 & 2006). Also important is that fact below the cut-off the number of Fe(III)PPIX molecules is high compared to the number of available lipid molecules or droplets. This may cause the precipitation of Fe(III)PPIX as there are not enough lipid droplets to keep the Fe(III)PPIX in the suspension and hence to facilitate their conversion to β-haematin. While at higher L/H mol ratio above 0.54, there are more than enough lipid droplets to maintain Fe(III)PPIX in the dissolved state and also to nucleate β-haematin crystal growth although it seems likely that small amounts of Fe(III)PPIX might still precipitate since a yield of 100% was never obtained.

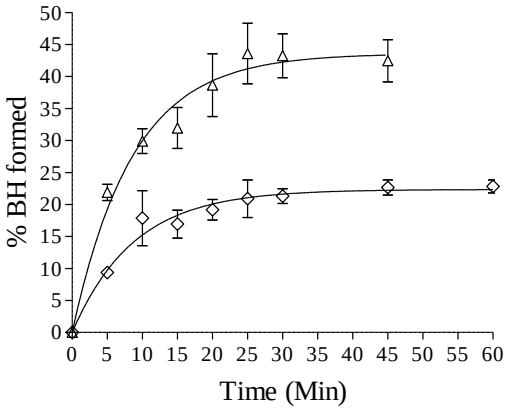

Figure 4.9: Kinetics of β-haematin formation at L/H mol ratios below the 0.54 cut-off of MPG. The kinetics of β-haematin formation at 0.46 L/H (Δ) gave k = 0.12 ± 0.02 and that at 0.36 L/H (◇) gave a k = 0.11 ± 0.02 min^{-1} which are similar to the rate constants obtained at 0.54 L/H (where k = 0.085 ± 0.006 min^{-1}). Reaction conditions: Incubation at different times, citric buffer (50 mM, pH 4.8), 37°C, MPG (16.06 μM). Total Fe(III)PPIX concentrations were 35 and 45 μM respectively. Error bars represent SEM (n = 4).

4.3.8 Effect of dish diameter on the kinetics of β-haematin formation

There was a change in the kinetics of β-haematin formation with change in diameter (5 cm) of the crystallization vessel used in the kinetic study as shown in Figure 4.10. This discrepancy in the rate of β-haematin formation resulting from a change in the diameter of the reaction vessel may either be due to the rate of mixing between the lipid solution and the citric acid buffer or the rate at which Fe(III)PPIX is efficiently transported to the lipid droplets through the solution which might depend on the thickness of the interface where the solutions mixed. As a result of this discrepancy in kinetics, all further studies on the effect of low molecular weight bio-molecules found in RBC or serum were done in the 9 cm internal diameter Schott-Duran crystallization vessel which had been used in all preceding work.

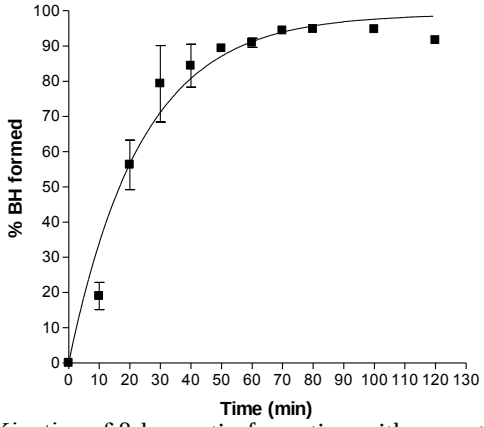

Figure 4.10: Kinetics of β-haematin formation with a reaction vessel of 5 cm internal diameter gave k =0.042 ± 0.005 min^{-1} which is half that of a 9 cm internal diameter dish with k = 0.085 ± 0.006 min^{-1}. Reaction conditions: Incubation at different times, citric buffer (50 mM, pH 4.8), 37 °C, MPG (16.06 μM). Error bars represent SEM (n=4).

4.3.9 Fluorescence study of β-haematin formed with MPG

To determine whether the macroscopic reaction rates described above are commensurate with crystal formation, advantage was taken of the exciton fluorescence properties of β-haematin. Bellemare et al. (2009) showed Hz to autoflourescence exhibiting excitation and emission maxima at 555 nm and 577 nm respectively. This autoflourescence phenomenon is exhibited by only the fully hydrated or fully dehydrated β-haematin crystal structures as partially hydrated β-haematin crystals were shown not to fluoresce. The fluorescence intensity of β-haematin crystals is dependent on the ordered nature of the crystals formed. It was therefore decided to use confocal microscopy to monitor the appearance of fluorescence from ordered β-haematin crystals formed in association with lipids as a function of time. The reaction for the formation of β-haematin with MPG at 0.54 L/H mol ratio was allowed to progress for 60 min and products formed were collected after 10, 20, 30 and 60 min for fluorescence measurement. Increase in fluorescence signal was observed from 10 min through 60 min (Figure 4.11A, B, C & D) even though there appear not to be any significant changes in the fluorescence intensity beyond 30 min (Figure 4.11C & D). The observed increase in fluorescence with time confirmed that β-haematin is formed with time in a range that is qualitatively in agreement with the kinetics of this process as shown in Figure 4.5 & 4.6A at 0.54 L/H mol ratio. The fluorescence approach is qualitative since factors such as evaporation of solution between the microscope slide and coverslip, aggregation of crystals and pathlength between microscopic slide and coverslip which may affect fluorescence, makes it unsuitable for quantitative comparison with the kinetic measurement shown in Figure 4.6 and 4.7A.

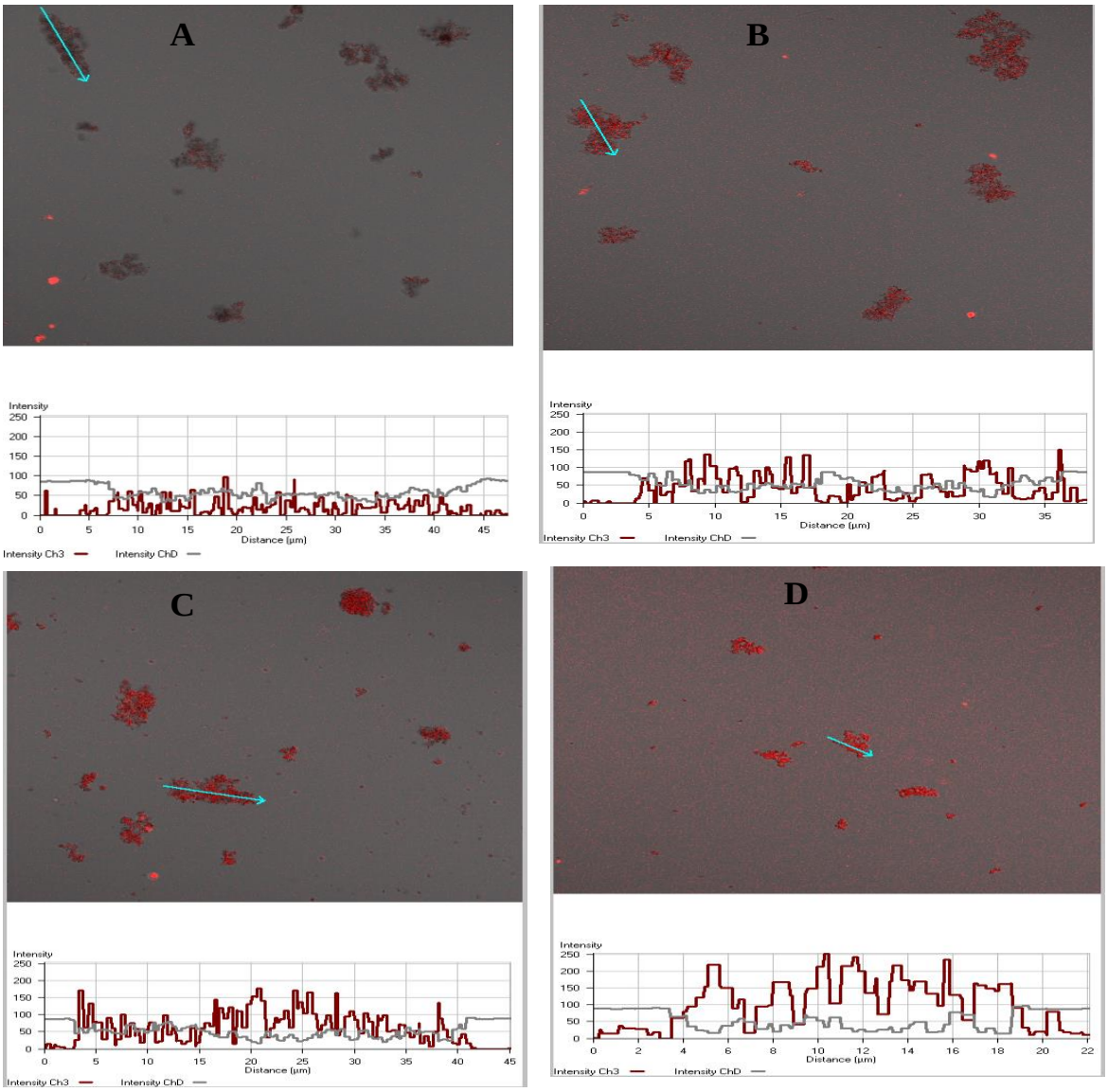

Figure 4.11: Fluorescence from β-haematin formed during a reaction time course. Confocal laser microscopy measurement of autoflourescence arising from wet samples of β-haematin formed with MPG and Fe(III)PPIX at different incubation times showed fluorescence signal to increase from products collected at 10 min (**A**), 20 (**B**), 30 (**C**), through 60 minutes (**D**). The fluorescence profiles taken along cross-Sections of the images (indicated by an arrow in each image) are given below the images as thick red lines. The grey trace (ChD line) represents the transmitted light channel. The steady increase in measured fluorescence signal with increasing incubation time signifies the steady formation of β-haematin with time during the reaction which qualitatively agrees with kinetic measurements with this lipid, showing that the reaction is completed in less than 60 min seen by the absence of a significant increase in fluorescence from 30 to 60 min. Excitation was at 516 nm, emission in the range 575–630 nm. Reaction mediated by MPG, 0.54 L/H ratio, citric buffer (50 mM, pH 4.8), 37°C.

4.3.10 Effect of buffers on the kinetics of β-haematin formation

All experiments for the formation β-haematin were done in the presence of buffers. It was necessary therefore to investigate their effect on yields and kinetics of this process. Previous work by Egan et al. (2006) showed the rate of β-haematin formation at the water-octanol interface to be similar in citric acid buffer and MES. It was therefore important to investigate

whether the rate of β-haematin formation at the water-lipid interface is also unaffected by differences in buffer solutions used. Acetate and MES were found to cause a decrease in the rate constant compared to that of citric acid (Figure 4.12). However, overall this seems not to be a major effect on the rate of β-haematin formation.

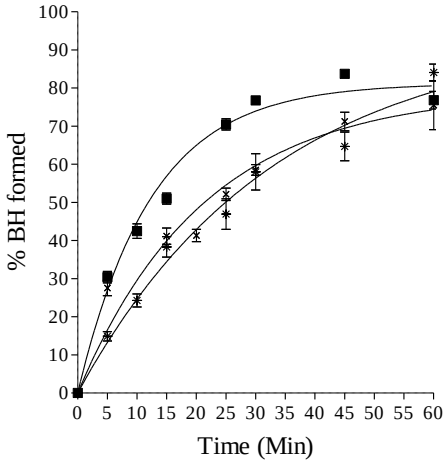

Figure 4.12: Effect of buffers on the kinetics of β-haematin formation. Citric (■), acetic (×) and MES buffers (✳) gave rate constants of 0.080±0.005, 0.047±0.006 and 0.030±0.004 min^{-1} respectively. Reaction conditions: Incubation at different times, buffer (50 mM, pH 4.8), 37°C, MPG (16.06 μM total lipid), constant total Fe(III)PPIX concentration of 30 μM. Error bars represent SEM (n = 4).

4.3.11 Effect of physiologically relevant ions and other low molecular weight bio-molecules on the kinetics of β-haematin formation

The membrane of the DV is known to have ion channels through which some ions move in and out of the DV depending on the physiological state or activity of the parasite. Also, some of the proteins found in DV and parasite cytoplasm require metal ions as co-factors for their activity. Some cations and anions from the RBC cytoplasm also may be ingested together with haemoglobin during the parasite feeding process and transported to the DV. Although the concentration of all these different ions inside the DV is not known, the parasite inside the RBC is known to greatly modify the RBC cytoplasm such that its ion content more closely resembles that in blood serum (Mauritz et al. 2009). Parasites in RBCs are also known to produce proteins that interact with the RBC membrane cytoskeleton thereby resulting in an increase in plasma membrane permeability and rigidity of the iRBC (Glenister et al. 2002). This further makes ion exchange between RBC cytoplasm and blood very easy as the RBC membrane may almost be described as "leaky". Therefore, the ionic concentrations inside RBCs and in blood serum would provide the two extreme possible concentrations that may affect Hz formation in the DV. It was for this reason, therefore, that all the major cations and

anions present in the RBC cytoplasm and serum were evaluated for their effect on the kinetics of β-haematin formation at their different physiological concentrations.

4.3.11.1 Cations at RBC cytoplasmic concentration

Sodium, potassium and magnesium are some of the relevant cations with known concentrations found to be present inside the RBC. Their concentrations inside RBCs are smaller compared to their concentrations in blood serum except for potassium which is present in larger amount in RBC than in serum. Sodium at 8.0 mM did not show any major effect on the kinetics of β-haematin formation. Potassium at 150 mM and magnesium at 1.75 mM appeared to have a small effect on the kinetics of β-haematin formation as the rate constants drop to almost half that of the control without any added ions (Figure 4.13).

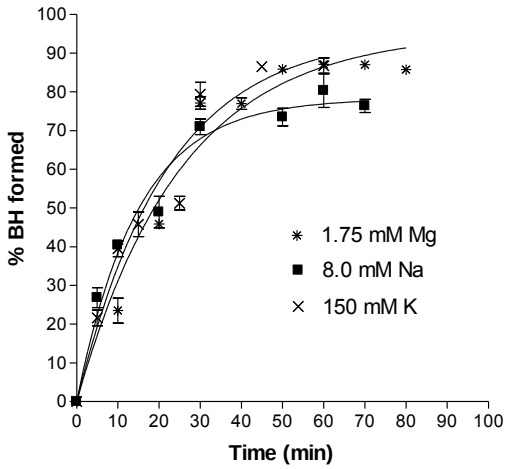

Figure 4.13: RBC concentration of sodium at 8.0 mM had no major effect on kinetic of β-haematin formation with k = 0.067±0.006min^{-1} while that of potassium and magnesium had small effects with k = 0.045±0.005 and 0.03943± 0.004 and min^{-1} respectively. Reaction conditions: Incubation at different times, citric buffer (50 mM, pH 4.8), 37°C, MPG (16.06 μM total lipid). Error bars represent SEM (n=4 for all ions).

4.3.11.2 Cations at serum concentration

As the parasite matures to complete its life cycle inside the RBC, the RBC membrane becomes increasingly permeable to the external environment (the serum) exposing the parasite to cations at concentration levels which exist in the serum. Magnesium at 1.5 mM, 3.0 mM calcium and 150 mM sodium seem to have a minor effect on the kinetics of β-haematin formation (Figure 4.14).

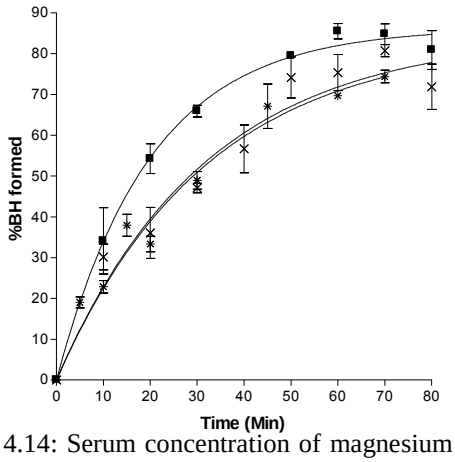

Figure 4.14: Serum concentration of magnesium (■) at 1.5 mM gave k = 0.050±0.005 min^{-1}, 3.0 mM calcium (×) and 150 mM sodium (✳) had minor effect with decreased rate constants of k= 0.031±0.005 and 0.031±0.004 min^{-1} respectively. Reaction conditions: Incubation at different times, citric buffer (50 mM, pH 4.8), 37°C, MPG (16.06 μM). Error bars represent SEM (n=4 for all ions).

4.3.11.3 Anions at RBC concentration

In the case of anions at RBC cytoplasmic concentrations, 1 mM phosphate ions and 15 mM carbonate ions which exist as sodium citrate in equilibrium with citric acid buffer in solution gave somewhat lower rate constants, half that of the standard reaction conditions with NLB or MPG (Figure 4.15).

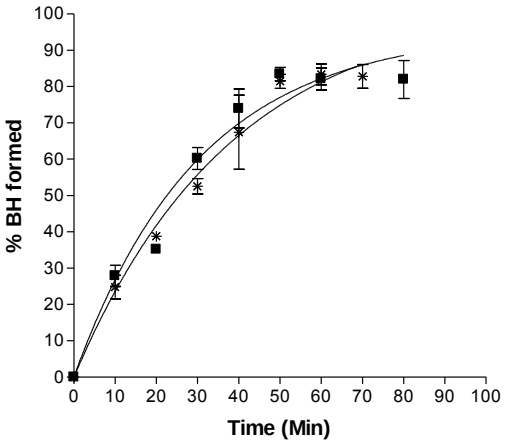

Figure 4.15: RBC concentrations of 15 mM carbonate (✳) and 1 mM phosphate ions (■) had a small effect with k = 0.026±0.004 and 0.033±0.004 min^{-1} respectively. Reaction conditions: Incubation at different times, citric buffer (50 mM, pH 4.8), 37 °C, MPG (16.06 μM). Error bars represent SEM (phosphate, n=4; carbonate, n=5).

4.2.12 Effect of Adenosine-5'-triphosphate (ATP)

ATP, the main energy storage molecule of the cell has only a slight effect on the kinetics of β-haematin formation at a concentration of 1.5 mM, comparable to that inside RBC, as the rate constant is decreased to a small extent (Figure 4.16).

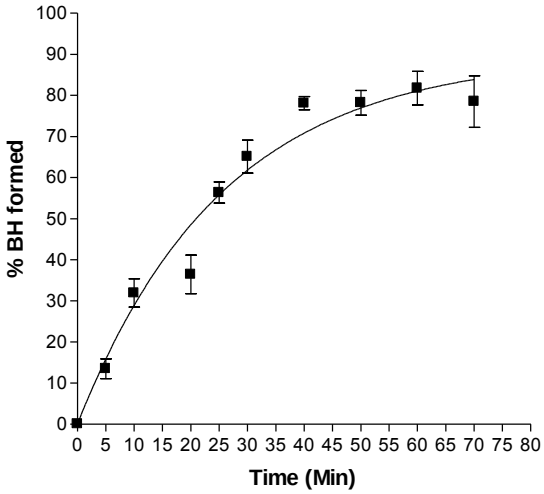

Figure 4.16: Kinetics of 1.5 mM ATP gave k = 0.039±0.005 min^{-1} which is lower than that of the control without any added ions. Reaction conditions: incubation at different times, citric buffer (50 mM, pH 4.8), 37°C, MPG (16.06 μM). Error bars represent SEM (n=5).

4.3.13 Effect of 2, 3-diphosphoglycerate

The yield of β-hematin formation obtained with 4.5 mM 2,3-diphosphoglycerate was measured instead of a full kinetic study since it was only available in a limited quantity and is also very expensive. The β-haematin yield was 70.7 ± 1.9% at 30 min incubation time which is similar to the yield obtained in the control experiment, therefore indicating that this molecule is unlikely to affect the overall kinetic process of β-hematin formation to a great extent.

4.3.14 Effect of glutathione

L-Glutathione also had only a minor effect on the kinetics of β-haematin formation with a fourfold decrease in rate constant (Figure 4.17) similar to that obtained with some of the other ions. The reaction was carried out under argon to prevent glutathione from producing reactive oxygen species which can occur under ambient conditions where oxygen is present. The four fold decrease in rate constant of β-haematin formation was not surprising as glutathione, a known antioxidant, is likely to act by reducing oxidized Fe(III)PPIX to Fe^{2+} thereby

preventing it from being incorporated into the growing β-haematin crystal thus resulting in an increase available free Fe(III)PPIX in solution and a decrease in the rate of β-haematin formed due to precipitation of some of the Fe(III)PPIX in solution as previously described (Egan et al. 2001& 2006).

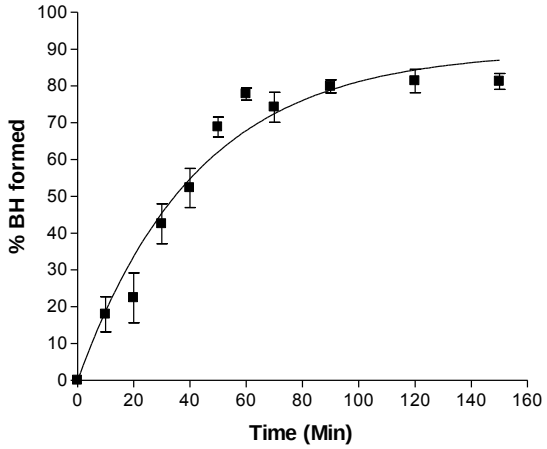

Figure 4.17: Glutathione alone at 2.48 mM RBC concentration decreases the rate constant of β-haematin formation about fourfold with k =0.024 ± 0.003 min^{-1}. Reaction conditions: incubation at different times, citric buffer (50 mM, pH 4.8), 37°C, MPG (16.06 μM). Error bars represent SEM (n=4).

4.3.15 Effect of all ions present in serum combined at serum concentrations

Since all ions found inside the RBC are present together rather than individually, it was then decided to investigate the combined effect of all these ions (150 mM Na^{+}, 1.75 mM Mg^{2+} and 3 mM Ca^{2+}) on the kinetics of β-haematin formation since synergistic effects might be present. It was thought that the effect of all the individual ions on the rate of β-haematin formation would be additive when combined together. Surprisingly, this was not the case as there was no significant change in the rate of formation of β-haematin in the presence of all these ions combined compared to the rate constant obtained with some of the individual ions as shown in Figure 4.18.

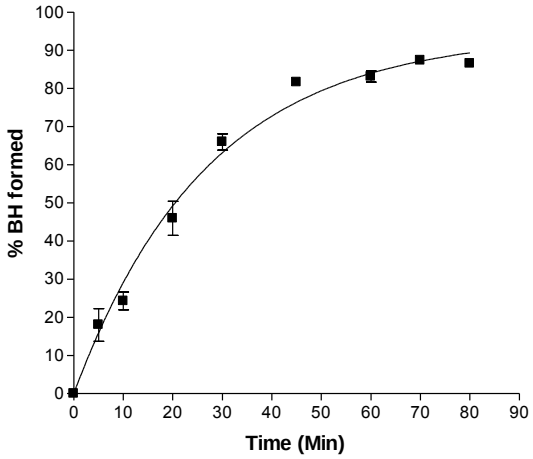

Figure 4.18: All ions present in serum combined at their respective serum concentration did not show any significant increase in the kinetics of β-haematin formation with k = 0.037 ± 0.003 min^{-1} compared to kinetics with the individual ions. Reaction conditions: incubation at different times, citric buffer (50 mM, pH 4.8), 37°C, MPG (16.06 μM). Error bars represent SEM (n=4).

4.3.16 Effect of all ions combined at RBC concentration

A combination of all the previously tested individual ions present in RBC (8 mM Na^+, 150 mM K^+, 1 mM $H_2PO_4^-$, 15 mM HCO_3^- and 1.5 mM ATP), except for 2,3-DPG which was in limited quantity, were used to study the kinetics of β-haematin formation. As expected from the effects observed at serum concentration, there was no overall major decrease in the kinetics of β-haematin formation (Figure 4.19). The effects of all biologically-relevant ions at concentrations which they exist individually or combined in RBC or serum on the kinetics of β-haematin formation is summarised in Table 4.1.

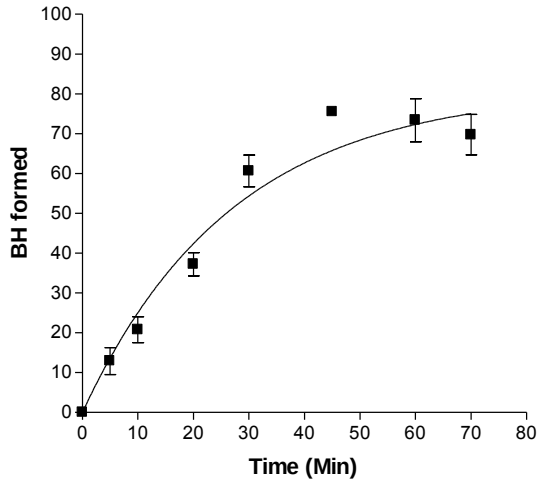

Figure 4.19: Combination of all ions present in RBC at cytoplasmic concentration showed no significant effect compared to the individual ions on the kinetics of β-haematin formation with k = 0.03693 ± 0.006 min^{-1}. Reaction conditions: incubation at different times, citric buffer (50 mM, pH 4.8), 37°C, MPG (16.06 μM). Error bars represent SEM (n=4).

Table 4.1: Effect of added biomolecules present in RBC or in blood serum on the kinetics of β-haematin formation with MPG (0.54 L/H), citric buffer (50 mM, pH 4.8) at 37°C.

Added biomolecules	Concentration (mM)		k (min^{-1})
-	Control		0.085±0.006
Na^+	8	RBC concentration	0.067±0.006
	150	Serum concentration	0.031±0.004
Mg^{2+}	1.75	RBC concentration	0.039±0.004
	1.5	Serum concentration	0.050±0.005
K^+	150	RBC concentration	0.045±0.005
$H_2PO_4^-$	1	RBC concentration	0.033±0.004
HCO_3^-	15	RBC concentration	0.026±0.004
ATP	1.5	RBC concentration	0.039±0.005
Glutathione	2.48	RBC concentration	0.024±0.003
Ca^{2+}	3	Serum concentration	0.031±0.005
all ions combined	a	RBC concentration	0.037±0.006
all ions combined	b	Serum concentration	0.037±0.003

[a] 8 mM Na^+, 150 mM K^+, 1 mM $H_2PO_4^-$, 15 mM HCO_3^- and 1.5 mM ATP
[b] 150 mM Na^+, 1.75 mM Mg^{2+} and 3 mM Ca^{2+}

4.4 CONCLUDING REMARKS

Lipid was proposed to be the most likely biomolecule responsible for Hz formation *in vivo* from proteomic and lipidomic studies of the Hz crystal in the previous chapter and the identified NLB found to be associated with the Hz crystal surface was used to study kinetics of β-haematin formation *in vitro*. The yield of β-haematin formed mediated by NLB and MPG, but not MSG, reaches about 80-90% and only starts to decrease when there are more than two molecules of Fe(III)PPIX to one molecule of lipid fatty acid chain. The high yield of above 80% β-haematin obtained with NLB is in agreement with previous studies by Pisciotta

et al. (2007). Furthermore, biologically-relevant ions likely to be present either in RBC or in serum at physiological concentrations did not have any major effect on the overall reaction of β-haematin formation and reaction rates remain adequate to account for Hz formation despite an overall drop in yields at physiologically-relevant lipid-to-Fe(III)PPIX ratios. This may mean that in a fully mature parasite inside the RBC, ions ingested together with haemoglobin from the RBC cytoplasm into the DV compartment where haemoglobin digestion and Hz formation takes place, may not have any major effect on the overall process of Fe(III)PPIX sequestration into Hz *in vivo* if the process is purely lipid-mediated as proposed. This further supports the process of Hz formation in malaria parasite being lipid-mediated and seems to suggest lipid to be the most important factor influencing this process *in vivo*. CLM studies showed autoflourescence arising from β-haematin crystals and clearly demonstrates that β-haematin formed *in situ* is in close association with the lipid component of the emulsion. The autoflourescence of β-haematin showed potential for use in monitoring the process of β-haematin formation and to adapt to follow the progress of Hz formation *in vivo* or to monitor the effect of antimalarial drugs that target the Hz formation process. However, a striking observation from TEM characterisation of the β-haematin crystals formed with lipid was that lipid particle size seems to have an effect on β-haematin crystal size and external morphology which would require further investigation. This is described in the next chapter.

5. THE NUCLEATION OF SYNTHETIC HAEMOZOIN (β-HAEMATIN) CRYSTALS AT THE SURFACE OF NEUTRAL LIPID DROPLETS: CONTROL OF CRYSTAL SIZE AND THE EFFECT OF CHLOROQUINE ON HAEMOZOIN CRYSTAL GROWTH IN THE MALARIA PARASITE

5.1 INTRODUCTION

Proteomic and lipid studies in Chapter 3 led to the identification of MSG/MPG/DPG/DOG/DLG (NLB) associated with the surface of Hz crystals. Thus lipids were suggested as the biomolecules most likely to be responsible for Hz formation *in vivo*. Kinetics studies of the NLB in Chapter 4 showed NLB to be very efficient in mediating β-haematin formation *in vitro* which is unlikely to be greatly affected by biologically-relevant ions present either in RBC or in serum. However, the crystal formed appeared externally distinct from Hz crystals. The β-haematin formed also appeared to fall in a similar size range to that of previously reported lipid droplets (Hoang et al. 2010a). Although it was proposed that the size of these droplets might control the size of β-haematin formed at the interface, this has not yet been fully investigated. Neither has the influence of lipid on shape, crystalline nature or localization of β-haematin been investigated.

Hz and β-haematin crystals have been shown to be chemically, spectroscopically and crystallographically identical. They have a triclinic unit cell structure with dimensions a = 12.2 Å, b = 14.7 Å, c = 8.0 Å, α = 90.2°, β = 96.8°, γ = 97.9° (Pagola et al. 2000). Studies have also described the theoretical growth form of β-haematin to be similar in overall shape and form to that of Hz as a lath-like structure that extends along the *c*-axis exhibiting dominant {100} and {010} side faces, a less-developed {011} face and a minor {001} face, with chloroquine (CQ) proposed to bind to the fastest-growing {001} face to inhibit growth (Buller et al. 2002 and Solomonov et al. 2007). However, direct evidence of the effect of this drug on Hz crystal habit and form in the parasite is lacking.

In this chapter, β-haematin produced with MPG and NLB emulsions prepared in three different ways, as well as at the pentanol-aqueous interface, was characterized and compared to Hz crystals isolated from the parasite itself. This was done using TEM and electron diffraction. In addition, the location of β-haematin crystals formed with respect to NLB particles, the nature and structure of NLB emulsions and the relationship between β-haematin

crystal length and NLB particle size was also investigated. Finally, the effect of CQ on Hz crystals in the parasite was also investigated.

5.2 METHODS

5.2.1 Preparation of β-haematin crystals with NLB, MPG and Pentanol

5.2.1.1 Experimental procedures

β-Haematin was prepared as previously described in Section 4.2.2.1 with some slight modifications as follows: The 1.5 mL pre-mixed solutions of lipid and Fe(III)PPIX (2.15, 1.07 and 0.54 lipid/ Fe(III)PPIX mol ratio) in 1:9 v/v acetone/methanol were either vortexed, ultrasonicated in a water bath sonicator (Bandelin SONOREX) or micromixed (by passing several times through a 10 µm filter using an Avanti® Mini-Extruder system which has been heated to about 60°C on a Snijders hot plate magnetic stirrer) before being deposited carefully on the surface of citric acid buffer using a 1 mL syringe and this was allowed to incubate further at 37°C for different lengths of time for β-haematin formation. In the case of β-haematin formation at the pentanol-water interface, 10 mL of pentanol was layered on the 50 mL citric acid (50 mM, pH 4.8) and pre-incubated for 30 min at 37°C. Pentanol is immiscible with water, thus it floats above the buffer solution creating an interface. A 1.5 mL solution of 2 mg/mL Fe(III)PPIX was then carefully introduced at this interface and allowed to incubate for about 4 h at 37°C in a water bath for β-haematin formation. The entire mixture was filtered through Whatman filter paper number 1 and the precipitate washed with 5% pyridine solution for TEM imaging using a TECNAI TF20 TEM.

5.2.2 Characterization of β-haematin crystals formed with NLB, MPG and pentanol using TEM and TEM-electron diffraction and the indexing of diffraction patterns

5.2.2.1 Experimental procedures

β-Haematin crystals formed from lipid (NLB or MPG) and Fe(III)PPIX (2.15, 1.07, or 0.54 L/H mole ratios) mixtures were prepared for TEM imaging as described previously in Section

4.2.7.1. Transmission electron microscopy-electron diffraction (TEM-ED) patterns were also obtained from some of the cystals using the same TECNAI TF20 TEM.

The SingleCrystal application of CrystalMaker® Software Version 2.2 was used to index the diffraction patterns obtained from β-haematin crystals (CrystalMaker® software Ltd, Oxford, 2009). The calculated structural data for β-haematin described by Pagola et al. was used to build a structural model of the β-haematin crystal using CrystalMaker®. The single crystal diffraction software was then used to predict a simulated diffraction pattern based on this structure. The Grid tool in SingleCrystal™ was used to index the diffraction pattern obtained from β-haematin crystals. Briefly, the observed electron diffraction pattern obtained from the β-haematin crystals was opened using the single crystal window of the software. In the same window, the CrystalMaker® file for the reported β-haematin crystal structure was loaded. The Grid tool was superimposed on the observed diffraction pattern, making sure that all observed diffraction spots coincided. The grid was adjusted such that all grid points lay directly over the observed points. The command "Calculate Orientation" was launched by selecting it from the Grid's contextual menu and this allowed the software to match the simulated pattern with the observed pattern, with the strongest reflections being indexed in this manner.

5.2.3 TEM characterisation of NLB droplet size as a function of time

5.2.3.1 Experimental procedures

Extruded NLB solution was carefully deposited using a 1 mL syringe (KIMIX) on the surface of 50 mL citric acid buffer (50 mM, pH 4.8) that had been pre-incubated for 30 min at 37°C in a water bath. This was allowed to incubate further at 37°C in a water bath. Solutions of NLB suspension were carefully taken from the NLB-water emulsion layer at 10, 30 and 60 min incubation time and placed on a glow-discharged grid which was further processed for TEM imaging using a TECNAI TF20 TEM as described in Section 4.2.7.1.

5.2.4 Confocal laser microscopy characterization of NLB emulsions

5.2.4.1 Experimental procedures

Solutions of NLB (prepared in 1:9 v/v acetone/methanol) stained with lipophilic 3,3'-dioctadecyloxacarbocyanine perchlorate fluorescent DiO dye (5 μL/mL) were carefully deposited using a 1 mL syringe (KIMIX) on the surface of 50 mL citric acid buffer (50 mM, pH 4.8) that had been pre-incubated for 30 min at 37°C in a water bath. Samples were carefully taken from the NLB-water emulsion layer for fluorescence measurement using an LSM510-META Zeiss confocal microscope as described in Section 4.2.8.1. Acquisition of continuous *z*-stacked images through NLB droplets were done under the following conditions; pin hole diameter of 444 μm, excitation laser at 488 nm, 20% transmission power out, detection band pass 500-530 nm (emission) and LD C-Apochromat 40x/1.1 W objective.

5.2.5 Preparation and characterization of liposomes by TEM and cryo-TEM and TEM characterization of NLB emulsions

5.2.5.1 Sample preparation

DMPC (1,2-dimyristoyl-sn-*glycero-3-phosphocholine) lipid solution:*

A 15 mg/mL DMPC lipid solution was prepared in chloroform.

5.2.5.2 Experimental procedures

A laboratory vacuum pump was used to evaporate the chloroform (lyophilization) for three days, leaving behind a dry lipid film or cake. The DMPC lipid film was hydrated with 6.75 mg/mL aqueous CsCl solution at 70 °C and the suspension was vortexed every 5-10 min for about 80 min to form predominantly large multilamellar vesicles (liposomes). The liposome suspension was then sonicated for 30 min in a water bath sonicator (Bandelin SONOREX) at 70°C. It was then extruded using an Avanti® Mini-Extruder by passing it back and forth 23 times through a 0.1 μm filter. The extruded suspension was placed on a glow-discharged carbon-coated grid and processed for TEM imaging as described in Section 4.2.7.1. NLB solution prepared in 1:9 v/v acetone/methanol was carefully deposited using a 1 mL syringe

on the surface of 50 mL citric acid buffer (50 mM, pH 4.8) containing 6.75 mg/mL CsCl which had been pre-incubated for 30 min at 37°C in a water bath. Solution containing suspended NLB droplets collected from the emulsion layer was placed on a glow-discharged carbon-coated grid and processed further for TEM imaging as described in Section 4.2.7.1. Elemental spectroscopic imaging/Electron energy loss spectroscopy (ESI/EELS) analysis of Cs distribution in liposome structures and NLB emulsions was carried out on a FEI TECNAI 20 with GIF 863 Tridiem transmission electron microscope using a slit width of 20 eV. Data were processed with Digital micrograph software from Gatan. Two images were recorded at energies before the $CsM_{4,5}$ absorption edge (681 and 711 eV), and a third was centered at 726 eV. The background images was then extrapolated from the data at 681 and 711 eV and subtracted from the image collected at 726 eV.

Liposomes were also prepared for imaging using Cryo-TEM as follows: A solution of suspended liposome preparation was placed on a glow-discharged quantifoil holey carbon-coated grid and mounted on a PC controlled automated sample preparation machine (Vitrobot MkIV). Excess solution on the grid was blotted on filter paper and the grid was immediately plunged into liquid ethane (ethane cooled to its melting point with liquid nitrogen). The grid was then taken out and mounted in a cryo-holder (Gatan) and imaged at liquid nitrogen temperature using the TECNAI TF20 TEM operating at 200kV.

5.2.6 Localization of β-haematin crystals formed with NLB

5.2.6.1 Experimental procedures

Samples containing product formed using MPG/Fe(III)PPIX or NLB/Fe(III)PPIX solutions either “micromixed” or ultrasonicated and then deposited on the buffer surface were carefully taken from the lipid-water emulsion layer at 10, 30 and 60 min incubation time and placed on a glow-discharged carbon-coated grid. Also, 2 mL citric acid buffer solution (50 mM, pH 7.0) was added to a 1 mL solution of NLB/Fe(III)PPIX solution at 1.07 L/H mol ratio which was then immediately extruded via a 10 µm filter using a miniextruder at about 60^{o}C before incubating it at 37°C for β-haematin formation. Samples were also taken from the reaction mixture and placed on a glow-discharged carbon-coated grid. Excess liquid on carbon-coated grids was carefully blotted with Whatman filter paper number1 and the sample stained with uranyl acetate. Excess stain was blotted with Whatman filter paper number1 and the grid was

allowed to dry at room temperature. Imaging was done using a TECNAI TF20 TEM operating at 200 kV equipped with a Gatan US4000 CCD camera. Electron spectroscopic imaging/Electron energy loss spectroscopy (ESI/EELS) analysis of Fe distribution in NLB droplets was performed using a FEI TECNAI 20 with GIF 863 Tridiem transmission electron microscope with a slit width of 20 eV. Data were processed with Digital micrograph software from Gatan. Images were recorded at two energies before the FeL_3 absorption edge (650 and 693 eV), and the third was centered at 708 eV. The background images was then extrapolated from the data at 650 and 693 eV and subtracted from the image collected at 708 eV.

5.2.7 Estimation of lipid droplet and crystal sizes

5.2.7.1 Experimental procedures

The sizes of NLB droplets and β-haematin crystals formed from a minimum of 34 randomly selected TEM image fields of NLB and β-haematin preparations in Sections 5.2.4.1 and 5.2.7.1, respectively, at different incubation times were manually measured. A total of 309 NLB droplets and 223 β-haematin crystals was measured in the case of the 10 min incubation time point and used for statistical analyses using a Kolmogorov-Smirnov test.

5.2.8 Parasite culturing, isolation of haemozoin crystals and TEM of both parasitized erythrocytes and isolated Hz crystals

5.2.8.1 Experimental procedures

Parasites (*P. falciparum* D10 strain) were maintained in continuous culture as described in Section 3.2.1. For TEM, parasites were synchronized with 5% sorbitol. The parasite culture was harvested after 24 h by centrifuging at 750 rpm for 5 min. The pellet consisting of infected and uninfected red blood cells was washed three times with 10 volumes of cacodylate wash buffer. Fixative (paraformaldehyde, glutaraldehyde and 0.1% malachite green) was then added to the washed pellet and the sample kept at 4°C for 24 h. The pellet was then washed again with wash buffer followed by fixation with 1% tannic acid in wash buffer while tumbling for 1 h. It was then washed twice with wash buffer and post fixed with

1% OsO_4 and 0.1% malachite green in wash buffer for 1 h while tumbling. Further washing was carried out three times with wash buffer followed by dehydration of cells by sequential incubation in 30, 50, 75 and 100% ethanol for 10 min each while tumbling. Further dehydration was effected with 100% acetone for 10 min. The dehydrated cells were resuspended and incubated in 25:75, 50:50 and 75:25 Spurr's resin/acetone mixture for 2 h each. The cells were finally incubated in 100% Spurr's resin overnight. They were then transferred into freshly prepared 100% Spurr's resin and tumbled for a day. The cells were then again transferred into fresh 100% Spurr's resin in a microfuge tube and heated at 60°C in a heating block to solidify. The solid blocks were cut into ultra-thin sections (60 – 80 nm) with a REICHERT ultra-microtome using a diamond knife. The cut sections were placed on a glow-discharged grid and imaged using a TECNAI TF20 TEM. Hz crystals were also isolated from parasites as described in Section 3.2.1 for TEM imaging.

5.2.9 Isolation of haemozoin crystals from chloroquine treated and untreated parasites for TEM imaging

5.2.9.1 Experimental procedures

Parasites (D10 strain) at the ring stage were maintained in culture as described in Section 3.2.1 in the presence of 30 nM and 60 nM CQ and after 32 h, the parasite cultures were harvested and Hz crystals isolated as described in Section 3.2.1 for TEM imaging. Hz crystals were also isolated from untreated parasites (D10 strain) maintained in culture for 12 h for TEM imaging and were used to compare with Hz crystals isolated from the CQ-treated parasites.

5.3 RESULTS AND DISCUSSION

5.3.1 The shape, size distribution and TEM-ED characterization of isolated haemozoin crystals

TEM images of Hz crystals isolated from malaria parasites (Figure 5.1A and B) showed they are in the range 177-1386 nm long and about 532 nm long on average (Figure 5.1C). Hz from parasites showed a regularly-shaped crystal with no evident defects in the crystal lattice as

exhibited by the well-ordered parallel lattice fringes (Figure 5.1D). Indexed TEM-ED patterns obtained from isolated Hz crystals showed most of the crystals to lie on their {100} or {$\bar{1}$00} faces, along the a* direction (Figure 5.1E and F) and this was in agreement with the interatomic distances of 12.57 Å measured from the visible lattice fringes of the isolated hemozoin crystals (Figure 5.1D) corresponding to the {100} or {$\bar{1}$00} faces of Hz.

The overall crystal morphology and indexed diffraction pattern exhibited by isolated haemozoin therefore showed that it grows along it c-axis, displaying well developed {100} faces and {010} side faces, a less developed {011} face and a minor {001}face which is consistent with other published data (Buller et al. 2002 and Solomonov et al. 2007). The {011} face seen from the indexed diffraction pattern corresponds to the stable end face of the theoretical growth form of β-haematin which is seen in other Hz crystals from different species (Buller et al. 2002) which showed that the diffraction vector *d*(011)* is perpendicular to the slanted end face as assigned in Figure 5.1E. The calculated average length-to-width ratio of isolated Hz crystals was 3.4. This value is consistent with the corresponding length-to-width ratio of 3.3 previously reported by Buller et al. (2002) calculated based on the ratio of attachment energy values (E_{att}{001}/E_{att}{100}) that were obtained for the theoretical growth form of β-haematin.

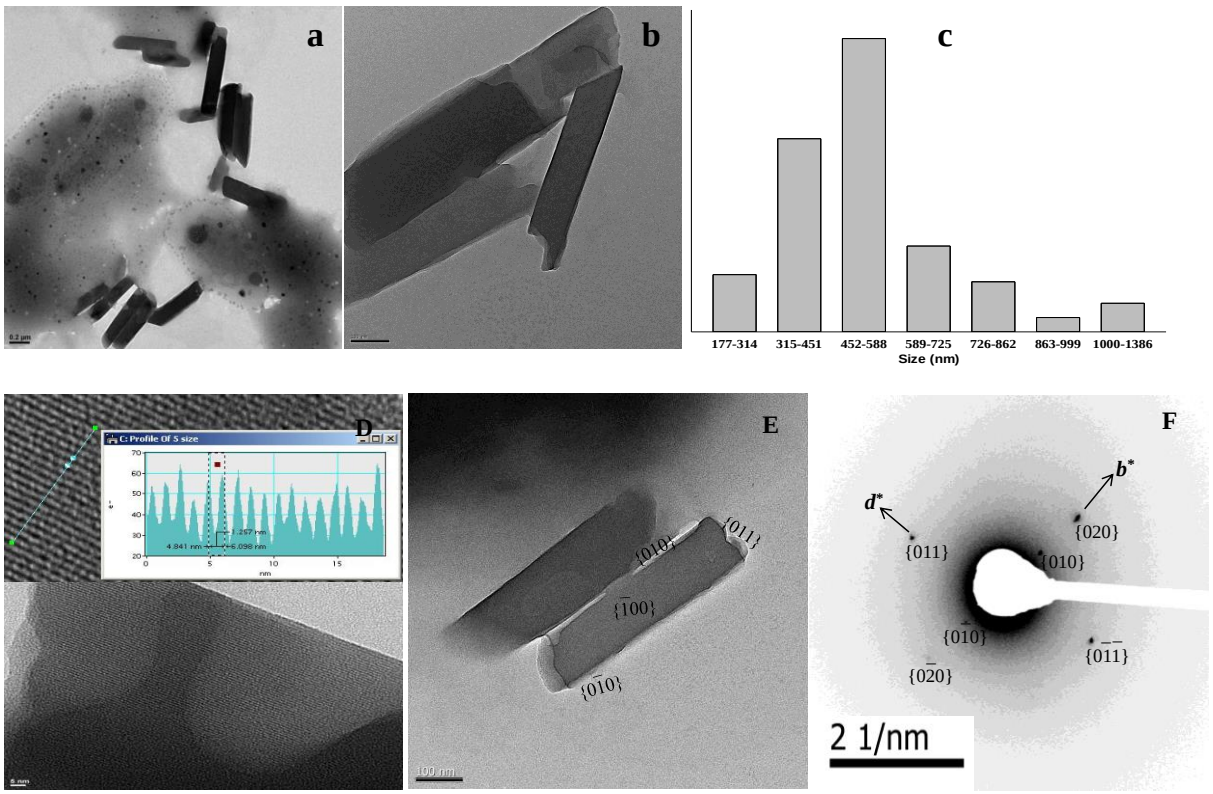

Figure 5.1. TEM imaging showed Hz crystals isolated from *P. falciparum* have a regular shape (A and B) and exhibited very regular lattice fringes with d-spacing of 12.57 Å (D), confirming that the crystals lie on their {100} or {$\bar{1}$00} faces (E). Size range distribution of the isolated Hz crystals showed a majority of them to be between 452 and 588 nm long (C). The electron diffraction pattern from the crystals in (E) showed they exhibit {010} and {011} crystal faces corresponding to the marked *d** and b* directions (F) which are normal to the {$\bar{1}$ 00} face.

5.3.2 The shape and size distribution of β-haematin crystals formed at the pentanol-water interface

β-Haematin crystals formed at the pentanol-water interface are in the range 233-2277 nm long (Figure 5.2A and B). Some of these crystals are even longer than Hz crystals isolated from parasites and appeared to be thinner and more fragile than Hz with some showing signs of broken ends marked * (Figure 5.2C). The overall external morphology and size of these crystals were similar to that of Hz. The increased lengths of these synthetic Hz crystals compared to that of natural isolated Hz might be as result of the long and flat continuous pentanol-water interface where the β-haematin crystals grow since the continuous interface offers no restriction or limitation to the growing crystal. Indexed TEM-ED patterns obtained from some of these β-haematin crystals (Figure 5.2D) showed the crystals to lie on their {100} or {$\bar{1}$00} faces (Figure 5.2E) as seen also with isolated Hz crystals. This is evident by measuring the inter-atomic distances of adjacent lattice fringes of some of the crystals (Figure

5.2F) which gives a value of 11.93 Å, corresponding to the principal a-axis denoting the {100} or {$\bar{1}$00} faces. β-Haematin crystals formed at the pentanol-water interface are therefore similar to that of natural Hz.

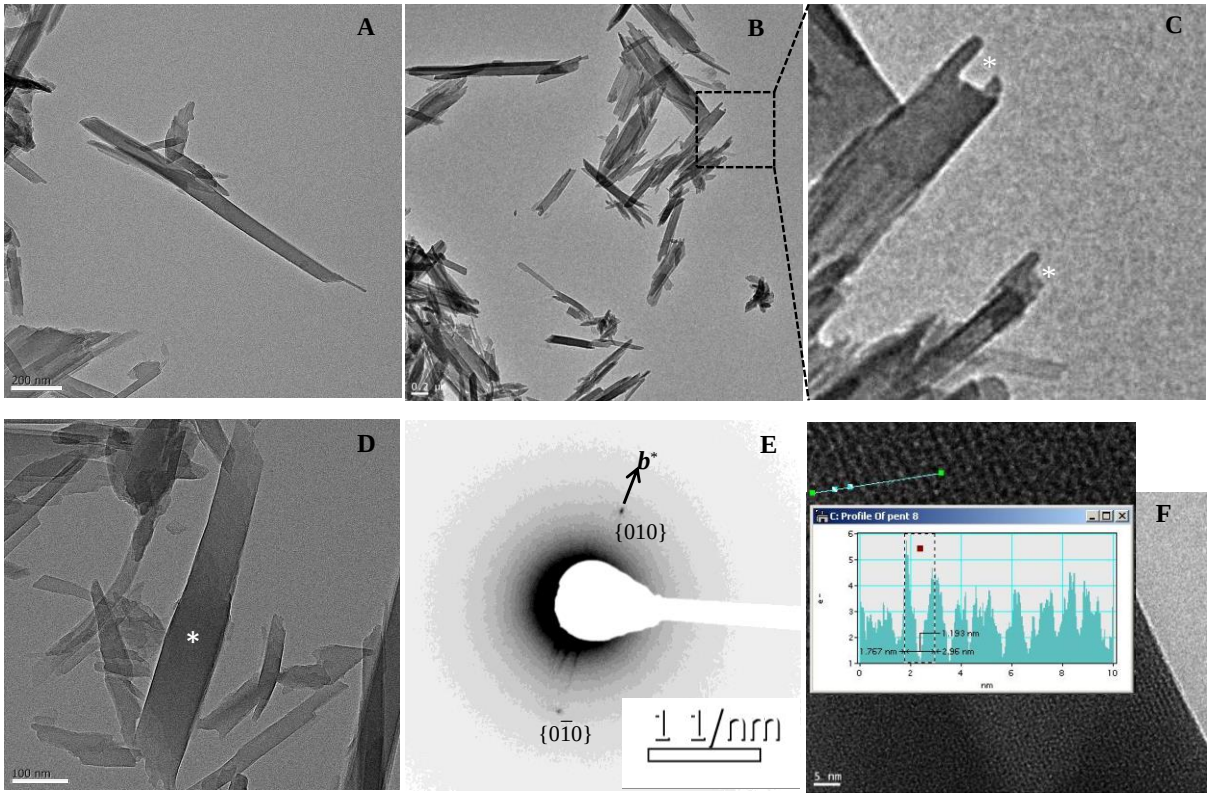

Figure 5.2. TEM imaging showing β-haematin crystals produced at the pentanol-water interface to be very long (A and B) with some even longer than Hz. These β-haematin crystals were thinner and seemed more fragile than Hz as some appeared to have broken ends marked * (C). TEM-ED of crystals such as that marked* (D) showed it forms the {010} crystal faces corresponding to the marked *b** directions (E) which are normal to the {$\bar{1}$00} face. Measured d-spacing of 11.93 Å between adjacent lattice fringes, corresponding to {100} or {$\bar{1}$00} faces confirm it lay on this crystal face.

5.3.3 The shape and size distribution of β-haematin crystals formed at MPG-water and NLB-water interfaces

TEM imaging showed most β-haematin crystals formed from a mixture of MPG and Fe(III)PPIX solution after vortexing and deposition on citrate buffer had a regular shape but were much smaller than Hz (Figure 5.3A) ranging between 17-102 nm and 55 nm long on average. A few of the β-haematin crystals formed were irregular in shape (Figure 5.3B) with their lattice fringes exhibiting signs of growth defects or a mosaic structure (Figure 5.3C). Presumably such complex β-haematin crystal shapes might be the result of an alteration in the lipid matrix during the growth process, as it is a phenomenon common for growth of

biocrystals mediated by lipid (Collier et al. 2001). Indexed TEM-ED obtained from some of these tiny crystals in Figure 5.3D showed they lay in arbitrary orrientations and exposed randomly selected diffraction planes to the electron beam as seen from diffraction spots arising from higher order Miller indices (Figure 5.3E). Diffraction patterns obtained from irregularly-shaped β-haematin crystals with growth defects (Figure 5.3F) gave a ring pattern which cannot be easily indexed using the SingleCrystal application of CrystalMaker® Software Version 2.2. The continuous ring pattern of this diffraction data shows that the material was polycrystalline with very small crystallites. Despite the difficulty of not finding any of the principal crystallographic axes from these extreamly small crystals even with the use of a double tilt goniometer stage, it has previously been confirmed by FT-IR characterization of this crystalline product in Section 4.3.7 to be β-haematin. This was also in agreement with previous studies in our laboratory using a combination of infrared spectroscopy and X-ray powder diffraction to characterize bulk materials produced in this system which demonstrated that this crystalline product is indeed β-haematin (Hoang et al. 2010a). The observed size range distribution of these β-haematin crystals formed with MPG showed a similar range to the major population of lipid droplets previously reported by Hoang et al. (2010a) with a larger population of the crystals in the range 31-70 nm with a smaller population below 30 nm and above 97 nm (Figure 5.3H).

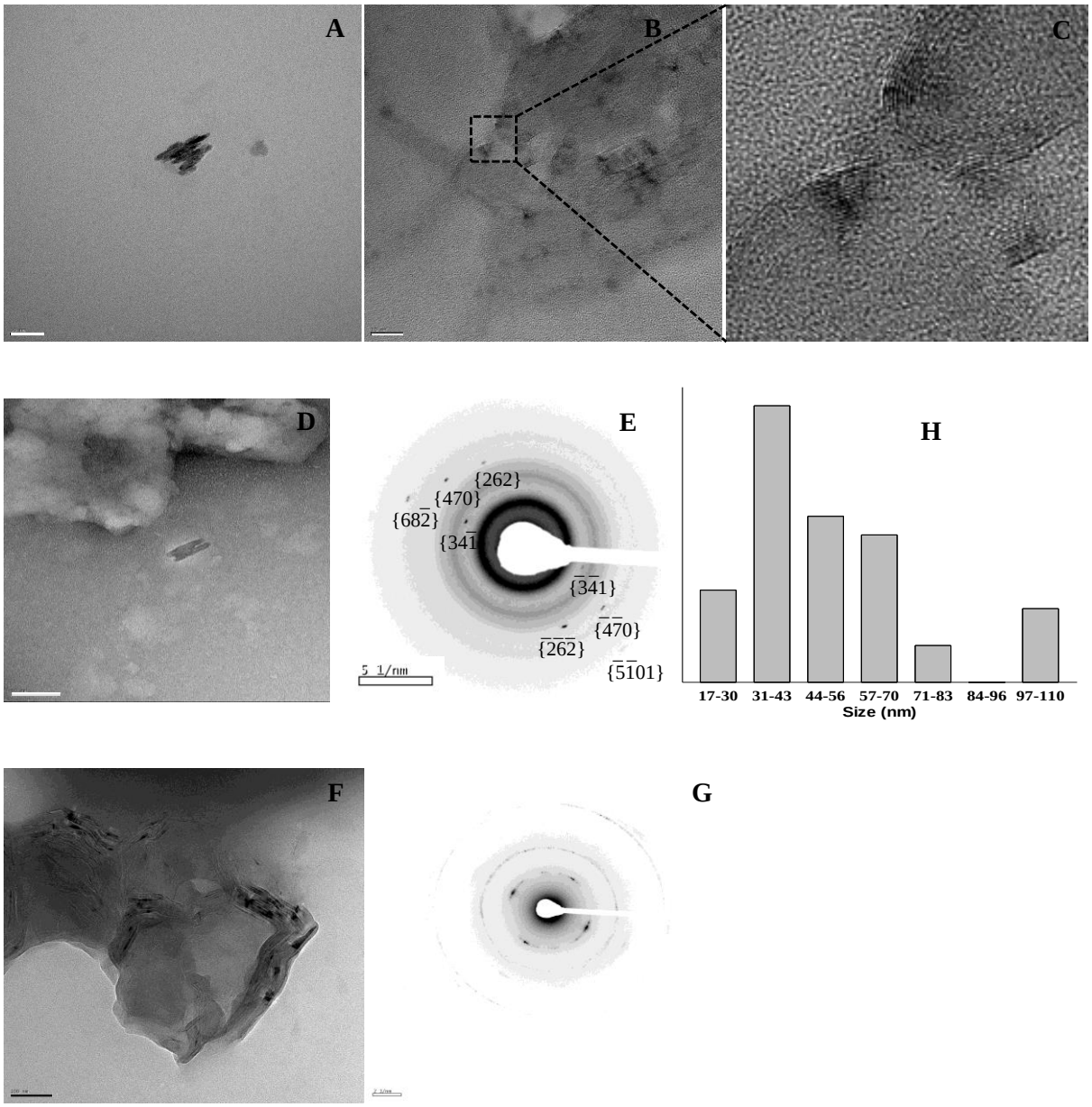

Figure 5.3. TEM imaging showed β-haematin crystals produced from vortexing mixtures of MPG and Fe(III)PPIX were smaller in size (A) than Hz with some having irregular shape (B). Lattice fringes exhibited a crystal growth defects (C). TEM-ED of tiny crystals such as those in (D) showed that they lay at an arbitrary angle with diffraction from a high index plane {7$\bar{4}$5} (E). The irregular shape crystal (F) gave ring diffraction pattern (G). Size range distribution of these crystals showed most of them lay between 31-43 nm (H).

β-Haematin crystals produced by either micromixing MPG and Fe(III)PPIX solution using an extruder (Figure 5.4A) or by ultrasonication (Figure 5.4B), followed by deposition on the surface of citrate buffer, were identical to one another. The crystals were considerably larger than those produced from vortexed mixtures of MPG and Fe(III)PPIX. Indexed TEM-ED patterns obtained from long crystals such as those in Figure 5.4C showed the same orientation as those produced at the pentanol-water interface and of Hz, exhibiting their

{100} or {$\bar{1}$00} faces (Figure 5.4D). Most of the β-haematin crystals were, however, found associated with visible MPG droplets (Figure 5.4E). The d-spacing of lattice fringes of the crystal face directly in contact with MPG lipid droplets was 12.1 Å (Figure 5.4F) which corresponds to the {100} or {$\bar{1}$00} faces of the crystals. This clearly demonstrates that the growing β-haematin crystal is in contact with the lipid via its {100} face.

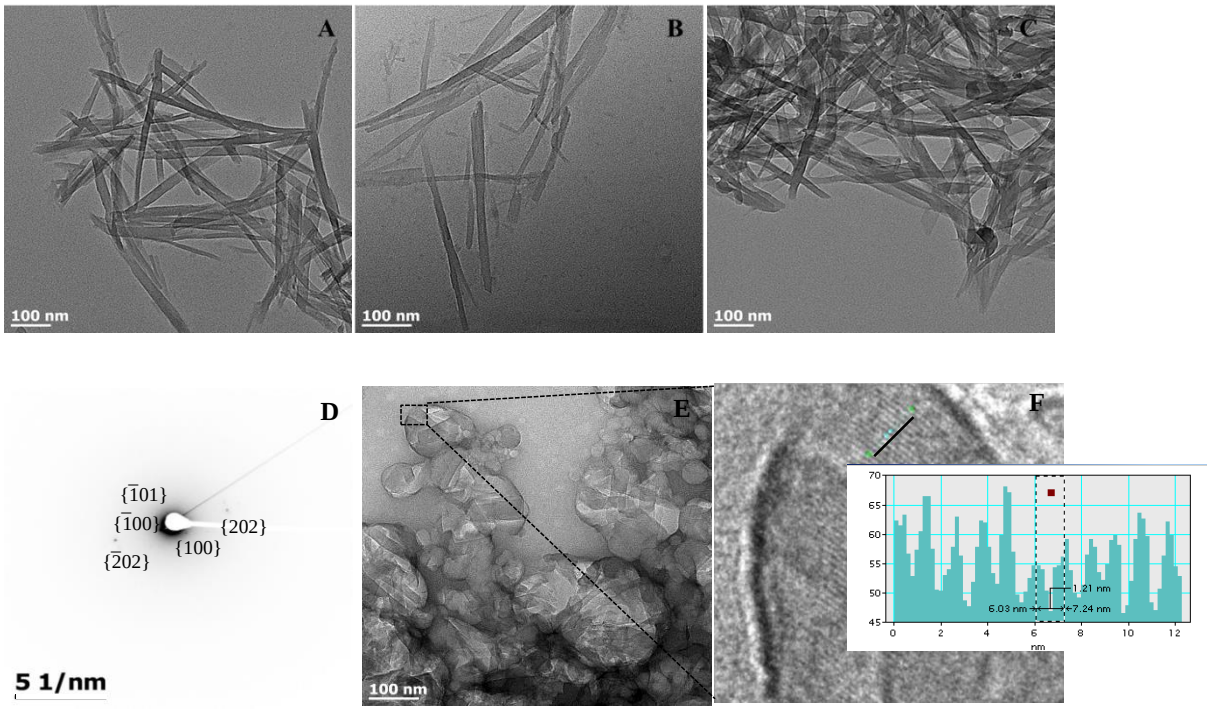

Figure 5.4. TEM imaging showed β-haematin crystals prepared by either micromixing (A) or ultrasonication (B) of MPG and Fe(III)PPIX are large and similar to Hz in external crystal morphology. TEM-ED of these crystals (C) showed that they lay on the principal {100} face (D) which is normal to *b**. Most of the β-haematin crystals formed remained in contact with lipid droplets (E) and lattice fringes with d-spacing of 12.1 Å showing the{100} or {$\bar{1}$00} of the crystal face was in contact with lipid (F).

TEM imaging showed β-haematin crystals formed from NLB and Fe(III)PPIX solution after vortexing have regular shapes and are somewhat bigger than those formed with vortexed mixtures of MPG and Fe(III)PPIX (Figure 5.5A). These marginally bigger β-haematin crystals were in the range 37-226 nm and 75 nm long on average (Figure 5.5C). The β-haematin crystals prepared using this method of vortexing generally had a different external morphology from Hz, from β-haematin prepared at the pentanol-water interface and even those formed from micromixing the NLB and Fe(III)PPIX mixture. However, unlike those formed with MPG, indexed TEM-ED patterns of these crystals gave bright spots corresponding to higher Miller indices with a clearly visible major crystallographic c-axis (Figure 5.5B) as indicated by the c* axis direction on the diffraction pattern. The {005} spot

represents diffraction from the c-axis ({001} face) at a higher-order reflection. Clearly visible lattice fringes from the crystal in Figure 5.5D with measured interplane distances of 2.87 Å (Figure 5.5E) correspond to the $\{\bar{3}\ \bar{3}\ 0\}$ face, a higher order reflection from the $\{\bar{1}\ \bar{1}0\}$ crystal face. The formation of the $\{\bar{1}\ \bar{1}0\}$ face of β-haematin seen with NLB is in accordance with the attachement energy (E_{att} = -52.6 kcal/mol) of this crystal face which is lower than E_{att} = -30.6 and E_{att} = -27.7 kcal/mol of {100} and {010} face respectively as predicted by Buller et al. (2002). The E_{att} of any crystal face controls the crystal growth rate perpendicular to that face and the more negative the E_{att} the less important that face is in the overall crystal morphology. The {001} face with very low E_{att} of -101.5 is the most important growing face of Hz but is not readily seen in the Hz crystal habit and form. It is reported to be the site to which CQ binds to exhibit its haemozoin-inhibiting antimalarial activity (Solomonov et al. 2007).

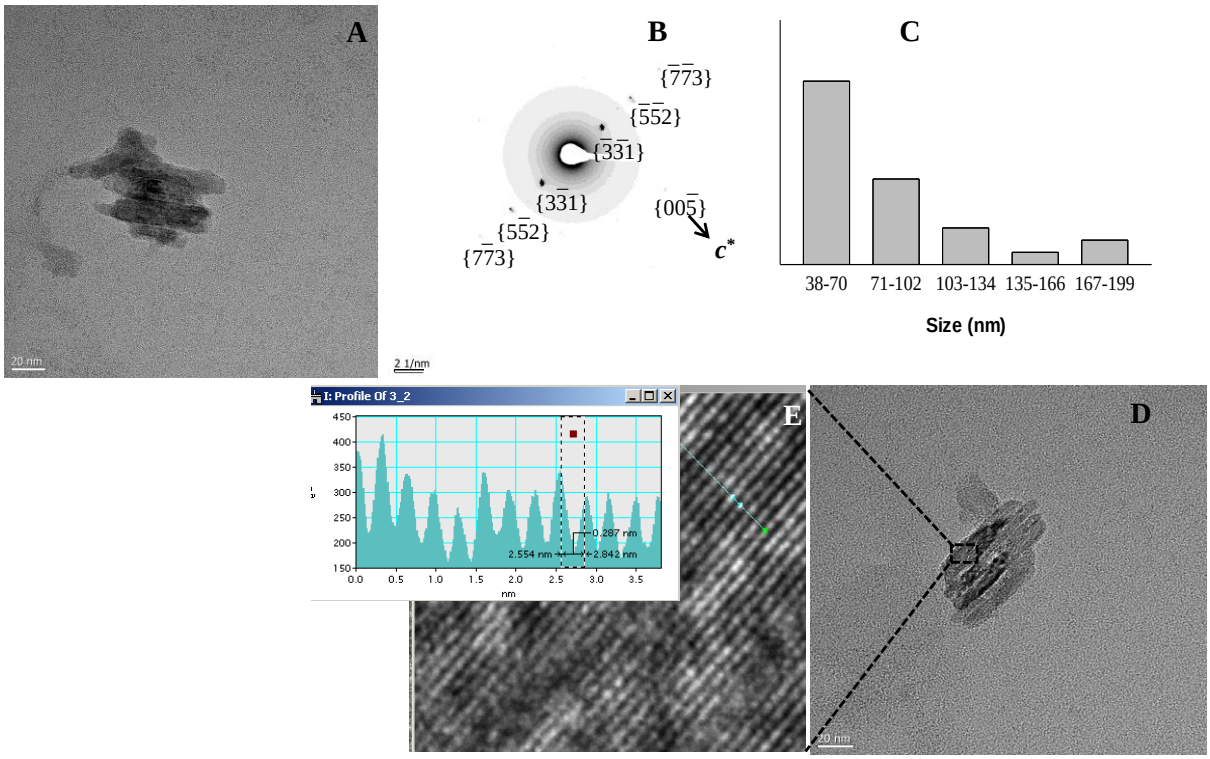

Figure 5.5. TEM imaging showed β-haematin crystals produced by vortexing a mixture of NLB and Fe(III)PPIX solution prior to deposition were smaller (A and D) than Hz although slightly larger than those produced with MPG using the same method. Indexed TEM-ED of these crystals showed it lay on an unusual $\{\bar{1}\ \bar{1}\ 0\}$ face (B) not seen with Hz or β-haematin formed at pentanol-water interface with lattice spacing of 2.87 Å corresponding to $\{\bar{3}\ \bar{3}\ 0\}$ Miller indices which represent higher order diffraction from the {110} face (E). Size range distribution of these crystals mostly lay between 38-70 nm (C).

Looking at the very small crystals formed in Figure 5.3 and 5.5 together with polycrystalline and mosaic material where lipid and Fe(III)PPIX solutions were vortexed prior to depositing on the citrate buffer surface, it was not clear whether these crystals seen here were essentially trapped on the pathway from an amorphous precursor to larger crystalline structures. However, several previous reports have suggested that this is probably not the case. Firstly, Egan et al. (2001) readily observed the conversion of β-haematin formed at 60°C in 4.5 M acetate medium from an amorphous glass-like solid which did not exhibit X-ray diffraction peaks, to a microcrystalline solid with a β-haematin X-ray diffraction pattern. This kind of amorphous structure was not evident in any of the images seen in this study although it could be difficult to observe, especially in the presence of lipid. Secondly, the existence of such a precursor (if it does exist) must be very short-lived because kinetic studies in the previous chapter using MPG under conditions where the reaction was slowed down about seven-fold (at 0.54 L/H) exhibited evidence of β-haematin fluorescence within 10 min. This fluorescence had been shown to arise from an excitation process specific to the β-haematin crystal lattice (Bellemare et al. 2009). This would translate into appearance of crystals within about 90 s of initiation of the process in this study. This rapid rate seems not to be consistent with the deposition of an amorphous phase and subsequent conversion to the crystalline product. Thirdly, the small crystals seen in Figures 5.3 and 5.5 were not seen in TEM images where premixing of lipid and Fe(III)PPIX was thoroughly carried out. However, it is also likely that they may not easily be noticed in the presence of many larger crystals or they may have all grown larger by the time of measurement.

β-Haematin crystals produced by either micromixing NLB and Fe(III)PPIX solution using an extruder (Figure 5.6A) or by sonication (Figure 5.6B), were identical to one another. The β-haematin crystals produced were much longer than those produced from a vortexed mixture of NLB and Fe(III)PPIX solution and were almost indistinguishable from β-haematin produced by either micromixing or sonication of MPG with Fe(III)PPIX solution. Indexed TEM-ED patterns obtained from some of the crystals in Figure 5.6C showed similar orientation to those produced at the pentanol-water interface and Hz as they also lay on their {100} or $\{\bar{1}00\}$ faces (Figure 5.6D). Most of the β-haematin crystals were found associated with visible NLB droplets (Figure 5.6E). The d-spacing of lattice fringes of the crystal face directly in contact with NLB lipid droplets was 11.8 Å (Figure 5.6F), corresponding to the {100} or $\{\bar{1}00\}$ faces of β-haematin crystals which again demonstrates that the growing β-haematin crystal was in contact with the lipid via this face. This is in agreement with earlier

reports by Hoang et al. that the NLB surface acts as a template for the growth of β-haematin crystals based on a suggestion that was previously made on the basis of findings obtained with self-assembled monolayers (de Villiers et al. 2009 and Wang et al. 2010) but was not directly demonstrated with lipid droplets. Furthermore, reports in other organisms where lipid has been shown to mediate nucleation of biocrystals showed that lipids can act by providing a suitable nucleation microenvironment favourable for electrostatic, sterochemical and geometric interactions between the nucleating crystal phase and the organic matrix (Young et al. 1992 and Collier et al. 2001). This suggests that NLB consistently seen in contact with β-haematin via its {100} face acts as a nucleation site, inducing the nucleation via this {100} face.

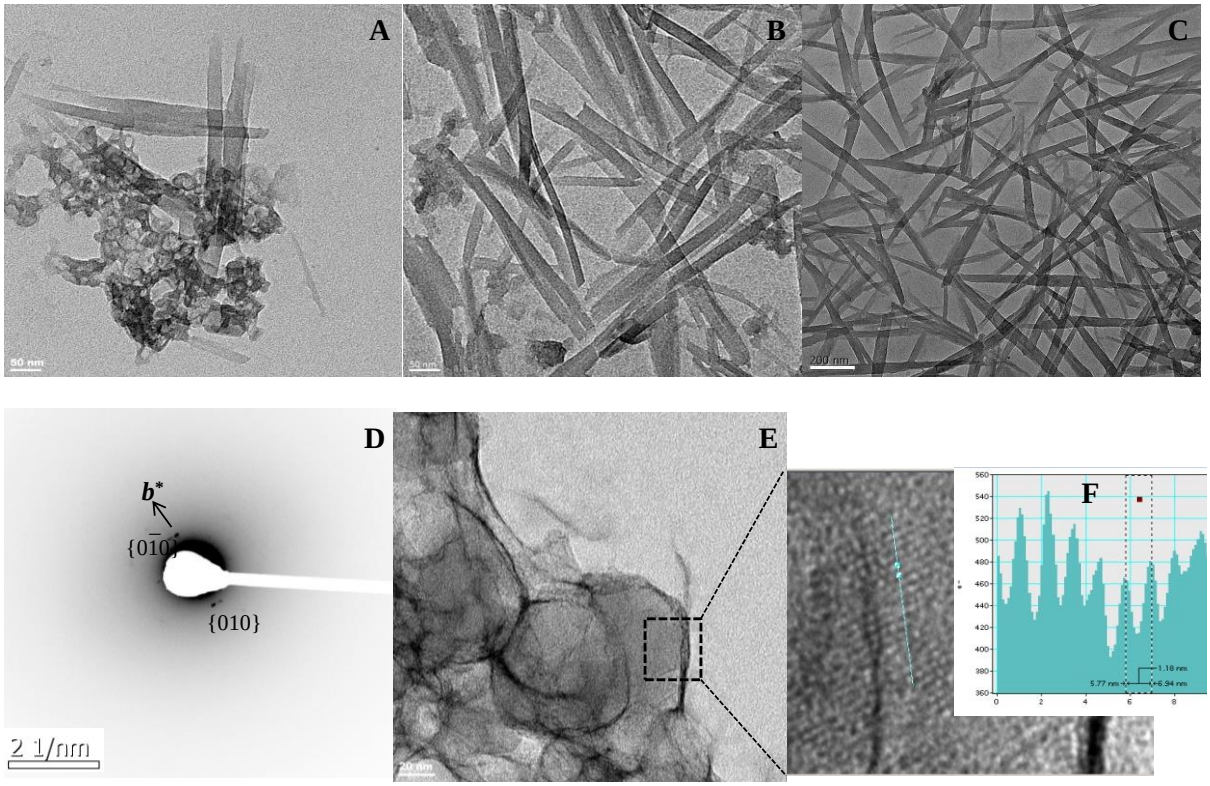

Figure 5.6. Characterization by TEM of β-haematin crystals produced using different methods of mixing NLB and Fe(III)PPIX solutions. TEM imaging showed β-haematin crystals prepared by either micromixing (A) or sonication (B) of NLB and Fe(III)PPIX solutions were longer and similar to those produced by MPG using the same method and also to Hz in external crystal morphology. Indexed TEM-ED of these crystals (C) showed the principal crystallographic b-axis indicated by *b** (D) which is normal to the {100} face. As with MPG crystals produced using the same method, most of the β-haematin crystals formed were also in contact with lipid droplets (E) and lattice fringes with d-spacing of 11.8 Å corresponding to the {100} or {$\bar{1}$00} of the crystal face in contact with lipid (F) were observed. This showed again that β-haematin made contact with lipid droplet via its {100} face.

It is therefore evident that mixing is an important factor that controls the overall crystal habit and form of β-haematin produced from lipids and Fe(III)PPIX since β-haematin crystals similar to Hz formed in the parasite can only be produced by thoroughly micromixing the two solutions of lipid (NLB or MPG) and Fe(III)PPIX either by using an extruder or by ultrasonication prior to deposition on aqueous citrate. This was a surprising factor as lipid and Fe(III)PPIX solution were expected to mix thoroughly with each other since they were both fully dissolved in the same 1:9 v/v acetone/methanol solvent. However, a possible explanation for this mixing effect may be that Fe(III)PPIX which bears a 2– charge when dissolved in 0.1 M NaOH, may form in a transient colloidal suspension when mixed with 1:9 v/v acetone/methanol which therefore requires thorough mixing with the lipid solution in order to bring Fe(III)PPIX into intimate contact with the lipid molecules. It has also been reported that the crystal habit exhibited by crystals grown in the presence of different solvents is strongly influenced by the solvent as a result of its interaction with the growing crystal surface (Bennema et al. 1992 and Elwenspoek et al. 1987). However, this does not appear to be the case here. Pentanol, acetone and methanol used in preparing β-haematin in this study appeared not to affect the crystal habit since the external morphology of the crystals produced were similar to that of Hz. Nonetheless, visual observation of Hz crystals from TEM images showed they appeared to be slightly different in texture compared to their synthetic counterparts. This might be due to the presence of lipids or proteins on the Hz crystal surface and in the crystal matrix as demonstrated by proteomic studies of the Hz crystals since previous studies of other biocrystals have reported clear evidence of the direct effect of proteins isolated from the biocrystals on the crystal texture (Berman et al. 1990 and 19993) and coherence length (Weissbuch et al. 1995). Finally, given the presence of NLB on the surface of Hz crystals in the DV and its proposed involvement in Hz formation *in vivo* as shown with lipidomics and *in vitro* kinetic studies, in addition to TEM characterization confirming NLB to produce synthetic Hz crystals similar to natural Hz when properly mixed with Fe(III)PPIX solutions, NLB was chosen for all further studies.

5.3.4 Effect of NLB-to-Fe(III)PPIX ratio on the appearance of β-haematin crystal formed at the lipid-water interface

It was also important to investigate how different amounts of lipid and Fe(III)PPIX present at the crystallization site at a particular time would affect the external appearance of the crystals formed. TEM images of β-haematin formed with NLB and Fe(III)PPIX at 2.15, 1.07 and 0.54

L/H showed no significant change in the overall crystal appearance. Thus, the crystal habit does not depend either on the ratio of L/H present or on the kinetics of the crystal growth process (Figure 5.7). This was important as it suggests that the shape of Hz crystals formed inside the parasite is unlikely to be affected by the amount of Fe(III)PPIX released from digested haemoglobin at the site where Hz crystal growth takes place. This phenomenon of the overall crystal shape not being affected by the amount of Fe(III)PPIX present or by kinetics of the crystal growth process can also be exploited to investigate the effect of some antimalarial drugs on Hz crystal growth *in vivo*, as any change in crystal morphology resulting from such treatment would be likely to be a direct effect or action of the antimalarial drug on the Hz crystallization process.

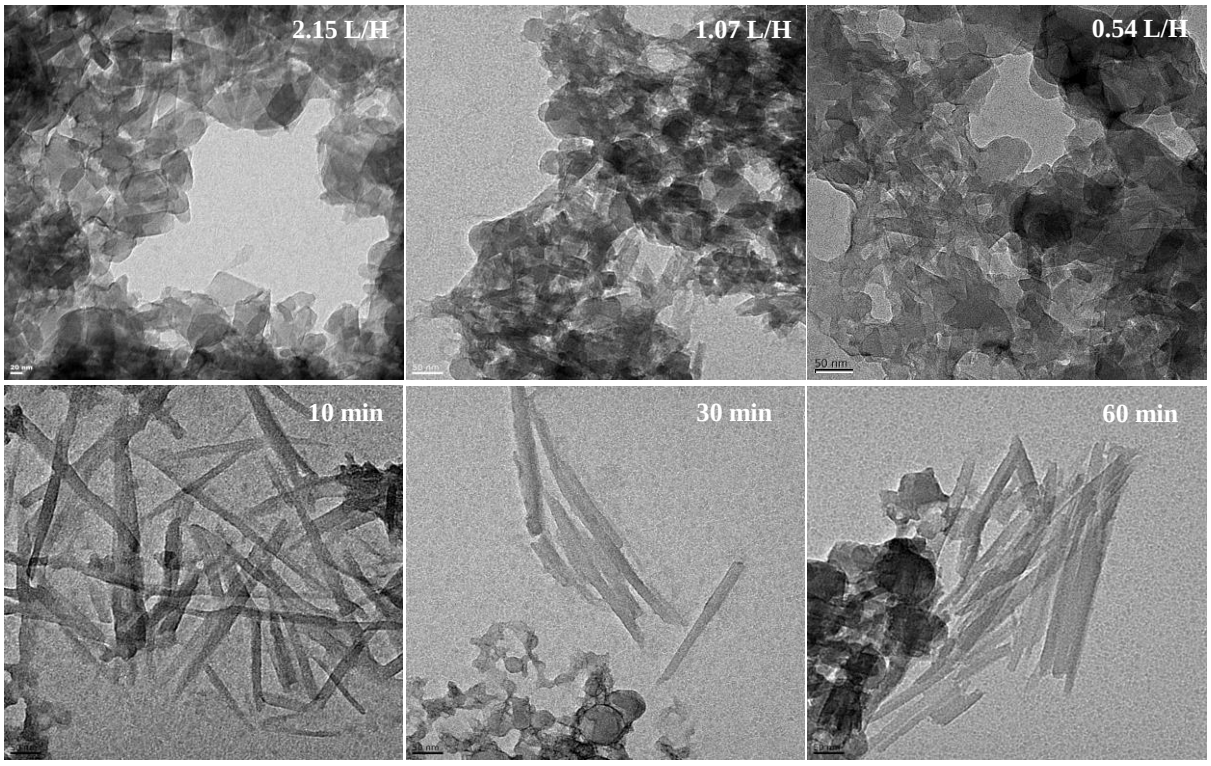

Figure 5.7. TEM characterization of β-haemtin crystal morphology formed at different lipid-to-Fe(III)PPIX mol ratios. TEM imaging of β-haematin crystals formed with NLB and Fe(III)PPIX at 2.15, 1.07 and 0.54 L/H showed no change in overal appearance of either the smaller or bigger crystals formed, despite changes in the amount of Fe(III)PPIX present and different incubation time points.

5.3.5 Characterization of the sizes and structures of NLB droplets formed at the lipid-water interface

Since the observed size range distribution of β-haematin crystals formed from vortexing MPG lipid with Fe(III)PPIX was similar to the major population of lipid droplets previously reported by Hoang et al. it was decided to investigate the sizes and structures of lipid droplets formed at the lipid-water interface to see how they compare to the sizes of β-haematin

produced at this inteface by the method of micromixing. Lipid droplets formed at the interface as during the β-haematin formation process were investigated at 10, 30 and 60 min incubation time using TEM. TEM images showed an increase in the population of small particle sized lipid droplets with increase in incubation time from 10 to 60 min (Figure 5.8). The measured diameter of the lipid droplets formed (assuming lipid droplets are spherical) at this interface showed the majority of them to be in the range 21-120 nm as shown in the population size distribution plot in Figure 5.8D. These smaller droplets may possibly be formed as a result of aggregation of even smaller droplets which could not be resolved in TEM images taken at earlier times, or more likely from dispersed lipid molecules which took a longer time to aggregate. Whatever the case, it is evident that these smaller droplets came to dominate the emulsion over time. However, since they appeared to form more slowly than β-haematin, they seemingly play little or no role in β-haematin formation.

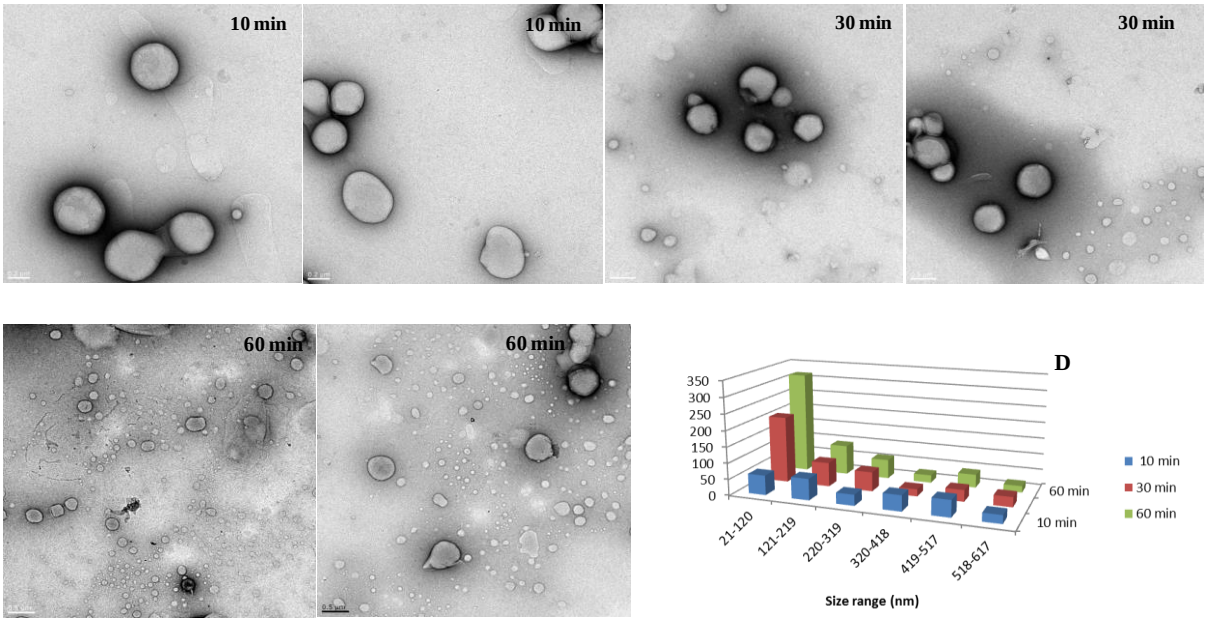

Figure 5.8: TEM characterization of NLB droplet sizes formed at the NLB-water interface. TEM imaging showed the population of smaller NLB droplets formed increases with increased in incubation time from 10 to 60 min. Scale bar represents 0.2 µm at 10 min and 0.5 µm at 30 and 60 min.

To investigate the nature and structure of NLB droplets formed, NLB solution stained with DiO dye and deposited on citric acid buffer was carefully taken from the NLB-water emulsion region for florescence imaging using confocal laser microscopy. Continuous z-stack images taken through NLB droplets using confocal microscopy showed continuous fluorescence right through the interior of the NLB droplets as shown in the resultant z-stacked image in Figure 5.9A. This showed that the interior portion of the lipid droplets

formed was hydrophobic. This is in agreement with previous studies which showed orthogonal projections of spontaneously formed NLB droplets stained with Nile Red (lipophilic dye) had a hydrophobic non-hollow and continuous interior (Hoang et al. 2010b).

Further characterization using TEM of NLB droplets prepared in the presence of aqueous CsCl was done. TEM images showed the interior portion of NLB droplets to have low electron density (Figure 5.9B and C) while liposomes prepared in the presence of aqueous CsCl (to serve as control structures) showed the inside of the vesicle to be darker. The dark area means it is electron dense thereby indicating the presence of aqueous Cs^+ as expected. Multilamellar (MLV), small unilamellar (SUV) and large unilamellar (LUV) vesicle structures could also be seen from the liposome preparation by TEM (Figure 5.9D and E); meanwhile, no such structure was seen with NLB droplets formed at the interface. Cryo-TEM of the liposome preparation clearly confirmed the presence these structures in suspension (Figure 5.9F).

ESI/EELS analysis of Cs^+ distribution in NLB and liposome structures showed Cs^+ was present inside the liposome vesicle (Figure 5.9H) as expected and completely absent inside NLB (Figure 5.9G). In summary, these studies unequivocally demonstrated that NLB droplets consist of lipid throughout their interiors which are non-hollow and hydrophobic.

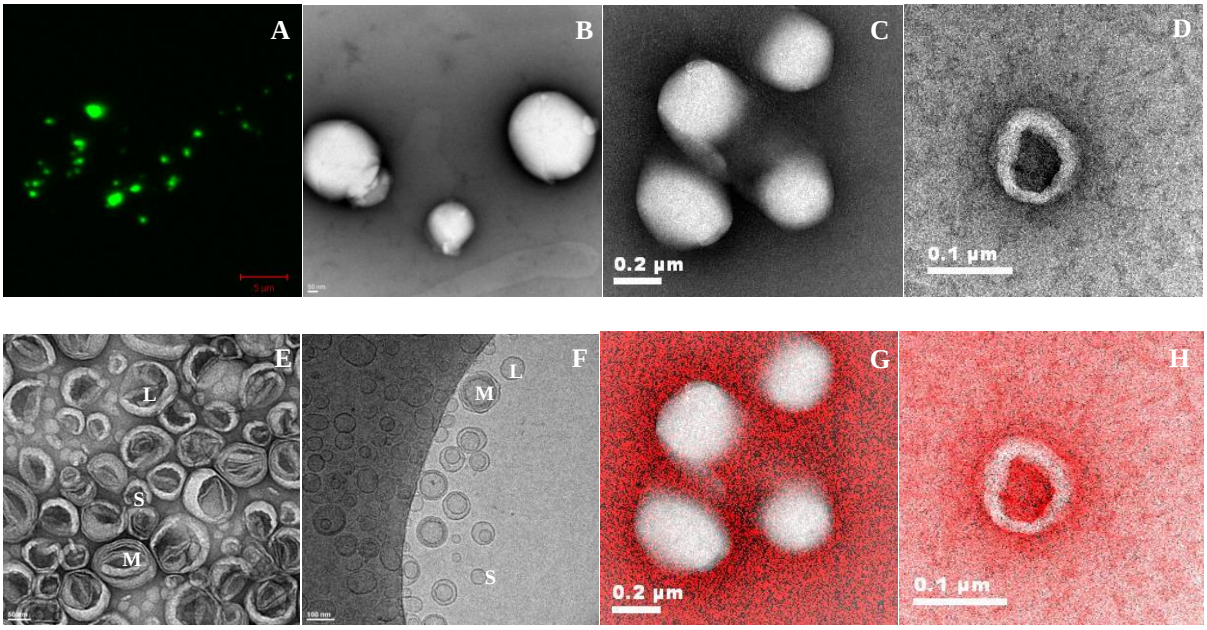

Figure 5.9: Confocal laser microscopy of Z-stacked images of DiO stained NLB droplets shows fluorescence right through the interior part of lipid droplets (A). TEM imaging showed aqueous Cs-treated NLB droplets to have a clear whitish interior (B and C) while liposome structures had a darker interior (D and E) and showed the presence of multilamellar (M), small unilamellar (S) and large unilamellar (L) structures formed which was confirmed using cryo-TEM imaging (F) while no such structures were seen with NLB. ESI/EELS analysis showed the interior of NLB to be devoid of Cs^+ (G) confirming it was completely hydrophobic while liposome structures were filled with aqueous Cs containing solution (H) indicating it was hydrophilic. This confirmed the lipid droplets have a non-hollow continuous hydrophobic interior.

5.3.6 Visualization of β-haematin crystals formed at NLB-water interface

Samples carefully collected from the NLB-water emulsion during the β-haematin formation process at different incubation time points of 10, 30 and 60 min were visualized using the TECNAI TF20 TEM. Interestingly, small crystalline structures (β-haematin) were consistently seen in association with lipid droplets (Figure 5.10A and B) and this was the case with all the products at the different incubation time points. In addition, a few longer crystals were seen not directly associated with NLB droplets (Figure 5.10C) but which may have grown from lipid-associated crystals. ESI/EELS analyzes of iron distribution in these images of products formed at the NLB-water interface (Figure 5.10B) confirmed these crystalline structures associated with NLB droplets corresponded to β-haematin (Figure 5.10D). Looking at some of the TEM images, it was difficult to tell the precise location of β-haematin crystals with respect to NLB droplets. However, close inspection of these associated structures showed clearly that β-haematin lay on the surface of NLB as seen in Figure 5.10E, F and G. Extruded NLB and Fe(III)PPIX in citric acid buffer unequivocally confirmed the growing β-haematin crystal to lie on the surface of lipid droplet (Figure 5.10H). Another striking observation was that the population of these crystals produced appeared to match the sizes of

the lipid droplets they were associated with. The lattice fringes of crystals in association with lipid droplets has shown that it is it {100} or {$\bar{1}$00} face which is in contact with the lipid droplets (Figure 5.6F), an observation also made with droplets from MPG lipid (Figure 5.4F). The appearance of these β-haematin crystals associated with NLB droplets is very similar to that in *S. mansoni* where hemozoin crystals have also been reported to be associated with lipid droplets (Corrêa and Egan et al., 2007).

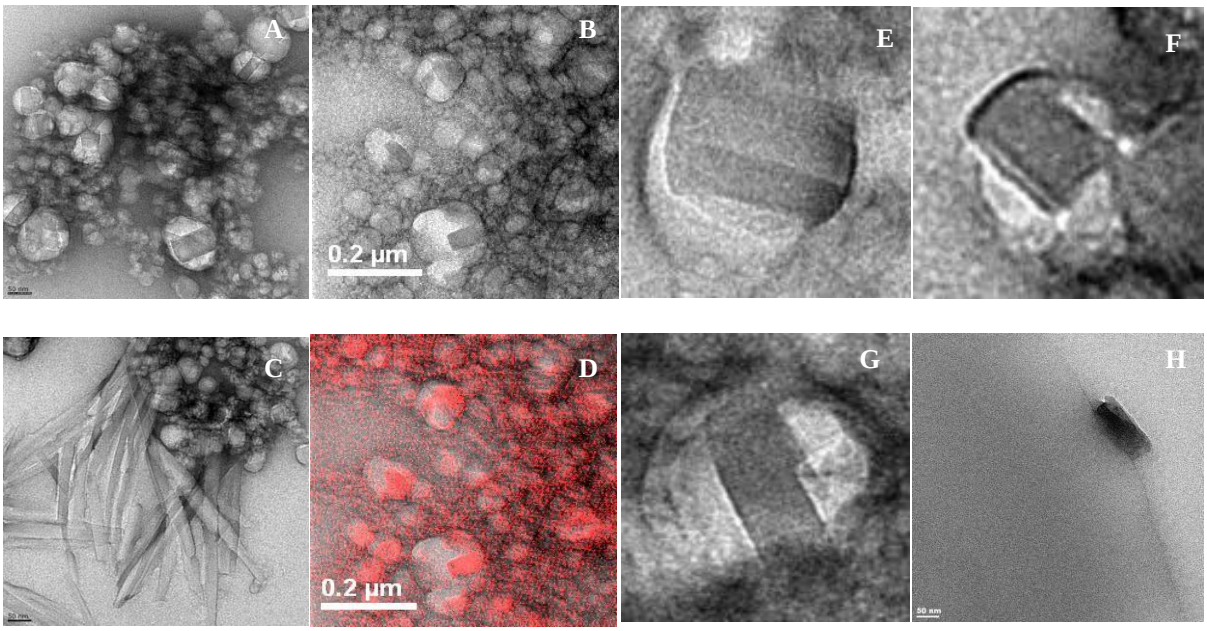

Figure 5.10: Visualization by TEM of β-haematin formed with NLB at the lipid-water interface.TEM imaging showed many crystalline structures to be associated with NLB droplets (A and B), which upon ESI/EELS analysis of iron distribution (D) confirmed clearly that they were iron containing. Some of the longer crystals were found already grown out from the lipid droplets (C). Careful examination of β-haematin crystals in contact with lipid droplets showed these crystals lie on the surface of the lipid droplets (E, F, G). TEM imaging of β-haematin prepared by extruding both NLB and Fe(III)PPIX together with citric acid buffer unequivocally confirmed the growing β-haematin crystal to be located on the surface of lipid droplet (H) at the lipid-water interface. Scale bar = 50 nm in A, C and H.

5.3.7 Relationship between size distribution of NLB droplets and β-haematin crystals formed at the NLB-water interface

The sizes of β-haematin crystals formed with NLB and that of NLB droplets were measured at different incubation times. Kinetic studies showed the reaction of β-haematin with NLB was completed within 10 min and so the relative numbers of β-haematin crystals and NLB particles formed at 10 min incubation time were examined. Their measured sizes were arranged into various size ranges as shown in Figure 5.11A and B. The distribution plot showed they both fell into similar size ranges with two distinct population maxima. The size distribution of NLB showed two maxima with one between 74-146 nm and the other between

366-438 nm representing a large population of small droplets and smaller population of larger NLB droplets respectively. The size distribution of β-haematin crystals also showed two maxima between 94-140 nm and between 188-234 nm representing a larger population of smaller β-haematin and smaller population of larger β-haematin crystals respectively. The average measured length of β-haematin crystals (206 nm) was found to be 0.62 times the average diameter of lipid particle droplets (331 nm). To check if there was any relationship between the sizes of both β-haematin crystals mediated by NLB and that of the NLB droplets themselves, a non-parametric Kolmogorov-Smirnov (K-S) test was conducted (Massey, 1951). This determines if the distribution of two populations are significantly different.

The null hypothesis (H_0) for this test was that the cumulative distribution of β-haematin crystal sizes are the same as that of 0.62 times diameter of NLB particle droplets, while the alternate hypothesis (H_A) was that their cumulative distributions are not the same at a given significance level. So H_0 is rejected if the inequality in Equation 2 holds, and vice versa.

$$\sqrt{\frac{nn'}{n+n'}} D_{nn'} > K_\alpha \text{ ---------- 2}$$

$$D_{nn'} = sup\left|F_{1,n}(x) - F_{2,n}(x')\right|$$

$D_{nn'}$ = absolute supremum difference between the cumulative distributions of the sizes of β-haematin and 0.62 times NLB diameter
K_α = critical value at a given confidence level α
n = number of β-haematin crystals measured
n' = number of lipid droplets measured
$F_{1,n}(x)$ = Empirical distribution function of β-haematin
$F_{2,n}(x')$ = Empirical distribution function of lipid droplets

Using an available free online version of K-S statistical analysis software (http://www.physics.csbsju.edu/stats/KS-test.n.plot_form.html), the computed $D_{nn'}$ obtained was 0.1124 (Figure 5.11C) giving a value for the left hand side (LHS) of Equation 2 of 1.28. The K_α on the right hand side (RHS) of Equation 2 was 1.36 at $\alpha = 0.05$. Thus, since the LHS was less than the RHS (1.28 versus 1.36), H_0 holds at the $\alpha = 0.05$ significance level which means that the distribution of β-haematin crystal sizes and lipid droplet diameters (× 0.62) was statistically indistinguishable at 10 min incubation time. However, the distributions of sizes between β-haematin crystals and NLB droplet diameters were found to be statistically different at 30 and 60 min incubation time. This may be due to the very large number of

small lipid droplets that appeared at these longer times which were not associated with smaller β-haematin crystals as can be seen in Figure 5.10A. However, this is not unexpected since the kinetic studies in Chapter 4 showed that the β-haematin formation process was completed with 10 min. Since these smaller droplets formed later (30 and 60 min) they could not contribute to the β-haematin formation process. Thus a size correlation would not be expected.

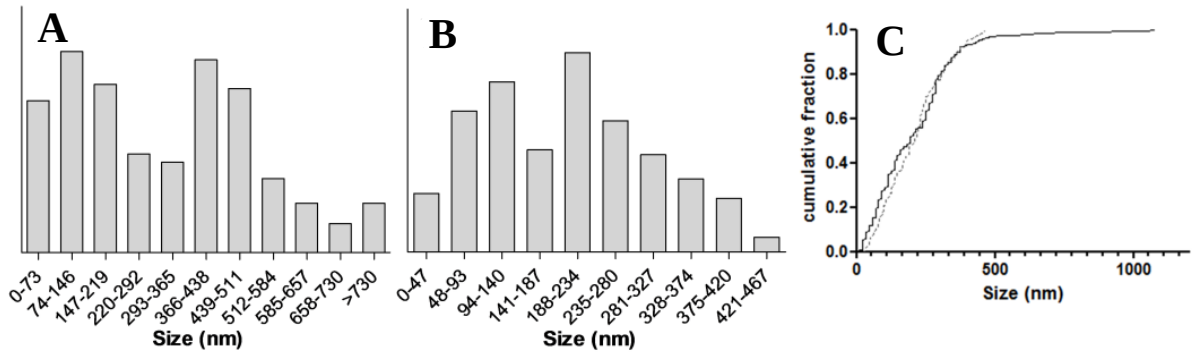

Figure 5.11: Plots showing the size distributions of NLB particles and β-haematin crystals. The plot showing the size range distribution of measured diameters of approximately 309 NLB particle droplets formed at the lipid-water interface at 10 min incubation time (A) showed larger populations of the droplets between 74-146 and 366-438 nm while a plot of the measured length of 223 β-haematin crystals formed at this lipid-water interface at 10 min incubation also showed maxima at 94-140 and 188-234 nm (B). The average length of β-haematin crystals was found to be 0.62 times the average diameter of lipid droplets and K-S statistical analysis of these two data sets, assuming β-haematin crystal grow to about 0.62 times the diameter of lipid droplet, showed there is no significant difference between these two data sets based on the cumulative size distribution of the lipid droplets normalized to 0.62 times their diameters (solid line) and that of β-haematin crystals (dotted line) (C) at $\alpha = 0.05$.

These findings suggest that β-haematin crystals grew to about 0.62 times the diameter of the lipid droplets, implying crystals at the lipid surfaces, which acts as a nucleator (Figure 5.12A), stop growing when the angle made between the growing crystal and lipid surface is 38° (Figure 5.12C). This is most probably because the surface tension exceeds the interaction between β-haematin and lipid droplets after this point and contact between the crystal and lipid can no longer be sustained, thereby preventing further growth as shown in the schematic representation in Figure 5.12B.

The strong correlation of the sizes of NLB droplets to that of β-haematin formed at NLB-water interface coupled with the location of β-haematin on the surface of lipid both *in vitro* (Figure 5.10E, F, G and H), and *in vivo* as seen in *S. mansoni* (Oliveira et al. 2005), convincingly suggest that the size of β-haematin/Hz crystals is controlled by the size of NLB

droplets. This is further supported by the evidence of extremely long β-haematin crystals formed at the flat continuous pentanol-water interface which offers no restriction or limit to β-haematin crystal growth length. However, β-haematin or Hz crystal growth in such an environment or compartment may also be limited by the growth inhibition effect of small amounts of the non-centrosymmetric isomer of μ-propionato dimer of Fe(III)PPIX present as was previously suggested (Buller et al. 2002).

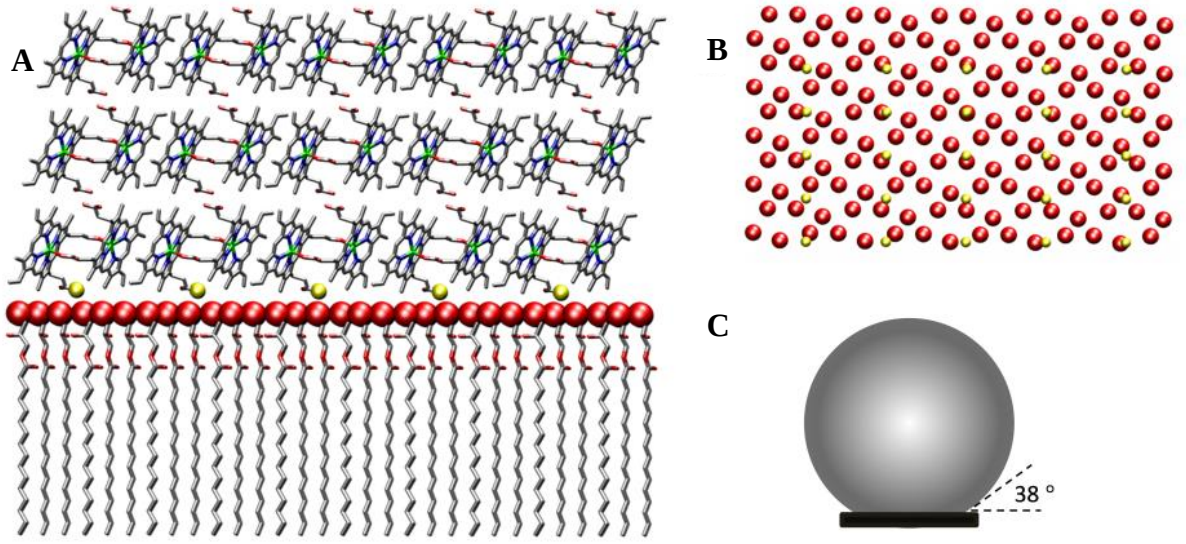

Figure 5.12. (A) A molecular graphics representation of nucleation and growth of the β-haematin at the surface of an MPG droplet. The MPG surface structure was based on the 2D unit cell of a monomyristoylglycerol (MMG) monolayer observed by de Villiers et al. (2009) at the air-water interface using grazing incidence x-ray diffraction and specular x-ray reflectivity. (B) shows the near match between positions of β-haematin propionic acid groups at the {100} surface of the crystal (rendered in gold) and every third glycerol –OH group of MPG (red). (C) shows the size of β-haematin crystals relative to lipid droplets as found in this study. The angle formed by β-haematin crystal with the surface of the droplet (assuming it is spherical) was 38° which is close to the angles observed in several TEM images such as in Figure 5.10H.

Lattice fringes and diffraction patterns of β-haematin crystals formed seen in association with both MPG and NLB droplets in Figures 5.4 and 5.6, respectively, showed that it makes contact with lipid via its prominent {100} or {$\bar{1}$00} faces. This observation, however, does not necessarily imply that the crystals nucleated from these faces or that they grew with these faces in contact with the lipid. Indeed, it is quite possible that the crystals could have nucleated from a different face and then subsequently interacted with the lipid on this face since this is the largest face in the crystal morphology. Even the match between crystal and lipid droplet sizes seen in Figures 5.6 and 5.10 could have arisen from lipid associating with these large crystal faces after formation of β-haematin. However, the observation that crystal lengths correlate with the diameters of lipid droplets formed independently of Fe(III)PPIX

(Figure 5.11) is difficult to explain unless one of the faces incorporating the long axis of the crystal ({100}, {$\bar{1}$00}, {010} or {0$\bar{1}$0}) was in contact with the lipid face during crystal growth. In view of the suitable complementary interaction between β-haematin propionic acid groups and glycerol head groups in Figure 5.12 as well as the previous observation of nucleation from the {100} face in the case of self-assembled monolayers (SAMs) with –OH head groups (de Villiers et al. 2009), it was suspected that this would more likely be the {100} face, although this still needs to be proven experimentally. This idea is consistent with the proposal that the neutral lipid surface acts as a template for the growth of β-haematin (de Villiers et al. 2009 and Hoang et al. 2010a), a suggestion that has been made previously on the basis of findings obtained with self-assembled monolayers (de Villiers et al. 2009, Solomonov et al. 2007 and Wang et al. 2010).

5.3.8 Haemozoin crystals imaged within the DV in *P. falciparum*

Malachite green, which is known to stain lipids in biological samples, was used to stain parasites during the fixation process for TEM imaging. Hz crystals seen by TEM seemed not to be associated with any visible stained lipid droplets inside the DV (Figure 5.13A, C and D) in contrast to what was clearly seen in the case of TEM images of β-haematin formed with NLB (Figure 5.10). Instead, the Hz crystals in the DV appeared to be aligned along the inner walls of the DV (Figure 5.13A and C), probably in association with the DV inner membrane. This observation is in agreement with recent reports by Kapishnikov et al. that showed with the use of 5.3D serial surface view microscopy and cryo-SEM smaller Hz crystals align with their {100} face along the inner membrane surface of DV which probably acts as the nucleation site of this crystal face. Some of the measured angles of the crystals marked * in Figure 5.12A and C are close to 120^{o} thereby indicating the crystal exposes it {100} as seen with β-haematin crystals formed with NLB. Measured inter-atomic distances of 12.6 Å and 12.37 Å in some of these crystals inside the DV (Figure 5.13B and E respectively), all corresponding to {100} or {$\bar{1}$00} faces, also confirmed that Hz crystals inside the parasite predominantly lie on their {100} or {$\bar{1}$00} faces in this image. The predominance of this crystal face in the morphology of Hz crystals aligned with the DV inner membrane surface in the parasite and also in β-haematin crystals in contact with lipid droplets at the lipid-water interface, suggest that the {100} face is actually the crystal face at which nucleation of Hz crystal growth occurs, as argued above.

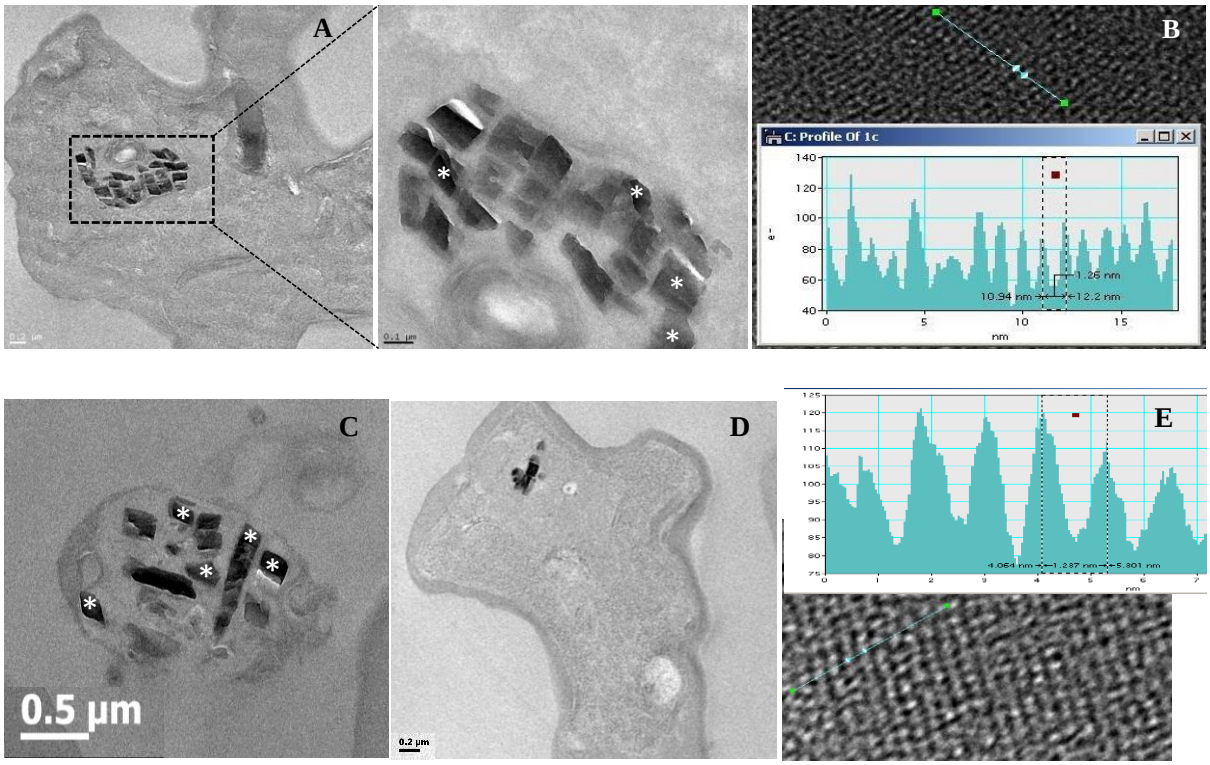

Figure 5.13: TEM imaging of Hz crystals inside the DV. Hz crystals appeard to align with the inner membrane surface of the DV (A and B) and d-spacing measurement of 12.6 Å (B) and 12.37 Å (E) for lattice fringes of some of these crystals inside parasite corresponding to the{100} or {$\bar{1}$00} faces showed this is the predominant face on which the crystals lie in the parasite.

5.3.9 The effect of the antimalarial drug chloroquine on Hz crystal growth *in vivo*

The β-haematin and Hz formation process has been shown to be the major target for many antimalarial drugs like CQ (Egan et al. 1994, Chou et al. 1980, Sullivan et al. 1996 and Sandlin et al. 2011). CQ has also been proposed to act by binding to the fastest growing {001} face of the theoretical growth form of β-haematin (Buller et al. 2002 and Solomonov et al. 2007). However, direct evidence of the effect of this drug on Hz crystal morphology *in vivo* has not been shown. TEM was therefore used to characterize Hz crystals isolated from parasites grown in the presence of 30 and 60 nM CQ at 32 h. Hz crystals isolated from 30 and 60 nM CQ-treated parasites showed significant decrease in the crystal length at 32 h with diffraction fringes exhibiting signs of growth defects at 60 nM (Figure 5.14A & B respectively) compared to a well-formed Hz crystals isolated from untreated parasites at 32 h (Figure 5.14C), exhibiting parallel straight lattice fringes (Figure 5.14F) with no signs of growth defects. The size of hemozoin crystals decreased from an average of 500 nm (untreated parasites) to about 250 nm and further down to 5 nm in the presence of 30 and 60 nM CQ concentrations respectively. The degree of crystal growth inhibition appeared to

increase with increase in the drug concentration (inhibition effect was concentration dependent).

It was also thought that the very tiny sizes of Hz isolated from parasite cultures grown in the presence of 60 nM CQ at 32 h might be similar to the sizes of Hz crystals at a very early stage of the parasite growth when the crystals just start growing. In this respect Hz crystals were also isolated from parasites grown in the absence of drug at 12 h (Figure 5.14D) and their lattice fringes were compared to those isolated from 60 nM CQ-treated parasites at 32 h. Interestingly, lattice fringes from 12 h parasites showed no defects in crystal growth (Figure 5.14E). Evidence in this study showed that besides the inhibition of Hz crystal growth by CQ, the crystal growth process is also affected as seen with lattice fringes exhibiting signs of growth defects. This unequivocally shows that CQ inhibits Hz crystal growth *in vivo* in a concentration-dependent manner.

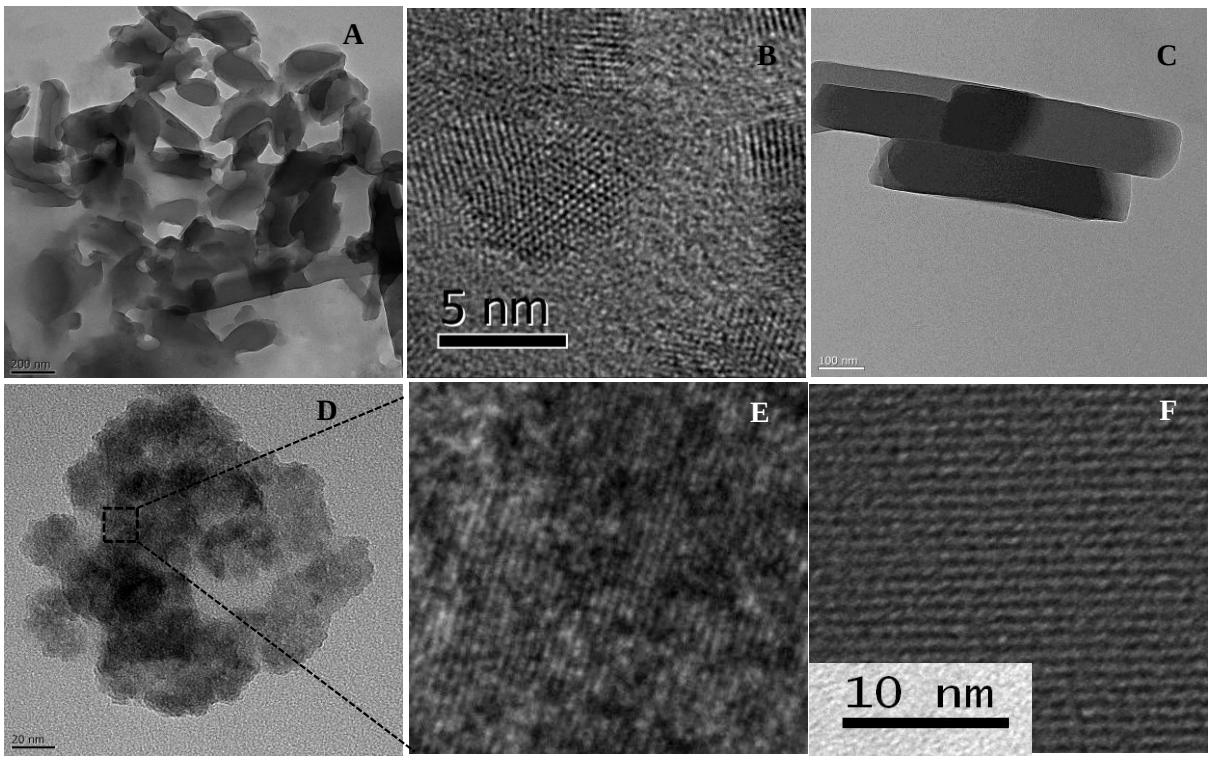

Figure 5.14: Effect of CQ on Hz crystal morphology. Hz isolated from parasite cultures grown in the presence of 30 (A) and 60 nM (B) CQ at 32 h caused a significant decrease in Hz crystal length from about 500 nm in untreated parasites (C) to about 250 and further down to 5 nm respectively. The sizes of Hz from 60 nM CQ treated parasite was superficially similar to Hz isolated from untreated parasites at 12 h (D); however, crystal lattice fringes from 60 nM treated parasites showed signs of growth defects while that of untreated parasites at 12 h (E) and 32 h (F) showed no defects in crystal growth.

5.4 CONCLUDING REMARKS

This study has shown that, under physiological conditions, MSG/MPG/DPG/DOG/DLG (NLB) lipids found associated with the surface of Hz crystals mediate the formation of β-haematin crystals which are identical in overall crystal habit and form to Hz crystals from the malaria parasite itself and also to β-haematin formed at the pentanol-water interface. The morphology of the β-haematin crystals formed with NLB was neither affected by the ratio of lipid-to-Fe(III)PPIX present at any given time nor by the kinetics of the crystal growth process, thus this may imply that the shape of Hz crystals formed *in vivo* might not be affected by either the amount of Fe(III)PPIX released into the crystallization compartment where crystal growth occurs or by the rate at which the Hz crystals grow. Nucleation of crystal growth mediated by lipids seems to occur via the prominent {100} face which is always seen in contact with the lipid droplet. It has also been demonstrated for the first time that the size of the lipid particle apparently controls the size of β-haematin crystals formed at short incubation times. The β-haematin crystals maintain contact with lipid particle until they stop growing when the angle of contact between them reaches 38^{o}. β-Haematin crystals have been shown to be located on the surface of lipid droplets which have a continuous non-hollow hydrophobic interior with no surrounding lipid bilayer membrane. NLB therefore acts as a nucleation site for β-haematin crystal growth by providing a suitable microenvironment for electrostatic, stereochemical and geometric complementarity between the lipid and nucleating {100} face of the growing crystal. Finally, CQ has been shown to unequivocally inhibit Hz crystal growth in a concentration-dependent manner in the parasite. This whole study points strongly to the nucleation of Hz crystals *in vivo* being aided by lipid and also gives new insight into the shape and sizes of the crystals formed during this process.

6. OVERALL CONCLUSIONS AND FUTURE WORK

6.1 OVERALL CONCLUSIONS

Malaria, a disease caused by a parasite belonging to the genus *Plasmodium*, affects about 3.3 billion people worldwide, the majority of whom live in Sub-Saharan Africa (WHO, 2011). *Plasmodium falciparum* is the most deadly species of this genus and pregnant women and children under the age of five are the most affected group. With little indication of a vaccine against malaria being developed in the near future, chemotherapy remains the most reliable method to successfully treat the disease. However, there is increasing evidence of resistance by parasites to many of the existing antimalarial drugs such as the artemisinin-based combination therapies (Alker et al. 2007 & Denis et al. 2006); therefore, there is an urgent need to development new antimalarial agents.

The biomineralization of Fe(III)PPIX into haemozoin (Hz) is a known target for many antimalarial drugs such as chloroquine (CQ), artesunate, amodiaquine, lumefantrine, mefloquine and quinine (Egan et al. 1994, Chou et al. 1980, Sullivan et al. 1996, Sandlin et al. 2011 & Combrinck et al. 2012). However, the widespread occurrence of parasitic resistance to this drug and other similar antimalarials means that many are no longer suitable for treating the disease. Therefore, elucidating the mechanism by which this biomineralization process occurs in the parasite would assist in the design and development of new antimalarial agents and could potentially identify new targets related to this process.

Proteins such as HDP (Jani et al. 2008) and HRPII (Sullivan et al. 1996) and lipids (Fitch et al. 1999 & Pisciotta et al. 2007) have been proposed to be responsible for this biomineralization process *in vivo*. However, evidence of the presence of any of these biomolecules interacting with the Hz crystal itself is lacking in contrast to what has been invariably shown with other biominerals (Alves et al. 2011, Mann et al. 2008, Arakaki et al. 2008, Marie et al. 2011, Nemoto et al. 2012 & Mann et al. 2006) where proteins are involved in the biomineralization process. In this current study, SDS-PAGE and LC-MS/MS used to study the proteome of the Hz crystal did not identify any of the proteins previously implicated in Hz crystal formation such as HDP and HRPII on either the Hz crystal surface or in the matrix proteome. Since about 40% of the *P. falciparum* genome is uncharacterized, it was also thought that by studying the proteome of the Hz crystal, new-uncharacterized putative proteins that could be implicated in the biomineralization process of Hz formation

could be identified. Surprisingly, no "stand-out" proteins that could be implicated in mediating this process were identified on either the Hz crystal surface or in the matrix proteome, even after using two different algorithms (MASCOT and X!Tandem) to interrogate both the *P. falciparum* and *H. sapiens* databank. On the other hand, the MSG/MPG/DPG/DOG/DLG blend (NLB) reported by Pisciotta et al. (2007) to be associated with Hz inside the parasite was easily identified associated with the surface of the Hz crystal. Lipids have been reported to be in an abundance 180 000-360 000 times greater than the detection limit of protein present in the Hz crystal. The absence, therefore, of any of the proteins previously implicated in Hz formation in the Hz crystal associated proteome coupled with the massive abundance of lipid over protein in the crystal shown in this study presumably points to lipids as the most likely biomolecules responsible for mediating the biomineralization of Hz formation *in vivo*.

The NLB identified associated with the Hz crystal surface in this study and some of its constituent lipids have previously been shown to efficiently mediate Hz formation *in vitro* (Picsiotta et al. 2007, Egan et al. 2006, Hoang et al. 2010a & Hoang et al. 2010b). However, information on the detailed kinetics of this process *in vitro* under conditions mimicking the DV is lacking. The effects of biologically-relevant ions on this process had not yet been investigated. Neither had the effects of Fe(III)PPIX and lipid concentrations on this process. This study has shown that NLB found associated with the surface of the Hz crystal is very efficient in mediating β-haematin formation giving a yield of about 90% and the reaction was completed in under 10 min at a NLB-to-Fe(III)PPIX mole ratio of about 1:1. The reaction rate only slowed down when there were about two molecules of Fe(III)PPIX to one molecule of the lipid fatty acid chain and still gave a high yield of about 90% in under 30 min. However, despite the decrease in reaction rates observed with a decrease in lipid concentrations, rates still remain adequate to account for Hz formation despite an overall drop in yields at physiologically-relevant lipid-to-Fe(III)PPIX ratios. The reaction rates of β-haematin formation with lipid were not greatly affected by the presence of physiologically-relevant ions. This seems to suggest that the process of Hz formation *in vivo* is greatly affected by lipid only and not by the presence of surrounding biological ions, if indeed the process is solely mediated by lipid as was suggested based on findings from proteomic and lipid studies of the Hz crystals in this current work. CLM measurement of autoflorescence arising from materials collected during the reaction process of β-haematin formation over time confirmed the formation of well-ordered crystalline β-haematin *in situ* in close

association with lipid emulsions. This method showed potential application to monitor β-haematin formation *in vitro*, Hz formation *in vivo* and the effects of antimalarial drugs that exploit this process as their target, in real time.

The average size of β-haematin crystals formed in the reaction mediated by NLB or MPG in this study appeared to be smaller than Hz *in vivo* and exhibited a different external morphology. The small size of β-haematin crystals formed with MPG fell in a similar range to that reported for NLB particles (Hoang et al. 2010a). However, detailed crystallographic characterization of the β-haematin crystals formed with NLB or MPG was not previously available. Neither was there any information on how the lipid droplet might influence the size of the crystals grown at the lipid-water interface and there was no clear evidence of the effect of CQ on the Hz formation process *in vivo*. This study explicitly showed by TEM and TEM-ED characterization that β-haematin produced under physiological conditions with the NLB found to be associated with the Hz surface is identical in overall crystal form and habit to that of Hz itself. Although there appears to be a minor difference in the texture of the two crystals, this may be due the presence of lipid and proteins present in the Hz crystal matrix as was clearly demonstrated in this study. The external morphology of the β-haematin formed was not affected by either a change in lipid-to-Fe(III)PPIX ratio or by the kinetics of the crystal growth process which may suggest that the morphology of the Hz crystal formed *in vivo* is not affected by the rate and amount of Fe(III)PPIX sequestered into the growing crystal inside the DV. This, again, is a very important finding as it may be exploited to investigate the direct effect of drugs on the morphology of the Hz crystal formed *in vivo* in the DV in the case of malaria parasites and also in other organisms such as *S. mansoni* (Oliveira et al. 2000), *H. columbae* (Chen et al. 2001) and *R. prolixus* (Oliveira et al. 1999) where Hz crystal formation is thought to be a lipid-mediated process. This is because any changes in the crystal morphology resulting from such treatment would be a direct effect of the drug on the Hz formation process. The β-haematin formed at lipid-water interface was consistently seen with its {100} face in contact with lipid droplets which were shown to have non-hollow lipid-filled interiors. Importantly, analysis of the distribution of sizes of independently-formed NLB droplets without Fe(III)PPIX (assuming droplets are spherical and their diameter normalized to 0.62 times that of the crystals) and that of β-haematin formed at the lipid-water interface at 10 min incubation time by the Kolmogorov-Smirnov test showed a very strong correlation between them. This suggest that the lipid droplets always seen in contact with the {100} face of crystals controls the size of the crystal grown at the lipid-water interface and

the crystal stops growing when the angle of contact made with the lipid droplet is 38^{o}. This major finding provides new insight into the role of lipid in Hz crystal formation. The consistent observations of lipid droplets in contact with the {100} face of β-haematin crystals, coupled with direct evidence that the lipid droplet controls the size of crystals grown, strongly suggest that lipid interacting with Fe(III)PPIX provides a suitable microenvironment for electrostatic, stereochemical and geometric complementarity between the lipid and the propionate group (nucleating face) of Fe(III)PPIX (as shown Figure 5.12) representing the {100} face for crystal growth. Thus, it is evident that the lipid nucleates the β-haematin crystal growth from its {100} face. Finally, this study unequivocally showed that CQ interferes with the Hz lattice in the cell.

6.2 FUTURE WORK

This study has shown that neither the proteins HDP or HRPII previously implicated in the biomineralization of Hz formation *in vivo* is present on the Hz crystal surface or matrix based on proteomic studies of the Hz crystal. In addition, no "stand-out" proteins were identified that could be implicated in the Hz crystal formation *in vivo*. However, lipids constituting the NLB found to be associated with the Hz crystal were proposed to be the most likely biomolecules responsible for Hz crystal formation. These lipids were shown to be very efficient in mediating β-haematin formation under biomimetic conditions similar to the DV and producing crystals that are identical in overall external morphology and form to that of Hz itself. Therefore, to completely support the hypothesis of this work that Hz formation *in vivo* is most likely to be purely a lipid-mediated process, further investigation needs to be done. In this regard, the following studies are proposed:

1. To use β-haematin produced from pentanol that has no associated lipid to pack a β-haematin column, run extract from the DV through the column followed by an SDS-PAGE gel to identify proteins which will possibly bind to β-haematin and therefore Hz.

2. To treat malaria parasites with drugs known to inhibit Hz formation, e.g. CQ, isolate the DV and, if possible, Hz to study their proteome to see if new proteins can be identified which are recruited during stress conditions to bind free haem.

3. To isolate Hz and treat the crystals with 1% (v/v) NaOCl at 4-6°C to completely destroy organic material located at the surface of Hz, leaving intact the intracrystalline proteins only. The crystals are then dissolved and run on an SDS-PAGE gel. The entire gel lane would be cut out for protein identification by LC-MS to detect only proteins found in the matrix for further characterization. This approach is commonly used to identify biomineral matrix proteins.

7. REFERENCES

Addadi, L. & Weiner, S. Biomineralization: A pavement of pearl. *Nature*. **1997**, 389, 912–915.

Addadi, L. & Weiner, S. Control and design principles in biological mineralization. *Angewandte Chemie-international Edition - ANGEW CHEM INT ED* . **1992**, 31, 153–169.

Allary, M., Schrevel, J. & Florent, I. Properties, Stage-Dependent Expression and Localization of *Plasmodium falciparum* M1 Family Zinc-Aminopeptidase. *Parasitology*. **2002**, 125, 1–10.

Alker, A. P., Lim, P., Sem, R., Shah, N. K., Yi, P., Bouth, D.M., Tsuyuoka, R., Maguire, J. D., Fandeur, T., Ariey, F., Wongsrichanalai, C. & Meshnick, S.R. Pfmdr1 and in vivo resistance to artesunate-mefloquine in falciparum malaria on the Cambodian-Thai border. *Am. J. Trop. Med. Hyg*. **2007**, 76, 641–647.

Alves, R. D., Demmers, J. A., Bezstarosti, K., van der Eerden, B. C., Verhaar, J. A., Eijken, M. & Van Leeuwen, J. P. Unraveling the Human Bone Microenvironment beyond the Classical Extracellular Matrix Proteins: A Human Bone Protein Library. *J. Proteome Res*. **2011**, 10, 4725–4733.

Anderson, H. C. Molecular biology of matrix vesicles. *Clin. Orthop. Rel. Res.* **1995**, 314, 266–280.

Arakaki, A., Nakazawa, H., Nemoto, M., Mori, T. & Matsunaga, T. Formation of magnetite by bacteria and its application. *J. R. Soc. Interface*. **2008**, 5, 977–999.

Banerjee, R., Liu, J., Beatty, W., Pelosof, L., Klemba, M. & Goldberg, D.E. Four plasmepsins are active in the *Plasmodium falciparum* food vacuole, including a protease with an active-site histidine. *Proc. Natl Acad. Sci. USA.* **2002**, 99, 990–995.

Bayoh, M. N. & Lindsay, S. W. Effect of temperature on the development of the aquatic stages of *Anopheles gambiae* sensu stricto (Diptera: Culicidae). *Bull. Entomol. Res.* **2003**. 93, 375–381.

Bellemare, M. J., Bohle, D.S., Brosseau, C. N., Georges, E., Godbout, M., Kelly, J., Leimanis, M. L., Leonelli, R., Olivier, M. & Smilkstein, M. Autofluorescence of condensed heme aggregates in malaria pigment and its synthetic equivalent hematin anhydride (beta-hematin). *J. Phys. Chem. B*. **2009**, 113, 8391–8401.

Bendrat, K., Berger, B.J. & Cerami, A. Haem polymerization in malaria. *Nature*. **1995**, 378, 138–139.

Bennema, P. Theory of growth and morphology applied to organic crystals; possible applications to protein crystals. *J. cryst. Growth*. **1992**, 122, 110–119

Bennema. P. & Gilmer. In crystal growth. An introduction, edited by P.Hartman. *Amsterdam: North-Holland*.**1973**, 272.

Berman, A., Addadi, L., Kvick, A., Leiserowitz, L., Nelson, M. & Weiner, S. Intercalation of sea urchin proteins in calcite: study of a crystalline composite material. *Science*. **1990**, 250, 664–667.

Berman, A., Hanson, J., Leiserowitz, L., Koetzle, T.F., Weiner, S. & Addadi, L. Biological control of crystal texture: a widespread strategy for adapting crystal properties to function. *Science*. **1993**, 259, 776–779.

Bohle, D. S., Dinnebier, R. E., Madsen, S. K. and Stephens, P. W. Characterization of the products of the heme detoxification pathway in malarial late trophozoites by x-ray diffraction. *J. Biol. Chem*. **1997**, 272, 713–716.

Bourne, J. R & Davey, R. J. Role of solvent-solute interactions in determining crystal-growth mechanisms from solution. 1. Surface entropy factor. *J. Cryst. Growth*. **1976**, 36, 278–286.

Brown, W. Malarial pigment (so-called melanin): Its nature and mode of production. *J. Exp. Med*. **1911**, 13, 290–299.

Buller, R., Peterson, M. L., Almarsson, O. & Leiserowitz, L. Quinoline Binding Site on Malaria Pigment Crystal: A Rational Pathway for Antimalaria Drug Design. *Cryst. Growth Des.* **2002**, 2, 553–562.

Carbone, T. About the chemical nature of malaria pigment. *Giornale della Regia Accademia di Medicina di Torino*. **1891**, 39, 901–906.

Carlton, J. M., Angiuoli, S.V., Suh, B. B., Kooij, T.W., Pertea, M., et al. Genome sequence and comparative analysis of the model rodent malaria parasite *Plasmodium yoelii yoelii*. *Nature*. **2002**, 419, 512–519.

Chen, M. M., Shi, L. and Sullivan, D. J. Haemoproteus and Schistosoma synthesize heme polymers similar to Plasmodium hemozoin and β-hematin. *Mol. Biochem. Parasitol*. **2001** 113, 1–8.

Chong, C. R., Sullivan, D. J. Jr. Inhibition of heme crystal growth by antimalarials and other compounds: implications for drug discovery. *Biochem. Pharmacol*. **2003**, 66, 2201–2212.

Chou, A. C. & Fitch, C. D. Heme polymerase: modulation by chloroquine treatment of a rodent malaria. *Life Sci.* **1992**, 51, 2073–2078.

Chou, A. C. and Fitch, C.D. Mechanism of hemolysis induced by ferriprotoporphyrin IX. *J. Clin. Invest.* **1981**, 68, 672–677.

Chou, A. C., Chevli, R. & Fitch, C. D. Ferriprotoporphyrin IX fulfills the criteria for identification as the chloroquine receptor of malaria parasites. *Biochemistry*. **1980**, 19, 1543–1549.

Chugh, M., Sundararaman, V., Kumar, S., Reddy, V.S., Siddiqui, W.A., Stuart, K.D. & Malhotra, P. Protein complex directs hemoglobin-to-hemozoin formation in *Plasmodium falciparum*. *Proc. Natl Acad. Sci. U S A.* **2013**, 110, 5392–5397.

Collier, J. H & Messersmith, P. B. Phospholipid strategies in biomineralization and biomaterials research. *Annu. Rev. Mater. Res*. **2001**, 31, 237–63.

Collins, W. E. *Plasmodium knowlesi*: a malaria parasite of monkeys and humans. *Annu. Rev. Entomol*. **2012**. 57, 107–121.

Combrinck, J. M., Mabotha, T. E., Ncokazi, K. K., Ambele, M. A., Taylor, D., Smith, P. J., Hoppe, H. C. and Egan, T. J. *ACS Chem. Biol.* **2013**, 8, 133.

Cook, L. B., Zhu, C. C. & Hinkle, P. M. Thyrotropin-releasing hormone receptor processing: role of ubiquitination and proteasomal degradation**.** *Mol. Endocrinol*. **2003**, 17, 1777–1791.

Corrêa Soares, J. B., Maya-Monteiro, C. M., Bittencourt-Cunha, P. R., Atella, G. C., Lara, F. A., d'Avila, J. C., Menezes, D., Vannier-Santos, M. A., Oliveira, P. L., Egan, T. J. & Oliveira, M. F. Extracellular lipid droplets promote hemozoin crystallization in the gut of the blood fluke *Schistosoma mansoni*. *FEBS Lett*. **2007**, 581, 1742–1750.

CrystalMaker® version 2.2; CrystalMaker Software Ltd.; Oxford, England, **2009**.

Dahl, E. L., Rosenthal, P. J., Biosynthesis. Localization and processing of falcipain cysteine proteases of *Plasmodium falciparum*. *Mol. Biochem. Parasitol*. **2005**,139, 205–212.

Dalal, S. & Klemba, M. Roles for Two Aminopeptidases in Vacuolar Hemoglobin Catabolism in *Plasmodium falciparum*. *J. Biol. Chem*. **2007**, 282, 35978–35987.

Dame, J. B., Yowell, C. A., Omara-Opyene, L., Carlton, J. M., Cooper, R.A. & Li, T. Plasmepsin 4, the food vacuole aspartic proteinase found in all *Plasmodium spp*.infecting man. *Mol. Biochem.Parasitol*. **2003**, 130, 1–12.

Davies M. J. Detection of peroxyl and alkoxyl radicals produced by reaction of hydroperoxides with heme-proteins by electron spin resonance spectroscopy. *Biochim Biophys Acta*. **1988**, 964, 28-35

de Villiers, K. A., Osipova, M., Mabotha, T. E., Solomonov, I., Feldman, Y., Kjaer, K., Weissbuch, I., Egan, T. J. and Leiserowitz, L. Oriented Nucleation ofβ-Hematin Crystals Induced at Various Interfaces: Relevance to Hemozoin Formation. *Cryst. Growth Des*. **2009**, 9, 626–632.

Denis, M. B., Tsuyuoka, R., Poravuth, Y., Narann, T. S., Seila, S., Lim, C., Incardona, S., Lim, P., Sem, R., Socheat, D., Christophel, E. M. & Ringwald, P. Surveillance of the efficacy of artesunate and mefloquine combination for the treatment of uncomplicated falciparum malaria in Cambodia. *Trop. Med. Int. Health*. **2006**, 11, 1360–1366.

Dorn, A., Stoffel, R., Matile, H., Bubendorf, A., Ridley, R.G. Malarial haemozoin/beta-haematin supports haem polymerization in the absence of protein. *Nature*. **1995**, 374, 269–271**.**

Dorn, A., Vippagunta, S. R., Matile, H., Jaquet, C., Vennerstrom, J. L., Ridley, R. G. An assessment of drug–haematin binding as a mechanism for inhibition of haematin polymerisation by quinoline antimalarials. *Biochem. Pharmacol*. **1998**, 55, 727–736.

Dua, M., Raphael, P., Sijwali, P. S., Rosenthal, P. J. & Hanspal, M. Recombinant falcipain-2 cleaves erythrocyte membrane ankyrin and protein 4.1. *Mol. Biochem. Parasitol*. **2001**, 116, 95–99.

Eckman, J. R., Modler, S., Eaton, J. W., Berger, E. & Engel, R. R. Host heme catabolism in drug-sensitive and drug- resistant malaria. *J. Lab. Clin. Med*. **1977**, 90, 767–70.

Egan, T. J. & Tshivhase, M. G. Kinetics of β-haematin formation from suspensions in aqueous benzoic acid. *Dalton Trans*. **2006**, 42, 5024–5032.

Egan, T. J. Recent advances in understanding the mechanism of hemozoin (malaria pigment) formation. *J. Inorg. Biochem*. **2008**, 102, 1288–1299.

Egan, T. J., Ross, D. C., and Adams, P. A. Quinoline antimalarial drugs inhibit spontaneous formation of b-haematin (malaria pigment). *FEBS Lett*. **1994**, 352, 54–57.

Egan, T.J. Interactions of quinoline antimalarials with hematin in solution. *J. Inorg. Biochem*. **2006**,100, 916–926.

Egan, T. J., Chen, J.Y-J., de Villiers, K. A., Mabotha, T. E., Naidoo, K. J., Ncokazi, K. K., Langford, S. J., McNaughton, D., Pandiancherri, S., Wood, B. R. Haemozoin (β-haematin) biomineralization occurs by self-assembly near the lipid/water interface. *FEBS Lett*. **2006**, 580, 5105–5110.

Egan, T. J., Combrinck, J. M., Egan, J., Hearne, G. R., Marques, H. M., Ntenteni, S., Sewell, B.T., Smith, P. J., Taylor, D., van Schalkwyk, D. A. and Walden, J. C. Fate of haem iron in the malaria parasite Plasmodium falciparum**.** *Biochem. J.* **2002**, 365, 343–347.

Egan, T. J., Mavuso, W. W. & Ncokazi, K. K. The mechanism of β-hematin formation in acetate solution. Parallels between hemozoin formation and biomineralization processes. *Biochemistry*. **2001**, 40, 204–13.

Elliott, D. A., McIntosh, M. T., Hosgood, H. D. 3rd., Chen, S., Zhang, G., Baevova, P. & Joiner, K. A. Four distinct pathways of hemoglobin uptake in the malaria parasite *Plasmodium falciparum*. *Proc. Natl Acad. Sci. USA.* **2008**, 105, 2463–8.

Elwenspoek. M., Bennema. P. & Van Eerden. J. P. Orientational order in naphthalene crystal-solution interfaces. *J. Cryst. Growth*. **1987**, 83, 297–305.

Famin, O. & Ginsburg, H. The treatment of *Plasmodium falciparum*-infected erythrocytes with chloroquine leads to accumulation of ferriprotoporphyrin IX bound to particular parasite proteins and to the inhibition of the parasite's 6-phosphogluconate dehydrogenase. *Parasite*. **2003**, 10, 39–50.

Fitch, C. D. & Kanjananggulpan, P. The state of ferriprotoporphyrin IX in malaria pigment. *J. Biol. Chem*. **1987**, 262, 15552–15555.

Fitch, C. D., Cai, G. Z., Chen, Y. F. & Shoemaker, J. D. Involvement of lipids in ferriprotoporphyrin IX polymerization in malaria. *Biochim. Biophys. Acta*. **1999**, 1454, 31–37.

Fontaine, A., Bourdon, S., Belghazi, M., Pophillat, M., Fourquet, P., Granjeaud, S., Torrentino-Madamet, M., Rogier, C., Fusai, T. & Almeras, L. *Plasmodium falciparum* infection-induced changes in erythrocyte membrane proteins. *Parasitol. Res*. **2012**, 110, 545–556.

Francis, S. E., Gluzman, I.Y., Oksman, A., Banerjee, D. & Goldberg, D. E. Characterization of native falcipain, an enzyme involved in *Plasmodium falciparum* hemoglobin degradation. *Mol. Biochem. Parasitol*. **1996**, 83, 189–200.

Francis, S. E., Gluzman, I.Y., Oksman, A., Knickerbocker, A., Mueller, R., Bryant, M. L., Sherman, D. R., Russell, D. G. & Goldberg, D. E. Molecular characterization and inhibition of a *Plasmodium falciparum* aspartic hemoglobinase. *EMBO J*. **1994**, 13, 306–317.

Francis, S. E., Sullivan, D. J. Jr.and Goldberg, D. E. Hemoglobin metabolism in the malaria parasite *Plasmodium falciparum. Annu. Rev. Microbiol*. **1997**, 51, 97–123.

Gavigan, C. S., Dalton, J. P. & Bell, A. The Role of Aminopeptidases in Haemoglobin Degradation *in Plasmodium falciparum*-Infected Erythrocytes. *Mol. Biochem. Parasitol*. **2001**, 117, 37–48.

Glenister, F. K., Coppel, R. L., Cowman, A. F., Mohandas, N. & Cooke, B. M. Contribution of parasite proteins to altered mechanical properties of malaria-infected red blood cells. *Blood*. **2002**, 99, 1060–1063.

Gluzman, I.Y., Francis, S. E., Oksman, A., Smith, C. E., Duffin, K. L. & Goldberg, D. E. Order and specificity of the *Plasmodium falciparum* hemoglobin degradation pathway. *J. Clin. Invest.* **1994**, 93, 1602–1608.

Goldberg, D. E. Hemoglobin Degradation in Plasmodium-Infected Red Blood Cells. *Semin. Cell Biol.* **1993**, 4, 355–361.

Goldberg, D. E., Slater, A. F., Cerami, A. & Henderson, G. B. Hemoglobin degradation in the malaria parasite *Plasmodium falciparum*: an ordered process in a unique organelle. *Proc. Natl Acad. Sci U S A.* **1990**, 87, 2931–2935.

Goldberg, D., Slater, A., Beavis, R., Chait, B., Cerami, A. & Henderson, G. Hemoglobin degradation in the human malaria pathogen *Plasmodium falciparum*: a catabolic pathway initiated by a specific aspartic protease. *J. Exp. Med*. **1991**, 173, 961–969.

Goldberg, D. E., Slater, A. F. G., Cerami, A. & Henderson, G. B. Hemoglobin degradation in the malaria parasite *Plasmodium falciparum*: An ordered process in a unique organelle. *Proc. Natl Acad. Sci. USA*. **1990**, 87, 2931–2935.

Gorka, A. P., de Dios, A. & Roepe, P. D. Quinoline Drug-Heme Interactions and Implications for Antimalarial Cytostatic versus Cytocidal Activities. *J. Med. Chem*. **2013**, 56, 5231–5246.

Gildenhuys, J., le Roex, T., Egan, T. J. & de Villiers, K. A. The single crystal X-ray structure of β-hematin DMSO solvate grown in the presence of chloroquine, a β-hematin growth-rate inhibitor. *J. Am. Chem. Soc*. **2013**, 135, 1037–1047.

Gouterman, M. In The Porphyrins: Physical Chemistry, Part A; Dolphin, D., Ed.; *Academic Press: New York*. **1978**, 3, 1–166.

Grembecka, J., Mucha, A., Cierpicki, T. & Kafarski, P. The Most Potent Organophosphorus Inhibitors of Leucine Aminopeptidase. Structure-Based Design, Chemistry, and Activity. *J. Med. Chem*. **2003**, 46, 2641–2655.

Hänscheid, T., Egan, T. J., Grobusch, M. P. Haemozoin: from melatonin pigment to drug target, diagnostic tool, and immune modulator. *Lancet Infect. Dis*. **2007**, 7, 675–685.

Hanspal, M., Dua, M., Takakuw, Y., Chishti, A. H. & Mizuno, A. *Plasmodium falciparum* cysteine protease falcipain-2 cleaves erythrocyte membrane skeletal proteins at late stages of parasite development. *Blood*. **2002**, 100, 1048–1054.

Hiller, N. L., Bhattacharjee, S., van Ooij, C., Liolios, K., Harrison, T., et al. A host-targeting signal in virulence proteins reveals a secretome in malarial infection. *Science*. **2004**, 306, 1934–1937.

Hoang, A. N., Ncokazi, K. K., de Villiers, K. A., Wright, D. W., Egan, T. J. Crystallization of synthetic haemozoin (β-haematin) nucleated at the surface of lipid particles. *Dalton Trans*. **2010**, 39:1235–1244.

Hoang, A. N., Sandlin, R. D., Omar, A., Egan, T. J. & Wright, D. W. The neutral lipid composition present in the digestive vacuole of Plasmodium falciparum concentrates heme and mediates β-hematin formation with an unusually low activation energy. *Biochemistry*. **2010**, 49, 10107–10116.

Huy, N. T., Uyen, D. T., Maeda, A., Trang, D. T. X., Oida, T., Harada, S. & Kamei, K. Simple colorimetric inhibition assay of heme crystallization for high throughput screening of antimalarial compounds. *Antimicrob. Agents Chemother*. **2007b**, 51, 350–353.

Huy, N. T., Maeda, A., Uyen, D. T., Trang, D. T., Sasai, M., Shiono, T., Oida. T., Harada, S. & Kamei, K. Alcohols induce beta-hematin formation via the dissociation of aggregated heme and reduction in interfacial tension of the solution. *Acta Trop*. **2007**, 101, 130–138.

Huy, N.T., Shima, Y., Maeda, A., Men, T.T., Hirayama, K., Hirase, A., Miyazawa, A. & Kamei, K. Phospholipid Membrane-Mediated Hemozoin Formation: The Effects of Physical Properties and Evidence of Membrane Surrounding Hemozoin. *PLoS One*. **2013**, 8.

Jackson, K. E., Klonis, N., Ferguson, D. J. P., Adisa, A., Dogovski, C. and Tilley, L. Food vacuole-associated lipid bodies and heterogeneous lipid environments in the malaria parasite, Plasmodium falciparum. *Mol. Microbiol.* **2004**, 54, 109.

Jani, D., Nagarkatti, R., Beatty, W., Angel, R., Slebodnick, C., Andersen, J., Kumar, S and Rathore, D. HDP-a novel heme detoxification protein from the malaria parasite. *PLoS Pathog*. **2008,** 4.

Kapishnikov, S., Berthing, T., Hviid, L., Dierolfd, M., Menzel, A., Pfeifferd, F., Als-Nielsenf, J. and Leiserowitz, L. Aligned hemozoin crystals in curved clusters in malarial red blood cells revealed by nanoprobe X-ray Fe fluorescence and diffraction. *Proc. Natl Acad. Sci. USA*. **2012a**, 109, 11184–11187.

Kapishnikov, S., Weiner, A., Shimoni, E., Guttmann, P., Schneiderc, G., Dahan-Pasternakd, N., Dzikowski, R., Leiserowitz, L. and Elbaum, M. Oriented nucleation of hemozoin at the digestive vacuole membrane in *Plasmodium falciparum*. *Proc. Natl Acad. Sci. USA*. **2012b**, 109 11188–11193.

Kapp, E. A., Schütz, F., Connolly, L. M, Chakel, J. A., Meza, J. E., Miller, C. A., Fenyo, D., Eng, J. K., Adkins, J. N., Omenn, G. S. and Simpson, R. J. An evaluation, comparison, and accurate benchmarking of several publicly available MS/MS search algorithms: sensitivity and specificity analysis. *Proteomics*. **2005**, 5, 3475-90.

Kissinger, J. C., Gajria, B., Li, L., Paulsen, I. T., Roos, D. S., Toxo, D. B. Accessing the Toxoplasma *gondii* genome. *Nucleic Acids Res*. **2003**, 31, 234–236.

Klemba, M., Gluzman, I. & Goldberg, D. E. A *Plasmodium falciparum* dipeptidyl aminopeptidase I participates in vacuolar hemoglobin degradation. *J. Biol. Chem*. **2004**, 279, 43000–43007.

Klonis, N., Dilanian, R., Hanssen, E., Darmanin, C., Streltsov, V., Deed, S., Quiney, H. and Tilley, L. Hematin-hematin self-association states involved in the formation and reactivity of the malaria parasite pigment, hemozoin. *Biochemistry*. **2010**, 49, 6804–6811.

Kolakovich, K. A., Gluzman, I. Y., Duffin, K. L., and Goldberg, D. E. Generation of hemoglobin peptides in the acidic digestive vacuole of *Plasmodium falciparum* implicates peptide transport in amino acid production. *Mol. Biochem. Parasitol*. **1997**, 87, 123–135.

Komeili A. Molecular mechanisms of magnetosome formation. *Annu. Rev. Biochem*. **2007**, 76, 351–366.

Kurosawa, Y., Dorn, A., Kitsuji-Shirane, M., Shimada, H., Satoh, T., Matile, H., Hofheinz, W., Masciadri, R., Kansy, M. & Ridley, R.G. Hematin polymerization assay as a high-throughput screen for identification of new antimalarial pharmacophores. *Antimicrob. Agents Chemother*. **2000**, 44, 2638–2644.

Kyte, J. & Doolittle, R.F. A simple method for displaying the hydropathic character of a protein. *J. Mol. Biol*. **1982**, 157, 105–32.

Lamarque, M., Tastet, C., Poncet, J., Demettre, E., Jouin, P., Vial, H. & Dubremetz, J.F.. Food vacuole proteome of the malaria parasite *Plasmodium falciparum*. *Proteomics Clin. Appl*. **2008**, 2, 1361–1374.

Lancisi, G. M. De noxiis paludum effluvius eorumque remediis. *J. M. Salvioni, Rome*. **1717**.

Laveran, C. L. A. A newly discovered parasite in the blood of patients suffering from malaria. Parasitic etiology of attacks of malaria. 1880. Translated from the French and reprinted in *Ithaca, New York, Cornell University Press*.**1978**.

Le Roch, K. G., Zhou, Y., Blair, P.L., Grainger, M., Moch, J. K., Haynes, J. D., De La Vega, P., Holder, A. A., Batalov, S., Carucci, D. J. & Winzeler, E. A. Discovery of gene function by expression profiling of the malaria parasite life cycle. *Science*. **2003**, 301, 1503–1508.

Lew, V. L., Tiffert, T. & Ginsburg, H. Excess hemoglobin digestion and the osmotic stability of *Plasmodium falciparum*-infected red blood cells. *Blood*. **2003**, 101(10), 4189–94.

Lowenstam, H. A. & Weiner, S. On Biomineralization. *Oxford University Press: New York*. **1989**.

Macomber, P. B., Sprinz, H., Tousimis, A. J. Morphological effects of chloroquine on *Plasmodium berghei* in mice. *Nature*. **1967**, 214, 937–939.

Mann, K., Macek, B. & Olsen, J.V. Proteomic analysis of the acid-soluble organic matrix of the chicken calcified eggshell layer. *Proteomics*. **2006**, 6, 3801–3810.

Mann, K., Poustka, A. J. & Mann, M. The sea urchin (Strongylocentrotuspurpuratus) test and spine proteomes. *Proteome Sci.* **2008**, 6, 22.

Mann, S. & Ozin, G. A. Synthesis of inorganic materials with complex form. *Nature*. **1996**, 382, 313–318.

Mann, S. Molecular recognition in biomineralization. *Nature*. **1988**, 332, 119–124.

Marie, B., Trinkler, N., Zanella-Cleon, I., Guichard, N., Becchi, M., Paillard, C. & Marin, F . Identification of Novel Proteins from the Calcifying Shell Matrix of the Manila Clam *Venerupis Philippinarum*. *Mar. Biotechnol. (NY)*. **2011**, 13, 955–962.

Marti, M., Good, R.T., Rug, M., Knuepfer, E., Cowman, A. F. Targeting malaria virulence and remodeling proteins to the host erythrocyte. *Science*. **2004**, 306, 1930–1933.

Massey Jr, F. J. The Kolmogorov-Smirnov Test for Goodness of Fit. *J. Am. Stat. Assoc.* **1951**, 46, 68–78.

Mauritz, J. M. A., Seear, R., Esposito, A., Kaminski, C. F., Skepper, J. N., Warley, A., Lew, V. L. & Tiffert, T. X-ray Microanalysis Investigation of the Changes in Na, K, and Hemoglobin Concentration in *Plasmodium falciparum*-Infected Red Blood Cells. *Biophys. J.* **2011**, 100, 1438–1445.

Mauritz, J. M., Esposito, A., Ginsburg, H., Kaminski, C. F., Tiffert, T. & Lew, V. L. The homeostasis of *Plasmodium falciparum*-infected red blood cells. *PLoS Comput. Biol*. **2009**, 5.

Meshnick, S. R., Taylor, T. E., Kamchonwongpaisan, S. Artesminin and the antimalarial endoperoxides: from herbal remedy to targeted chemotherapy. *Microbiol. Rev*. **1996**, 60, 301–15.

Mikolajczak, S. A & Kappe, S. H . A Clash to Conquer: the Malaria Parasite Liver Infection. *Mol. Microbiol*. **2006**, 62, 1499–1506.

Murata, C. E. & Goldberg, D. E. *Plasmodium falciparum* falcilysin: a metalloprotease with dual specificity. *J. Biol. Chem*. **2003**,278, 38022–38028.

Murphy, S. C., Fernandez-Pol, S., Chung, P. H., Prasanna Murthy, S. N., Milne, S. B., Salomao, M., Brown, H. A., Lomasney, J. W., Mohandas, N. & Haldar, K. Cytoplasmic remodeling of erythrocyte raft lipids during infection by the human malaria parasite *Plasmodium falciparum*. *Blood*. **2007**, 110, 2132–2139.

Nawabi, P., Lykidis, A., Ji, D. and Haldar, K. Neutral lipid analysis reveals elevation of acylglycerols and lack of cholesterol esters in *Plasmodium falciparum*-infected erythrocytes. *Eukaryot. Cell.* **2003**, 2, 1128–1131.

Ncokazi, K.K. and Egan, T.J. A colorimetric high-throughput β-hematin inhibition screening assay for use in the search for antimalarial compounds. *Anal Biochem*. **2005**, 338, 306–319.

Nemoto, M., Wang, Q., Li, D., Pan, S., Matsunaga, T. & Kisailus, D. Proteomic analysis from the mineralized radular teeth of the giant Pacific chiton, *Cryptochiton stelleri* (Mollusca). *Proteomics*. **2012**, 12, 2890–2894.

Nickel, C., Rahlfs, S., Deponte, M., Koncarevic, S. & Becker, K. Thioredoxin Networks in the Malaria Parasite Plasmodium falciparum. *Antioxid. Redox Signal*. **2006**, 8, 1227–1239.

Noland, G. S., Briones, N. & Sullivan, D. J. The shape and size of hemozoin crystals distinguishes diverse *Plasmodium* species. *Mol. Biochem. Parasitol.* **2003**,130, 91–99.

Oliveira, M. F., Kycia, S., Gonzales, A., Kosar, A. D., Bohle, D. S., Hempelmann, E., Menezes, D., Vannier-Santos, M., Oliveira, P. L. & Ferreira, S. T. Structural and morphological characterization of hemozoin produced by Schistosoma mansoniand Rhodnius prolixus. *FEBS Lett*. **2005**, 579, 6010–6016.

Oliveira, M. F., d'Avila, J. C., Torres, C. R., Oliveira, P. L., Tempone, A. J., Rumjanek, F. D., Braga, C. M., Silva, J. R., Dansa-Petretski, M., Oliveira, M. A., de Souza, W. & Ferreira, S.T. Haemozoin in *Schistosoma mansoni*. *Mol. Biochem. Parasitol*. **2000**, 111, 217–221.

Oliveira, M.F., Silva, J.R., Dansa-Petretski, M., de Souza, W., Braga, C.M., Masuda, H. & Oliveira, P.L. Haemozoin formation in the midgut of the blood-sucking insect *Rhodnius prolixus*. *FEBS Lett.* **2000**, 477, 95–98.

Oliveira, M.F., Silva, J.R., Dansa-Petretski, M., de Souza, W., Lins, U., Braga, C.M.S., Masuda, H. and Oliveira, P.L. Haem detoxification by an insect. *Nature*. **1999**, 400, 517–518.

Pagola, S., Stephens, P. W., Bohle, D. S., Kosar,A. D. & Madsen, S. K. The structure of malaria pigment (β-haematin). *Nature*. **2000**, 404, 307–310.

Pain, A., Renauld, H., Berriman, M., Murphy, L., Yeats, C.A., et al. Genome of the host-cell transforming parasite Theileria annulata compared with *T. parva*. *Science*. **2005**, 309, 131–133.

Palacpac, N. M., Hiramine, Y., Mi-ichi, F., Torii, M., Kita, K., Hiramatsu, R., Horii, T. & Mitamura, T. Developmental-stagespecific triacylglycerol biosynthesis, degradation and trafficking as lipid bodies in *Plasmodium falciparum*-infected erythrocytes. *J. Cell Sci*. **2004**, 117, 1469–1480.

Pandey, A. V., Babbarwal, V. K., Okoyeh, J. N., Joshi, R. M., Puri, S. K., Singh, R. L. & Chauhan, V. S. Hemozoin formation in malaria: a two-step process involving histidine-rich proteins and lipids. *Biochem. Biophys. Res. Commun.* **2003**, 308, 736–743

Papalexis, V., Siomos, M. A., Campanale, N., Guo, X. G., Kocak, G., Foley, M. & Tilley, L. Histidine-rich protein 2 of the malaria parasite, *Plasmodium falciparum*, is involved in detoxification of the by-products of haemoglobin degradation. *Mol. Biochem. Parasitol.* **2001**, 115, 77–86.

Pappin, D. J., Hojrup, P. and Bleasby, A. J. Rapid identification of proteins by peptide-mass fingerprinting. *Curr Biol*. **1993**, 3, 327-332.

Pasini, E. M., Kirkegaard, M., Mortensen, P., Lutz, H. U., Thomas, A. W. & Mann, M. In-depth analysis of the membrane and cytosolic proteome of red blood cells. *Blood*. **2006**, 108, 791–801.

Pavithra, S. R., Kumar, R. & Tatu, U. Systems Analysis of Chaperone Networks in the Malarial Parasite *Plasmodium falciparum*. *PLoS Comput. Biol*. **2007**, 3, 1701–1715.

Pei X, Guo X, Coppel R, Bhattacharjee S, Haldar K, Gratzer W, Mohandas N, An X. The ring-infected erythrocyte surface antigen (RESA) of *Plasmodium falciparum* stabilizes spectrin tetramers and suppresses further invasion. *Blood*. **2007**, 110, 1036–1042.

Pei, X., An, X., Guo, X., Tarnawski, M., Coppel, R. & Mohandas, N. Structural and functional studies of interaction between *Plasmodium falciparum* knob-associated histidine-rich protein (KAHRP) and erythrocyte spectrin. *J. Biol. Chem*. **2005**, 280, 31166–31171.

Pesce, E. R., Cockburn, I. L., Goble, J. L., Stephens, L. L. & Blatch, G. L. Malaria heat shock proteins: drug targets that chaperone other drug targets. *Infect. Disord. Drug Targets*. **2010**, 10, 147–157.

Pisciotta, J. M., Coppens, I., Tripathi, A. K., Scholl, P. F., Shuman, J., Bajad, S., Shulaev, V. and Sullivan, D. J. The role of neutral lipid nanospheres in Plasmodium falciparum haem crystallization. *Biochem. J.* **2007**, 402, 197–204.

Poly, W. J. Nongenetic variation, genetic-environmental interactions and altered gene expression. III. Posttranslational modifications. *Comp. Biochem. Physiol. A. Physiol*. **1997**, 118, 551–72.

Ponka, P. Cell Biology of Heme. *Am. J. Med. Sci*. **1999**, 318, 241–256.

Pouget, E., Dujardin, E., Cavalie, A., Moreac, A., Valéry, C., Marchi-Artzner, V., Weiss, T., Renault, A., Paternostre, M. & Artzner, F. Hierarchical architectures by synergy between dynamical template self-assembly and biomineralization. *Nat. Mater*. **2007**, 6, 434–439.

Protozoan genomes **2008**. http://www.sanger.ac.uk/Projects/Protozoa/.

Rosenthal, P. J. Cysteine proteases of malaria parasites. *Int. J. Parasitol*. **2004**, 34, 1489–1499.

Rosenthal, P. J. Falcipains and other cysteine proteases of malaria parasites. *Adv Exp Med Biol*. **2011**, 712, 30–48.

Rosenthal, P. J., McKerrow, J. H., Aikawa, M., Nagasawa, H., and Leech, J. H. A malarial cysteine proteinase is necessary for hemoglobin degradation by *Plasmodium falciparum*. *J. Clin. Invest*. **1988**, 82, 1560–1566.

Ross, R. On some peculiar pigmented cells found in two mosquitoes fed on malarial blood. *British Medical Journal*. **1897**, 18, 1736–1788.

Ryter, S. W. and Tyrrel, R. M. The haem synthesis and degradation pathways: role in oxidant sensitivity. Haem oxygenase has both pro- and antioxidant properties. Free. *Rad. Biol. Med*. **2000**, 28, 289–309.

Sandlin, R. D., Carter, M. D., Lee, P. J., Auschwitz, J. M., Leed, S. E., Johnson, J. D., and Wright, D. W. Use of the NP-40 detergent-mediated assay in discovery of inhibitors of β-hematin crystallization. *Antimicrob. Agents Chemother*. **2011**, 55, 3363–3369.

Schacter, B. Heme catabolism by heme oxygenase: physiology, regulation, and mechanism of action. *Semin. Hematol*. **1988**, 25, 349–369.

Schlagenhauf, P., Adamcova, M., Regep, L., Schaerer, M. T. & Rhein, H. G. The Position of Mefloquine as a 21st Century Malaria Chemoprophylaxis. *Malaria J*. **2010**, 9, 357.

Schmitt, T. H., Frezzatti Jr., W. A. and Schreier, S. Hemininduced lipid membrane disorder and increased permeability: a molecular model for the mechanism of cell lysis. *Arch. Biochem. Biophys*. **1993**, 307, 96–103.

Scholl, P. F., Tripathi, A. K. and Sullivan, D. J. Bioavailable iron and heme metabolism in *Plasmodium* Sensitive versus Resistant Malaria. *Biochemistry*. **2006**, 45, 12400–12410.

Shenai, B. R., Sijwali, P. S., Singh, A. & Rosenthal, P. J. Characterization of Native and Recombinant Falcipain-2, a Principal Trophozoite Cysteine Protease and Essential Hemoglobinase of *Plasmodium falciparum*. *J. Biol. Chem*. **2000**, 275, 29000–29010.

Shirai, A., Matsuyama, A., Yashiroda, Y., Hashimoto, A., Kawamura, Y., Arai, R., Komatsu, Y., Horinouchi, S. & Yoshida, M. Global Analysis of Gel Mobility of Proteins and Its Use in Target Identification. *J. Biol. Chem*. **2008**, 283, 10745–10752.

Shonhai A. Plasmodial heat shock proteins: targets for chemotherapy. *FEMS Immunol Med. Microbiol*. **2010**, 58, 61–74.

Shonhai, A., Boshoff, A. & Blatch, G.L. The structural and functional diversity of Hsp70 proteins from *Plasmodium falciparum*. *Protein Sci*. **2007**, 16, 1803–18.

Shonhai, A., Boshoff, A., Blatch, G.L. *Plasmodium falciparum* heat shock protein 70 is able to suppress the thermosensitivity of an *Escherichia coli* DnaK mutant strain. *Mol. Genet. Genomics*. **2005**, 274, 70–78.

Sijwali, P. S. & Rosenthal, P. J. Gene disruption confirms a critical role for the cysteine protease falcipain-2 in hemoglobin hydrolysis by *Plasmodium falciparum*. *Proc. Natl Acad. Sci. USA*. **2004**, 101, 4384–4389.

Sijwali, P. S., Shenai, B. R., Gut, J., Singh, A. & Rosenthal, P. J. Expression and Characterization of the *Plasmodium falciparum* Haemoglobinase Falcipain-3. *Biochem. J*. **2001**, 360, 481–489.

Skinner-Adams, T. S., Lowther, J., Teuscher, F., Stack, C. M., Grembecka, J., Mucha, A., Kafarski, P., Trenholme, K. R., Dalton, J. P. & Gardiner, D. L. Identification of Phosphinate Dipeptide Analog Inhibitors Directed against the *Plasmodium falciparum* M17 Leucine Aminopeptidase as Lead Antimalarial Compounds. *J. Med. Chem*. **2007**, 50, 6024–6031.

Slater, A. F. G. and Cerami, A. Inhibition by chloroquine of a novel haem polymerase enzyme activity in malaria trophozoites. *Nature*. **1992**, 355, 167–169.

Slater, A. F. G., Swiggard, W. J., Orton, B. R., Flitter, W. D., Goldberg, D. E., Cerami, A. & Henderson, G. B. An iron-carboxylate bond links the heme units of malaria pigment. *Proc. Natl Acad. Sci. USA*. **1991**, 88 325–329.

Slomianny, C. Three-dimensional reconstruction of the feeding process of the malaria parasite. *Blood Cells*. **1990**, 16, 369–78.

Solomonov, I., Osipova, M., Feldman, Y., Baehtz, C., Kjaer, K., Robinson, I. K., Webster, G. T., McNaughton, D., Wood, B. R., Weissbuch, I. & Leiserowitz, L. *J. Am. Chem. Soc.* **2007**, 129, 2615–2627.

Srivastava, I. K., Rottenberg, H., Vaidya, A. B. Atovaquone, a broad spectrum antiparasitic drug, collapses mitochondrial membrane potential in a malarial parasite. *J. Biol. Chem*. **1997**, 272, 3961–3966.

Stebbins, C. E., Russo, A. A., Schneider, C., Rosen, N., Hartl, F. U. & Pavletich, N. P. Crystal structure of an Hsp90-geldanamycin complex: Targeting of a protein chaperone by an antitumor agent. *Cell*. **1997**, 89, 239–350.

Stiebler, R., Hoang, A. N., Egan, T. J., Wright, D. W. & Oliveira, M. F. Increase on the initial soluble heme levels in acidic conditions is an important mechanism for spontaneous heme crystallization in vitro. *PloS One*. **2010**, 5.

Sullivan, D. J. Theories on malarial pigment formation and quinoline action. *Int. J. Parasitol*. **2002**, 32, 1645–53.

Sullivan, D. J., Gluzman, I. Y., Russell, D. G., and Goldberg, D. E. On the molecular mechanism of chloroquine's antimalarial action. *Proc. Natl Acad. Sci. U.S.A*. **1996**, 93, 11865–11870.

Sullivan, D. J., Matile, H., Ridley, R. G. & Goldberg, D. E. A common mechanism for blockade of heme polymerization by antimalarial quinolines. *J. Biol. Chem*. **1998**, 273, 31103–31107.

Sullivan, D. J. Jr., Gluzman, I.Y and Goldberg, D. E. Plasmodium hemozoin formation mediated by histidine-rich proteins. *Science*. **1996**, 271, 219–222.

Tan, S.Y. & Ahana, A. Charles Laveran (1845-1922): Nobel laureate pioneer of malaria. *Singapore Med. J*. **2009**, 50, 657–658.

Tekwani, B. L. and Walker, L. A. Targeting the hemozoin synthesis pathway for new antimalarial drug discovery: technologies for in vitro β-hematin formation assay. *Comb. Chem. High Throughput Screen*. **2005**, 8:61–77.

Trager, W. & Jensen, J. B. Human malaria parasites in continuous culture. *J. Parasitol*. **2005**, 91, 484–486.

Van der Zee J., Barr D. P and Mason R. P. ESR spin trapping investigation of radical formation from the reaction between hematin and tert-Butyl hydroperoxide. *Free Radic Biol Med*. **1996**, 20, 199-206.

Vial, H. J. and Ancelin, M. L. Malarial lipids. An overview. *Subcell. Biochem*. **1992**, 18, 259–306.

Virchow, R. About the pathophysiology of blood. *Archiv für Pathologische Anatomie* . **1849**, 2, 587–598.

Walczak, M., Lawniczak-Janlonska, K., Sienkiewicz, A., Demchenko, I. N., Piskorska, E., Chatain, G. and Bohle, D. S. Local environment of iron in malarial pigment and its substitute β-hematin. *Nuclear Instruments and Methods in Physics Research B*. **2005**, 238, 32–38.

Waller, K.L., Nunomura, W., An, X., Cooke, B.M., Mohandas, N. & Coppel, R. L. Mature parasite-infected erythrocyte surface antigen (MESA) of Plasmodium falciparum binds to the 30-kDa domain of protein 4.1 in malaria-infected red blood cells. *Blood*. **2003**, 102, 1911–1914.

Waller, K. L., Stubberfield, L. M., Dubljevic, V., Nunomura, W., An, X., Mason, A. J., Mohandas, N., Cooke, B. M. & Coppel, R. L. Interactions of *Plasmodium falciparum* erythrocyte membrane protein 3 with the red blood cell membrane skeleton. *Biochim. Biophys. Acta*. **2007**, 1768, 2145–2156.

Wang, X., Ingall, E., Lai, B. & Stack, A. G. Self-assembled monolayers as templates for heme crystallization. *Cryst. Growth Des.* **2010**, 10, 798–805.

Weiner, S. & Addadi, L. Design strategies in mineralized biologicalmaterials. *J. Mater. Chem.* **1997**, 7, 689–702.

Weissbuch, I., Popovitz-Biro, I., Lahav, M. and Leiserowitz, L. Understanding and control of Nucleation, Growth, Habit, Dissolution and Structure of Two-and Three-Dimensional Crystals Using 'Tailor-Made' Auxiliaries. *Acta Cryst.* **1995**, B51, 115–148.

WHO World Malaria Report; http://www.who.int/malaria/en/.

WHO World Report
http://www.who.int/malaria/publications/world_malaria_report_2012/wmr2012_no_profiles.pdf.

William, E. C. *Plasmodium knowlesi*: a Malaria Parasite of Monkeys and Humans. *Annu. Rev. Entomol*. **2012**, 57, 107–21.

Wilt, F. H. Developmental biology meets materials science:morphogenesis of biomineralized structures. *Dev. Biol*. **2005**, 280, 15–25.

Wyatt, D. M. & Berry, C. Activity and Inhibition of Plasmepsin IV, a New Aspartic Proteinase from the Malaria Parasite, *Plasmodium falciparum*. *FEBS Lett*. **2002**, 513, 159–162.

Young, J. R., Didymus, J. M., Bown, P. R., Prins, B. & Mann. S. Crystal assembly and phylogenetic evolution in heterococcoliths. *Nature*. **1992**, 356, 516–518.

Zhu, C. C., Cook, L. B & Hinkle, P. M. Dimerization and phosphorylation of thyrotropin-releasing hormone receptors are modulated by agonist stimulation. *J. Biol. Chem*. **2002**, 277, 28228–28237.

Ziegler, J., Linck, R. & Wright, D. W. Heme Aggregation inhibitors: antimalarial drugs targeting an essential biomineralization process. *Curr. Med. Chem*. **2001**, 8, 171–189.

Appendix 1

All *P. falciparum* (Pf) and human proteins identified from the respective gel sections in Figure 3.4

Bands on 15% SDS PAGE Coomassie (C) and silver (S) stained gels		Protein name	Predicted protein mass (KDa)	Location (compartment and/or subcellular location)	Intact,I or digested ,D
C1		(P13830) Ring-infected erythrocyte surface antigen precursor RESA_PLAFF	124.907	Cell membrane	I
		(P13819) Merozoite surface protein 1 precursor PMMSA) MSP1_PLAFF	193.72	Cell membrane	D
		(P04932) Merozoite surface protein 1 precursor (PMMSA) (P190)	187.291	Cell membrane	D
		(Q8I4V5) Probable U3 small nucleolar RNA-associated protein 11 (U3 snoRNA-associated protein 11)	25.668	Nucleus	
		(Q8IBS5) Calcium-dependent protein kinase 4 CDPK4_PLAF7	60.780	Unknown	
		(P40282) Histone H2A H2A_PLAFA	14.122	Nucleus	
		(O97231) 60S ribosomal protein L44 RL44_PLAFA	12.157	Ribosome	
		(Q9NJU9) Calcium-dependent protein kinase 3 CDPK3_PLAF7	65.288	Unknown	
		(P21421) DNA-directed RNA polymerase beta chain RPOB_PLAFA	122.186	Plastid, apicoplast	I
		(Q02595) Probable serine/threonine-protein kinase 2 (EC 2.7.1.37) KPK2_PLAFK	59.006	Membrane of young trophs&schizonts	
		(P68875) Transmission-blocking target antigen S230 precursor S230_PLAFO	363.218	Cell membrane	
		(Q05866) 78 kDa glucose-regulated protein homolog precursor (GRP 78) GRP78_PLAFO	72.776	ER Lumen	
		(O97249) 40S ribosomal protein S12 RS12_PLAFA	15.396	Ribosome	
		(P30315) DNA polymerase delta catalytic subunit DPOD_PLAFK	126.884	Nucleus	I
C1	**Human**	None			
C2	**Pf**	(P33948) ER lumen protein retaining receptor ERD2_PLAFA	26.447	ER membrane	
		(P13819) Merozoite surface protein 1 precursorMSP1_PLAFF	193.72		D
		(P04932) Merozoite surface protein 1 precursor (PMMSA) (P190)	187.291		D

		MSP1_PLAFK			
		(Q04956) Probable cation-transporting ATPase 1 ATX1_PLAFA	230.286	Membrane	D
		(P40282) Histone H2A H2A_PLAFA	14.122		D
		(P34940) Chaperonin CPN60, mitochondrial precursor CH60_PLAFG	79.445	Mitochondria	D
		(P21421) DNA-directed RNA polymerase beta chain RPOB_PLAFA	122.186		D
		(P13830) Ring-infected erythrocyte surface antigen precursor RESA_PLAFF	124.907		D
		(P27625) DNA-directed RNA polymerase III largest subunitRPC1_PLAFA	272.832	Nucleus	D
		(P02895) Glycophorin-binding protein (GBP-130) GBP_PLAFG	90.018	Cytoplasm	D
		(P05691) Circumsporozoite protein (CS) (Fragment) CSP_PLAFL	33.649	Cell membrane	
		(P14643) Tubulin beta chain (Beta tubulin) TBB_PLAFK	49.751	Cytoskeleton	
		(P12078) Heat shock 70 kDa protein PPF203 (fragment) HSP73_PLAFA	23.058	DV	
		(P41001) DNA topoisomerase II (EC 5.99.1.3) TOP2_PLAFK	161.029	Nucleus	D
		(P13922) Bifunctionaldihydrofolate DRTS_PLAFK	71.817	Unknown	D
		(Q08210) Dihydroorotate dehydrogenase homolog, mitochondrial precursor PYRD_PLAFA	65.558	Mitochondrion inner membrane	I
		(P30315) DNA polymerase delta catalytic subunit DPOD_PLAFK	126.884		D
C2	**Human**	(P68871) Haemoglobin beta chain HBB_HUMAN	15.998	Cytoplasm	
		(P11166) Solute carrier family 2, facilitated glucose transporter, member 1 (Glucose transporter type 1, RBC/brain) GTR1_HUMAN	54.084	Cell membrane	I
		(P02768) Serum albumin precursor ALBU_HUMAN	69.367	Plasma(secreted)	I
		(P69905) Haemoglobin alpha chain HBA_HUMAN	15.258	Cytoplasm	
		(P02730) Band 3 anion transport protein B3AT_HUMAN	101.792	Membrane protein	D
		(P11678) Eosinophil peroxidase precursor PERE_HUMAN	81.040	Cytoplasmic granules of eosinophil	D
		(P62988) Ubiquitin UBIQ_HUMAN; demerged into P0CG47 (UBB_HUMAN), P0CG48 (UBC_HUMAN, P62979 (RS27A_HUMAN), P62987 (RL40_HUMAN)	25.762, 77.039, 17.965, 14.728	Nucleus	D

		(Q99569) Plakophilin 4 (p0071) PKP4_HUMAN	131.868	Cytoskeleton	D
		(P27105) Erythrocyte band 7 integral membrane protein (Stomatin) (Protein 7.2b) STOM_HUMAN	31.731	Inner surface of plasma membrane, binds cytoskeleton	
		(Q05996) Zonapellucida sperm-binding protein 2 precursor ZP2_HUMAN	82.357	Cell membrane	D
		(P12273) Prolactin-inducible protein precursor PIP_HUMAN	16.572	Secreted	
C3	**Pf**	(P40282) Histone H2A H2A_PLAFA	14.112		
		(P13830) Ring-infected erythrocyte surface antigen precursor RESA_PLAFF	124.907		D
		(P13819) Merozoite surface protein 1 precursor MSP1_PLAFF	193.72		D
		(P04932) Merozoite surface protein 1 precursor (P190) MSP1_PLAFK	187.291		D
		(O96935) M1-family aminopeptidase AMP1_PLAFQ	126.062	Cytosol, DV	D
		(P05691) Circumsporozoite protein (CS) (Fragment) CSP_PLAFL	33.649		
		(P13922) Bifunctionaldihydrofolatereductase-thymidylate synthase DRTS_PLAFK	71.817	Unknown	D
		(P34940) Chaperonin CPN60, mitochondrial precursor CH60_PLAFG	79.445		D
C3	**Human**	(P68871) Haemoglobin beta chain HBB_HUMAN	15.998		
		(P69905) Haemoglobin alpha chain HBA_HUMAN	15.258		
		(P14136) Glial fibrillary acidic protein, astrocyte GFAP_HUMAN	49.880	Cytoplasm	D
		(P11166) Solute carrier family 2, facilitated glucose transporter, member 1 GTR1_HUMAN	54.084		D
		(P02261) Histone H2A.c/d/i/n/p (H2A.1) (H2A/c) (H2A/d) (H2A/i) (H2A/n) (H2A/p) (H2A.1b) H2AC_HUMAN; Demerged into P0C0S8 (H2A1_HUMAN)	14.09	Nucleus	
		(P02730) Band 3 anion transport protein B3AT_HUMAN	101.792		D
C4	**Pf**	(P13819) Merozoite surface protein 1 precursor MSP1_PLAFF	193.72		D
		(P04932) Merozoitesurface protein 1 precursor (P190) MSP1_PLAFK	193.72		D
		(P40282) Histone H2A H2A_PLAFA	14.112		
		(P13830) Ring-infected erythrocyte surface antigen precursorRESA_PLAFF	124.907		D

		(P13922) Bifunctionaldihydrofolatereductase-thymidylate synthase DRTS_PLAFK	71.817		D
		(P41001) DNA topoisomerase II TOP2_PLAFK	161.029		D
		(P27625) DNA-directed RNA polymerase III largest subunitRPC1_PLAFA	272.832		D
		(P38545) GTP-binding nuclear protein Ran RAN_PLAFA	24.875	Nucleus	
		(P14248) DNA-directed RNA polymerase II largest subunitRPB1_PLAFD	278.168	Nucleus	D
		(P33948) ER lumen protein retaining receptor ERD2_PLAFA	26.447		
		(P62343) Calcium-dependent protein kinase 1 CDPK1_PLAFK	60.800	Membrane	D
		(P34940) Chaperonin CPN60, mitochondrial precursor CH60_PLAFG	79.445		D
		(P39898) Plasmepsin 1 precursor (PFAPG)	51.461	DV	D
		(P30315) DNA polymerase delta catalytic subunit DPOD_PLAFK	126.884		D
		(Q08210) Dihydroorotate dehydrogenase homolog, mitochondrial precursor PYRD_PLAFA	65.558		D
		(P13824) Clustered-asparagine-rich protein ARP2_PLAFA	51.176	Unknown	D
		(Q27743) L-lactate dehydrogenase LDH1_PLAFD	34.108	DV	I
		(Q08853) Calcium-transporting ATPase (EC 3.6.3.8) (Calcium pump)	139.415	Membrane	D
		(P25407) Hypothetical protein in calmodulin 5'region (Fragment)	29.324		
		(P13568) Multidrug resistance protein (Chloroquine resistance protein) MDR_PLAFF	162.252	DV	D
		(P05691) Circumsporozoite protein (CS) (Fragment) CSP_PLAFL	33.649		I
		(P61076) ThioredoxinreductaseTRXR_PLAF7	68.698	Cytoplasm	I(mon)
		(P50647) Ribonucleoside-diphosphatereductase large chain RIR1_PLAFG	92.403	Unknown	D
		(Q00080) Elongation factor 1-alpha (EF-1-alpha) EF1A_PLAFK	49.041	Cytoplasm	D
		(P25805) Trophozoite cysteine proteinase precursor CYSP_PLAFA	66.880		D
		(P16405) Octapeptide-repeat antigen (ORA) (Fragment) ORA_PLAFN	79.049	PV	D
		(P11144) Heat shock 70 kDa protein (HSP70) HSP70_PLAFA	74.287	DV	D
		(Q02155) Hexokinase (EC 2.7.1.1) HXK_PLAFA	55.346	Unknown	D
		(P69193) Serine-repeat antigen protein precursor SERA_PLAFD	111.095		D
		(P46468) Putative cell division cycle ATPase CDAT_PLAF7	142.080	Unknown	D
		(Q05866) 78 kDa glucose-regulated protein homolog precursor GRP78_PLAFO	72.776		D

		(O96935) M1-family aminopeptidaseAMP1_PLAFQ	126.062		D
		(P22620) 101 kDa malaria antigen (P101) (Acidic basic repeat antigen) ABRA_PLAFC	86.622	PV membrane	D
		(P34787) Tubulin gamma chain (Gamma tubulin) TBG_PLAFO	51.538	Cytoskeleton	D
C4	**Human**	(P68871) Haemoglobin beta chain HBB_HUMAN	15.998		
		(P02730) Band 3 anion transport protein B3AT_HUMAN	101.972		D
		(P11166) Solute carrier family 2, facilitated glucose transporter, member 1 GTR1_HUMAN	54.084		D
		(P69905) Haemoglobin alpha chain HBA_HUMAN	15.258		
		(P62805) Histone H4 H4_HUMAN	11.367	Nucleus	
		(P02261) Histone H2A.c/d/i/n/p (H2A.1) (H2A/c) (H2A/d) (H2A/i) (H2A/n) (H2A/p) (H2A.1b) H2AC_HUMAN	14.09		
		(P02768) Serum albumin precursor ALBU_HUMAN	69.367		D
		(Q01543) Friend leukemia integration 1 transcription factorFLI1_HUMAN	50.982	Nucleus	D
		(Q13683) Integrin alpha-7 precursor ITA7_HUMAN	128.948	Membrane	D
		(P27105) Erythrocyte band 7 integral membrane protein (Stomatin) (Protein 7.2b) STOM_HUMAN	31.731		
		(Q8N511) Protein C17orf32 CQ032_HUMAN	23.130	Membrane	
		(Q9H293) Interleukin-17E precursor (IL-17E) IL17E_HUMAN	20.330	Secreted	
		(Q02094) Rhesus blood group-associated glycoprotein RHAG_HUMAN	44.198	Membrane	D
		(Q9Y5I4) Protocadherin alpha C2 precursor PCDC2_HUMAN	109.450	Membrane	D
		(P62988) Ubiquitin UBIQ_HUMAN; demerged into P0CG47 (UBB_HUMAN), P0CG48 (UBC_HUMAN) P62979 (RS27A_HUMAN) P62987 (RL40_HUMAN)	25.762, 77.039, 17.965, 14.728		
		(Q92844) TRAF family member-associated NF-kappa-B activator TANK_HUMAN	47.816	Cytoplasm (Ubiquitous)	D
		(P14778) Interleukin-1 receptor, type I precursor IL1R1_HUMAN	65.402	Cell membrane (secreted)	D
		(Q9BXS1) Isopentenyl-diphosphate delta-isomerase 2 IDI2_HUMAN	26.753	Peroxisome	

				(detected in skeletal muscle)	
		(O94973) Adapter-related protein complex 2 alpha 2 subunit AP2A2_HUMAN	103.960	Membrane	D
		(Q96NR8) Retinol dehydrogenase 12 RDH12_HUMAN	35.094	Unknown (Widely expressed, mostly in eye, kidney, brain, skeletal muscle and stomach)	I
		(Q9C0E2) Exportin 4 (Exp4) XPO4_HUMAN	130.139	Nucleus	D
		(Q9NQT8) Kinesin-like protein KIF13B KI13B_HUMAN	202.666	(cytoskeleton	D
		(P25100) Alpha-1D adrenergic receptor ADA1D_HUMAN	60.463	Membrane	D
		(O43150) Development and differentiation-enhancing factor 2 DDEF2_HUMAN	111.651	Golgi apparatus	D
		(Q15124) Phosphoglucomutase-like protein 5PGM5_HUMAN	62.225	Cytoskeleton (detected in cardiac & skeletal muscle, liver, kidney, skin & brain)	D
		(Q92545) RW1 protein (Fragment) RW1_HUMAN	205.138	Membrane	D
		(Q05682) Caldesmon (CDM) CALD1_HUMAN	93.231	Cytoskeleton	D
C5	**Pf**	(P13819) Merozoite surface protein 1 precursor MSP1_PLAFF	193.72		D
		(P19598) Merozoite surface protein 1 precursor (P190) MSP1_PLAF3	192.463	Cell membrane	D
		(P40282) Histone H2A H2A_PLAFA	14.122		
C5	**Human**	(P33948) ER lumen protein retaining receptor ERD2_PLAFA	26.447		
		(P13830) Ring-infected erythrocyte surface antigen precursor RESA_PLAFF	124.907		D
		(P05691) Circumsporozoite protein CSP_PLAFL	33.649		
		(P61076) Thioredoxinreductase TRXR_PLAF7	68.698		D
		(P69193) Serine-repeat antigen protein precursor SERA_PLAFD	111.095		D

		(P38545) GTP-binding nuclear protein Ran (GTPase Ran) (Ras-like protein TC4) RAN_PLAFA	24.875		
		(P68871) Haemoglobin beta chain HBB_HUMAN	15.998		
		(P11166) Solute carrier family 2, facilitated glucose transporter, member 1 GTR1_HUMAN	54.084		D
		(P69905) Haemoglobin alpha chain HBA_HUMAN	15.258		
		(P02768) Serum albumin precursor ALBU_HUMAN	69.367		D
		(P02261) Histone H2A.c/d/i/n/p (H2A.1) (H2A/c) (H2A/d) (H2A/i) (H2A/n) (H2A/p) (H2A.1b) H2AC_HUMAN	14.09		
		(P62988) Ubiquitin UBIQ_HUMAN demerged into P0CG47 (UBB_HUMAN) P0CG48 (UBC_HUMAN) P62979 (RS27A_HUMAN) P62987 (RL40_HUMAN)	25.762, 77.039, 17.965, 14.728		
		(Q92844) TRAF family member-associated NF-kappa-B activator TANK_HUMAN	47.816		D
C6	**Pf**	(P13819) Merozoite surface protein 1 precursor MSP1_PLAFF	193.72		D
		(P19598) Merozoite surface protein 1 precursor (P190)	192.463		D
		(P13830) Ring-infected erythrocyte surface antigen precursor RESA_PLAFF	124.907		D
		(P40282) Histone H2A H2A_PLAFA	14.122		
		(P27625) DNA-directed RNA polymerase III largest subunitRPC1_PLAFA	272.832		D
		(P14248) DNA-directed RNA polymerase II largest subunitRPB1_PLAFD	278.168		D
		(P34940) Chaperonin CPN60, mitochondrial precursor CH60_PLAFG	79.445		D
		(P13922) Bifunctionaldihydrofolatereductase-thymidylate synthase DRTS_PLAFK	71.817		D
		(P30315) DNA polymerase delta catalytic subunit DPOD_PLAFK	126.884		D
		(Q08210) Dihydroorotate dehydrogenase homolog, mitochondrial precursor PYRD_PLAFA	65.558		D
		(P13824) Clustered-asparagine-rich protein ARP2_PLAFA	51.176		D
		(Q08853) Calcium-transporting ATPase (EC 3.6.3.8) (Calcium pump) ATC_PLAFK	139.415		D

		(P25407) Hypothetical protein in calmodulin 5'region (Fragment) YCA1_PLAFA	29.324		
		(P05691) Circumsporozoite protein (CS) (Fragment) CSP_PLAFL	33.649		
		(P16405) Octapeptide-repeat antigen (ORA) (Fragment) ORA_PLAFN	79.049		D
		(P38545) GTP-binding nuclear protein Ran (GTPase Ran) (Ras-like protein TC4) RAN_PLAFA	24.875		
		(P41001) DNA topoisomerase II (EC 5.99.1.3) TOP2_PLAFK	161.029		D
		(Q02155) Hexokinase (EC 2.7.1.1) HXK_PLAFA	55.346		D
		(Q05866) 78 kDa glucose-regulated protein homolog precursor GRP78_PLAFO	72.776		D
C6	**Human**	(P27105) Erythrocyte band 7 integral membrane protein (Stomatin) (Protein 7.2b) STOM_HUMAN	31.731		
		(P68871) Haemoglobin beta chain HBB_HUMAN	15.998		
		(P11166) Solute carrier family 2, facilitated glucose transporter, member 1 GTR1_HUMAN	54.084		D
		(P69905) Haemoglobin alpha chain HBA_HUMAN	15.258		
		(P02768) Serum albumin precursor ALBU_HUMAN	69.367		D
		(P02261) Histone H2A.c/d/i/n/p (H2A.1) (H2A/c) (H2A/d) (H2A/i) (H2A/n) (H2A/p) (H2A.1b) H2AC_HUMAN	14.09		
		(Q16352) Alpha-internexin (Alpha-Inx) AINX_HUMAN	55.391	Intermediate filament	D
		(Q8WWR8) Sialidase 4 NEUR4_HUMAN	51.572	Membrane & Lysosome lumen	D
C7	**Pf**	(P11144) Heat shock 70 kDa protein (HSP70) HSP70_PLAFA	74.287		D
		(P39898) Plasmepsin 1 precursor PLM1_PLAFA	51.461		D
		(Q07805) Ornithine aminotransferase (EC 2.6.1.13) (Ornithine--oxo-acid aminotransferase) OAT_PLAFD	46.055	Cytoplasm, DV	D
		(P38545) GTP-binding nuclear protein Ran (GTPase Ran) (Ras-like protein TC4) RAN_PLAFA	24.875		D

		(Q94650) ADP-ribosylation factor ARF_PLAFA	20.912	Golgi apparatus, DV	D
		(Q00080) Elongation factor 1-alpha (EF-1-alpha) EF1A_PLAFK	49.041		D
		(P13568) Multidrug resistance protein MDR_PLAFF	162.252		D
		(P10988) Actin I ACT1_PLAFA	41.843	Cytoskeleton & DV	D
		(P14883) Actin II ACT2_PLAFA	42.679	Cytoskeleton & DV	D
		(P33948) ER lumen protein retaining receptor ERD2_PLAFA	26.447		D
		(P14643) Tubulin beta chain (Beta tubulin) TBB_PLAFK	49.751		D
		(Q8I3H7) T-cell immunomodulatory protein homolog precursor TIP_PLAF7	82.905	Membrane	D
		(P40282) Histone H2A H2A_PLAFA	14.122		I
		(Q04956) Probable cation-transporting ATPase 1 ATX1_PLAFA	230.286		D
		(P13830) Ring-infected erythrocyte surface antigen precursor RESA_PLAFF	124.907		D
		(P20147) Heat shock 90 kDa protein homolog (Fragment) HSP90_PLAFP	21.968	Cytoplasm	D
		(Q07785) Cell division control protein 2 homolog CDC2H_PLAFK	32.996	Cytoplasm	D
		(P13819) Merozoite surface protein 1 precursor MSP1_PLAFF	193.72		D
		(P04932) Merozoite surface protein 1 precursor (P190) MSP1_PLAFK	187.291		D
		(P13825) Aspartic acid-rich protein precursor ASP_PLAFS	30.248	Nucleus	D
		(Q27727) Enolase ENO_PLAFA	48.702	Cytoplasm	D
		(P50489) Apical membrane antigen 1 precursor AMA1_PLAFC	71.944	Membrane	D
		(Q02155) Hexokinase HXK_PLAFA	55.346		D
		(P34940) Chaperonin CPN60, mitochondrial precursor CH60_PLAFG	79.445		D
		(O15865) Calcium-dependent protein kinase 2 CDPK2_PLAFK	59.048	Myristoylation may target it to different subcellular compartments	D
		(P50647) Ribonucleoside-diphosphatereductase large chainRIR1_PLAFG	92.403		D
		(P34787) Tubulin gamma chain (Gamma tubulin) TBG_PLAFO	51.538		D
		(P30315) DNA polymerase delta catalytic subunit DPOD_PLAFK	126.884		D
		(Q05866) 78 kDa glucose-regulated protein homolog precursor	72.776		D

		GRP78_PLAFO			
		(P09593) S-antigen protein precursor SANT_PLAFV	35.500	PV	D
		(Q08853) Calcium-transporting ATPase (Calcium pump) ATC_PLAFK	139.415		D
		(P68875) Transmission-blocking target antigen S230 precursor S230_PLAFO	363.218		D
		(P12078) Heat shock 70 kDa protein PPF203 (Fragment) HSP73_PLAFA	23.058		D
		(P13922) Bifunctionaldihydrofolatereductase-thymidylate synthase DRTS_PLAFK	71.817		D
		(P21422) DNA-directed RNA polymerase beta' chain (EC 2.7.7.6) RPOC_PLAFA	69.406	Plastid, apicoplast	D
		(P27625) DNA-directed RNA polymerase III largest subunit (EC 2.7.7.6) RPC1_PLAFA	272.832		D
		(P04928) S-antigen protein precursor SANT_PLAFN	33.695	PV	D
C7	**Human**	(P68871) Haemoglobin beta chain HBB_HUMAN	15.998		I
		(P62805) Histone H4 H4_HUMAN	11.367		I
		(P11166) Solute carrier family 2, facilitated glucose transporter, member 1 GTR1_HUMAN	54.084		D
		(P11171) Protein 4.1 (Band 4.1) (P4.1) (EPB4.1) (4.1R) 41_HUMAN	97.017	Cytoskeleton & Nucleus	D
		(P69905) Haemoglobin alpha chain HBA_HUMAN	15.258		I
		(P62241) 40S ribosomal protein S8 RS8_HUMAN	24.205	Cytoplasm	D
		(P63261) Actin, cytoplasmic 2 (Gamma-actin) ACTG_HUMAN	41.793	Cytoplasm (cytoskeleton)	D
		(P02768) Serum albumin precursor ALBU_HUMAN	69.367		D
		(Q8WUD1) Ras-related protein Rab-2B RAB2B_HUMAN	24.214	ER membrane	D
		(Q15907) Ras-related protein Rab-11B (GTP-binding protein YPT3) RB11B_HUMAN	24.489	Cytoplasmic vesicle membrane	D
		(Q9NP58) ATP-binding cassette, sub-family B, member 6, mitochondrial precursor ABCB6_HUMAN	93.886	Mitochondria outer membrane,ER,Golgi	D

				apparatus	
		(P59190) Ras-related protein Rab-15 RAB15_HUMAN	24.391	Membrane	D
		(Q9H082) Ras-related protein Rab-33B RB33B_HUMAN	25.718	Golgi apparatus membrane	D
		(O95716) Ras-related protein Rab-3D RAB3D_HUMAN	24.267	Cell membrane	D
		(Q9NRW1) Ras-related protein Rab-6B RAB6B_HUMAN	23.462	Golgi apparatus membrane	D
		(P62826) GTP-binding nuclear protein Ran (GTPase Ran) (Ras-like protein TC4) RAN_HUMAN	24.423	Nucleus	D
		(P02730) Band 3 anion transport protein B3AT_HUMAN	101.792		D
		(P39023) 60S ribosomal protein L3 (HIV-1 TAR RNA binding protein B)RL3_HUMAN	46.109	Cytoplasm (nucleus,nucleolus)	D
		(P62988) Ubiquitin UBIQ_HUMAN demerged into P0CG47 (UBB_HUMAN), P0CG48 (UBC_HUMAN) P62979 (RS27A_HUMAN) P62987 (RL40_HUMAN)	25.762, 77.039, 17.965, 14.728		D
		(P62280) 40S ribosomal protein S11 RS11_HUMAN	18.431	Cytoplasm (ribosome)	D
		(P42330) Aldo-ketoreductase family 1 member C3 (EC 1.1.1.-) (Trans-1,2-dihydrobenzene-1,2-diol deh AK1C3_HUMAN	36.853	Cytoplasm	D
		(P08107) Heat shock 70 kDa protein 1 (HSP70.1) (HSP70-1/HSP70-2) HSP71_HUMAN	70.052	Cytoplasm	D
		(Q9Y6X8) Zinc fingers and homeoboxes protein 2 ZHX2_HUMAN	92.307	Nucleus	D
		(P27105) Erythrocyte band 7 integral membrane protein (Stomatin) (Protein 7.2b) STOM_HUMAN	31.731		D
		(P04406) Glyceraldehyde-3-phosphate dehydrogenase, liver G3P2_HUMAN	36.053	Cytosol, Nucleus, &cytoskeleton	D
		(P02261) Histone H2A.c/d/i/n/p (H2A.1) (H2A/c) (H2A/d) (H2A/i) (H2A/n) (H2A/p) (H2A.1b) H2AC_HUMAN	14.09		I

C25k	**Pf**	(P13819) Merozoite surface protein 1 precursor MSP1_PLAFF	193.72		D
		(P04932) Merozoite surface protein 1 precursor (P190) MSP1_PLAFK	187.291		D
		(P11144) Heat shock 70 kDa protein (HSP70) HSP70_PLAFA	74.287		D
		(Q08853) Calcium-transporting ATPase (Calcium pump) ATC_PLAFK	139.415		D
		(P13830) Ring-infected erythrocyte surface antigen precursor RESA_PLAFF	124.907		D
		(Q07805) Ornithine aminotransferase OAT_PLAFD	46.055		D
		(P33948) ER lumen protein retaining receptor ERD2_PLAFA	26.447		I
		(P40282) Histone H2A H2A_PLAFA	14.122		
		(Q8I3H7) T-cell immunomodulatory protein homolog precursor TIP_PLAF7	82.905		D
		(P14248) DNA-directed RNA polymerase II largest subunit RPB1_PLAFD	278.168		D
		(Q94660) 60S acidic ribosomal protein P0 RLA0_PLAF8	34.998	Ribosome	D
		(Q04956) Probable cation-transporting ATPase 1 ATX1_PLAFA	230.286		D
		(P16405) Octapeptide-repeat antigen (ORA) (Fragment) ORA_PLAFN	79.049		D
		(Q03400) S-antigen protein precursor SANT_PLAF7	62.947	PV	D
C25k	**Human**	(P68871) Haemoglobin beta chain HBB_HUMAN	15.998		
		(P27105) Erythrocyte band 7 integral membrane protein (Stomatin) (Protein 7.2b) STOM_HUMAN	31.731		D
		(P11166) Solute carrier family 2, facilitated glucose transporter, member 1 GTR1_HUMAN	54.084		D
		(P02768) Serum albumin precursor ALBU_HUMAN	69.367		D
		(P11678) Eosinophil peroxidase precursor PERE_HUMAN	81.040		D
		(P04004) Vitronectin precursor (Serum spreading factor) VTNC_HUMAN	54.306	In plasma (secreted)	D
		(P69905) Haemoglobin alpha chain HBA_HUMAN	15.258		
		(P62988) Ubiquitin UBIQ_HUMAN demerged into P0CG47 (UBB_HUMAN), P0CG48 (UBC_HUMAN) P62979 (RS27A_HUMAN) P62987 (RL40_HUMAN)	25.762, 77.039, 17.965, 14.728		I
		(Q9NR81) Rho guanine nucleotide exchange factor 3 ARHG3_HUMAN	59.783	Cytoplasm	D

		(P39023) 60S ribosomal protein L3 RL3_HUMAN	46.109		D
		(P02730) Band 3 anion transport protein B3AT_HUMAN	101.792		D
		(P55268) Laminin beta-2 chain precursor LAMB2_HUMAN	195.981	Extracellular space & matrix (secreted)	D
		(P08311) Cathepsin G precursor CATG_HUMAN	28.837	Cell membrane	I
		(P62805) Histone H4 H4_HUMAN	11.367		
		(O75131) Copine III CPNE3_HUMAN	60.131	Cytosol	D
S1	**Pf**	None			
S1	**Human**	(Q8WXH0) Nesprin 2 (Nuclear envelope spectrin repeat protein 2) SYNE2_HUMAN	796.442	Nucleus outer membrane	D
		(P99999) Cytochrome c CYC_HUMAN	11.749	Mitochondria intermembrane space	
		(Q15746) Myosin light chain kinase, smooth muscle and non-muscle isozymes MYLK_HUMAN	210.715	Cytoskeleton	D
		(Q92616) GCN1-like protein 1 (HsGCN1) GCN1L_HUMAN (Translational activator GCN1)	292.758	Ribosome (Ubiquitously expressed)	D
		(Q9NQ29) Putative RNA-binding protein Luc7-like 1 LUC7L_HUMAN	43.728	(Ubiquitous.) Nucleus	D
		(P51956) Serine/threonine-protein kinase Nek3 NEK3_HUMAN	57.705	Cytoplasm	D
S2	**Pf**	(P19214) Erythrocyte-binding antigen EBA-175 EBA1_PLAFC	167.390	Membrane	D
		(P04933) Merozoite surface protein 1 precursor (P195) MSP1_PLAFW	187.619		D
S2	**Human**	None			
S4	**Pf**	(Q9UAR6) Myosin A (PfM-A) MYOA_PLAFB	92.277		D
		(P13814) Circumsporozoite protein precursor (CS) CSP_PLAFT	45.611	Cell membrane	D

S4	**Human**	(Q14980) Nuclear mitotic apparatus protein 1 NUMA1_HUMAN	238.260	Nucleus	D
		(Q9Y3Y4) Pygopus homolog 1 PYGO1_HUMAN	45.116	Nucleus	D
		(P13727) Eosinophil granule major basic protein precursor EMBP_HUMAN	25.206		I
		(O14830) Serine/threonine protein phosphatase with EF-hands-2PPE2_HUMAN	86.518	Cytoplasm	D
		(Q9UIF7) A/G-specific adenine DNA glycosylaseMUTYH_HUMAN	60.069	Nucleus	D
		(Q9NRI5) Disrupted in schizophrenia 1 protein DISC1_HUMAN	93.611	Cytoskeleton	D
S5	**Pf**	(P14140) Tubulin beta chain (Beta tubulin) TBB_PLAFA	49.814	Cytoskeleton, DV	D
		(P24044) Calmodulin (CaM) CALM_PLAFA	16.931	Unknown	D
		(Q25998) DNA primase small subunit PRI1_PLAFK	53.489	Replisome	D
		(P22621) Apical membrane antigen 1 precursor	72.010	Membrane	D
S5	**Human**	(Q9BXT6) Potential helicase Mov10l1 M10L1_HUMAN	135.293	Unknown	D
		(P05164) Myeloperoxidase precursor PERM_HUMAN	83.869	Lysosome	D
		(P02748) Complement component C9 precursor CO9_HUMAN	63.173	Cell membrane	D
CHz	**Pf**	(Q00080) Elongation factor 1-alpha (EF-1-alpha) EF1A_PLAFK	49.041		D
		(P11144) Heat shock 70 kDa protein (HSP70) HSP70_PLAFA	74.287		D
		(P39898) Plasmepsin 1 precursor PLM1_PLAFA	51.461		D
		(P04934) Merozoite surface protein 1 precursor (P195) MSP1_PLAFC	196.198	Cell membrane	D
		(P04933) Merozoite surface protein 1 precursor (P195) MSP1_PLAFW	187.619	Cell membrane	D
		(P38545) GTP-binding nuclear protein Ran (GTPase Ran) (Ras-like protein TC4) RAN_PLAFA	24.874		I
		(Q07805) Ornithine aminotransferase OAT_PLAFD	46.055		D
		(P10988) Actin I ACT1_PLAFA	41.843		D
		(P14643) Tubulin beta chain (Beta tubulin) TBB_PLAFK	49.751		D
		(Q04956) Probable cation-transporting ATPase 1 ATX1_PLAFA	230.286		D
		(P40282) Histone H2A H2A_PLAFA	14.112		
		(P50647) Ribonucleoside-diphosphatereductase large chainRIR1_PLAFG	92.403		D
		(P13830) Ring-infected erythrocyte surface antigen RESA_PLAFF	124.907		D

		(P14883) Actin II ACT2_PLAFA	42.679		D
		(P13922) Bifunctionaldihydrofolatereductase-thymidylate synthase DRTS_PLAFK	71.817		D
		(P25805) Trophozoite cysteine proteinase precursor CYSP_PLAFA	66.880		D
		(Q8I3H7) T-cell immunomodulatory protein homolog precursor TIP_PLAF7	82.905		D
		(P25408) Hypothetical protein in calmodulin 3'region (Fragment)	28.100	Unknown	I
		(Q9UAR6) Myosin A (PfM-A) MYOA_PLAFB	92.277	Cell membrane	D
		(P16405) Octapeptide-repeat antigen (ORA) (Fragment) ORA_PLAFN	79.049		D
		(Q08210) Dihydroorotate dehydrogenase homolog, mitochondrial precursor PYRD_PLAFA	65.558		D
		(P34787) Tubulin gamma chain (Gamma tubulin) TBG_PLAFO	51.538		D
		(P16893) Thrombospondin related anonymous protein precursor TRAP_PLAFA	63.300	Cell membrane	D
		(P50250) Adenosylhomocysteinase SAHH_PLAF7	53.839	Cytoplasm, DV	D
CHz	**Human**	(P68871) Haemoglobin beta chain HBB_HUMAN	15.998		D
		(P27105) Erythrocyte band 7 integral membrane protein (Stomatin) (Protein 7.2b) STOM_HUMAN	31.731		D
		(P62805) Histone H4 H4_HUMAN	11.367		
		(P02768) Serum albumin precursor ALBU_HUMAN	69.367		D
		(P11166) Solute carrier family 2, facilitated glucose transporter, member 1 GTR1_HUMAN	58.084		D
		(P69905) Haemoglobin alpha chain HBA_HUMAN	15.258		
		(P02730) Band 3 anion transport protein B3AT_HUMAN	101.792		D
		(P13727) Eosinophil granule major basic protein precursor EMBP_HUMAN	25.206	Eosinophil granule	I
		(Q9Y6X8) Zinc fingers and homeoboxes protein 2 ZHX2_HUMAN	92.307		D
		(P62241) 40S ribosomal protein S8 RS8_HUMAN	24.205		I
		(P39023) 60S ribosomal protein L3 RL3_HUMAN	46.109		D
		(P62988) Ubiquitin UBIQ_HUMAN demerged into P0CG47 (UBB_HUMAN), P0CG48 (UBC_HUMAN) P62979 (RS27A_HUMAN)	25.762, 77.039, 17.965,		I

		P62987 (RL40_HUMAN)	14.728		
		(P08107) Heat shock 70 kDa protein 1 (HSP70.1) (HSP70-1/HSP70-2)HSP71_HUMAN	70.052		D
		(P59190) Ras-related protein Rab-15 RAB15_HUMAN	24.391		I
		(Q9H082) Ras-related protein Rab-33B RB33B_HUMAN	25.718		I
		(P61106) Ras-related protein Rab-14 RAB14_HUMAN	23.897	Early endosome membrane, golgi apparatus membrane	I
		(Q9NRW1) Ras-related protein Rab-6B RAB6B_HUMAN	23.462		I
		(P08311) Cathepsin G precursor CATG_HUMAN	28.837		I
		(P02261) Histone H2A.c/d/i/n/p (H2A.1) (H2A/c) (H2A/d) (H2A/i) (H2A/n) (H2A/p) (H2A.1b) H2AC_HUMAN	14.09		

Appendix 2

All 73 human proteins identified from sample Hs

Protein name	No. of unique peptide fragments	Subcellular location	Compartment
(P11166) Solute carrier family 2, facilitated glucose transporter, member 1 GTR1_HUMAN	4	Cell membrane	
(P02730) Band 3 anion transport protein (Anion exchange protein 1) B3AT_HUMAN	6		
(Q99569) Plakophilin 4 (p0071) PKP4_HUMAN	1		
(P27105) Erythrocyte band 7 integral membrane protein (Stomatin)STOM_HUMAN	5		
(O75131) Copine III CPNE3_HUMAN	1		
(Q13683) Integrin alpha-7 precursor (UNQ406/PRO768) ITA7_HUMAN	1		
(Q02094) Rhesus blood group-associated glycoprotein RHAG_HUMAN	1		
(O94973) Adapter-related protein complex 2 alpha 2 subunit AP2A2_HUMAN	1		
(Q8WUD1) Ras-related protein Rab-2B RAB2B_HUMAN	1		
(P59190) Ras-related protein Rab-15 RAB15_HUMAN	1		
(Q15907) Ras-related protein Rab-11B (GTP-binding protein YPT3)	1		
(P02768) Serum albumin precursor ALBU_HUMAN	2		
(Q9Y5I4) Protocadherin alpha C2 precursor (PCDH-alpha-C2) PCDC2_HUMAN	1		
(P25100) Alpha-1D adrenergic receptor (Alpha 1D-adrenoceptor ADA1D_HUMAN	1		
(Q8N511) Protein C17orf32 (transmembrane 199) CQ032_HUMAN	1		
(P08311) Cathepsin G precursor (EC 3.4.21.20) (CG) CATG_HUMAN	1		
O95716) Ras-related protein Rab-3D RAB3D_HUMAN	2		
(Q05996) Zonapellucida sperm-binding protein 2 precursor ZP2_HUMAN			
(P51956) Serine/threonine-protein kinase Nek3 (EC 2.7.1.37) (HSPK 3 NEK3_HUMAN	1		
(P02748) Complement component C9 precursor CO9_HUMAN	1		
(Q92545) RW1 protein (Transmembrane protein 131) RW1_HUMAN			
(P68871) Haemoglobin beta chain HBB_HUMAN	10	Cytosol	
(P69905) Haemoglobin alpha chain HBA_HUMAN	1		
(Q9H293) Interleukin-17E precursor (IL-17E) IL17E_HUMAN	1		

(P14778) Interleukin-1 receptor, type I precursor IL1R1_HUMAN	1	Cytosol	
(P42330) Aldo-ketoreductase family 1 member C3 (EC 1.1.1) AK1C3_HUMAN	1		
(P04406) Glyceraldehyde-3-phosphate dehydrogenase, liver (EC 1.2.1.12) (GAPDH) G3P2_HUMAN	1		
(P08107) Heat shock 70 kDa protein 1 (HSP70.1) HSP71_HUMAN	1		
(P13727) Eosinophil granule major basic protein precursor	2		
(Q9BXS1) Isopentenyl-diphosphate delta-isomerase 2 DI2_HUMAN	1		
(P63261) Actin, cytoplasmic 2 (Gamma-actin) ACTG_HUMAN	1		
(P11678) Eosinophil peroxidase precursor (EC 1.11.1.7) PERE_HUMAN	4		
(P14136) Glial fibrillary acidic protein, astrocyte GFAP_HUMAN	1		
(Q92844) TRAF family member-associated NF-kappa-B activator (TRAF-interacting protein) (I-TRAF) TANK_HUMAN	1		
(Q9NR81) Rho guanine nucleotide exchange factor 3 ARHG3_HUMAN	1		
(Q9NQ29) Putative RNA-binding protein Luc7-like 1 (SR+89) (Putative SR protein LUC7B1) LUC7L_HUMAN	1		
(P62241) 40S ribosomal protein S8 RS8_HUMAN	2		
(P62988) Ubiquitin (P0CG47,P0CG48,P62979,P62987)	1	Nucleus	
(P02261) Histone H2A.c/d/i/n/p (H2A.1) (H2A/c) (H2A/d) (H2A/i) (H2A/n) (H2A/p) (H2A.1b) H2AC_HUMAN; Demerged into P0C0S8 (H2A1_HUMAN)	1		
(P62805) Histone H4 H4_HUMAN	3		
(Q01543) Friend leukemia integration 1 transcription factor FLI1_HUMAN	1		
(P62826) GTP-binding nuclear protein Ran (GTPase Ran) (Ras-like protein TC4) RAN_HUMAN	1		
(O14830) Serine/threonine protein phosphatase with EF-hands-2 (EC 3.1.3.16) (PPEF-2) PPE2_HUMAN	1		
(Q9Y6X8) Zinc fingers and homeoboxes protein 2 ZHX2_HUMAN	1		
(Q9C0E2) Exportin 4 (Exp4) XPO4_HUMAN	1		
(P39023) 60S ribosomal protein L3 (HIV-1 TAR RNA binding protein B) (TARBP-B) (OK/SW-cl.32)	1		
(Q8WXH0) Nesprin 2 (Nuclear envelope spectrin repeat protein 2) SYNE2_	1		
(Q9Y3Y4) Pygopus homolog 1 PYGO1_HUMAN	1		

(Q9UIF7) A/G-specific adenine DNA glycosylase (EC 3.2.2.-) (MutY homolog) (hMYH) MUTYH_HUMAN			
(Q8WWR8) Sialidase 4 (EC 3.2.1.18) NEUR4_HUMAN	1	Lysosome	
(P05164) Myeloperoxidase precursor (EC 1.11.1.7) (MPO) PERM_HUMAN			
(Q8WUD1) Ras-related protein Rab-2B RAB2B_HUMAN	1	ER	
(Q9H082) Ras-related protein Rab-33B RB33B_HUMAN	1	Golgi	
(Q9NRW1) Ras-related protein Rab-6B RAB6B_HUMAN	1		
(P61106)Ras-related protein Rab-14 RAB14_HUMAN	2		
(Q9NP58) ATP-binding cassette, sub-family B, member 6, mitochondrial precursor ABCB6_HUMAN	1	Mitochondria	
(P99999) Cytochrome c CYC_HUMAN	1		
(Q99569) Plakophilin 4 (p0071) PKP4_HUMAN	1	Cytoskeleton	
(P27105) Erythrocyte band 7 integral membrane protein (Stomatin) (Protein 7.2b) STOM_HUMAN	5		
(P11171) Protein 4.1 (Band 4.1) (P4.1) (EPB4.1) (4.1R)	2		
(Q15124) Phosphoglucomutase-like protein 5 PGM5_HUMAN	1		
(Q05682) Caldesmon (CDM) CALD1_HUMAN			
(Q9NQT8) Kinesin-like protein KIF13B (Kinesin-like protein GAKIN) KI13B_HUMAN			
(Q15746) Myosin light chain kinase, smooth muscle and non-muscle isozymes (EC 2.7.1.117) MYLK_HUMAN	1		
(Q9NRI5) Disrupted in schizophrenia 1 protein DISC1_HUMAN			
(Q16352) Alpha-internexin (Alpha-Inx) (Neurofilament-66) (NF-66) AINX_HUMAN	1	Intermediate filament	
(P62280) 40S ribosomal protein S11 RS11_HUMAN		Ribosome	
(P12273) Prolactin-inducible protein precursor (Secretory actin-binding protein) PIP_HUMAN	1	Unknown	
(P04004) Vitronectin precursor (Serum spreading factor) (S-protein) (V75) VTNC_HUMAN	1		
(P55268) Laminin beta-2 chain precursor (S-laminin) LAMB2_HUMAN	1		
(Q92616) GCN1-like protein 1 (HsGCN1) GCN1L_HUMAN	1		
(Q9BXT6) Potential helicase Mov10l1 (EC 3.6.1) M10L1_HUMAN			

Appendix 3

P. falciparum proteins identified using X! Tandem search algorithm

Protein name	No. of unique peptides identified	Total no. of independent spectra
HSP70_PLAFA Heat shock 70 kDa protein	3	6
PLM1_PLAFA Plasmepsin-1	6	7
B0M0V9_PLAFA RhopH2	6	8
B3L435_PLAKH 40s ribosomal protein s11, putative	3	8
B3L4K2_PLAKH Histone H4	10	21
B3L4K3_PLAKH Histone H2B	2	2
B3LBQ3_PLAKH 60S ribosomal protein L24, putative	2	2
O77389_PLAF7 Formate-nitrate transporter, putative	7	23
Q4XSB6_PLACH 40S ribosomal protein S16	2	3
Q6T755_PLAFA Phosphoethanolamine N-methyltransferase	3	3
Q8I2Q0_PLAF7 Putative uncharacterized protein	2	3
Q8I488_PLAF7 PIESP2 erythrocyte surface protein	2	2
Q8IE85_PLAF7 60S ribosomal protein L6, putative	2	3
Q8IEJ0_PLAF7 Uncharacterized protein	4	9
Q8II36_PLAF7 Aquaglyceroporin OS	3	19
Q8ILE3_PLAF7 Putative uncharacterized protein	2	4
Q8IM15_PLAF7 HAP protein	3	4
ERD2_PLAFA ER lumen protein retaining receptor	2	3
RAN_PLAFA GTP-binding nuclear protein Ran	2	3
Q8I0P6_PLAF7 Elongation factor 1-alpha	3	5
OAT_PLAFD Ornithine aminotransferase	4	5
ARF1_PLAFO ADP-ribosylation factor 1	2	2
CRT_PLAF7 Putative chloroquine resistance transporter	5	18
Q9BHT6_PLAFA Small GTPase Rab2, putative	3	3
B3L7Q9_PLAKH 60S ribosomal protein L19	2	4

B3L9A1_PLAKH Ribosomal protein S3, putative	4	6
Q8I2X3_PLAF7 Acid phosphatase	7	9
C6KT11_PLAF7 Mitochondrial import receptor subunit tom40	3	4
Q8IKC8_PLAF7 Exp-2 protein	3	4
O97250_PLAF7 60S ribosomal protein L7, putative	3	11
Q8IJ34_PLAF7 Adenine nucleotide translocase	3	4
Q4YP98_PLABA Ribosomal protein L10, putative	4	9
Q8I305_PLAF7 Transporter, putative	2	3
Q8I431_PLAF7 60S ribosomal protein L4, putative	3	7
Q8I4R5_PLAF7 Rhoptry neck protein 3, putative	3	3
Q8I546_PLAF7 Conserved Plasmodium membrane protein	2	14
Q8IDH5_PLAF7 Thioredoxin-related protein, putative	5	22
Q8IFP2_PLAF7 40S ribosomal protein S19, putative	3	5
Q9NFS5_PLAFA Spermidine synthase	5	14
Q8IIU8_PLAF7 40S ribosomal protein S4, putative	3	4
Q8IJC6_PLAF7 60S ribosomal protein L3, putative	4	16
Q8ILE8_PLAF7 60S ribosomal protein L14, putative	3	5
Q8ILM8_PLAF7 Putative uncharacterized protein	3	3
Q8ILY8_PLAF7 Putative uncharacterized protein	4	7
Q8IBQ5_PLAF7 40S ribosomal protein S10, putative	2	2
Q8IBN5_PLAF7 40S ribosomal protein S5, putative	2	3
Q8IJR6_PLAF7 Putative uncharacterized protein	2	4
C0H4A6_PLAF7 Ribosomal protein L15 OS	3	9
Q8IDV0_PLAF7 Elongation factor 1-gamma, putative	2	2
Q8IM26_PLAF7 Putative uncharacterized protein	2	7
B3KZ74_PLAKH Rab18 GTPase, putative	2	2
P13568|MDR_PLAFF Multidrug resistance protein	2	2
Q9GRI2_PLAFA Protein disulfide isomerase	2	2
Q9TZT4_PLAFA Merozoite surface protein 1 OS	3	14
Q8IE80_PLAF7 Uncharacterized protein	3	4
Q4YNS1_PLABA Putative uncharacterized protein (Fragment)	2	4

Q8I502_PLAF7 40S ribosomal protein S17, putative	2	2
Q9U445_PLAFA P-type ATPase	2	2
Q9NIH9_PLAFA Nucleoside transporter 1	2	12
O77395_PLAF7 40S ribosomal protein S15A, putative	2	2
Q8IBY4_PLAF7 60S ribosomal protein L34-A, putative	2	2
Q8IJH8_PLAF7 Phospholipid scramblase 1, putative	2	3
Q8T6B1_PLAFA Glyceraldehyde-3-phosphate dehydrogenase (Fragment)	1	1
Q9GVA9_PLAFA Conserved Plasmodium protein	1	1
Q8IDR9_PLAF7 40S ribosomal protein S6, putative	1	1
Q4YSE1_PLABA 40S ribosomal protein S3a	1	3
Q8II62_PLAF7 60S ribosomal protein L38e, putative	1	1
B3L086_PLAKH 60S ribosomal protein L11a	1	2
B3LAS9_PLAKH 40S ribosomal protein S8	1	2
Q8I490_PLAF7 Putative uncharacterized protein	1	2
Q8IJU2_PLAF7 Conserved Plasmodium protein	1	1
Q8IJK8_PLAF7 60S ribosomal protein L30e, putative	1	1
B3L8I9_PLAKH GTP-binding protein, putative	1	1
Q8II93_PLAF7 Protein phosphatase, putative	1	3
Q8IDB0_PLAF7 40S ribosomal protein S13, putative	1	1
P40282|H2A_PLAFA Histone H2A	1	8
B3L9U8_PLAKH Ribosomal protein S2, putative	1	1
B3L6W2_PLAKH Ubiquitin/ribosomal fusion protein uba52 homologue, putative	1	2
B3L3J3_PLAKH DNA/RNA-binding protein, putative	1	1
Q8I433_PLAF7 Rhomboid protease ROM4	1	1
B3L2Q6_PLAKH RNA-binding protein, putative	1	1
TIP_PLAF7 T-cell immunomodulatory protein homolog	1	1
Q8IAU7_PLAF7 Putative uncharacterized protein	1	1
B3L9V6_PLAKH Leucineaminopeptidase, putative	1	1
C6KSQ7_PLAF7 Long chain polyunsaturated fatty acid elongation enzyme, putative	1	2

B3L567_PLAKH Ribosomal protein s18, putative	1	2
Q8I0U9_PLAF7 Triose phosphate transporter	1	1
B3L2G4_PLAKH Major facilitator, transporter protein,putative	1	1
K6ULC9_9APIC Protein transport protein Sec61 alpha subunit (Fragment)	1	1
Q8IDF7_PLAF7 V-type ATPase, putative	1	1

Appendix 4

P. falciparum proteins identified from sample Hd

Protein name	No. of unique peptide fragments	Subcellular location
(P25408) Hypothetical protein in calmodulin 3'region (Fragment) (QueuinetRNA-ribosyltransferase-like protein)	1	unknown
(P16893) Thrombospondin related anonymous protein	1	Cell membrane
(P50250) Adenosylhomocysteinase	1	Cytoplasm and DV
(Q8I3H7) T-cell immunomodulatory protein homolog precursor	3	Cell membrane
(Q00080) Elongation factor 1-alpha	5	Cytoplasm
(P11144) Heat shock 70 kDa protein	8	DV
(P39898) Plasmepsin 1 precursor	5	DV
(P04932) Merozoite surface protein 1	5	Cell membrane,DV
(P38545) GTP-binding nuclear protein Ran (GTPase Ran)	4	Nucleus & DV
(Q07805) Ornithine aminotransferase	4	Cytosol & DV
(P10988) Actin I	2	Cytoskeleton DV
(P14643) Tubulin beta chain (Beta tubulin)	2	Cytoskeleton,DV
(Q04956) Probable cation-transporting ATPase 1	3	Cell membrane
(P40282) Histone H2A	3	Nucleus
(P50647) Ribonucleoside-diphosphatereductase large chain	2	Unknown
(P13830) Ring-infected erythrocyte surface antigen	5	Cell membrane,DV
(P14883) Actin II	1	Cytoskeleton, DV
(P13922) Bifunctionaldihydrofolatereductase-thymidylate synthase	3	Unknown
(P25805) Trophozoite cysteine proteinase precursor	2	Unknown
(Q8I3H7) T-cell immunomodulatory protein homolog precursor	3	Cell membrane
(Q9UAR6) Myosin A	2	Cell membrane
(P16405) Octapeptide-repeat antigen	2	PV
(Q08210) Dihydroorotate dehydrogenase homolog, mitochondrial precursor	2	Mitochondria
(P34787) Tubulin gamma chain (Gamma tubulin) TBG_PLAFO	2	Cytoskeleton

Human Proteins identified from sample Hd

Human proteins	No. of unique peptide fragments	Subcellular location
(P13727) Eosinophil granule major basic protein precursor	2	Cell membrane
(P61106) Ras-related protein Rab-14	2	Golgi apparatus
(P68871) Haemoglobin beta chain	10	Gytosol
(P27105) Erythrocyte band 7 integral membrane protein (Stomatin)	5	Cytoskeleton
(P62805) Histone H4	3	Nucleus
(P02768) Serum albumin precursor	2	Cell membrane
(P11166) Solute carrier family 2, facilitated glucose transporter,	4	Cell membrane
(P69905) Haemoglobin alpha chain	1	Cytosol
(P02730) Band 3 anion transport protein	6	Cell membrane
(Q9Y6X8) Zinc fingers and homeoboxes protein 2	1	Nucleus
(P62241) 40S ribosomal protein S8	2	Nucleus
(P39023) 60S ribosomal protein L3 (HIV-1 TAR RNA binding protein B)	1	Nucleus
(P62988) Ubiquitin (P0CG47) (UBB_HUMAN),P0CG48(UBC_HUMAN),P62979 (RS27A_HUMAN) P62987 (RL40_HUMAN)	1	Nucleus
(P08107) Heat shock 70 kDa protein 1	1	Cytosol
(P59190) Ras-related protein Rab-15	1	Cell membrane
(Q9H082) Ras-related protein Rab-33B	1	Golgi apparatus
(Q9NRW1) Ras-related protein Rab-6B	1	Golgi apparatus
(P08311) Cathepsin G precursor	1	Cell membrane
(P02261) Histone H2A.c/d/i/n/p (H2A.1) (H2A/c) (H2A/d) (H2A/i) (H2A/n) (H2A/p) (H2A.1b) H2AC_HUMAN	1	Nucleus